Doctoral Dissertation
Doctoral Program in Energy Engineering (37th Cycle)

# Characterization of hydrogen mixing and combustion properties in spark ignition engines investigated through optical techniques

By

**Giovanni Cecere**

* * * * * *

**Supervisor(s):**
Prof. Federico Millo, Academic Supervisor
Prof. Luciano Rolando, Academic Co-Supervisor
Dr. Simona Silvia Merola, CNR Supervisor
Dr. Eng. Adrian Irimescu, CNR Co-Supervisor

**Doctoral Examination Committee:**
Prof. Santiago Daniel Martinez Boggio
Prof. Michele Battistoni
Prof. Adrian Clenci
Prof. Stanislaw Szwaja
Prof. Alessandro D'Adamo

Politecnico di Torino
2025

## Declaration

I hereby declare that, the contents and organisation of this dissertation constitute my own original work and does not compromise in any way the rights of third parties, including those relating to the security of personal data.

Giovanni Cecere
16/12/2024

# List of Publications

- Irimescu, A., Cecere, G., and Sementa, P., "Combustion Phasing Indicators for Optimized Spark Timing Settings for Methane-Hydrogen Powered Small Size Engines," SAE Technical Paper 2022-01-0603, 2022, https://doi.org/10.4271/2022-01-0603.
- Cecere, G. (2024). Hydrogen as Fuel for ICEs: State of Art and Technological Challenges. Journal of Engineering, 2024(1), 9930258. https://doi.org/10.1155/2024/9930258.
- Merola, S.S., Irimescu, A., Cecere, G. (2025). 0D/1D Modeling of Lean-Burn Conditions in a Hydrogen SI Engine for Closer Correlation of In-Cylinder Chemical Species with Optical Data. In: Chiru, A., Covaciu, D. (eds) CONAT 2024 International Congress of Automotive and Transport Engineering. CONAT 2024. Proceedings in Automotive Engineering. Springer, Cham. https://doi.org/10.1007/978-3-031-77627-4_1.
- Cecere, G., Mats, A., Merola, S.S., Irimescu, A., Vaglieco, B.M., Analysis of structure and velocity of jets from gas fuel injectors using PIV, under review at journal of Flow, Turbulence and Combustion, Springer.

To everyone who supported me.

And to you, Ida

# Acknowledgment

Beyond myself, this experience could have been very different without the right people in the right place to guide me. PhD is sometimes told just as a series of challenges and a stressful experience, not for me. Regardless of what the future holds for me, I will never forget these past three years.

To Dr. Merola and Dr. Irimescu, for the way you made me live this choice,
Prof. Millo and Prof. Rolando for including me in the PoliTO research group
and thanks to Prof. Andersson, for the time you spent helping me with PIV lab.

# Summary

This doctoral thesis scrutinises in detail multiple aspects concerning the use of hydrogen in Internal Combustion Engines (ICEs), as a suitable alternative to conventional liquid fuels such as gasoline and diesel. The achievements of the last three years of research activity performed by the author are resumed within this text. The scientific contribution to the treated topic is supported by the results obtained by applying different techniques and methodologies. The reason for this activity is probably well known to most readers; for those not completely familiar with this specific research field, the question can be broadly resumed with a single word: transition. Transition because hydrogen is part of a larger process, full of uncertainties and consequent mutable scenarios which render quite difficult to predict exactly what role it will play. Therefore, hydrogen occupies a delicate "position", where the line between practical application and theory is very thin and debated in many scientific papers.

Experimental activities constitute the core of this thesis, and they covered multiple aspects that ranged from the fundamental analysis of gaseous jet distribution through the use of a sophisticated optical technique, i.e. particle image velocimetry (PIV), to the practical application of hydrogen in an optically accessible single cylinder engine. In this way, the discussion covers both non-reacting (PIV) and reacting ($H_2$-ICE) activities.

The non-reacting investigations implied the use of helium gas as a hydrogen substitute. Experimental tests were carried out inside a constant volume chamber with an injector mounted on the top wall. The injector modularity made it possible to change the tip with three different nozzle geometries. Depending on the operating conditions, the injection pressure ranged from a minimum of 5 up to 20 bar, while the pressure inside the chamber was swept from atmospheric to 7 bar. Green light from a dual cavity Nd:YAG laser was used as luminous source and a

4-megapixel PIV-camera for the image capture. Vegetable oil particles have been seeded inside the chamber and used as particle tracers. The test campaign planned during the research stage period at Chalmers University of Technology, involved the acquisition of a large dataset. Given the technical characteristics of the injector, most of the selected cases featured low-pressure conditions, representative of fuel delivery during the intake stroke; tests with higher injection pressure can be seen as closer to injection during the compression stroke, i.e. with the intake valves closed. The large number of conditions resulted in a comprehensive analysis capable of providing valuable insight on the role of nozzle tip geometry, as well as the capability of a certain configuration to ensure longer jet penetration or the formation of vortex structures that improve air entertainment.

The reacting analysis (i.e. combustion in a spark ignition engine) was implemented as part of two different experimental test campaigns. The first set of operative conditions entailed the use of hydrogen - methane blends (in various ratios); the second set of data involved the use of pure hydrogen as fuel. $H_2$ delivery (as well as that of $CH_4$–$H_2$ blends) was performed via port fuel injection (PFI) and the engine speed was varied from 1000 to 2000 rpm. The duration of injection was swept to ensure a relative air-fuel ratio ($AFR_{rel}$) range from 1.9 to 3.6. The experimental setup allowed digital imaging to be applied in cycle resolved mode by using a CMOS high speed camera, and natural emission spectroscopy was implemented with an ICCD camera coupled with a spectrometer. The digital imaging data was used for the evaluation of flame front properties in terms of morphological parameters and how these variables relate with the cycle-to-cycle evolution of combustion. This analysis covered the process from kernel inception to the fully developed flame stage, thus providing comprehensive understanding of flame development patterns. Optical Emission Spectroscopy (OES) was employed for identifying atomic and molecular species; specifically, Spark Induced Breakdown Spectroscopy (SIBS) was implemented for the investigation of molecular $H_2$ related emissions. Balmer α and Fulcher α

bands were examined throughout the ignition phase after spark timing and their intensity correlated to the local fuel concentration.

# Contents

List of Figures ..... i
List of appendix Figures ..... vi
List of Equations ..... vi
List of Tables ..... vii
Nomenclature ..... viii

1. Introduction ..... 1

1.1 World energy outlook ..... 1
1.2 Why hydrogen does have a future? ..... 5
1.3 Hydrogen for road transport technologies ..... 7
1.4 $H_2$, the fuel for tomorrow's ICEs? ..... 9

2. Hydrogen in SI engines ..... 11

2.1 Bi-fuel operation ..... 11

2.1.1 Hydrogen – Methane ..... 11
2.1.2 Hydrogen – Gasoline ..... 12

2.2 Hydrogen operations ..... 13

2.2.1 PFI configuration ..... 13
2.2.2 DI configuration ..... 14

2.3 NOx: Emissions and mitigation strategies ..... 15
2.4 Combustion Anomalies ..... 16

2.4.1 Preignition ..... 17
2.4.2 Knock ..... 17
2.4.3 Backfire ..... 18

2.5 Hydrogen mixing properties ..... 20

2.5.1 $H_2$ substitutes, definition and properties ..... 20
2.5.2 Gaseous jet model and current state of art ..... 21

2.6 Optical technique for characterizing $H_2$ combustion ..... 24
2.7 Thesis Objectives ..... 27

3. Experimental setup ..... 29

3.1 Research engine ..... 29

3.1.1 Engine technical specifications ..... 29
3.1.2 Data acquisition system and layout ..... 31
3.1.3 Optical setup ..... 32
3.2 PIV measurement activity ..... 34
3.2.1 Constant volume chamber ..... 35
4. Non-reactive analysis results ..... 38
4.1 Velocity magnitude ..... 39
4.2 Vector plots analysis ..... 49
4.2.1 1st Nozzle pattern ..... 52
4.2.2 2nd Nozzle pattern ..... 54
4.2.3 3rd Nozzle pattern ..... 56
4.3 Vorticity intensity ..... 58
4.4 Jet morphology ..... 59
5. Reactive analysis results ..... 63
5.1 Rate of heat release analysis ..... 63
5.2 Methane – Hydrogen: Thermodynamic parameters ..... 65
5.2.1 Cycle-to-cycle performance and variability ..... 67
5.3 Methane – Hydrogen: Flame morphology analysis ..... 69
5.3.1 Early stages ..... 70
5.3.2 Flame rapid burning ..... 75
5.4 Hydrogen: Thermodynamic parameters ..... 98
5.5 Hydrogen: Flame imaging ..... 106
5.5.1 Morphological analysis ..... 107
5.5.2 Luminosity analysis ..... 116
5.6 Hydrogen: Optical Emission Spectroscopy analysis ..... 124
6. Summary and conclusions ..... 131
6.1 Non – reactive study conclusions ..... 131
6.2 Reactive study conclusions ..... 133
6.2.1 Thermodynamic-based outcomes ..... 133
Methane – Hydrogen blends ..... 133
Hydrogen ..... 133

6.2.2 Morphological analysis results ..... 134
Methane – Hydrogen blends ..... 134
Hydrogen ..... 134
6.2.3 Spectroscopic-based outcomes ..... 135
7. References ..... 137
8. Appendix A ..... 149
A.1 Research engine calibration and optical setup ..... 149
A.2 Optical emission spectroscopy ..... 153
9. Appendix B ..... 158
B.1 PIV optical technique: applied methodology ..... 158

# List of Figures

Figure 1. Prices for oil, natural gas and coal, January 2019 to September 2023 (Covid-19 spreading and Russia – Ukraine conflict highlighted by the red lines) [1].....1
Figure 2. Global investment by energy source [1].....2
Figure 3. Green hydrogen current production costs (top), forecast by 2030 (middle) and 2050 (bottom) [5]. .....5
Figure 4. Typical efficiency characteristics for FC system (red line) and H2-ICE (blue line).....8
Figure 5. Cross-sectional view of the single-cylinder research engine used for the experiments described in this doctoral thesis. .....15
Figure 6. Example of backfire recorded (red line) during test at 3000 rpm, ER=0.9, spark timing 38 CAD bTDC [57].....19
Figure 7. Example of schlieren imaging, adapted from [66], (left) and vector plot obtained from the PIV analysis (right). .....22
Figure 8. Diagram of the front of a starting plume [72]. .....24
Figure 9. Averaged electrical discharge characteristics for stoichiometric methane-air mixtures ignited at 10 bar, indicating the breakdown- (blue), arc- (red) and glow-phases (green). Adapted from [85]. .....26
Figure 10. Experimental setup and its components. .....32
Figure 11. Side-view of the research engine – high-speed camera setup. .....33
Figure 12. Schematization with the location of the spectroscopic regions of interest.....34
Figure 13. Schematization of the experimental setup used for PIV measurements (top) and nozzle tip patterns (bottom).....37
Figure 14. Velocity distribution at 3.4 ms aSOE, GEO-1. Single pair of frames (left) and averaged frames (right) PR10. .....40
Figure 15. Velocity distribution, GEO-1, averaged frames PR4. .....41
Figure 16. Velocity distribution, GEO-1, averaged frames PR20. .....42
Figure 17. Velocity distribution, GEO-2, averaged frames PR4. .....43
Figure 18. Velocity distribution, GEO-2, averaged frames PR20. .....44
Figure 19. Velocity distribution, GEO-3, averaged frames PR4. .....46
Figure 20. Velocity distribution, GEO-3, averaged frames PR20. .....47

Figure 21. Average velocity peaks for the three nozzle patterns at different PRs. 48
Figure 22. Vector plot (left) at 5.0 ms aSOE. PR4, single pair of frames. .....51
Figure 23. GEO-1, vector plot (left) and vorticity intensity (right) at 3.4, 4.0 and 5.0 ms aSOE. PR4, averaged data. .....53
Figure 24. GEO-2, vector plot (left) and vorticity intensity (right) at 3.4, 4.0 and 5.0 ms aSOE. PR4, averaged data. .....55
Figure 25. GEO-3, vector plot (left) and vorticity intensity (right) at 3.4, 4.0 and 5.0 ms aSOE. PR4, averaged data. .....57
Figure 26. Average vorticity peaks for the three nozzle patterns at different PRs. .....58
Figure 27. Helium jet penetration for different PRs. .....60
Figure 28. Example of half plume angle measurement procedure, 2nd nozzle pattern, PR5, 4ms aSOE, averaged frames. .....61
Figure 29. Helium jet plume angle for different PRs. .....62
Figure 30. In-cylinder pressure traces (solid lines) and mass fraction burnt (dashed lines). λ 1.0, spark timing 10 CAD bTDC. .....66
Figure 31. In-cylinder pressure traces (solid lines) and mass fraction burnt (dashed lines). λ 1.3, blend 50% $CH_4$ – 50% $H_2$. .....67
Figure 32. IMEP and COV-IMEP. λ 1.0, spark timing 10 CAD bTDC. .....68
Figure 33. IMEP and COV-IMEP. λ 1.3, blend 50%$CH_4$ – 50%$H_2$. .....69
Figure 34. Flame kernel position (100%$CH_4$ top, 80 % $CH_4$ – 20 % $H_2$ at middle and 50 % $CH_4$ – 50% $H_2$ bottom), and corresponding radial distribution (right column). .....71
Figure 35. Kernel Feret Diameter and percentage of empty frames. λ 1.0, spark timing 10 CAD bTDC. .....72
Figure 36. Flame kernel position (ST10 on top, ST15 at middle and ST20 at bottom), and corresponding distribution (right column). λ 1.3, blend 50%$CH_4$ – 50%$H_2$. .....74
Figure 37. Kernel Feret Diameter and percentage of empty frames. λ 1.3, blend 50%$CH_4$ – 50%$H_2$. .....74
Figure 38. Coloured flame front intensity (8-bit). λ 1.0, 100% $CH_4$, averaged data. .....76
Figure 39. Coloured flame front intensity (8-bit). λ 1.0, 80% $CH_4$ – 20% $H_2$, averaged data. .....77

Figure 40. Coloured flame front intensity (8-bit). λ 1.0, 50% $CH_4$ – 50% $H_2$, averaged data. ....78
Figure 41. Flame area development (top), Max Feret Diameter (middle) and Heywood circularity factor (Bottom). 1.0, spark timing 10 CAD bTDC. ....80
Figure 42. Flame front speed profiles along X-Y axes. λ 1.0, spark timing 10 CAD bTDC. ....82
Figure 43. Maximum luminosity gradient over X (top) and Y (bottom) direction. λ 1.0, spark timing 10 CAD bTDC. ....83
Figure 44. Luminosity signal along horizontal direction (left) and vertical (right). Time steps 2.4 – 7.2 – 12.0 CAD aST. 100% $CH_4$ (Black), 80% $CH_4$ – 20%$H_2$ (Blue) and 50%$CH_4$ – 50%$H_2$ (Red).....84
Figure 45. Luminosity signal along horizontal direction (left) and vertical (right). Time steps 16.8 – 21.6 – 26.4 CAD aST. 100% $CH_4$ (Black), 80% $CH_4$ – 20%$H_2$ (Blue) and 50%$CH_4$ – 50%$H_2$ (Red).....86
Figure 46. Overall luminosity evolution (solid lines) and corresponding standard deviation (dashed lines). λ 1.0, spark timing 10 CAD bTDC. ....87
Figure 47. Coloured flame front intensity (8-bit). λ 1.3, blend 50%$CH_4$ – 50%$H_2$, ST10. ....89
Figure 48. Coloured flame front intensity (8-bit). λ 1.3, blend 50%$CH_4$ – 50%$H_2$, ST15. ....90
Figure 49. Coloured flame front intensity (8-bit). λ 1.3, blend 50%$CH_4$ – 50%$H_2$, ST20. ....91
Figure 50. Flame area development (top), Max Feret Diameter (middle) and Heywood circularity factor (Bottom). λ 1.3, 50% $CH_4$ – 50% $H_2$. ....93
Figure 51. Flame front speed profiles along X-Y axes. λ 1.3, blend 50% $CH_4$ – 50% $H_2$. ....94
Figure 52. Maximum luminosity gradient over X (top) and Y (bottom) direction. λ 1.3, blend 50% $CH_4$ – 50% $H_2$. ....95
Figure 53. Luminosity signal along horizontal direction (left) and vertical (right). Time steps 2.4 – 7.2 – 12.0 CAD aST. 50% $CH_4$ – 50% $H_2$, ST10 (Black line), ST15 (Blue line) and ST20 (Red line). ....96
Figure 54. Luminosity signal along horizontal direction (left) and vertical (right). Time steps 16.8 – 21.6 – 26.4 CAD aST. 50% $CH_4$ – 50% $H_2$, ST10 (Black line), ST15 (Blue line) and ST20 (Red line). ....97

Figure 55. Overall luminosity evolution (solid lines) and corresponding standard deviation (dashed lines). λ 1.3, 50% $CH_4$ – 50% $H_2$.....98
Figure 56. Cylinder pressure traces (solid lines) and mass fraction burnt (dashed lines), 1000rpm, λ 2.6. .....100
Figure 57. Cylinder pressure traces (solid lines) and mass fraction burnt (dashed lines), 1000rpm, λ 2.3. .....101
Figure 58. Cylinder pressure traces (solid lines) and mass fraction burnt (dashed lines), 1000rpm, λ 2.1. .....101
Figure 59. Cylinder pressure traces (solid lines) and mass fraction burnt (dashed lines), 1000rpm, λ 2.0. .....102
Figure 60. Cylinder pressure trace (solid line) and mass fraction burnt (dashed line), 1000rpm, λ 1.9.....102
Figure 61. IMEP and COV-IMEP, 1000 rpm. .....103
Figure 62. Cylinder pressure trace (solid line) and mass fraction burnt (dashed line), 2000rpm, λ 3.6.....104
Figure 63. Cylinder pressure traces (solid lines) and mass fraction burnt (dashed lines), 2000rpm, λ 3.0. .....104
Figure 64. Cylinder pressure traces (solid lines) and mass fraction burnt (dashed lines), 2000rpm, λ 2.6. .....105
Figure 65. Cylinder pressure trace (solid line) and mass fraction burnt (dashed line), 2000rpm, λ 2.3.....105
Figure 66. IMEP and COV-IMEP, 2000 rpm. .....106
Figure 67. Flame centre coordinates (top) and maximum dislocation (bottom). Hydrogen, 1000 rpm. .....110
Figure 68. Flame centre coordinates (top). Hydrogen, 2000 rpm.....111
Figure 69. Flame area development (top) and Clamp Y/X (bottom). Hydrogen, 1000 rpm. .....112
Figure 70. Flame area development (top) and Clamp Y/X (bottom). Hydrogen, 2000 rpm. .....114
Figure 71. Flame front speed profiles along X-Y axes. Hydrogen, 1000rpm (top) and 2000 rpm (bottom). .....115
Figure 72. Luminous signal coming from flame front, 1000rpm, λ 2.0, ST05 - 10 and λ 1.9 ST05. .....117

Figure 73. Luminous signal coming from flame front, 2000rpm, λ 2.6, ST10-20 and λ 2.3 ST10. ..... 118
Figure 74. Luminosity traces; hydrogen, 1000rpm. ..... 120
Figure 75. Luminosity standard deviation; hydrogen, 1000rpm. ..... 120
Figure 76. IMEP vs ∑Lum (top), Pmax vs ∑Lum (middle) and COV-IMEP vs St.Dv. Luminosity (bottom); hydrogen, 1000rpm. ..... 123
Figure 77. Luminosity traces (top) and related standard deviation (bottom). Operative conditions at 2000rpm. ..... 124
Figure 78. Single cycle spectrum acquisition; 2000 rpm, λ 3.2, spark timing 10 CAD bTDC, acquisition timing from 8 to 32 μs aST. ..... 126
Figure 79. Average spectrum acquisition on 100 cycles. Operative condition; 2000 rpm, λ 3.2, Spark timing 10 CAD bTDC. Acquisition time 400μs aST. ..... 127
Figure 80. Evolution of $H_2$ Fulcher intensity (average on 100 cycles) after the spark timing (10 CAD bTDC) recorded at 2000 rpm.; comparison of emissions (top) at fixed λ (3.2) with the corresponding secondary current signal and (bottom) at different λ values. All intensities were normalised to the absolute maximum. 128
Figure 81. $H_2$ Fulcher intensity (average on 100 cycles) at different times after the spark timing (10 CAD bTDC) recorded at 2000 rpm versus the measured λ values. All intensities were normalised to the absolute maximum. ..... 129
Figure 82. $H_2$ Fulcher α average intensity at 1000 and 2000 rpm. Acquisition time 1000 μs. ..... 129

# List of appendix Figures

Figure A.1 Bowditch design piston (left) and conventional counterpart (right). 150
Figure A.2. Teflon – bronze deposits on the piston quartz window. ..... 150
Figure A.3. Backfire – Misfire phenomena (left column) and subsequent knocking occurrence (middle – right columns). ..... 151
Figure A.4. Sequence of steps applied for image processing: original raw data, circular mask and gamma/brightness improvement, image binarization, FFT correction. ..... 152
Figure A. 5 Energy levels of Hydrogen atom with the wavelength associated to each emission line of the different series. ..... 154
Figure A. 6. Example of an energy level diagram of Hydrogen molecule [111]. 155
Figure A. 7. Molecular excitation and radiation for the ground state and two excited states of molecular hydrogen [111]. ..... 156
Figure A. 8. $H_2$ plasma spectrum detected at 2Pa gas pressure. From [114]. ..... 157
Figure A. 9. Typical UV-Visible emission spectrum detected in region near the plug in the first 16μs after the spark timing fixed at 10 CAD BTDC (engine speed 2000 rpm and $\lambda \cong 3.2$). ..... 157

Figure B.1. Steps of the PIV image post processing procedure. ..... 160
Figure B.2. Influence of the interrogation area dimension on vector distribution (left) and velocity magnitude (right). ..... 161
Figure B. 3 Edge detection for first geometry. Operative condition:4.0 ms aSOE, PR5, Single pair of frames. ..... 162

# List of Equations

Eq. 1 ..... 49
Eq. 2 ..... 49
Eq. 3 ..... 64
Eq. 4 ..... 64
Eq. 5 ..... 127

# List of Tables

Table 1. Fuels properties at 298K and 1 atm *(except CNG at 250 bar).....9
Table 2. Engine Specifications. .....30
Table 3. PIV experimental operative cases.....39
Table 4. Average velocity peaks recorded at 8.0 ms aSOE. .....49
Table 5. Average vorticity peaks recorded at 8.0 ms aSOE. .....59
Table 6. Methane – Hydrogen operative conditions.....65
Table 7. Hydrogen thermodynamic operative conditions.....99
Table 8. Flame morphology analysis of hydrogen fuelled cases. .....107
Table 9. Hydrogen, optical operative cases, luminosity. .....116
Table 10. Test cases for spectroscopic investigations. .....125

# Nomenclature

| | |
|---|---|
| **AC** | Auto Contrast |
| **$AFR_{rel}$** | Air Fuel Ratio relative |
| **BEV** | Battery Electric Vehicle |
| **BTE** | Brake Thermal Efficiency |
| **CAD** | Crank Angle Degree |
| **CCUS** | Carbon Capture Utilization and Storage |
| **CCV** | Cycle to Cycle Variability |
| **CFR** | Cooperative Fuel Research |
| **CI** | Compression Ignition |
| **CLAHE** | Contrast Limited Adaptive Histogram Equalization |
| **CMOS** | Complementary Metal Oxide Semiconductor |
| **CNG** | Compressed Natural Gas |
| **COP** | Conference of the Parties |
| **COV** | Coefficient Of Variation |
| **DI** | Direct Injection |
| **DOI** | Duration Of Injection |
| **EGR** | Exhaust Gas Recirculation |
| **EV** | Electric vehicle |
| **EV** | Exhaust Valve |
| **EVC** | Exhaust Valve Closing |
| **EVO** | Exhaust Valve Opening |
| **FC** | Fuel Cell |
| **FD** | Feret Diameter |
| **FFT** | Fast Fourier Transform |
| **HCF** | Heywood Circularity factor |
| **HRR** | Heat Release Rate |
| **IA** | Interrogation Area |
| **ICCD** | Intensified Charge Coupled Device |
| **ICE** | Internal Combustion Engine |
| **IEA** | International Energy Agency |
| **IMEP** | Indicated Mean Effective Pressure |
| **IV** | Intake Valve |

| | |
|---|---|
| **IVC** | Intake Valve Closing |
| **IVO** | Intake Valve Opening |
| **LEL** | Lower Explosion Limit |
| **LPP** | Location of Pressure Peak |
| **MFB** | Mass Fraction Burnt |
| **MN** | Methane Number |
| **MON** | Motor Octane Number |
| **MPRR** | Maximum Pressure Rise Rate |
| **NDC** | Nationally Determined Contribution |
| **NHRR** | Net Heat Release Rate |
| **NI** | National Instrument |
| **PEMFC** | Proton Exchange Membrane Fuel Cell |
| **PFI** | Port Fuel Injection |
| **PIV** | Particle Image Velocimetry |
| **PLIF** | Planar Light Image Fluorescence |
| **PM** | Particle Matter |
| **PR** | Pressure Ratio |
| **ROI** | Region Of Interest |
| **RON** | Research Octane Number |
| **Rpm** | radius per minute |
| **RSD** | Rainbow Schlieren Reflectometry |
| **SCRAMJET** | Supersonic Combustion Ramjet |
| **SDC** | Spark Discharge Characteristic |
| **SI** | Spark Ignition |
| **SIBS** | Spark Ignition Breakdown Spectroscopy |
| **SMR** | Steam Methane Reforming |
| **SOE** | Start Of Energization |
| **SOFC** | Solix Oxide Fuel Cell |
| **ST** | Spark Timing |
| **TDC** | Top Dead Centre |
| **UEGO** | Universal Exhaust Gas Oxygen |
| **WG** | Wall Guided |
| **λ** | Lambda |
| **Φ** | Equivalent Ratio |

# Chapter 1

# Introduction

## 1.1 World energy outlook

The world, as well as the energy sector, has been strongly shaken in recent years, first by the Covid-19 pandemic spread, then by Russia's invasion of Ukraine, showing the fragility of an interconnected system where major economies are far from being immune to other countries' policies and national instabilities (See Figure 1).

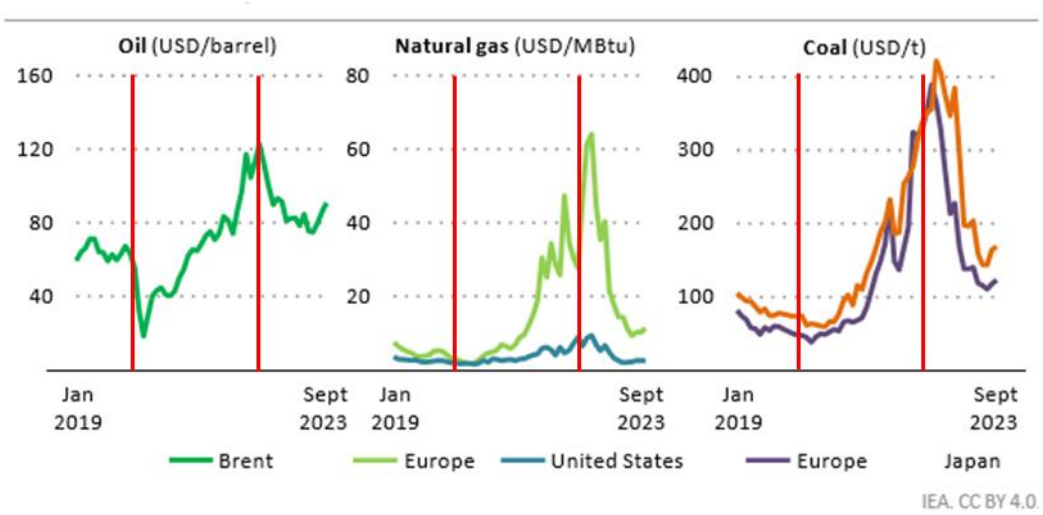


Figure 1. Prices for oil, natural gas and coal, January 2019 to September 2023 (Covid-19 spreading and Russia – Ukraine conflict highlighted by the red lines) [1]

According to the International Energy Agency (IEA), the energy demand rebounded to 2019 levels only in the second half of last year, 2023. Therefore, with the "economy machine" fully restored, emissions started to accumulate again, implying the rising of climate-related risks such as ever more frequent

heatwaves and extreme weather events. As the global energy mix still depends on fossil fuel by more than 80% [2], it is necessary to take into account that the combustion of these sources, most of which are hydrocarbons, entails the release of $CO_2$ into atmosphere. This gas species is designated as the largest contributor to the radiative forcing of sun light into the atmosphere, thus the so-called greenhouse gas effect (GHG). In addition, the combustion of fossil fuels also leads to the emission of pollutants harmful to human health. One of the known "culprits" is the fine particulate matter (PM2.5), to which are attributed around 238000 premature deaths in EU-27 each year [3]. Just to provide an idea of the magnitude of the life losses, the number of deaths is comparable to that addressed to the Indian ocean tsunami of 2004 [4], recognized as one of the worst natural disasters ever. For these reasons, the need for a new clean energy economy prompted governments to increase their investment into development of alternative energy sources facilities.

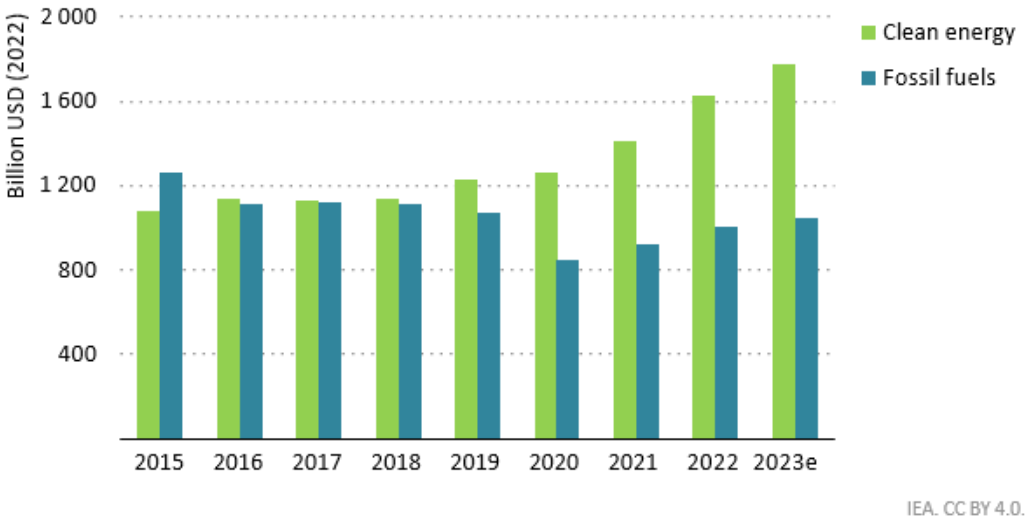


Figure 2. Global investment by energy source [1].

Despite geopolitical friction, visible changes in the current energy system are coming into view with the global investment in clean energy sources that have considerably outpaced those in the fossil counterpart (See Figure 2). These policies approached by governments turned out to be fundamental for the promotion of new technologies capable of mitigating air pollution. In the road transport sector, Electric Vehicles (EVs) account for around 15% of car sales, and a new record in terms of solar capacity has been achieved in 2022 with 220

gigawatts produced. Carbon capture utilization and storage (CCUS) techniques are making significant progress and pipeline projects reveal that more than 400 GW of electrolysis for Hydrogen and over 400 million tonnes of $CO_2$ capture capacity are vying to be operational by 2030. Nevertheless, the flip side of the coin is given by the high prices for some key components/materials. Critical minerals, semiconductors and bulk materials such as steel and cement still play a fundamental role for these technologies, without taking into account that there are several sectors whose emissions are hard to abate, from the aviation sector to on-road heavy duty vehicles. Within this framework, the last Conference of the Parties (COP 28) held in Dubai consisted of a crucial moment to mark the first global stocktake since the definition of the Paris agreement in 2015 at COP 21. The establishment of a "loss and damage" fund to provide financial support to the countries that are already suffering from the effects of climate change, as well as the adoption of a common fossil fuel phase-out agreement are just some of the historical results achieved during the COP 28 event. Nevertheless, these cannot justify some of the criticisms and controversies that arose after that event. Starting from the geographical location chosen for the conference, in a country, United Arab Emirates, whose economy is almost fully based on fossil fuels, to the same position of the president of COP 28, who is also the CEO of the UAE's state-owned oil company. Furthermore, a lot of dissatisfaction and frustration was expressed by the scientific community for the unwillingness by countries such as China, India and Russia to submit new or updated nationally determined contributions (NDCs), thus without any pledges to reduce emissions to stay within Paris agreement levels to keep global temperature rise below 1.5 °C. Come to this point, one could argue that the reduction of emissions is becoming less effective and that the green transition is turning out to be just a slogan. The truth, according to a less idealistic approach, as always lies somewhere in between. Nowadays, researchers and policymakers agree on the necessity to invest on a wide number of technologies rather than the only electrification, as the latter is coming to view that alone cannot drive the energy transition. Therefore, among the valuable options, hydrogen is viewed as a mean to enhance energy security to gradually detach from fossil fuels reserves that are mostly concentrated in politically unstable regions.

One of the main reasons underlying the researchers' renewed interest in hydrogen utilization, relies in the possibility of producing it through various methods: from large-scale diffused steam methane reforming (SMR) to electrolysis. Depending on the energy source and $CO_2$ emissions throughout the process, it is possible to attribute different "colours" to hydrogen. These colours are representative of the environmental sustainability of the different methods. Therefore, hydrogen is often referred to by various colours to indicate its origin, some of which are: the widely diffused grey $H_2$, produced by using fossil-based energy sources, blue hydrogen that implies the addition of the carbon dioxide capture procedures with net zero or minimal $CO_2$ emissions throughout the production cycle, and lastly, green that is referred to hydrogen gas derived by renewable energy sources. Unfortunately, most of the global hydrogen production is implemented through SMR. In 2024 the latter accounts for around 95% of global production. Moreover, the spread of green hydrogen is severely limited by its prohibitive cost of production, i.e. from 3 to 8€/kg depending on the region, which is still uncompetitive to the grey counterpart, i.e. 1 - 2€/kg (See Figure 3) [5]. The high cost of green $H_2$ is due to three main factors: the price of electricity, i.e. that coming from renewable sources, the upfront investment in purchasing and installing electrolysers, and finally the cost for the development of green hydrogen facilities for commercial-scale distribution. In this sense, the efforts made by policymakers to increase investments in spreading renewable energy led to scenarios predicting that hydrogen prices will quickly drop to competitive levels by 2035-2040. More in detail, the cost of hydrogen is forecasted to drop by around 50% by 2030 and then keep decreasing steadily at slower rate until 2050.

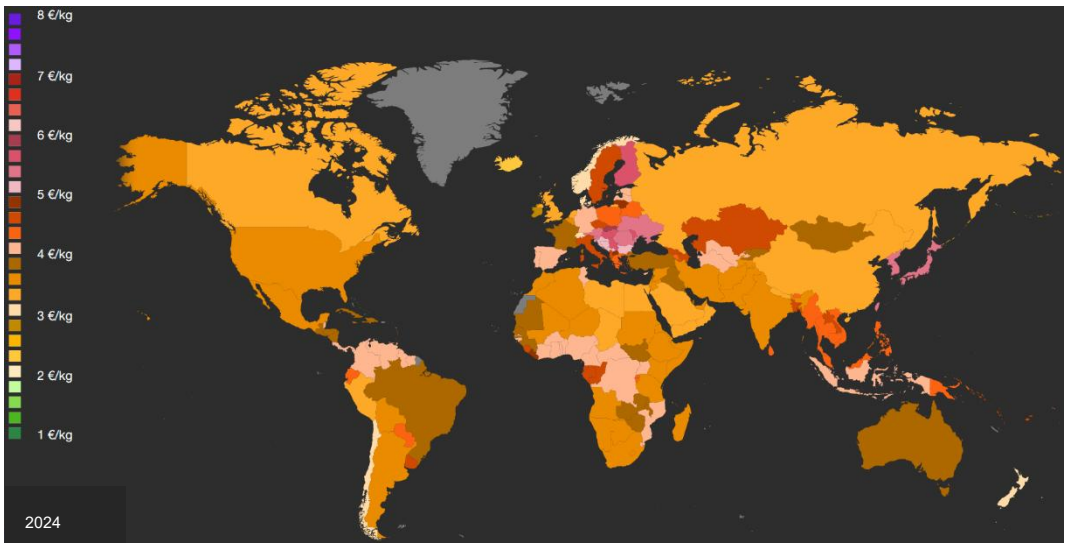

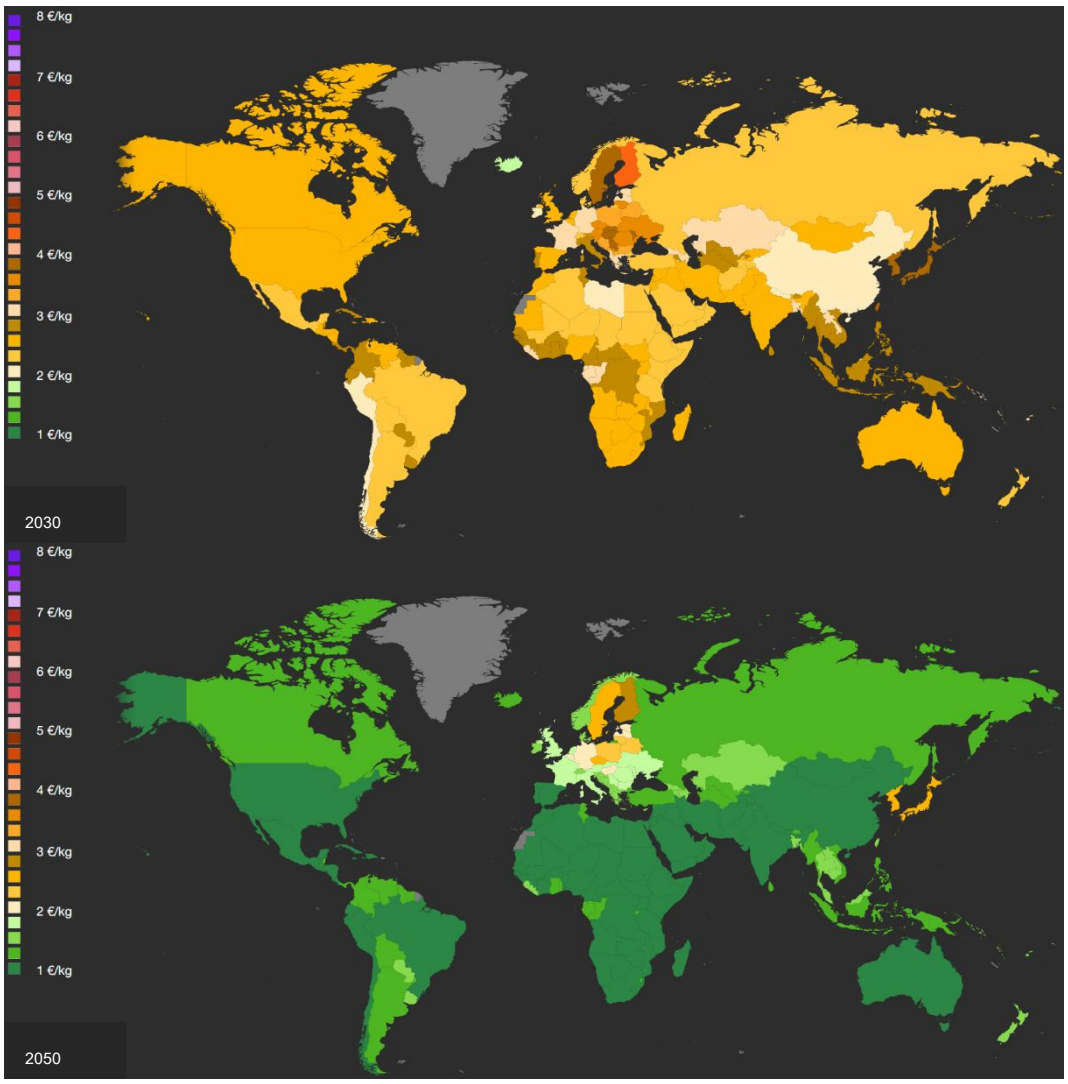

Figure 3. Green hydrogen current production costs (top), forecast by 2030 (middle) and 2050 (bottom) [5].

## 1.2 Why hydrogen does have a future?

Hydrogen has long been considered as a middle term option to render the transition towards more sustainable productive patterns smoother and easier to be assimilated from the current energy system. Contrary to popular belief, hydrogen has been the subject of several studies along recent history [6]-[7]-[8]-[9], with researchers that cyclically looked to this fuel as a silver bullet to tackle down most of the challenges concerning the energy crisis. A fuel relatively easy to produce, which abundance could potentially eliminate any supply problem, except that it is almost never found chemically untied. In its free state, and at atmospheric pressure, it is a diatomic gas, odourless, colourless and most important, extremely flammable. The latter property means that hydrogen utilization needs to be

carefully handled, as it can ignite at volumetric concentrations in air that range from 4 to 75%. In any case, what really makes this element so attractive is its structure and related absence of carbon atoms. Therefore, hydrogen combustion ideally only implies the production of water vapour, rather than conventional fuels like gasoline, diesel or methane whose use entails the emissions of carbon-based pollutants, sulphur and other compounds wastes harmful to human health. These advantages lend themselves well to those who first mentioned the so-called Hydrogen economy. John Bockris first coined this term in [10], and those who support such a vision attribute to hydrogen a leading role as an energy carrier that would help decarbonize the current energy system. Bringing this vision to present days and looking at its application in road transportation, the possibility of retrofitting conventional internal combustion engines (ICEs) and the development of fuel cell (FC) technology is highlighted as a primary objective to make the use of hydrogen cost-efficient and facilitate its distribution.

Nevertheless, what is also noticed nowadays is the rising tendency by researchers to approach to this transition framework like a “fan base”, and that has led to the unhealthy habit of masking the technologies disadvantages depending on their orientation. Hydrogen included. Therefore, as a matter of fairness and in order to gain a more complete insight about hydrogen employment, it is necessary to unravel each characteristic of its utilization, disadvantages included.

First of all, as already stated, free state hydrogen is almost absent in nature, thus it needs to be produced from other sources. Therefore, it is imperative to clearly state that as matter of fact hydrogen is not a primary source like natural gas, crude oil or coal. Moreover, its production is a quite energy-intensive process that makes its production via renewable sources still uncompetitive. For this reason, nowadays its production mainly consists of steam methane reforming (SMR) technique, but such a method relies on a fossil fuel, destined to run out and which utilization involves direct $CO_2$ emissions. In addition, one of the most discussed aspects of hydrogen is its low density which involves for the need of an additional step of compression, which further reduces its energy efficiency all over its production cycle and the design of specific storage tanks to ensure satisfactory safety standards and operative ranges. Considering these arguments, one could conclude that there are serious doubts on the effectiveness of approaching research on $H_2$. Once again, it is important to remember that, despite some

misleading slogans, future will probably be characterized by the development and commissioning of a series of technologies based on different energy sources, and their application field will depend on their duty cycle. For example, electrification intended as replacement of ICEs with electric motors for propulsion, is already showing the side to an increasing number of difficulties that until recently were not even discussed [11]-[12]. From the forecast of rare minerals supply issues to the development of a suitable energy grid able to satisfy the expected energy demand. The critical aspects identified previously, without mentioning other technical aspects that would require extensive and multi-faceted analysis, have raised several doubts about the recent electrification-fever, thus driving the search of alternative solutions.

## 1.3 Hydrogen for road transport technologies

As already mentioned, there are two main modes of implementing hydrogen in the road transport sector: via injection in internal combustion engines ($H_2$-ICEs) or through an electrochemical reaction in a fuel cell (FC). Currently, there are many studies providing different opinions on the validity of using a technology over another [13]-[14], as well as the many comparisons in literature with battery electric vehicles [15]-[16] (BEVs). Focusing on $H_2$-ICEs and FCs, both use hydrogen as "fuel" but the working principles are completely different as well as the outcome in terms of type of energy conversion. A fuel cell consists of two electrodes, i.e. anode and cathode, and an electrolyte that allows ions to move between the two FC's sides. Therefore, hydrogen is supplied to the anode and its atoms split into protons and electrons, which take different paths to the cathode. The electrons follow an external circuit creating an electricity flow, while protons flow through the electrolyte to the cathode where they react with oxygen and electrons to produce water. Instead, inside an $H_2$-ICE, hydrogen works like conventional fuels. Depending on the injection strategy, it can be delivered via PFI or DI configuration, then, once it is mixed with air, or entertained into the combustion chamber if in PFI configuration, a spark plug ignites the mixture in order to start the explosive reaction and transfer the chemical energy to the engine crankshaft that will convert it into mechanical energy.

Looking at the available literature, fuel cells are characterized by higher efficiency rather than $H_2$-ICEs [17] as showed in Figure 4.

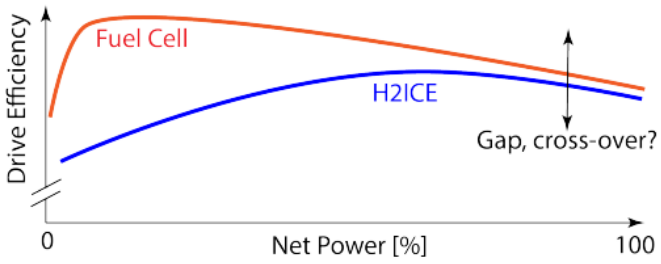


Figure 4. Typical efficiency characteristics for FC system (red line) and H2-ICE (blue line).

In addition, they can be divided into two main types: proton exchange membrane fuel cells (PEMFC) and solid oxide fuel cells (SOFC). The latter type is poorly suited for automotive applications due to the high light-off temperature, i.e. 600-700°C, and the presence of ceramic materials which fragility limits its practical use in the transport sector. PEMFCs are more common, and they have the advantage of operating at low temperature. However, the main "Achille heels" of this technology are the high costs of production and the necessity to operate with extremely pure hydrogen. Because of the high sensitivity of the electrolyte, i.e. the membrane, to impurities. In fact, the presence of sulphates, even in small quantities, can lead to the poisoning effects with the subsequent chemical deactivation of the bound sites, with an irreversible loss of catalytic activity towards hydrogen oxidation reaction. Switching the discussion to $H_2$-ICEs, there are several injection and combustion strategies that can be implemented, thus improving its versatility. The mainstream option involves the retrofit of conventional spark plug ignition units, avoiding most of the costs for the design and manufacture of a new powertrain. In such engines, hydrogen can be delivered just outside the combustion chamber (PFI) or inside (DI), allowing bi-fuel or $H_2$ operation, depending on the application. The continuous development of ICEs for more than a century allows for relatively easy conversion of these units, even if it is not as straight forward as simply substituting gasoline or diesel. In addition, the difference in efficiency between ICEs fuelled with hydrogen and FCs is much smaller than the theoretical gap [18]. In any case, both technologies have their advantages and challenges to be faced before talking of the possibility of mass production. As far as hydrogen fuelled engines, they consist of a near-term option for faster transition towards more sustainable transport patterns, particularly suitable to abate emissions in such sectors where electrification can hardly play a central role.

## 1.4 $H_2$, the fuel for tomorrow's ICEs?

Hydrogen physical properties are quite different compared to those of conventional liquid fuels currently used, as well as from those of CNG and ammonia. Table 1 summarizes the most important properties under atmospheric temperature and pressure conditions.

Table 1. Fuels properties at 298K and 1 atm *(except CNG at 250 bar).

| Property | Hydrogen | CNG | Gasoline | Diesel | Ammonia |
|---|---|---|---|---|---|
| Density [kg/m$^3$] | 0.09 | 0.70 - 0.72 | 720 - 760 | 820- 845 | 0.73 |
| Flammability limits [volume % in air] | 4 – 75 | 4.3 - 15 | 1.4 – 7.6 | 0.6-5.6 | 15-28 |
| Flammability limits [ø] | 0.1 – 7.1 | 0.4 – 1.6 | 0.7 – 4 | - | - |
| Autoignition temperature in air [K] | 858 | 723 | 550 | 527 | 914 |
| Minimum Ignition energy [mJ] | 0.02 | 0.28 | 0.24 | 0.25 | 8 |
| Flame speed [m/s] | 1.85 | 0.38 | 0.37 – 0.43 | 0.2 – 0.8 | 0.015 |
| Adiabatic flame temperature [K] | 2480 | 2214 | 2580 | 2600 | 2070 |
| Quenching distance [mm] | 0.64 | 2.1 | ~2 | ~2 | - |
| Stoichiometric fuel/air mass ratio | 0.029 | 0.069 | 0.068 | 0.068 | 0.165 |
| Lower heating value [MJ/kg] | 119.7 | 45.8 | 44.79 | 42.78 | 18.8 |
| Energy density [MJ/m$^3$] | 10.7 | ~30-40 | ~34000 | ~37000 | 13.7 |

What immediately stands out is the very low density of hydrogen compared to other fuels; it is of different orders of magnitude lower compared to gasoline and diesel. This deficit completely counterbalances the almost tripled mass based lower heating value (LHV) compared to that of CNG, gasoline and diesel. Furthermore, this peculiar property is not only a challenge for the design of high-pressure storage systems, but also in terms of flow ratings, i.e. higher volumetric flow is required, with consequences on e.g. the choice of turbochargers, especially under high loads conditions. In addition, taking into account the gas-compressed storage systems, the high diffusivity of hydrogen could be an issue for most materials that compose the current types of vessels [19] leading to embrittlement. Looking at combustion related properties, the high value of autoignition temperature and low stoichiometric fuel-air ratio render hydrogen more prone for operation in spark ignition (SI) engines rather than the compression ignition (CI)

counterparts. The extremely extended flammability range of hydrogen in air highlights the possibility of operating engines in lean and ultra-lean conditions, thus minimizing NOx (given the carbo free nature of $H_2$); this however significantly decreases the energy content of the air-fuel mixture. Another parameter to be taken carefully into account is the low ignition energy. The latter increases its sensitivity to the presence of hot spots, i.e. spark plug surface, exhaust valves, carbon deposits or residual charge in the ignition circuit, rendering hydrogen–air mixtures more prone to the occurrence of abnormal combustion phenomena. Another characteristic which implies prudent use of hydrogen is its very short quenching distance that allows the flame front to propagate into small volumes. In this sense, in an engine such as the one for the experimental tests described in this doctoral thesis, the crevices are way more extended than that of a commercial one. Therefore, the undesired propagation of flame in these volumes involves the release of impurities into the combustion chamber during subsequent cycles. During the intake stroke, these impurities with high enough temperature can determine the start of uncontrolled combustion that can propagate along the intake manifold if the intake valves are still open, thus resulting in backfiring phenomenon. The effects of these anomalies are well known and can range from weak shockwaves to the failure of the intake manifold in case of particularly intense or repetitive backfire. Finally, one of the most scrutinized aspects of hydrogen relies in its flame laminar speed, a characteristic that is still the subject of several studies; depending on the operating conditions, it can feature values from 5 to 10 times higher than those of gasoline. Most of the experiments aimed at measuring the laminar flame speed of hydrogen involve the use of constant volume chambers; optical accessibility allows for the definition of empirical models in a wide range of air fuel ratio (AFR) [20]-[21]-[22]. The problem arises when switching to the engine environment, where the dynamic working principle of these units implies the generation of complex turbulent structures that depend on a huge number of parameters, i.e. the design of the combustion chamber, engine head and valve ducts, the crankshaft rotational speed and so on. Faced with such difficulties, turbulent combustion is still the subject of several studies comprehensive of experimental test campaigns [23]-[24], or exploiting the increasing computational capacity of modern computers [25]-[26]-[27].

# Chapter 2

# Hydrogen in SI engines

The mainstream application of hydrogen in internal combustion engines (ICEs) involves its use in spark ignited units. Depending on the injection layout, it is possible to recognize two categories: PFI and DI configurations. The use of a setup or another implies different advantages and criticisms to be faced that are briefly discussed below.

## 2.1 Bi-fuel operation

Among available methods of implementing hydrogen in internal combustion engines, there has always been a part of the scientific community fascinated by the potential benefits of adding it to other fuels like methane, gasoline and diesel. In these studies, rather than the solely performances, the researchers paid attention to the reduction of the $CO_2$ emissions and fuel consumption.

### 2.1.1 Hydrogen – Methane

Methane is certainly the leading candidate for enriched operation with hydrogen. Its affordable cost and low carbon content make it an attractive mid-term solution to which hydrogen can be added. Methane has excellent knock resistance; compared to liquid hydrocarbon fuels, its low carbon generates less emission of carbon dioxide [28]. The main “weakness” of this fuel relies in its low density, extra energy required for their compression, gas losses during production and transportation, thus resulting in a decrease of output power of approximately 5-10% [29]. This prompted for the study of the influence of adding hydrogen to

methane and the flame velocity characteristics of the resulting blend [30]. The current literature extensively covers this topic with many studies that focused their attention on the early stages of combustion, as well as overall performance [31]-[32]. Other investigations evaluated the effect of using different types of igniter controllers and corresponding effect on the flame development under lean operations in optically accessible engines [33]. These investigations emphasised the overall benefits of hydrogen addition to methane, showing reduced cycle-to-cycle variability with limited loss of IMEP at high loads. This is due to the augmented reactivity of the mixture during the early stage of the combustion process, therefore resulting in high probability of presence of a stable and fully developed flame kernel. Furthermore, the low density of hydrogen means that the influence becomes relevant for volumetric contents over 60-70%. In these conditions, the chemiluminescence of reaction strongly increases, resulting in homogeneous propagation of the flame front in all direction, improving the thermal efficiency. Lastly, the high diffusivity of hydrogen contributes to the distribution of the fresh charge, enhancing the combustion efficiency and reducing the polluting emissions [34].

### 2.1.2 Hydrogen – Gasoline

Engines built to run on gasoline can also benefit from small amounts of hydrogen added to the mixture, e.g. 10% in volume fraction can extend stable engine operation in lean burn conditions ($AFR_{rel}$ ~ 1 to 2), keeping the CCV well below the automotive standard value of 5% [35]. Given the augmented global flame laminar speed, spark timing can be delayed, shifting the combustion process towards the TDC, hence increasing the thermal efficiency and fuel economy [36]. Valve timing plays a key role in increasing volumetric efficiency, an aspect especially important for $H_2$; by anticipating the intake valve opening (IVO) at medium and high-loads operating conditions, it was found that indeed this parameter was enhanced. However, a key aspect to be taken into account is the possible presence of unburnt fractions of the fresh charge into the exhaust line, with subsequent occurrences of explosive phenomena. In fact, in its pure state hydrogen has a low explosion limit (LEL) of 4% by volume. Therefore, it is of paramount importance to use the best mixture formation strategy to ensure an efficient combustion process and avoid undesired phenomena. Furthermore, given

the carbon content of this hydrocarbon, which results in CO2 emissions, the addition of hydrogen can also lead to a reduction in harmful emissions.

## 2.2 Hydrogen operations

### 2.2.1 PFI configuration

In the PFI layout the injector is mounted on the intake runner with the jet axis directed towards the back surface of the intake valves. One of the benefits of this setup is given by the longer time for mixture preparation, reducing the probability of presence of rich areas, thus limiting NOx formation and occurrence of abnormal combustion. Because of the low density of hydrogen, after being injected it quickly expands, therefore replacing the air. This reduction of volumetric efficiency can be partially mitigated by adopting the use of an external turbocharger unit to force air into the cylinders. Nevertheless, this task can become critical during operation at low-speed while in high-load, as well as at high-speed and high-load [37]-[38]. In fact, at low crankshaft rotational velocities the reduced flow of exhaust gases limits boosting capabilities; in this scenario the required pressure ratio is high enough to push the compressor close to the surge limit, thus consisting of a serious risk of complete failure of the component. In the second scenario the problem is related to the operational “limit” of the compressor, rather than a destructive phenomenon. In fact, under high-speed and high–load operation, the compressor can reach choked conditions, thus becoming unable to provide the required flowrate. These issues can be partially overcome through the implementation of an electric booster [39] or by implementing a variable geometry turbine (VGT) [40], but it is obviously that the need for the design of dedicated components erodes the advantage given by the retrofit logic. Other studies focused on the evaluation of alternative ignition system to improve the cycle-to-cycle stability by shortening the early stages of the combustion process[41]. Unfortunately, the PFI configuration is prone to the occurrence of backfire and such phenomena of uncontrolled combustion propagating into the intake runner could become a serious constraint for performance. Therefore, it becomes essential to optimize the valve timing set-up and the design of a proper intake manifold to minimize backfiring and its effects.

### 2.2.2 DI configuration

The second option available consists of the DI layout. With a high-pressure injector air displacement can be mitigated completely and backfiring phenomena can be greatly overcome. On the other hand, the drawback of this solution lies in the increasing occurrence of other abnormal combustion phenomena, such as pre-ignition and knocking events. The mixture formed inside the combustion chamber is more prone to pre-ignition, and before spark timing, it is necessary to avoid any undesired reaction that triggers the fresh charge. For example, the need for high flow rate prompts the design of nozzles with large holes or bores, thus resulting in extended jets. In this scenario the high diffusivity, combined with the short quenching distance of hydrogen, make the jet prone to react with the lubricant oil deposited on the cylinder walls. Therefore, during subsequent cycles these molecules evaporate and detach from the wall under the action of the low pressure during the intake stroke. Considering the high temperatures of the latter, these can react with the fresh charge, leading to the occurrence of pre-ignition [42]-[43]. However, the DI configuration implies different advantages, among which a higher efficiency than PFI mode, extending the performance efficiency over a wide range of operative conditions [44]. In this configuration the turbocharger is less stressed and the possibility to concentrate the fresh charge to the TDC strongly increase the brake thermal efficiency (BTE) [45]. What really limits the spread of this layout is the need for high-tech injectors, as they must be able to provide high flow rates. This normally results in larger dimensions of the entire injector body and subsequent criticisms on the retrofit possibility [46]-[47]-[48]. Figure 5 shows a cross-section of the research engine used for the experiments described in this doctoral thesis. The engine can operate both in DI and PFI configurations. More in detail, the original configuration implied the solely DI of gasoline, therefore the intake runner has been customized to allow the PFI operations with hydrogen. Therefore, it is possible to clearly observe the differences in terms of dimensions between a gasoline (DI) and $H_2$ port fuel injector.

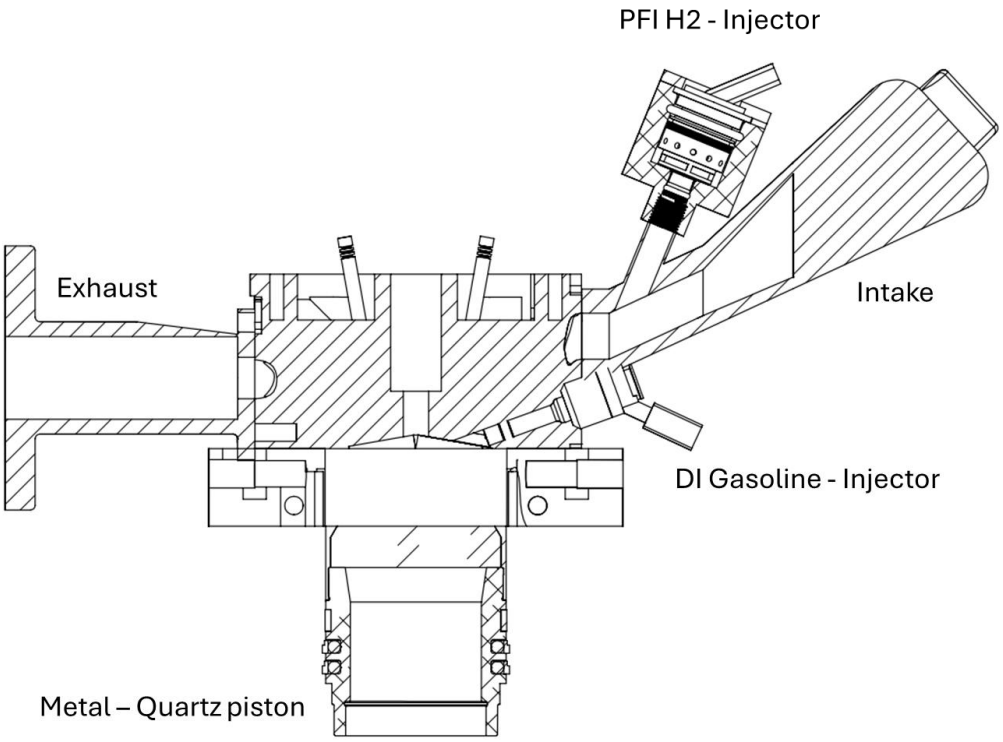


Figure 5. Cross-sectional view of the single-cylinder research engine used for the experiments described in this doctoral thesis.

## 2.3 NOx: Emissions and mitigation strategies

Thanks to the absence of carbon particles, the regulation on harmful emissions generated by the use of hydrogen in internal combustion engines should theoretically focus only to limit the emission of nitrogen oxides. Nevertheless, albeit hydrogen is a carbon free fuel, its application into ICEs always involve a small number of carbon-based particles coming from "secondary" sources, i.e. lubricant oil and wearing of gaskets. Obviously, these sources produce a negligible amount of pollutant, compared to an ICE running on a conventional fuel, thus the current section is mainly focused on NOx. In addition, given the target of this thesis to scrutinize the combustion characteristics of hydrogen in detail, from a thermodynamic and optical point of view, the following lines are only intended to provide a brief overview of this specific topic.

Fundamentally, when talking about NOx production, it is possible to re-call four different kinetic pathways: from the **Zeldovich mechanisms** [49], that first proposed the thermal route, the **Malte & Pratt $NO_2$ route** [50] (lean-burn combustion for which oxygen atoms cause $N_2O$ to act as an important

intermediate leading to NOx formation), the **Fenimore Prompt** [51] (which becomes prevalent in rich flames where there is an overall oxygen lack) and the relatively recent **NNH route** [52]. Among these mechanisms, the thermal route suggested by Zeldovich is the dominant one, corresponding to the almost totality of NOx emissions [53]. This mechanism activates when the combustion reaction inside the chamber, combined with an adequate presence of oxygen, reaches temperatures of around 1800K.

Several studies examined the influences of engine control parameters and mitigation strategies on NOx formation. EGR, as well as water injection, proved to be two different methods that significantly reduce NOx emissions, with limited drawback on performance. Other studies investigated the local phenomena underlying the NOx formation, shedding light on the role of the flame front temperature on the decomposition of NO and investigating the variability in its composition under several engine load conditions. It is noteworthy to underline that increasing the load, thus the temperature, the backward reaction of the NNH and NO2 pathways increases to such an extent that NOx is decomposed faster than its production rate, resulting in a negative contribution. In addition, to lower the temperature into the combustion chamber it is possible to exploit the extended range of flammability of hydrogen by implementing lean-burn combustion strategies. These kinds of operative conditions lead to the almost complete abatement of NOx emissions, and with adequate turbocharging can lead to satisfactory performance [54].

Finally, it is also important to highlight the increasing capacity of modern computational units that allow the application of advanced chemistry theory models to get new elucidation on the formation and reduction mechanisms.

## 2.4 Combustion Anomalies

This section deals with the main challenges of applying $H_2$ fuelling in ICEs. As already anticipated in the previous section (See 1.4 $H_2$, the fuel for tomorrow's ICEs?), the wide flammability limits as well as the low energy of ignition can result in undesired phenomena such preignition, knock and backfire. Therefore, these abnormal combustion phenomena are briefly described in the following paragraphs.

### 2.4.1 Preignition

Preignition is intended as the phenomenon whereby the air-fuel mixture ignites before spark timing, but after the closure of the intake valves, thus when the in-cylinder environment is isolated. This anomaly results in an uncontrolled pressure rise during the compression stroke, with subsequent loss of performance. Due to its stochastic nature, investigations already available in the literature usually attribute the cause to several sources: from spark plug deposits, exhaust valves hotspots, to the entertainments from the crevices of oil particles evaporated during previous combustion cycles [55]-[56]. The dependence of this phenomenon on the minimum autoignition energy determines an increase in frequency and intensity as the hydrogen-air mixture becomes richer. In addition, once it occurred, if not immediately interrupted it keeps repeating cycle after cycle, continuously anticipating until reaching IVO; this drives the flame to propagate in the intake manifold: in other words, it generates backfiring. There are various measures to avoid preignition; some of these imply the use of a properly designed spark plug and ignition system with low residual charge. Others involve late injection of hydrogen into the combustion chamber, i.e. with DI, to shorten the interaction of the fuel with the surrounding environment.

### 2.4.2 Knock

Once the fresh charge is ignited, the term ‘knock’ refers to the attainment of pressure and temperature conditions by the end gases that promote self-combustion. As intuitable, the main difference to the pre-ignition phenomenon lies in the fact that knocking occurs after spark ignition. The subsequent simultaneous combustion of large amounts of fresh charge leads to a violent heat release, corresponding to pressure waves that strike the cylinder walls and generate the characteristic metallic sound from which the phenomenon takes its name. The occurrence of knock implies relevant mechanical stresses on combustion chamber’s components, thus resulting in possible mechanical failure. The octane rating method can be used for measuring the knocking tendency of a fuel. Depending on the settings of the procedure, it is possible to obtain the research octane number (RON) and the motor octane number (MON) of the analysed fuel. The differences between these two indicators lie in the operating conditions of the engine in terms of temperature and speed at which the tests are

performed. In this sense, these parameters are more stressful for the MON procedure. A cooperative fuel research (CFR) engine is used for both methods by comparing the knock resistance of the investigated fuel to that of a standardized mixture of heptane and iso-octane. The problem with such an approach is that it was thought for liquid fuels, thus resulting poorly suited for application with air-hydrogen mixtures. In fact, looking at the current literature, it is possible to find different values of the RON for hydrogen, ranging from less than 90 to more than 130, thus attributing higher knock resistance compared to that of gasoline for example. This uncertainty increases in rich conditions in which the high laminar speed of hydrogen implies extremely fast build-up of pressure inside the combustion chamber, which can be mistakenly identified as knock. In this framework, it is noteworthy to mention the existence of the methane number (MN) that is used to characterize the knock tendency of gaseous fuels. Unfortunately, this method uses methane as reference with a MN of 100 and hydrogen with a MN of 0 per definition, thus making this method unsuitable. Because of the difficulty to attribute the causes underlying the knock occurrence to a single source, several studies evaluated the main operating parameters that contribute to the achievement of such critical conditions. As a matter of fact, there is no common line to avoid the occurrence of such phenomena but rather approaches that mitigate it depending on the type of experimental setup.

### 2.4.3 Backfire

Unlike the phenomena described previously, backfire refers to an uncontrolled propagation of the flame in the intake manifold (See Figure 6). It can occur in two modes: the first if the flame comes from the cylinder, the second if the explosive phenomenon starts in the intake environment. The first scenario is quite rare and can depend on the presence of irregularities on the back surfaces of the intake valves that do not match properly with their seats when closed. The second, and most diffused one, owes its causes in the presence of hot spots, gas residual from previous cycles or wrong phasing between injection duration and IVO [57]-[58]. Backfiring results in drastic increase of intake manifold pressure and causes cycles with negative work. Unlike preignition, a single cycle influenced by backfire can lead to engine shutoff. Considering only the PFI configuration, methods for avoiding backfire phenomena have been studied, and

most of them point to the start of injection and valve timing as key factors. Another option is the implementation of strategies for which the fuel concentration around the intake valves is reduced, i.e. homogeneous charge strategies [59]. In addition, the intake efficiency can be improved by increasing the pressure of injection, thus shortening the duration of the injection event which results in a relevant enhancement of the power output at high-speed regimes.

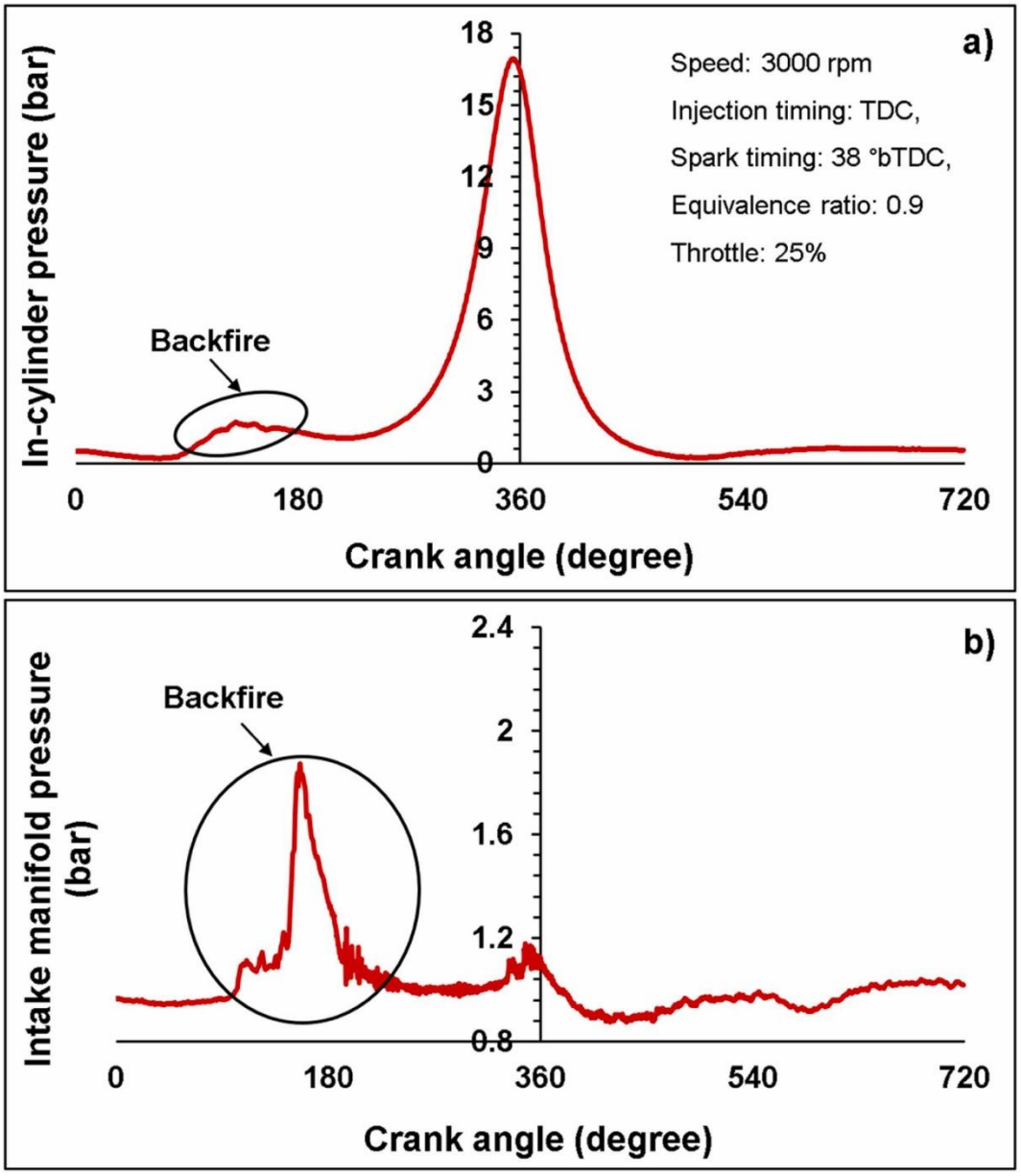


Figure 6. Example of backfire recorded (red line) during test at 3000 rpm, ER=0.9, spark timing 38 CAD bTDC [57].

## 2.5 Hydrogen mixing properties

The following section refers to the results of this doctoral thesis obtained through investigations performed during the period at Chalmers University of Technology (SE). To describe this research activity, the author decided to add this paragraph to include a brief description of the key parameters that define a substitute component that properly mimics the targeted fuel. More to the point, helium was used as hydrogen substitute for non-reacting analysis, and a comprehensive test campaign was carried out to investigate its mixing properties through the use of the particle image velocimetry (PIV) investigation technique. Further insights and current literature state of art are discussed.

### 2.5.1 $H_2$ substitutes, definition and properties

A fuel surrogate is defined as a mixture of one or more components designed to emulate the behaviour of a more complex one. In that sense, it would be erroneous to call helium "fuel surrogate", as it is just one element and not a mixture. Its scientific application is limited to non-reacting studies; thus, it would be more correct to refer to it just as "substitute", at least for the scope of this doctoral thesis. Evidently, hydrogen is the lightest element in the universe, with helium coming as second. This already hints to similarities between the two species.

Therefore, the causes underlying the search for a substitute to reproduce the hydrogen behaviour rely in its physical properties, the same that make it so attractive but also difficult to be managed. Without repeating the properties shown in Table 1, it is evident that hydrogen utilization must be approached with care. In terms of implementing experimental investigations, this means more complex instrumentation and infrastructure, with specific safety measures. Therefore, an increasing number of researchers moved their attention to the use of surrogate gases to emulate hydrogen mixing behaviour. Helium, that as previously mentioned is the second lightest element, is already considered the best candidate to mimic $H_2$ mixing properties for the investigations that do not involve combustion. The current literature shows an extensive number of studies aimed at scrutinizing the use of helium to reproduce several phenomena associated to hydrogen. From the reproduction of gas leaks in enclosed spaces [60]-[61] to its practical application in aerospace field, where researchers analysed the similarity

between helium and hydrogen to compare and observe the distribution field in supersonic combustion ramjet (Scramjet) engines. These studies are normally carried out with the jet injected under supersonic conditions and according to some of the most recent articles, helium showed an overall difference in mixing efficiency of about 10% compared to hydrogen [62], making it suitable for a global evaluation of the jet distribution. In addition, that difference has been mainly attributed to the difference in molecular mass, further highlighting the adequacy of helium to emulate hydrogen. However, there is an overall shortage of studies concerning the use of PIV, and this lack aspect is even more evident when it comes to analyses that compare the flow-mixing properties of hydrogen with other gases or involving the use of injectors with complex nozzle patterns. Among the few investigations available, Erdem E. et al in [63] compared the properties of transverse jets of air, $CO_2$ and helium through an experimental investigation. The optical techniques used by authors highlighted the key role of the molecular mass in defining the main morphologic parameters of the jets, thus the penetration and vortex large-scale structures. More to the point, the study confirmed the suitability of helium in reproducing the hydrogen behaviour rather than air and $CO_2$.

### 2.5.2 Gaseous jet model and current state of art

In this framework, the use of advanced optical techniques like schlieren photography [64] and PIV [65] can bring to additional margins for understanding the phenomena governing the jet flow-field distribution (See Figure 7). The working principle of schlieren photography is based on the presence of a refractive index gradient. The latter can be generated by temperature differences or by the presence of another gas with different properties that lead to inhomogeneities in density. Between the two, the Schlieren technique is probably more diffused than PIV, thanks to the relative ease of implementation and affordable cost of the components needed to assemble the overall configuration. In addition, in recent years several advanced methods were developed to improve and extend its range of application, i.e. extension of visualizable scale-flow [66], molecular species concentration detection [67] (rainbow schlieren reflectometry RSD) and local heat transfer pattern analysis [68]. Nevertheless, one of the major drawbacks of using schlieren photography is related to its high sensitivity in pressure gradients, causing the production of images not always readily

interpretable. Furthermore, another problem is that this technique does not provide precise quantitative information about the inside structure velocity flow-field.

Instead, PIV is a quantitative optical technique capable of providing a complete overview of the velocity field by measuring the displacement at seeded particles in two consecutive frames. The reliability of using such a technique makes it suitable for the development of computational fluid dynamics codes (CFD) [69]-[70]. During several decades, various alternative techniques were developed starting from PIV; one example is the planar laser induces fluorescence (PLIF). The working principle of the latter exploits the absorption of a laser photon by a targeted species that will move to the excited sate, thus realising a luminous emission that can be detected by the software [71].

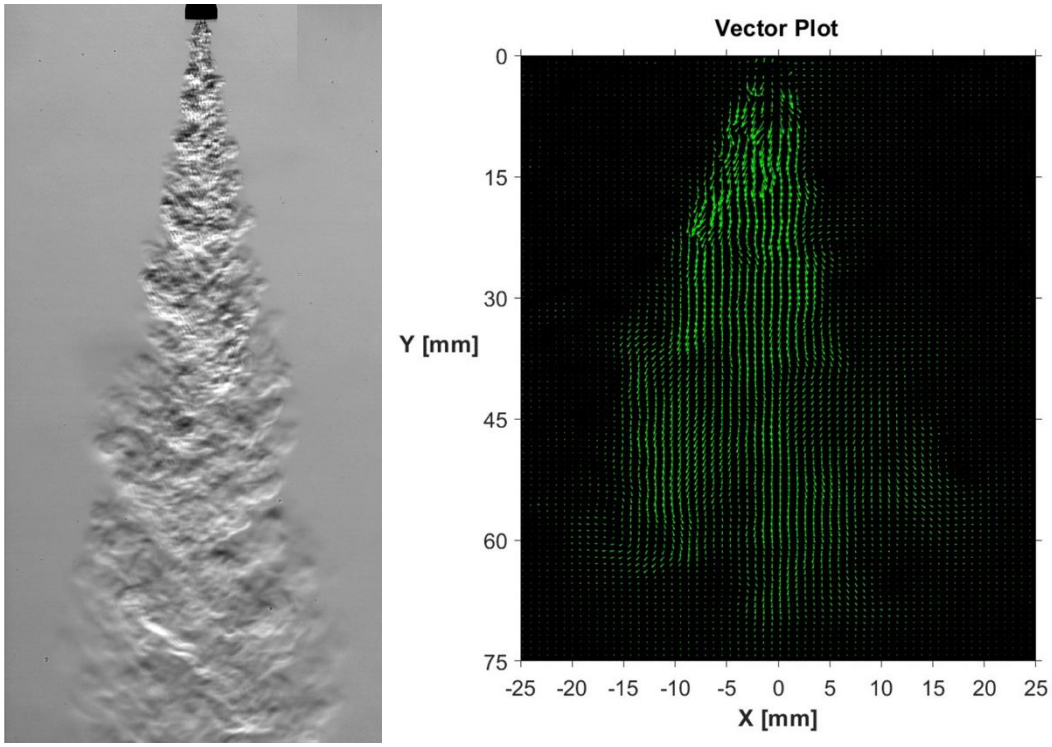


Figure 7. Example of schlieren imaging, adapted from [66], (left) and vector plot obtained from the PIV analysis (right).

One of the first gaseous jet model to be proposed that of Turner JS. in 1962 [72]. According to this model, if the injector features round nozzle holes, then the gaseous jet is assumed to develop with a conical shape, resulting in an almost axial symmetric head vortex (See Figure 8). In this scenario, most of air is entertained inside fuel structure from the back of the jet head, in the steady-state region. Given the unique physical properties of $H_2$, its jet morphology strongly relies on the pressure characteristics and nozzle pattern geometry. Zhao J. et al in

[73] implemented schlieren technique to record the injection process of hydrogen by using an outward opening injector. The study revealed that the self-similarity factor (S), defined as the ratio between radial penetration to the axial penetration, results always larger than unit in the initial stage. Nevertheless, as the jet develop the S factor decreases below unit, regardless of ambient and injection pressure. This phenomenon may be addressed to the high diffusivity of hydrogen that pushes the particles to rapidly fill the low-pressure area that take place along the injector axis faster than the surrounding space. In view of a possible application in the automotive field, other studies investigated the characteristics of jet morphology with very high-pressure ratios values [74]. These investigations confirmed the tendency of the fuel structure to remain around of the injector axis, thus falling on itself. However, it should be noted that most of these investigations exploit the use of the schlieren technique, which is unable to provide quantitative information about flow-field streamlines, therefore leaving the unknown aspects to free interpretation. In any case, it is worthy of note that the PIV measurement measures (ideally) the velocity field, i.e. the velocity of the seeded particles and does not provide any direct information about the mixing. However, this is true as long as the particles follow the flow perfectly, which might not be the case where acceleration is strong.

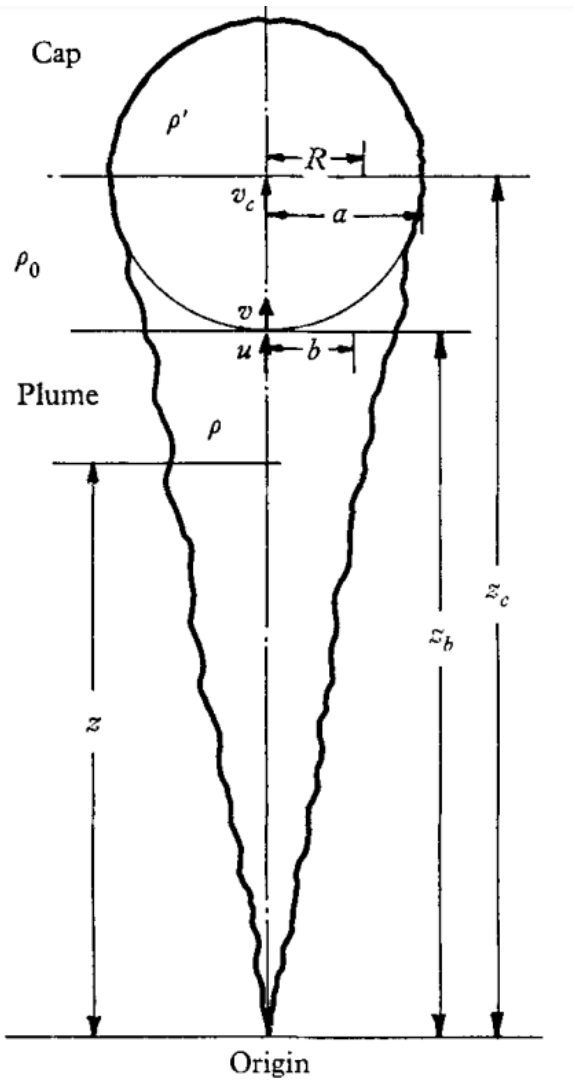


Figure 8. Diagram of the front of a starting plume [72].

## 2.6 Optical technique for characterizing $H_2$ combustion

The use of optical investigation techniques to gain insight on phenomena that would be otherwise impossible to observe is an approach already known and widespread in past and current literature [75]. Among the benefits of using such research units, there is the possibility of correlating the digital imaging results with the thermodynamic data. The core of this doctoral thesis itself describes the results obtained on a single cylinder optically accessible engine. Depending on the type of analysis, it is possible to recognize different designs of these units, some including lateral transparent windows or cylinder walls made of quartz. Nevertheless, one of the most diffused applications concerns the implementation of the Bowditch extended piston [76]. The customized piston is obtained as an ensemble of components. Specifically, a circular quartz window is mounted on

the piston crown, and the latter screwed onto a support that is mechanically linked to the connecting rod. This type of solution reduces the possibility of having complex piston bowl geometries, thus resulting more appropriate for spark ignition-based studies, rather than compression ignition. The Bowditch piston is relatively easy to implement, as it mostly involves the modification of the cylinder block, rather than the head where there are located most of the moving components, e.g. intake-exhaust valves, camshaft, and so on. A 45°-degree UV mirror is normally used to deviate the light coming from the combustion chamber to an external camera sensor. The optical access to the combustion chamber allows for the implementation of several configurations, extending the investigations to the visible and non-visible spectrum. Within this framework, two optical instruments were used: a high-speed CMOS camera and an intensified ICCD camera coupled to a spectrometer.

The first setup was employed for evaluating the natural emissions within the visible spectral range, therefore making it possible to perform flame morphological and luminosity analysis [77]-[78]. With this regard, several studies present in literature used this layout to focus their attention on flame development, investigating in detail its correlation to the engine output characteristics. These studies ranged from the analysis of the influence of early stage on cyclic variability, to the evaluation of the flame front morphology and how these relate with the efficiency of the combustion process. In any case, it is important to emphasize that the effect of the turbulent motions and their impact on the flame development cannot be quantified with the solely optical analysis. Parameters such as turbulent kinetic energy must be obtained through 3D CFD codes, supported by thermodynamic experimental data on in-cylinder pressure etc., which are a fundamental means for developing predictive 0D/1D numerical models. The second configuration discussed in this thesis implied the use of an ICCD camera and a spectrometer for detecting the visible and non-visible emission intensity of the excited species involved in the combustion process. The use of such a methodology allows for defining spark discharge characteristics (SDCs) for fuels with low ignition energy such as hydrogen or for attaining the spectral signature of $H_2$/air flames. These data are of essential importance for developing components and control strategies that maximize the benefits of this carbon-free energy source. A well-known approach consists in Spark Ignition

Breakdown Spectroscopy (SIBS) investigation. The working principle of this technique relies in the generation of a spark discharge between two high-voltage electrodes, which causes the formation of a high-temperature and short-duration plasma. This plasma brings the particles to the excited state particles, then, as the plasma cools, the excited atoms return to their ground states, causing the emission of light with discrete spectral peaks. Many studies exploited the use of this technique for local fuel concentration measurements, ranging from conventional fuels to the investigations of Hydrogen–air mixtures [79], [80] and [81]. Also, the SIBS technique proved its suitability in providing data useful for correlation of the radical species emissions intensity to the combustion efficiency [82]. Anyway, contrary to the simplicity of the molecule, hydrogen has a rather complex emission spectrum. The numerous electron transitions and resulting wavelengths mean that the spectral signal is influenced by mixing and overlapping phenomena of different series. Spectrum that rises in complexity if measured during operation with an internal combustion engine. For these reasons, a limited number of studies implied the use OES techniques inside an ICE [83]-[84]. Therefore, most part of the studies involve the use of controlled environment featuring spark plug to influence SDCs on spectral emissions. To this end, it is important to mention the three phases composing the spark discharge: breakdown, arc discharge and glow discharge [85]. Figure 9 presents typical secondary circuit profiles of voltage and current.

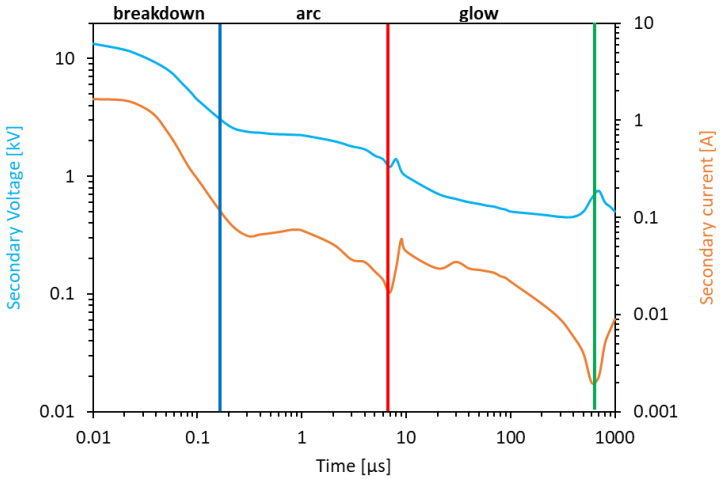


Figure 9. Averaged electrical discharge characteristics for stoichiometric methane-air mixtures ignited at 10 bar, indicating the breakdown- (blue), arc- (red) and glow-phases (green). Adapted from [85].

## 2.7 Thesis Objectives

In this doctoral thesis, primary attention is given to hydrogen utilization in an optically accessible single-cylinder engine. Several experimental tests have been carried out and $H_2$ addition was examined to gain insights about its influence on cycle-to-cycle variability. The recording of optical data, combined with the acquisition of thermodynamic parameters allowed detailed understanding of the different phases of combustion. Hydrogen addition ($CH_4$ - $H_2$ blended operation) and lean burn combustion strategies ($H_2$ - air) were examined and the variation of the flame morphology studied. Cycle-resolved data was recorded with a high-speed CMOS camera, while natural emission spectroscopy was applied with an ICCD camera coupled to a spectrometer. The latter configuration enabled detailed analysis of the radical emission from excited species and their evolution during spark discharge though the use of the SIBS technique. The spectral signature of $H_2$-air mixtures was correlated to emission of molecular hydrogen in the early stages after ignition. In this sense, the main novel associated with this investigation relies in the use of the $H_2$ Fulcher α band as marker for hydrogen concentration. More in detail, most of the works currently available in literature propose similar studies in controlled environment, thus far from being representative of the combustion chamber condition. This thesis is therefore one of the first to demonstrate the usability of this technique in an engine. The above premises drive this thesis to an extensive investigation of the key mechanisms governing the hydrogen combustion process, from the correlation between flame morphology and thermodynamic parameters, to the considerations on the radiative emissions of $H_2$ Balmer α and Fulcher α bands. Concerning the PIV analysis, the reason for this activity is found in the current gap in the literature. Most part of the investigations available exploit the use of the Schlieren technique which is unable to provide quantitative information about flow-field streamlines and vortex structures identification, therefore leaving the unknown aspects to free interpretation. In fact, the search of studies concerning the use of PIV techniques becomes quite difficult as the number of available articles reduces dramatically. This shortcoming is further highlighted by the almost complete absence of investigations comparing the flow-mixing properties of hydrogen with those of

other surrogate gases. In short, the gap found in the current literature on this topic is mainly given by the absence of an extended dataset capable of providing a comprehensive overview on the impact of the main setup variables on jet structure. In view of this gap, the current thesis proposes the analysis of velocity and flow-field structure of helium through the use of the particle image velocimetry (PIV) technique over a wide range of pressure ratio conditions and with three different nozzle tip geometries.

# Chapter 3

# Experimental setup

## 3.1 Research engine

An optically accessible single-cylinder engine was used to carry out the experimental test campaigns, with the target of investigating and correlating flame characteristics to the thermodynamic parameters (focused on in-cylinder pressure). Most of the details concerning the architecture of the research unit are accurately described in [77]-[78]-[86]-[87]. Therefore, the following subsections are intended to provide a quick overview on the main engine specifications and data acquisition system. Following the description of the research engine there is an additional section related to the PIV experimental activity implemented at Chalmers University of Technology.

### 3.1.1 Engine technical specifications

The single cylinder engine that featured a customized optical accessibility to the combustion chamber through a customised piston was fitted with a cylinder head derived from a commercial automotive power unit, four valve per cylinder, 4-cylinder in line unit. The extended piston features a Bowditch design, with a UV-enhanced 45° mirror housed in the elongated part. Engine specifications are listed in Table 2; where the intake-exhaust valves timings are marked with respect to the nearest top- or bottom- dead center. Reference is made to the firing top dead centre (TDC) throughout the text; indications a and b mean after and before.

Table 2. Engine Specifications.

| Parameter | Description |
|---|---|
| Displacement | 399.9 cm3 |
| Stroke | 81.3 mm |
| Bore | 79.0 mm |
| Connecting Rod | 143.0 mm |
| Compression Ratio | 10:1 |
| Number of Valves | 4 |
| Exhaust Valves Opening | 153 CAD aTDC |
| Exhaust Valves Closing | 360 CAD aTDC |
| Intake Valves Opening | 363 CAD bTDC |
| Intake Valves Closing | 144 CAD bTDC |
| Fuel Injection System | DI WG (Gasoline) – PFI (Hydrogen) |
| Mixture Formation technique | Homogeneous Charge |

The cylinder head featured two valves per side, intake and exhaust, and a side mounted DI injector previously used for conventional liquid fuels. Given the unique properties of hydrogen and the required flow rate, a gaseous PFI injector was mounted inside a customised rail and then was connected to the intake runner. This arrangement allows the fuel to be delivered as close as possible to the backside surface of the intake valves. The combustion process was controlled through an inductive ignition system, and by using two different types of spark plugs. The first one, a single J-type electrode (Bosch YR7LEU), was implemented during experimental tests with methane - hydrogen blends. The latter is representative of the most used configuration for current automotive application [88]-[89]-[90], thus consisting of a starting point for the current research program. Once the influence of hydrogen addition on flame kernel development was verified, it was decided to also investigate the effect of a double J-type electrode spark plug (NGK DCPR8EKC); this version allowed the flame kernel to be visualized right from its inception. The start of injection (SOI) was varied slightly, from 340 CAD bTDC for the fuel blends, to 320 CAD bTDC for the pure hydrogen operation; these two settings were chosen so as to reduce as much as possible the interaction with residual gas, as well as to minimize the concentration of fuel in the intake port during the closed valves period. The operation with blends were characterized by a crossflow configuration of the spark plug (with respect to the direction of tumble), thus representative of the situation most widely considered in the literature. Instead, in lean burn conditions ($H_2$), the double

electrode spark plug was set in uniflow configuration. More details on spark plug configurations are available in [77].

### 3.1.2 Data acquisition system and layout

The in-cylinder pressure traces were obtained as ensemble-averages of 200 consecutive cycles recorded by using a piezo-electric transducer (AVL GH12D) with an accuracy of ±1% and a crank angle resolution of 0.2 CAD. A piezo-resistive sensor was used for measuring the absolute intake pressure with an accuracy of ±1%. Oil and water temperatures were recorded and subsequently regulated by a thermal conditioning system including an electric heater and a heat exchanger. The water coolant temperature was kept in the range between 330–335 K for each operative condition. The synchronization of various control triggers for ignition, injection, and camera recording was achieved by using an optical encoder mounted on the crankshaft to generate an external clock signal connected to an AVL engine timing unit. The relative air-fuel-ratio ($AFR_{rel}$) was changed by varying the duration of injection (DOI) and this parameter was monitored by using a Universal Exhaust Gas Oxygen (UEGO) sensor positioned downstream exhaust valves. More to the point, the signal was integrated throughout the working cycle. The engine was fuelled with hydrogen by using a port fuel injection system specifically designed for ensuring high flow rate that requires only a brief crank angle window for $H_2$ delivery. Other details on the experimental setup and sensors position are shown in Figure 10. Finally, to calculate the main engine performance and combustion parameters, i.e., the indicated mean effective pressure (IMEP), its coefficient of variation (COV), net heat release rate (HRR) and so on, a dedicated script was built using the National Instrument (NI) LabView 2020 software. The specific procedures implemented for investigating the thermodynamic data are described in [77]-[78].

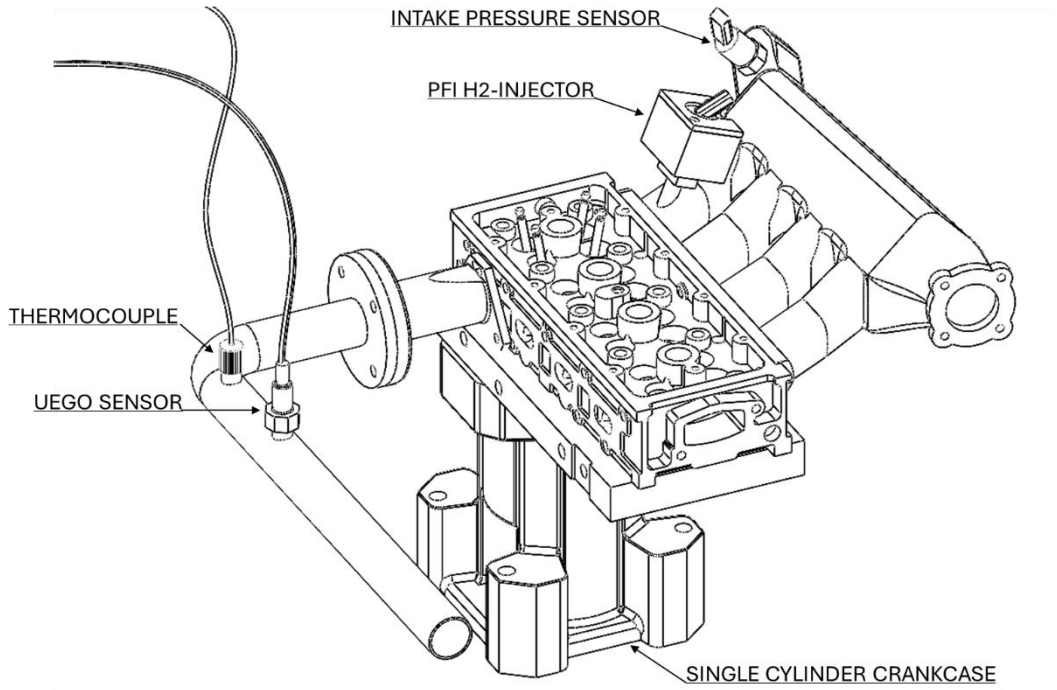


Figure 10. Experimental setup and its components.

### 3.1.3 Optical setup

The optical access to the combustion chamber was made possible via a Bowditch extended piston equipped with a flat quartz window fitted in the piston crown. In order to better understand the phenomena that characterize the early stages of hydrogen combustion, two different optical techniques were applied, both based on the acquisition of the natural spark/flame emission. The aim of this approach was to avoid the use of laser or other light sources and additional optical accesses. Cycle-resolved digital imaging allowed the analysis of the morphology of the flame, from kernel inception, and successively follow its evolution through the 2D detection of visible-near-infrared luminosity. The images reflected by the 45° mirror at the bottom of the elongated piston were acquired by using a high-speed CMOS camera (CamRecord 5000, 8-bit, 16 μm x 16 μm pixel size by Optronis, Kehl, Germany) equipped with a 50 mm Nikon objective. The camera operated in full chip configuration (512x512 pixel) at 5000 frames per second (equivalent to a dwell time between two images of 1.2 CAD at 1000 rpm and 2.4 CAD at 2000rpm). The exposure time was set at 166.6 μs and the f-stop of the objective at 2.8 to improve the signal-to-noise ratio without extensive saturation effects. The

current setup allowed a spatial resolution of 0.18 mm/pixel. For each engine operative conditions, 100 consecutive sequences were recorded. The camera saturation level was kept unchanged for comparative reason, evidencing the change in flame luminosity recorded during the entire experimental test campaign. Figure 11 presents a sketch of the experimental apparatus with the cycle resolved optical set-up. The analysis of flame characteristics was performed by using an image processing routine built in the NI Vision software environment. Specifically, the flame kernel position with respect to the geometrical center of the spark plug (named displacement) and its morphology were evaluated with a solid statistical approach. Further details of the methodology are reported in [77]-[78].

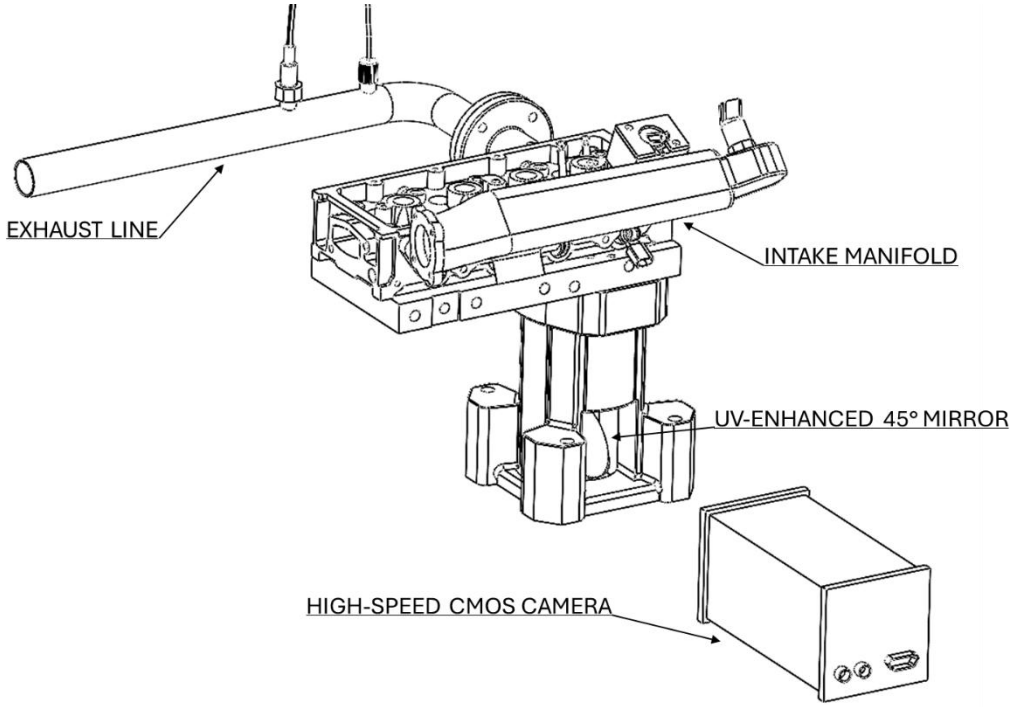


Figure 11. Side-view of the research engine – high-speed camera setup.

To obtain more information on the chemical species involved in the hydrogen combustion process, a second methodology based on Optical Emission Spectroscopy (OES) was applied.

The radiative emissions from the combustion chamber were reflected and then focused by a Nikon objective with quartz lenses (78-mm focal length, f/3.8) onto the 250 μm micrometric controlled entrance slit of a wide-range spectrometer (Acton SP2150i, Princeton Instruments, Acton, MA, USA). The spectrometer

(150 mm focal length f/4) mounted a 300 groove/mm grating blazed at 300 nm; it diffracted the light on the 1024x1024 pixel back-illuminated sensor of an intensified charge coupled device (ICCD) camera (Princeton Instruments PI-MAX3 Gen II–UV, Princeton Instruments, Trenton, NJ, USA). The ICCD operated at 16 bit and allowed 45 lp/mm resolution. The optical setup allowed to detect 1024 spectra that covered a length of around 90 mm along the vertical direction (along a line from the intake to the exhaust valves) centred on the spark plug. In order to increase the signal-to-noise ratio, 128-rows binning was performed. In this way, for each acquisition the recorded 8 spectra were representative of a 0.2 x 10.0 mm region as shown in Figure 12. For the current investigations, only the region corresponding to the location of the spark plug was considered. To optimise the detection of different chemical species, two different acquisition modes were applied, both consisting in 100 acquisitions at the same delay from spark timing. First, the ICCD exposure time was fixed at 16 µs and the delay from the spark timing was changed from 8 to 32 µs, by fixing the central wavelength (W) of the spectrometer at 700 nm. Then the exposure time was increased at 42 µs and the early stages of the combustion process were investigated from 200 to 1200 µs. In this case, the spectra were recorded by fixing the CW at 400 nm and 650 nm to cover a wavelength range from UV to visible.

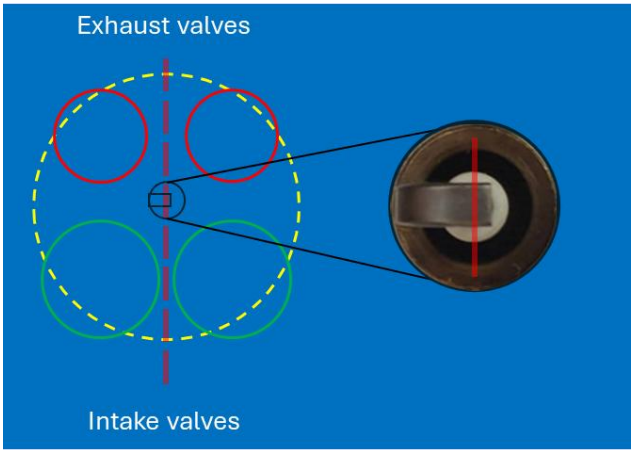


Figure 12. Schematization with the location of the spectroscopic regions of interest.

## 3.2 PIV measurement activity

In order to provide a comprehensive overview of the various aspects regarding the use of $H_2$ into internal combustion engines, this doctoral thesis includes the description of the research activity aimed at evaluating the $H_2$ jet

distribution properties. As already stated in the Introduction chapter, the experimental tests involved the use of helium as hydrogen substitute. The results are therefore intended to provide insight into non-reactive phenomena, i.e. mixing properties.

### 3.2.1 Constant volume chamber

The schematic representation of the experimental setup and of three nozzle patterns are shown in Figure 13. A dual cavity Nd:YAG laser (Spectra Physics, Quanta Ray PIV-400) was used for the generation of the luminous background. The latter device was able to generate two pulsed signals of light with a wavelength of 532 nm. The nominal energy of pulsed light was approximately of 60 mJ, having a duration of 6 ns and a time separation of 3 μs. Since it was not possible to know a priori the correct setting of time delay between the two pulses, the above value was found by linearly increasing it from 1 to 15 μs. In this phase, an operative condition with an intermediate pressure ratio, i.e. PR10, was recorded by varying the frame separation time and the resulting data was post-processed. The outcome confirmed the suitability of setting the time delay to 3 μs to minimize the presence of spur vectors. The two laser beams coming from the cavity are deviated by a series of mirrors and directed towards the chamber as shown in Figure 13. Before reaching the latter, the two signals pass through three lenses; the first concave lens with a focal length of -50 mm and for others two large lenses it was +500 mm. The laser beams are so converted onto sheet with a thickness of about 1mm in correspondence of the injector axis. The air supply line achieves a maximum pressure of 8 bar, it was connected to both chamber and particle seeder. The air supply system in the chamber, as well as the tracer particle system, are designed in such a way that they do not affect the formation of the jet structure. More in detail, the air is supplied through a duct positioned on the upper wall away from the injector axis. Differently, for the delivery of the vegetable oils a toroidal pipe is positioned on the upper wall and the presence of multiple holes allows for a homogeneous emission of tracers inside the chamber. Worthy of note at this stage is the calibration of the particle seeder, which must be approached carefully to avoid two opposing conditions: lack or oversaturation of the tracer particles. This task is achieved by managing the pressure of the particle seeder in relation to that of the pressure line. Specifically, taking into account the OEM

information, for the current study the particle seeded was set to operate in order to produce tracers of 200 ± 50 μm. The resulting images of scattered light were recorded using an interline transfer camera (TSI 630090) with a resolution of 2352x1768 pixels and a 16-bit concentration per pixel. Helium was supplied from a tank at 200 bar and the gas injector mounted in the top wall of the chamber. The effective pressure of injection was set through the use of a choke valve and monitored during injection with a sensor able to capture the fluctuations. It is noteworthy that the injector used for the PIV operation differs from the one mounted on the single-cylinder engine. More specifically, the one mounted on the power unit has a single hole with a diameter of 2.8 mm. In contrast, the three nozzle tips used for the PIV analysis present more complicated patterns (See Figure 13), aimed at highlighting the role of the shape and orientation of the holes on the jet structure. The pressure was observed to suffer a maximum reduction of less than 5% with respect to the nominal value, therefore influencing in a negligible way the flowrate characteristics. The optical access to the inside of the chamber was rendered possible by the four circular windows on the side walls with an inner diameter of 130 mm. For the current study two windows were obscured with two laser beam stoppers. For the three nozzle models, the geometric angle of divergence of the hole paths from the injector axis was of 15° for the first nozzle, 18° (outer holes) - 12° (inner holes) for the second and of 20° (outer holes) for the third. The total area of the holes on the nozzle tips is equal to 7.0, 4.3 and 4.0 $mm^2$ for the $1^{st}$, $2^{nd}$ and $3^{rd}$ geometry respectively. As for the geometry of the channels inside the nozzle tip, these are covered by trade secret and cannot be directly displayed in this thesis.

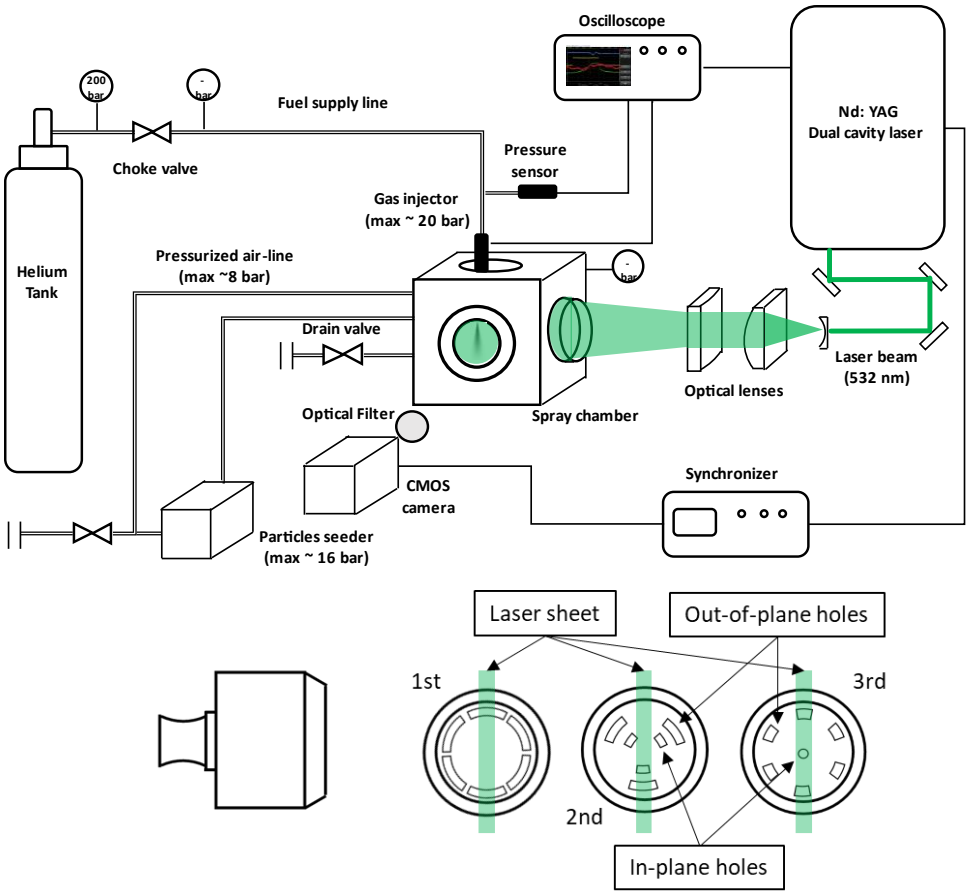


Figure 13. Schematization of the experimental setup used for PIV measurements (top) and nozzle tip patterns (bottom).

# Chapter 4

# Non-reactive analysis results

In this chapter the experimental test campaign concerning the use of helium as hydrogen substitute is presented and results are discussed. The following paragraphs focus on the fundamental study of the gaseous jet morphology and its distribution characteristics. The setup was designed to avoid the presence of any plate or obstacle inside the chamber. This configuration, renamed as “free path” setup (See B.1 PIV optical technique: applied methodology), made it possible to gain a comprehensive overview of the jet development pattern over a long distance. The injector featured a modular nozzle tip, allowing for the use of three different nozzle tip geometries (See Figure 13). Table 3 lists the operative conditions selected for the current analysis. It should be noted that the pressure ratios adopted during the experimental test campaign ranged from 2.9 to 20, with injection pressure values far removed from those of the PFI layout discussed in the chapter Reactive analysis results. The reasons behind this decision lie in the large margin of the recorded data to cover the injection settings during the intake stroke, as well as during compression, as well as the possibility of emphasising the differences recorded as the pressure inside the chamber changes. Furthermore, the large number of selected cases can provide a comprehensive understanding of the phenomena governing the mixing process. In this regard, the examined range of the pressure ratios made it possible to observe significant variations in velocity magnitude distribution, as well as for the vorticity intensity. Under these operative conditions the velocity magnitude ranged from less than 100 to around 300 m/s, remaining always in the subsonic regime. Lastly, the main morphological

parameters, e.g. jet penetration and plume angle, were evaluated by using a digital image processing procedure.

Table 3. PIV experimental operative cases

| Geometry nozzle | Pressure chamber [bar] | Pressure of Injection [bar] | Pressure Ratio [-] |
|---|---|---|---|
| All geometries | 1 | 20 | 20.0 |
| | | 10 | 10.0 |
| | | 5 | 5.0 |
| | 5 | 20 | 4.0 |
| | | 10 | 2.0 |
| | 7 | 20 | 2.9 |

## 4.1 Velocity magnitude

The results that are discussed in this section come from an analysis performed on 20 pair of frames recorded at different time instants after the start of energizing (aSOE) of the injector solenoid. It was observed that the first frame at which it was possible to see the jet coming out from the nozzle tip corresponded to the time instant at 2.7 ms aSOE. Specifically, the jet structure becomes evident at 3.0 ms aSOE, thus all the data discussed in this work range from this time instant onwards. Figure 14 compares the velocity distributions and resulting magnitude (intended as vectorial sum of the -x, -y components of speed) generated by a single pair of frames and that obtained by an ensemble of 20 pair of frames. The two images refer to the operative condition recorded by using the first geometry with the PR set at 10, 3.4 ms aSOE. As expected, the averaged image appears much more homogeneous and the velocity distribution is well defined, highlighting the regions featuring different levels of velocity magnitude. On the contrary, the information coming from the single pair of frames appears fragmented with a more chaotic distribution of the sub-structures. In fact, the latter type of data is hardly suitable for the actual analysis of jet propagation. For this reason, most of the figures treated in this manuscript refer to the post-processed frames obtained by using the averaged data. However, the drawback of using such type of data is related to the loss of part of the details in local vortex structures, as well as an overall reduction of the velocity magnitude (≈ 10 - 15%)

compared to the values obtained by averaging the peaks of individual frame pairs. More in detail, the decrease in maximum velocity of the averaged data is caused by the random position of the peaks in the individual frame pairs, thus resulting in a lower value when "spatially" averaged. In view of this, in order to avoid the underestimation of this parameter, the evaluation of quantitative values was made by considering the individual peaks measured for each pair of frames, then calculating the average value.

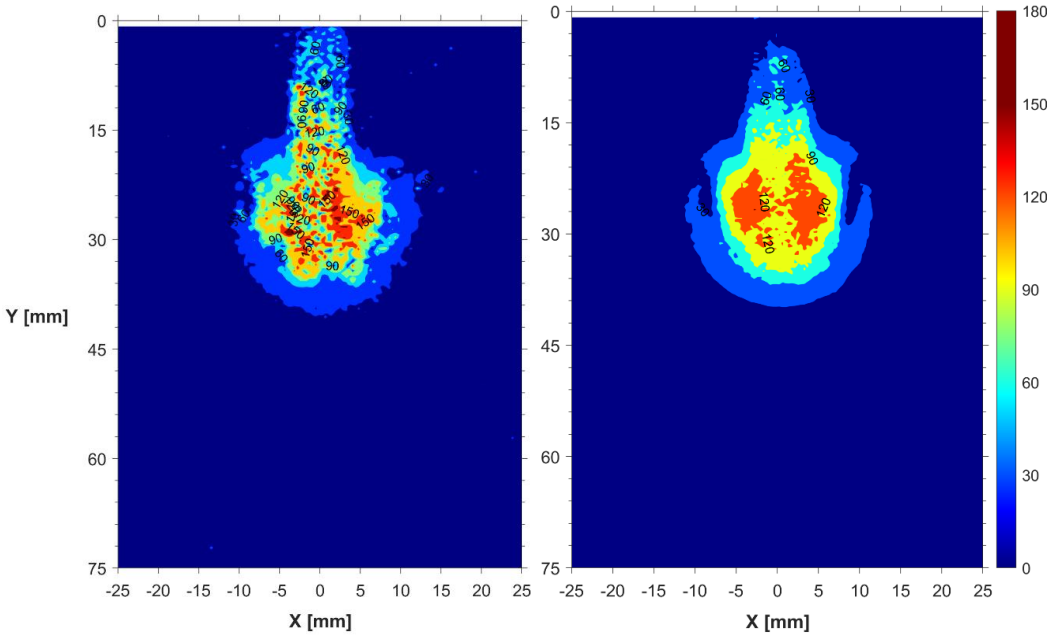


Figure 14. Velocity distribution at 3.4 ms aSOE, GEO-1. Single pair of frames (left) and averaged frames (right) PR10.

Before proceeding, it is important to premise that these data, resulting from an ensemble of 20 pairs of frames, represent probability density areas. For the sake of brevity, the next graphs will show the solely data recorded with PR 4 and 20, representative of the low- and high-pressure ratio conditions. Figure 15 and Figure 16 shown the jet development pattern generated by the first geometry in these two PR conditions, highlighting the differences in terms of spatial extension, as well as the phenomena coupled to the formation of vortex structures. Specifically, both cases reveal the formation of two lateral vortexes (recognizable by the presence of a quasi-static area surrounded by non-zero velocity regions) right form the very early stages of jet development. At PR4, as the jet extends these structures start stretching trying to keep pace with the jet head region. . In the advanced stages of injection, the latter are no longer able to follow the jet, thus collapsing. Worthy of note is the jet core length (V ≈ 80% Vmax) which extends  until achieving steady

state conditions (50mm), then it rapidly reduces to 41 mm. On the other hand, at PR20 the lateral vortex structures improve their capacity to keep up with the jet. More in detail, rather than the centre of the vortexes, the vortexes become able to stretch more before breaking. In this condition, the jet rapidly reaches the border of the ROI, i.e. ≈ 3.6 ms.

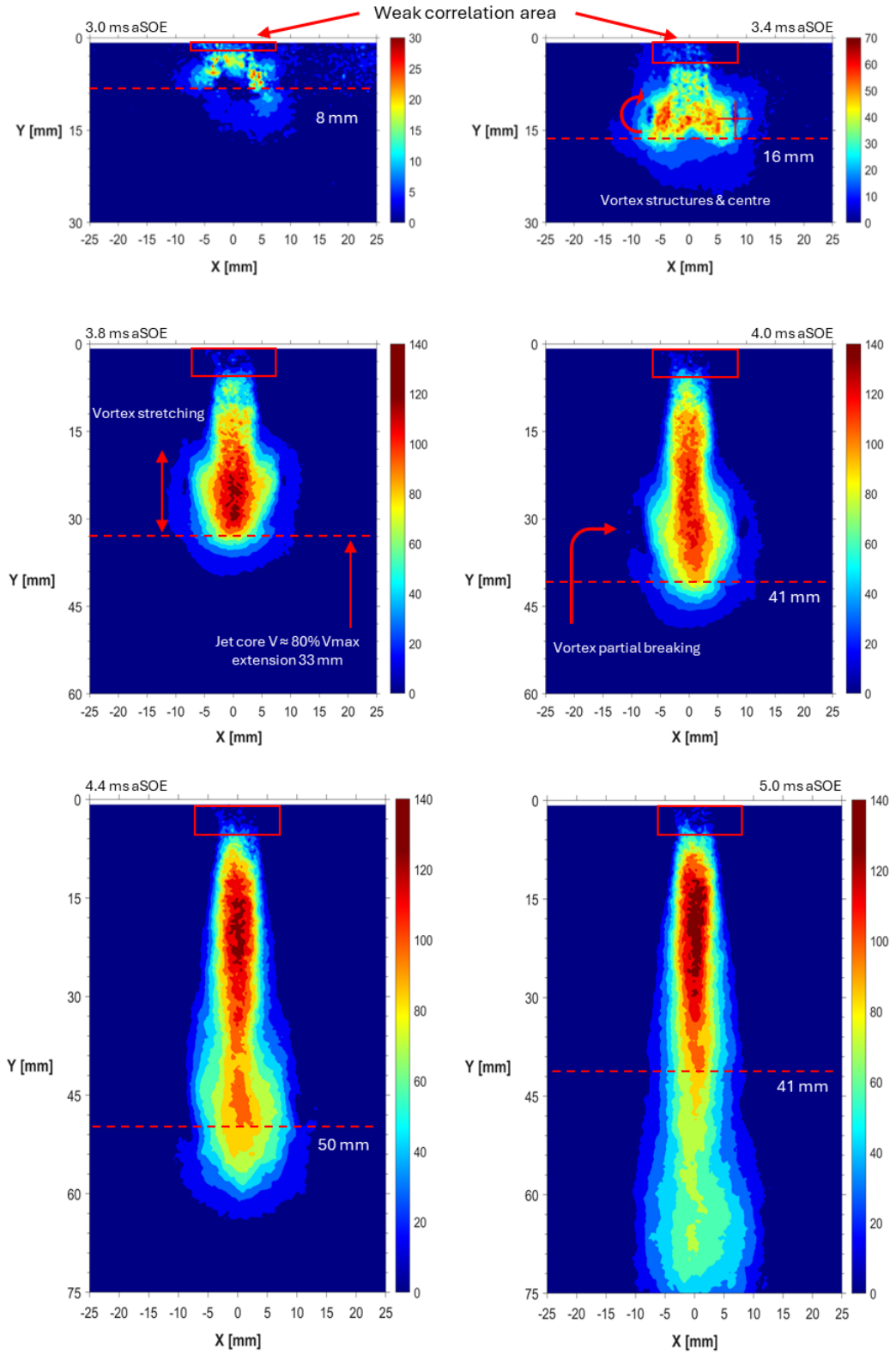


Figure 15. Velocity distribution, GEO-1, averaged frames PR4.

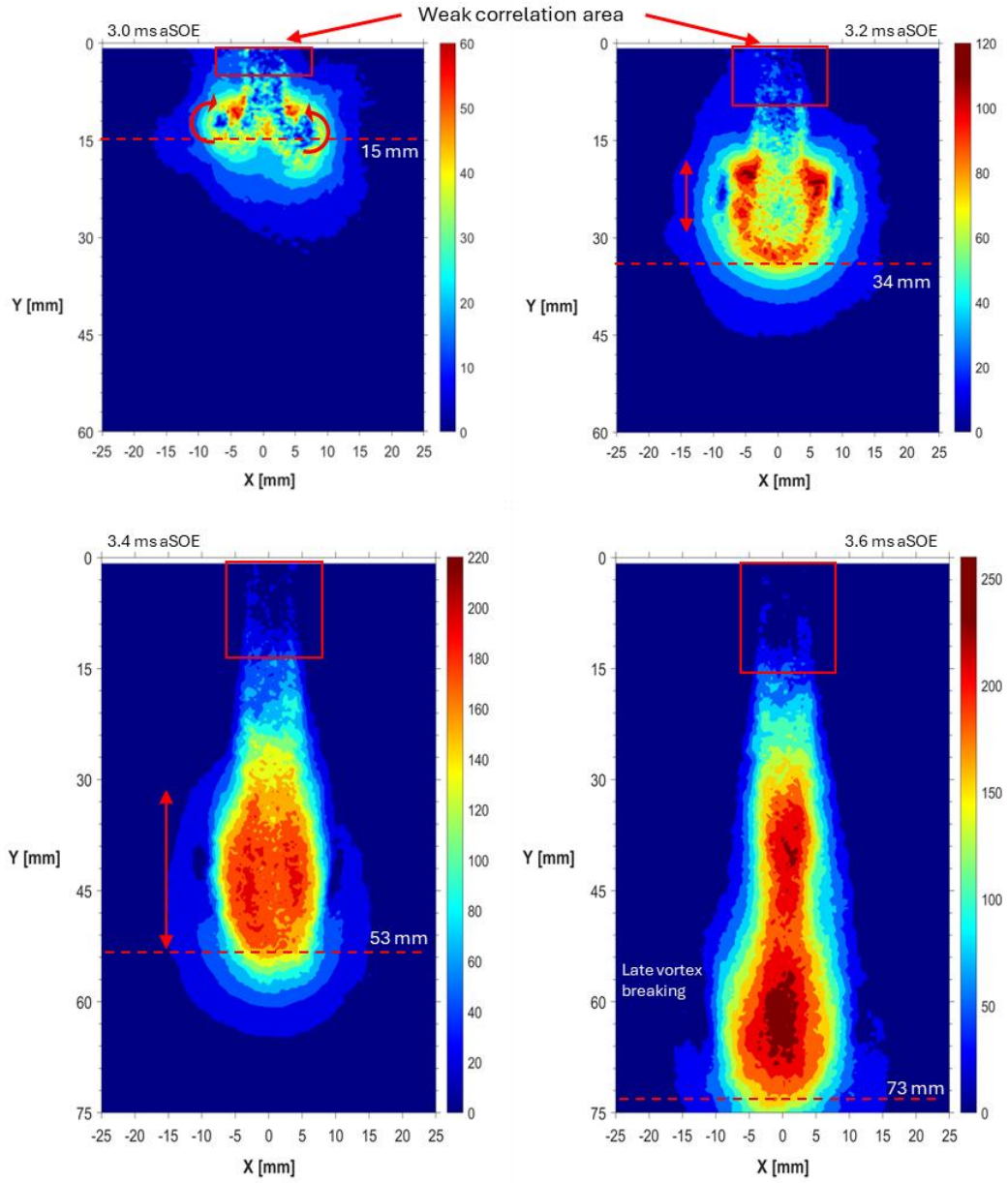


Figure 16. Velocity distribution, GEO-1, averaged frames PR20.

In a 3D perspective, the two visible vortex structures can be assumed to generate a toroidal corona surrounding the gaseous structure, and this is the main contributor to air dragging from the rear area of the jet. In this sense, the mixing efficiency is mainly attributed to these structures. In addition, the higher size of the holes of this geometry implies a great acceleration of the fluid in the region close to the nozzle tip. Here the oil particles are pushed away, rendering the software incapable of providing any information. The length of this weak correlation area varies from a few millimetres of the low PR conditions up to the 15 mm mark showed by the current case at PR20, GEO-1.

Figure 17 and Figure 18 illustrate the velocity distribution given by the jet evolution of the second geometry examined. At PR4 condition, both external and internal jet remain recognizable during the entire duration of the sequence recorded. The interaction with surrounding air leads to the formation of two vortex structures.

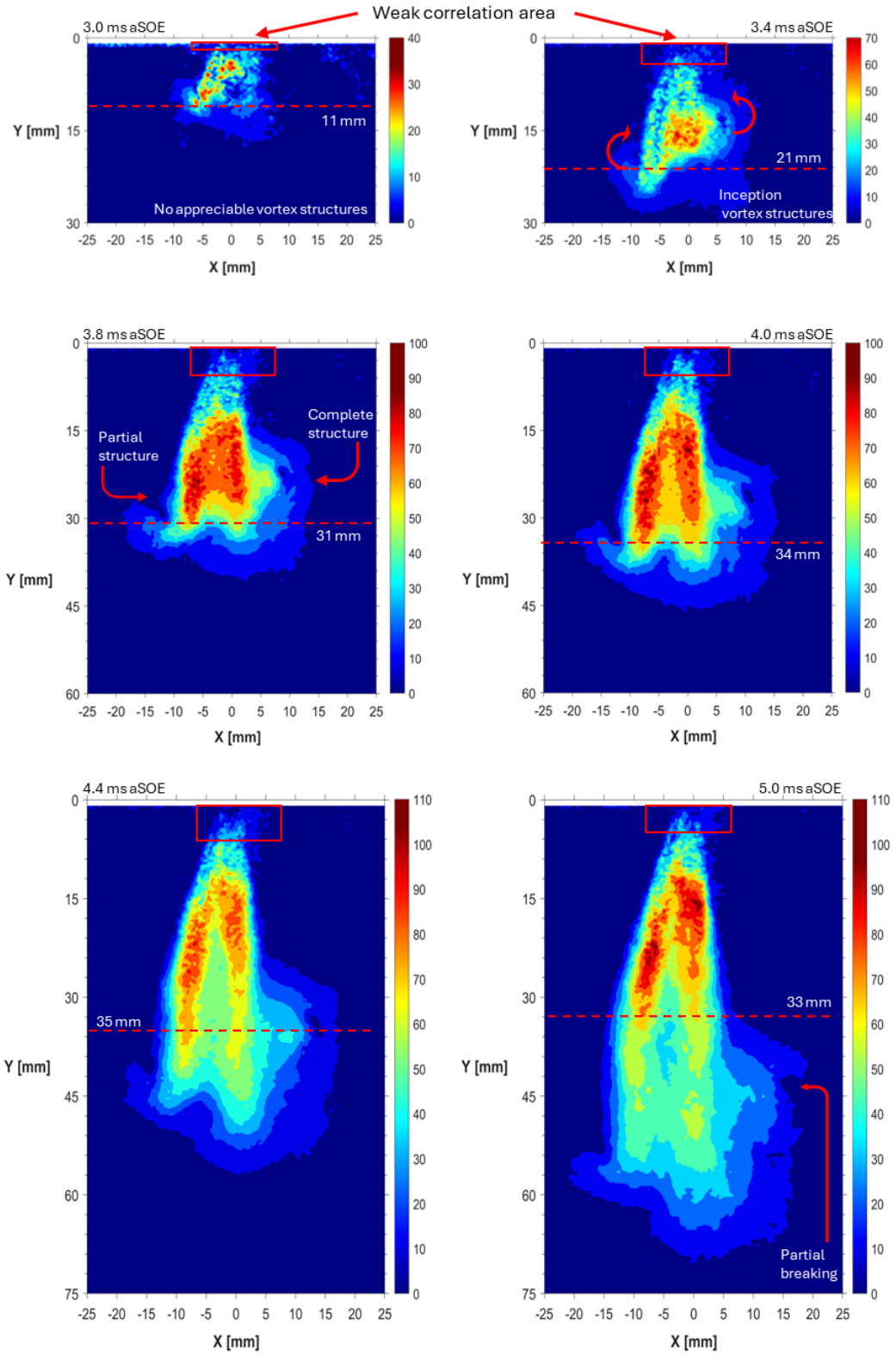


Figure 17. Velocity distribution, GEO-2, averaged frames PR4.

The one on the inner side appears more stable, with a well-defined centre lasting almost the entire duration of the injection. Differently, on the outer side the vortex lasts for a short period, i.e., ≈ 3.4 – 3.8 ms. Further details on the reasons underlying for these different behaviours are provided in the next section where the vector plots are discussed.

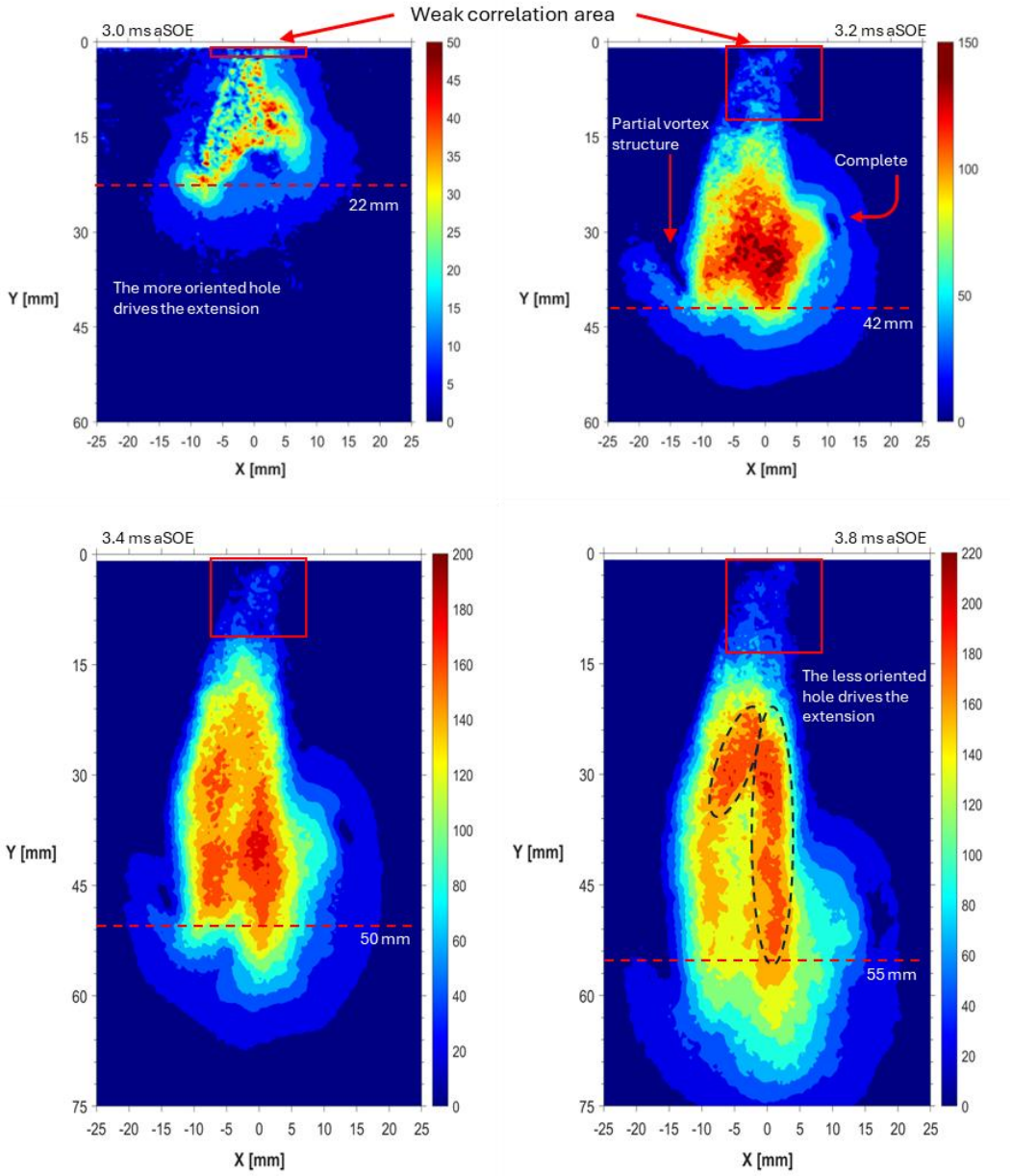


Figure 18. Velocity distribution, GEO-2, averaged frames PR20.

The presence of a low-speed region between the two jets was noted to form before achieving steady state conditions. This area can be attributed to the presence of air in-between the two jets. This region becomes stable when steady state conditions are reached, resulting in a velocity around of 45 - 50 m/s, while surrounded by the tail of the two jets at 90 - 100 m/s. In PR 20 conditions,

similarly to what was observed for the first geometry, the overall increased momentum of the particles allows them to create more stable vortex structures. In addition, unlike the low- PR condition, the less oriented hole becomes predominant to the gaseous structure extension, with the outer jet that appears to be deviated towards the injector axis. Rather than for the low air backpressure (1 atm at PR20), this phenomenon can be explained by low-speed area in-between the two jets, that generates a vacuum effect.

Lastly, third geometry jet development pattern is shown in Figure 19 and Figure 20. The higher orientation of the outer holes, as well as the increased distance between these and the central hole, renders it possible to clearly observe the three structures after injection. At this stage, it was not possible to recognize any relevant vortex structures, regardless of the PR condition. Specifically, the radial extension of the jet keeps growing for a certain time, depending on the injection pressure, until the head of the lateral jets deviates toward external regions. In this phase, the velocity magnitude of the lateral jets rapidly decreases to less than half of the maximum value. Rather than along the injector axis, the velocity perpendicular component becomes predominant. In this condition, the fresh charge of helium coming from the rear area sweeps away the lateral jets ahead. The subsequent vortex structures last only for a few instants as the new charge proceeds following injector axis without supporting the rotating motion of the particles, regardless of the two PR conditions illustrated. Among the nozzle patterns investigated, the third geometry resulted in the shortest structure extension, and the reduced distance between the external holes did not allow for the presence of low-speed regions, thus limiting air dragging to small eddies rather than well recognizable rings or vortexes. Furthermore, the velocity magnitude measured is the lowest within the observed range, with an overall gap of about 15-20 % compared to first geometry and 5–10 % with respect to the second. The observed differences were noted to persist until the achievement of steady state conditions; afterwards, all configurations stabilized around similar values, i.e. 300 m/s. In fact, rather than observing only the peaks, in this phase it is important to focus on the dimensions of the regions that feature velocity values equal to or higher than 80% of the recorded maximum. In this sense, at low pressure ratio conditions the first and second geometries are predominant, while at increasing the PR the third nozzle pattern overcomes the second.

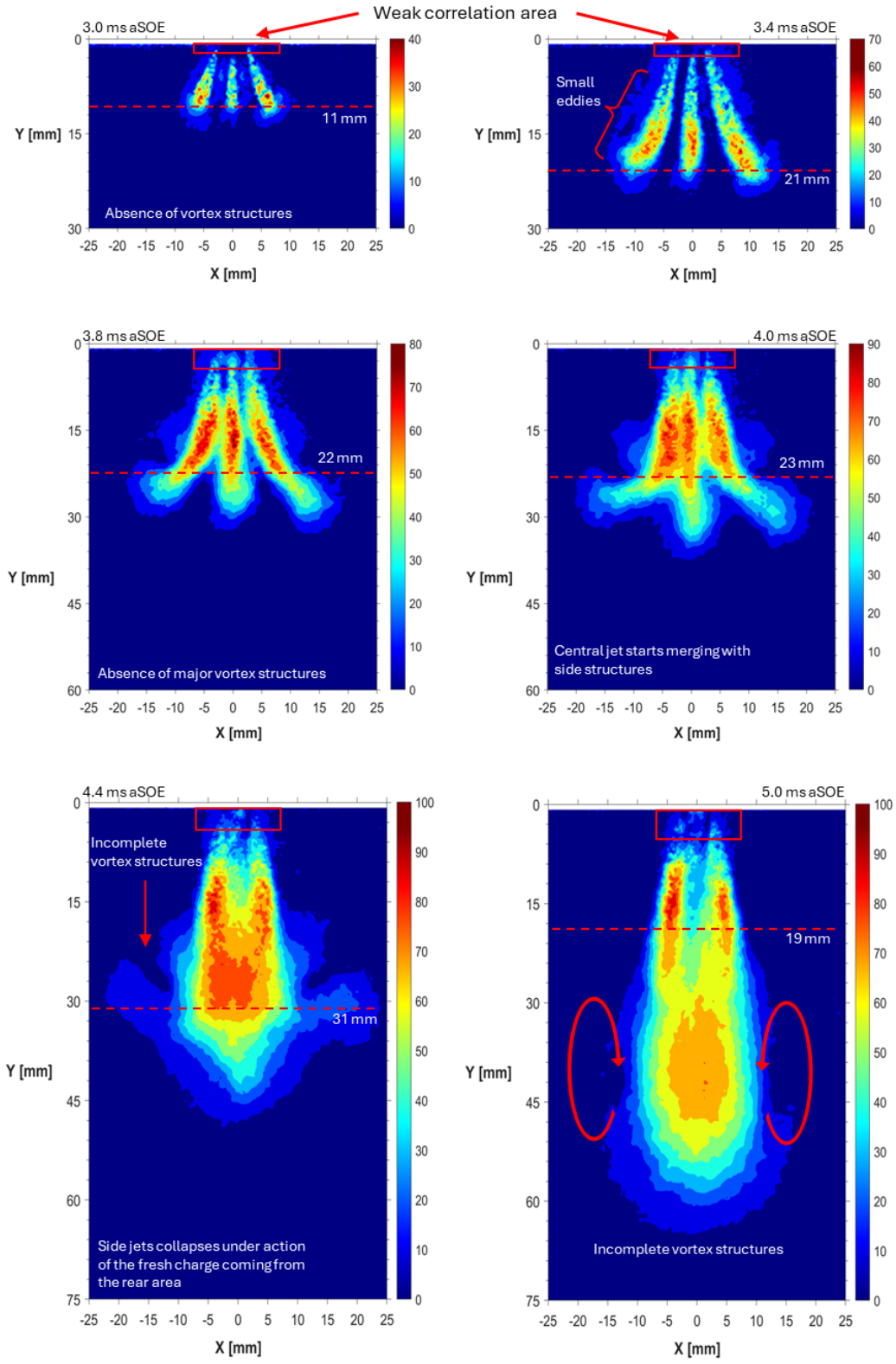


Figure 19. Velocity distribution, GEO-3, averaged frames PR4.

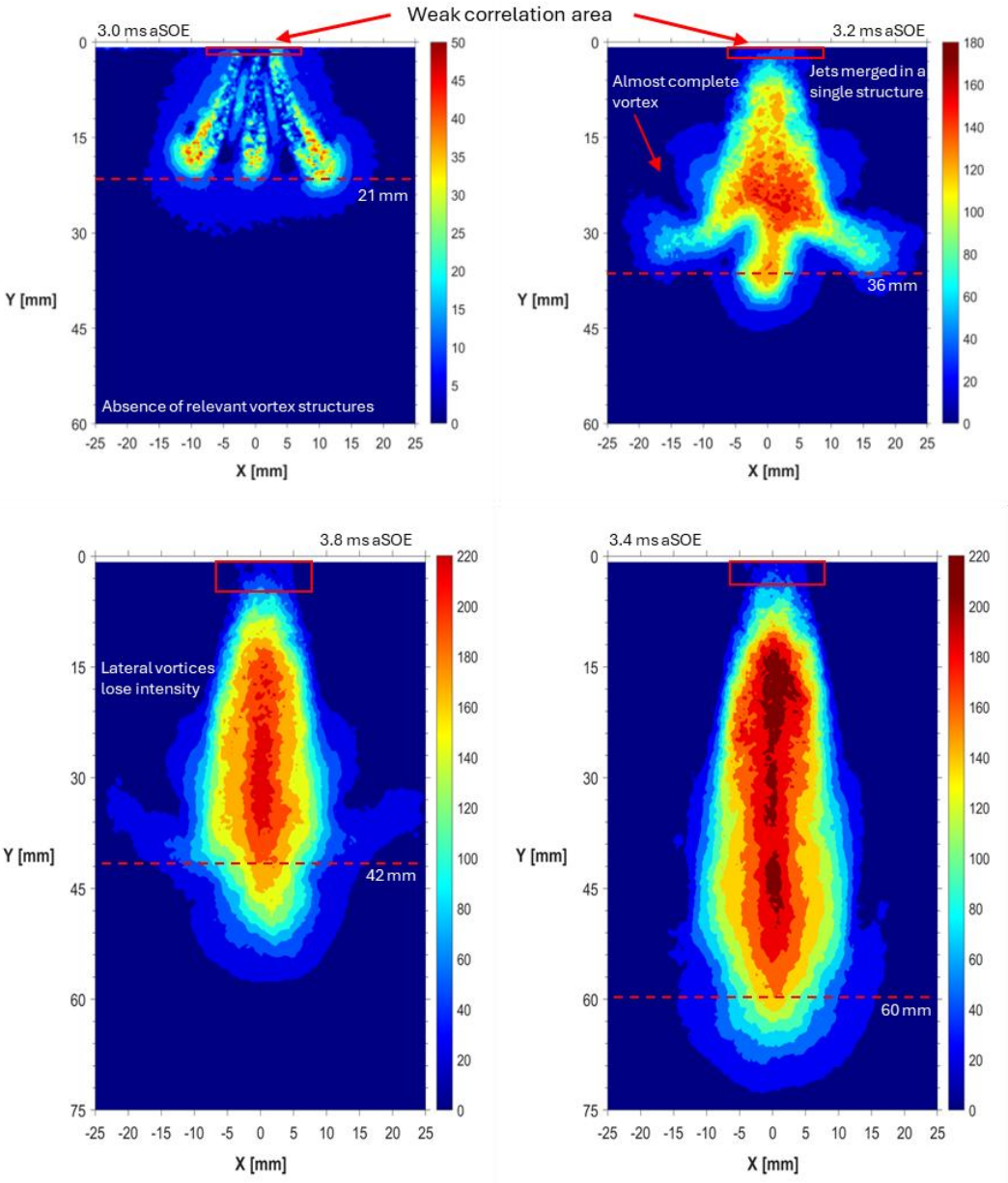

Figure 20. Velocity distribution, GEO-3, averaged frames PR20.

For quantitative oriented comprehension of the results, Figure 21 illustrates the maximum velocity values recorded during experimental test campaign for each condition that was examined. The graphs show average values calculated by using the 20 peaks measured for each single pair of frames, while the dashed triangle area represents the point in which the lower edge reaches the ROI limit. In line with the outcomes on that treated jet extension, the first geometry ensured featured the highest values of velocity magnitude, regardless of the PR condition; it ranged from 108 to 242 m/s. Specifically, during the early stages the 2nd and 3rd geometries were found to feature a slightly faster pattern compared to the 1st nozzle, with a difference ranging from 10 to 20%. In this phase, it is the size of

the holes on the nozzle tip that play a key role, rather than their orientation; this is due to restriction of the jet, resulting in increased penetration in the air contained in the chamber. This trend is reversed between 3.4 – 4.0 ms aSOE, after which the 1st geometry results "faster" than the other configurations. The gap among the three configurations is more evident as the PR increases, with the 1st nozzle leading with a difference of a few percentages at low PR, to slightly more than 20% for PR10 and PR20.

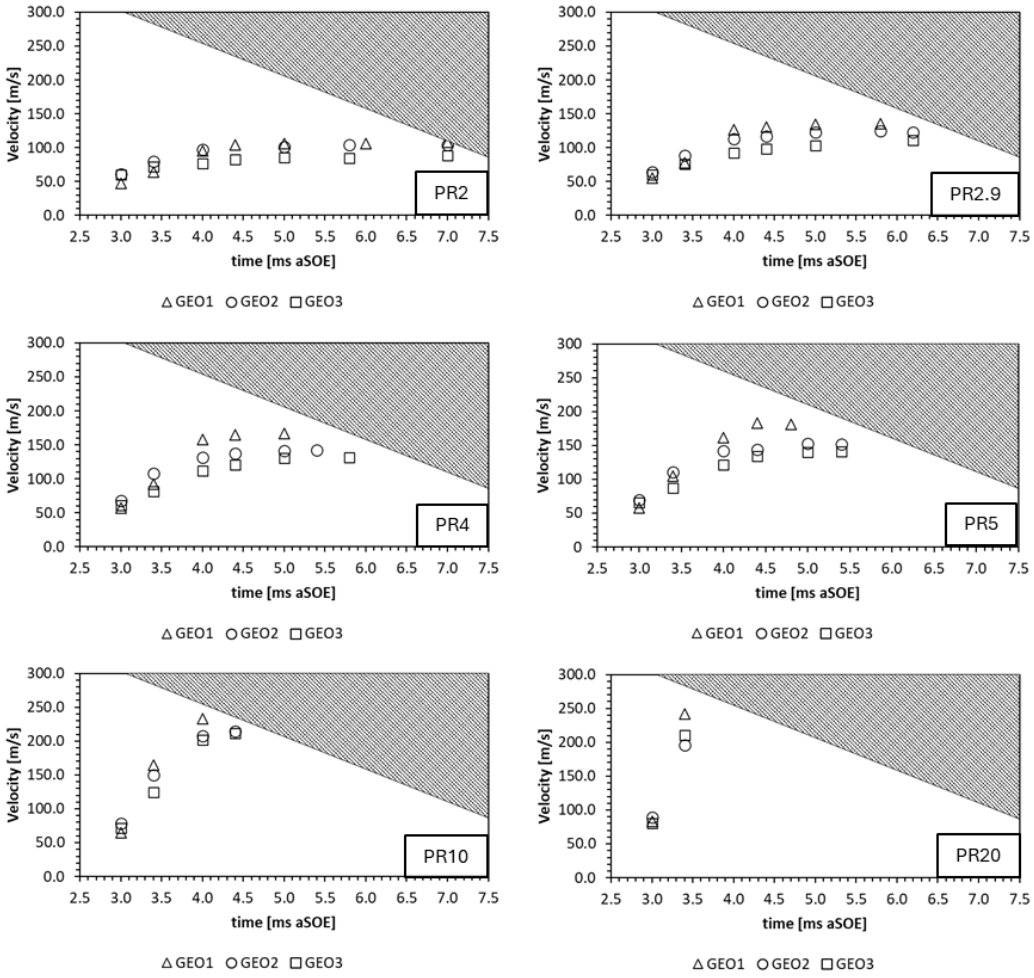


Figure 21. Average velocity peaks for the three nozzle patterns at different PRs.

However, it is important to emphasize that all values shown in Figure 21 were obtained when the gaseous jet was entirely located inside the ROI. An additional set of 20 pair of frames recorded at 8.0 ms aSOE revealed that the peaks measured so far were already close to plateau conditions except for the condition at PR20. The latter in fact was the only case to record a further increase in velocity at 8.0 ms aSOE, achieving values from 280 to 309 m/s as presented in Table 4.

Table 4. Average velocity peaks recorded at 8.0 ms aSOE.

| 8 ms aSOE | **PR2** | **PR2.9** | **PR4** | **PR5** | **PR10** | **PR20** |
|---|---|---|---|---|---|---|
| **GEO-1** | 105.4 | 138.1 | 167.0 | 179.2 | 248.7 | 309.4 |
| **GEO-2** | 108.1 | 125.2 | 141.9 | 154.4 | 211.6 | 280.6 |
| **GEO-3** | 90.8 | 109.3 | 127.6 | 142.5 | 208.6 | 297.3 |

## 4.2 Vector plots analysis

A detailed discussion on the resulting vector plots is necessary for analysing vorticity intensity; this is essential for achieving correct recognition and analysis of the different phases of gas-air interaction. For a given flow and considering a certain random point that moves along with it, vorticity intensity is defined as the pseudovector field which describes the local spinning motion of such a point. Mathematically, the vorticity ω is the curl of the flow velocity v, expressed by the Eq. 1:

$$\omega \equiv \nabla * v$$

Eq. 1

where ∇ is the nabla operator. This equation, in a 2D flow becomes:

$$\omega = \left(\frac{\partial v_y}{\partial x} - \frac{\partial v_x}{\partial x}\right) * e_z$$

Eq. 2

where $e_z$ is the versor along the zeta-axis. So, this type of analysis focuses on the investigation of those flow phenomena such as the formation of vortex rings, small eddies and so on. It is important to note that during post-processing of images, it became evident that the vector field did not change significantly. In fact, rather than the development pattern, the pressure ratio acts on the timing necessary for reaching a certain stage of the gas-air interaction. These premises, coupled with the large amount of data recorded, convinced the author to illustrate in this section the solely images related to the operative condition at PR4. More to the point, information shown in were obtained from an ensemble of 20 pair of frames. Figure 22 highlights the vector plot obtained from a single pair of frames when the jet is fully developed. This figure was added to emphasize the differences between averaged data and single point analysis, showing the waveform trend of the vectors composing the gaseous jet structure. Furthermore,

to render Figure 23, Figure 24 and Figure 25 easier to interpret, the density of the vectors has been reduced by a quarter. Similarly to the velocity distribution, the averaged graphs represent probability density areas of the investigated parameter. Specifically, per definition the vorticity is related to velocity and instantaneous radius, thus the differences in terms of absolute maximum values compared to single frame peaks is higher than that observed for the velocity. This gap increases up to 45-50% compared to the average of the 20 peaks of the individual frame pairs (See values in Figure 26). The averaged data are therefore supposed to provide insight into the major structures observed, which dominate the different stages of jet development, as well as for the intensity images used to relate these motions to the corresponding peaks.

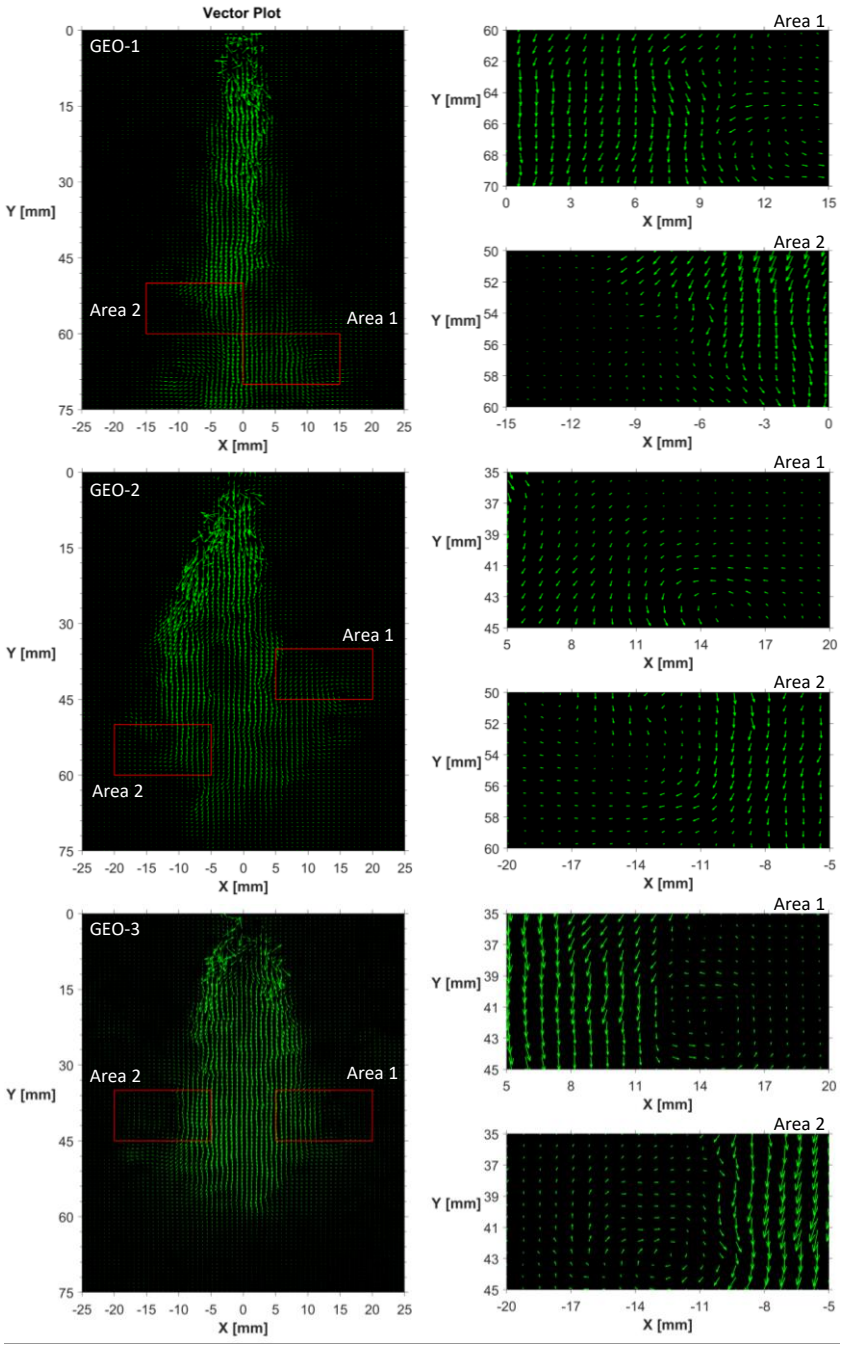


Figure 22. Vector plot (left) at 5.0 ms aSOE. PR4, single pair of frames.

In order to emphasize the differences between the averaged data and that related to the single pair of frames, Figure 22 shows the vector plot generated by the software when the jet is fully developed. What is immediately evident is the presence of wavy flow lines, representative of irregularities in the injected gas–air concentration. Further on, the spur vectors increase in number close to the nozzle tip, but despite their size, these consist in few points. Specifically, the amount of

spur vectors was always kept below 4% compared to the total amount of points present in the discrete grid.

### 4.2.1 1st Nozzle pattern

Figure 23 presents the vector plot and vorticity distribution generated by using the first nozzle tip geometry. During the early stages, the two major vortex structures on the head section of the jet appear clearly visible in the vector plot graph, and the instantaneous centre of these rotational motions correspond to the position of the vorticity peaks. Very close to the centre of the vortexes, the intensity reaches values of around 85000 1/s. In a 3D perspective, these two vortexes can be assumed to be connected by a toroidal ring surrounding the jet head. In this phase, the latter is the main contributor to the interaction between gas and air, dragging the air inside the gaseous structure from the rear area. Close to the nozzle tip, the acceleration caused by the continuous supply of fresh charge renders the steady state region (0 – 25 mm) to be characterised by increased vorticity throughout the duration of the injection. The two vortexes on the head section are initially able to keep up with the extension of the jet. At 4.0 ms part of the vorticity intensity on the jet head was dissipated but still contributed to the mixing of the injected gas with air. At this stage, the vorticity image makes it possible to observe two discontinuities separating the steady state region from the head region of the jet. In these areas the external particles of air coming into the jet with an oblique direction deviate the vectors coming from the nozzle tip towards the centre. This phenomenon leads to a flow “disconnection” of the head section from the fresh charge. Without the supply of new particles, the two vortexes positioned on the head become unable to sustain the rotative motion, rapidly dissipating their vorticity intensity. At 5.0 ms aSOE the only relevant regions for the interaction between gas-air remain that close to the nozzle tip; there, the fresh supply of helium contributes to the establishment of small eddies.

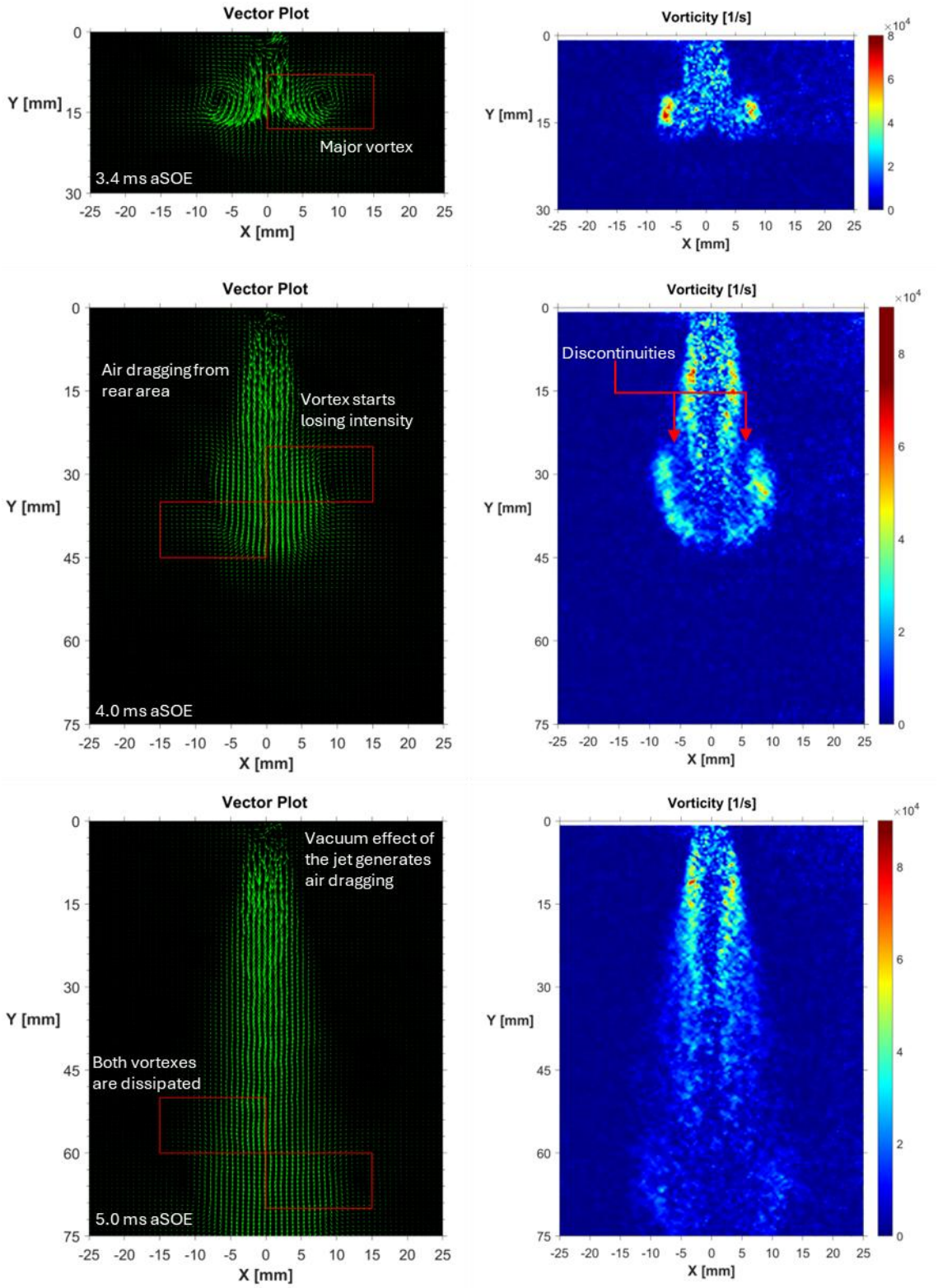


Figure 23. GEO-1, vector plot (left) and vorticity intensity (right) at 3.4, 4.0 and 5.0 ms aSOE. PR4, averaged data.

### 4.2.2 2nd Nozzle pattern

Figure 24 provides a closer look at the flow behaviour for the second geometry. At 3.4 ms aSOE, it is noticeable how the two jets coming from the in/out-of-plane holes work differently in terms of interaction with air. On the left side, the out-of-plane hole, which is the most oriented one, generates an oblique jet able to keep momentum better than the in-plane component, resulting in greater extension. In this phase the vector plot shows the presence of a complete ring structure on the inner side. Given the asymmetry of nozzle pattern (See Figure 13 Bottom), it can be supposed that this vortex is taking place for each pair of holes, but not leading to the formation of a single structure like the toroidal ring described for the first geometry. Despite the high maximum intensity, the actual peaks that can be seen on the intensity graph are isolated points, leaving the vortex structure on the inner side as the only one to be recognizable. On the outer side, the jet proceeds with minor influence from the surrounding environment. Given the reduced open area on the nozzle tip, this case features greater extension (≈26 mm) compared to the 1st geometry, renders it possible to keep the collected particles along the direction of the jet without giving rise to the formation of vortex structures. At 4.0 ms, the inner ring is starting to lose intensity for similar reasons to that observed for the first geometry. In fact, the anticlockwise motion triggered by the inner ring results in the opening of a discontinuity in the vorticity distribution. This lack in supply of fresh charge from the steady state zone contributes to a significant loss in intensity of the inner ring, with resulting values around 40000 1/s. On the contrary, the outer jet started slowing its radial spreading. The presence of an incomplete ring on the head section of the outer jet can partially justify such phenomena. In fact, the clockwise motion of the particles is plausible to act in the opposite way to the radial extension of the jet. In addition, slow radial propagation of the gaseous structure can also be attributed to the presence of a low-pressure area in between the two jets, that combined with the action of the ambient pressure, result in a sort of “confinement” action by the air on the helium. To pursue this hypothesis, the plume angle of the jet was observed to reduce as the air backpressures was increased (See Figure 29). Nevertheless, these above are hypothesis for which further investigations are needed. At 5.0 ms aSOE most of the vorticity intensity is located in the steady state region. Both jets

are surrounded by multiple peaks, with the inner side showing slightly higher values.

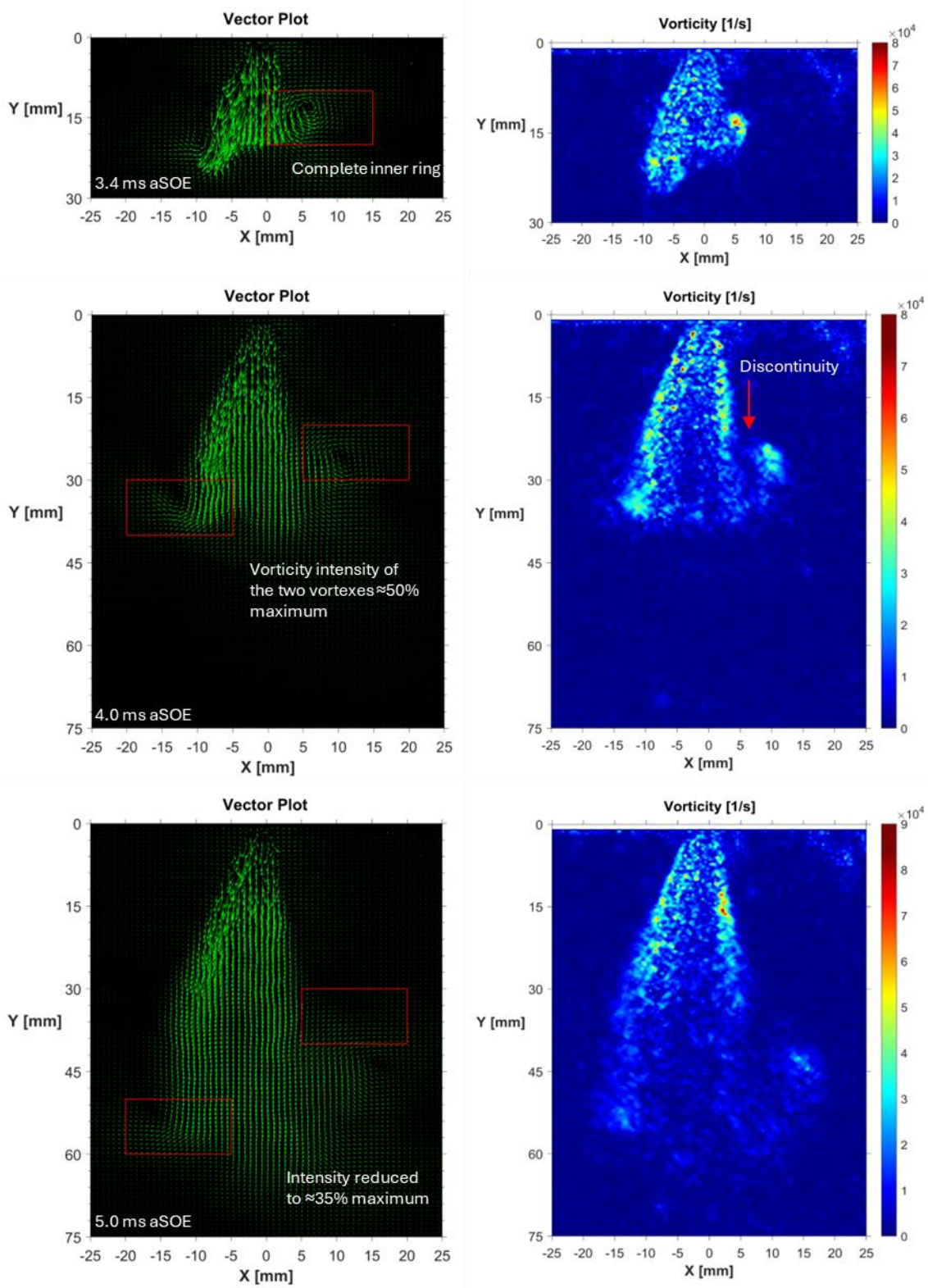


Figure 24. GEO-2, vector plot (left) and vorticity intensity (right) at 3.4, 4.0 and 5.0 ms aSOE. PR4, averaged data.

Despite, similarly to the first geometry, rather than significant vortex structures, are the small eddies to drive the mixing efficiency of the investigated geometry when the jet is fully developed. In this phase the maximum intensity value is of around 85000 1/s and observed on the inner side of the jet edge.

### 4.2.3 3rd Nozzle pattern

Figure 25 shows the various stages of the flow field for the 3rd geometry. In the first phase, subsequent to the start of the injection, the three jets are clearly recognizable and feature comparable value of vorticity intensity, i.e. ≈75000 1/s. Even though the central hole is smaller in size, the corresponding jet shows similar penetration compared to the other two, due to the shorter path that it has to follow when passing through the hole. Unlike the previous geometries, there are no appreciable vortex structures formed at 3.4 ms aSOE. Specifically, the outer jets contribute to the formation of two lateral rings, with quite reduced intensity compared to the small eddies that were formed over the jet edges. The reasons for the absence of a relevant vortex structure can be attributed to the relatively small size of the holes and their orientation, which led to the generation of narrow and separate jets, that are able to keep the momentum without losing energy to the surrounding air. At 4.0 ms aSOE, the vector plot illustrates the deviation of the head section of the later jets towards the external regions. In this phase it is possible to observe the air dragged from the steady state region. Despite the entrainment, the two lateral jets lost most part of their momentum (in the same regions in which the measured average velocity measured is less than half the maximum, see Figure 19 and Figure 20), thus hindering the formation of complete rings. On the other hand, the fresh charge coming from the nozzle tip reaches these areas with higher velocity, dominated by the vertical component and leading to the breakup, given that they are unable to follow the deviation. At this stage, the out-of-plane jets collapse, leaving the central jet alone to drive the extension. The two structures on the lateral regions, that are now disconnected by the main structure, did not generate any relevant vortex, and air entertainment from the rear zone remains homogeneously distributed but still characterized by low intensity. At 5.0 ms aSOE, as a result of the action of fresh gas from within the main flow, the two side structures are no longer visible leaving a single larger jet that is

characterized by higher plume angle compared to the first geometry (See Figure 29), but with lower velocity magnitude.

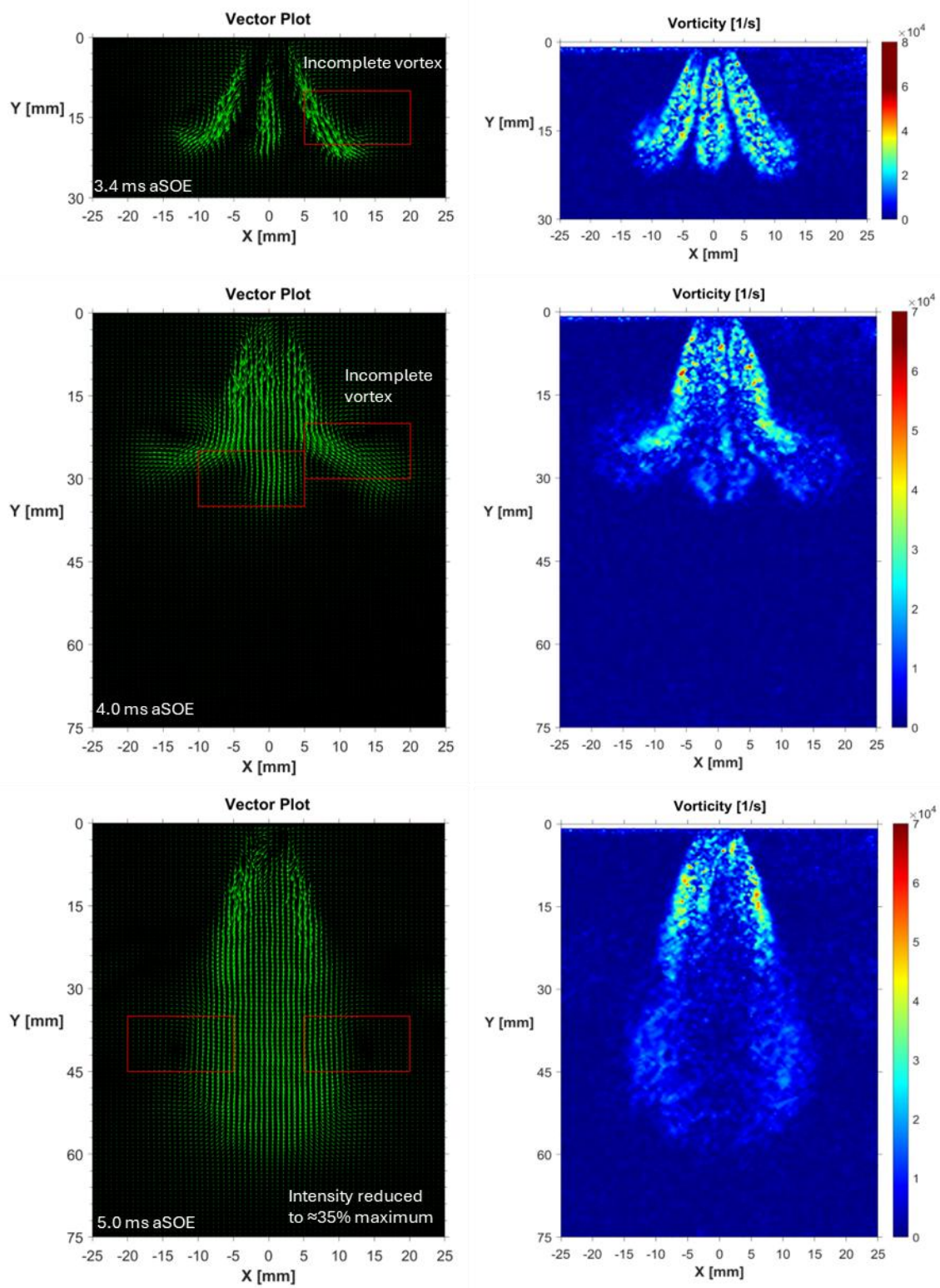


Figure 25. GEO-3, vector plot (left) and vorticity intensity (right) at 3.4, 4.0 and 5.0 ms aSOE. PR4, averaged data.

## 4.3 Vorticity intensity

Figure 26 presents the absolute peaks of the vorticity intensity recorded by the three geometry nozzles for the various PRs examined. The difference among the three configurations appears more contained with major differences between 1st and 3rd geometries at PR4, equal to around 15%. Specifically, 1st and 2nd geometries alternate randomly, while 3rd geometry showed an overall lower values of vorticity intensity.

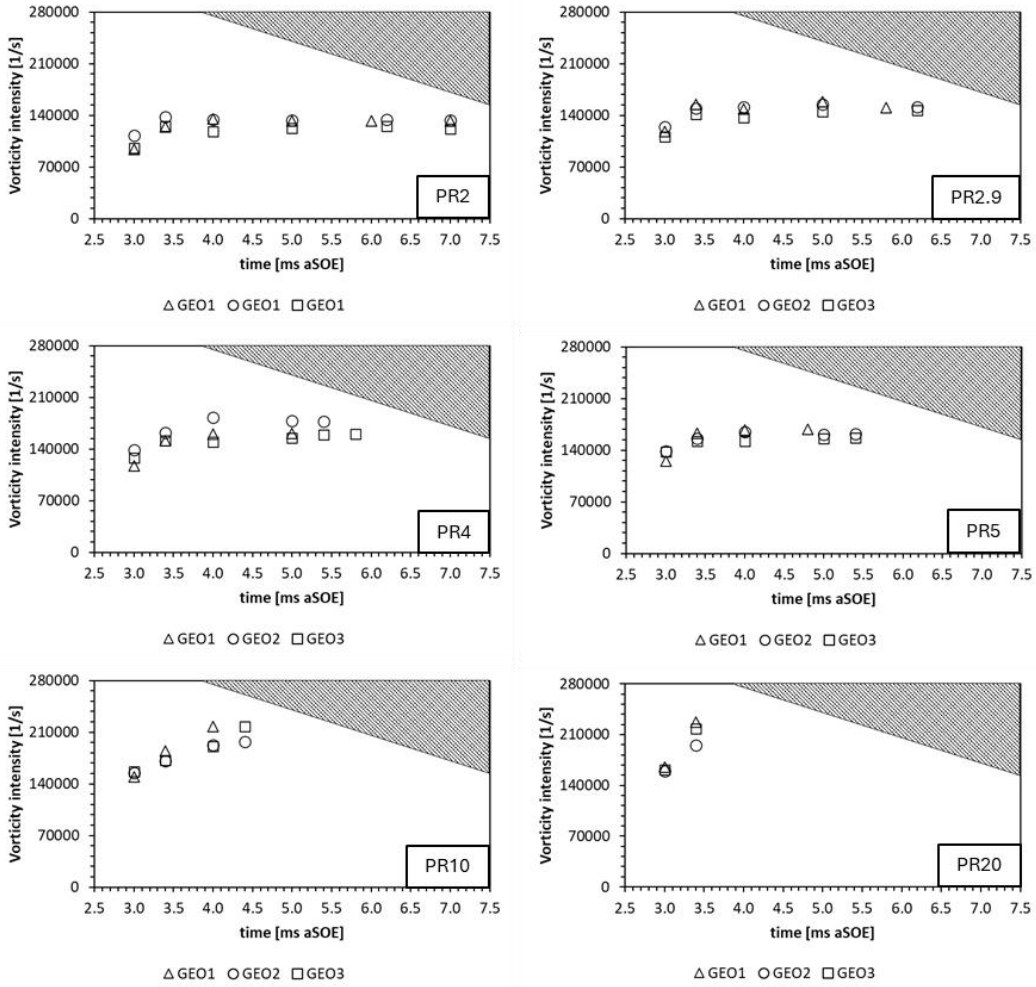


Figure 26. Average vorticity peaks for the three nozzle patterns at different PRs.

Furthermore, unlike the velocity that increases linearly until reaching the lower edge of the ROI, the peaks in vorticity were observed to stabilise at almost constant values after 3.5 ms aSOE, regardless of the nozzle tip. Given the definition of the vorticity intensity, it is therefore possible to assume that as the average velocity of the jet increases, the instantaneous radius of the vortex structure decreases. This hypothesis is in line with the observed tendency of the

major rotational structures to extinguish as the jet develops. However, looking to the peak's values, another difference compared to velocity is that when increasing the PR, it does not undergo the same variation in magnitude (considering a specific value at a fixed time instant). For example, at PR2 and 3.4 ms aSOE, the average velocity recorded for all geometries was about 80 m/s; it then increased up to 200-250 m/s for PR20. On the other hand, vorticity increases from 120000-140000 to 200000-235000 1/s. The ratio between the low and high PR conditions is thus reduced from almost 3.0 in velocity to 1.8 in vorticity.

Lastly, the values recorded at 8.0 ms aSOE are listed in Table 5. The vorticity intensity featured more comparable values, with the largest difference measured between 1st and 3rd geometry at PR5, thus equal to slightly less than 10%.

Table 5. Average vorticity peaks recorded at 8.0 ms aSOE.

| 8 ms aSOE | PR2 | PR2.9 | PR4 | PR5 | PR10 | PR20 |
|---|---|---|---|---|---|---|
| **GEO-1** | 130196.4 | 150371.9 | 163636.1 | 170049.6 | 199911.5 | 239255.5 |
| **GEO-2** | 130663.6 | 159241.1 | 160284.6 | 161613.8 | 192116.3 | 221887.2 |
| **GEO-3** | 122528.1 | 142982.7 | 158985.9 | 154918.1 | 202046.9 | 229685.7 |

## 4.4 Jet morphology

Another aspect examined in this work is the morphology of the jet/s, in terms of its penetration and the plume angle. Both parameters were analysed by running a routine (built as code in Matlab) able to detect the edges. The working principle of the routine was based on the velocity threshold defined by the user to identify the coordinates of the borders all around the jet perimeter. More in the detail, considering a generic operative condition, the threshold value was set equal to the 20% the mean value of the peak velocities of all 20 frame pairs. Taking into account that the data yielded by the PIV software are in the form of matrices, the code found step-by-step along the injector axis the first and last coordinate within which the condition of velocity equal or major to the threshold is matched. The results obtained were validated with the optical findings for the operating conditions with 1 bar backpressure, providing an error of less than 3%. The main reason for which it was unsuitable to directly use an optical software to measure the jet penetration was due to the influence of the backpressure on global luminosity of raw images. In fact, it was noted that as backpressure was raised,

the global luminosity of the frames rapidly decreased making it difficult the detect jet edges.

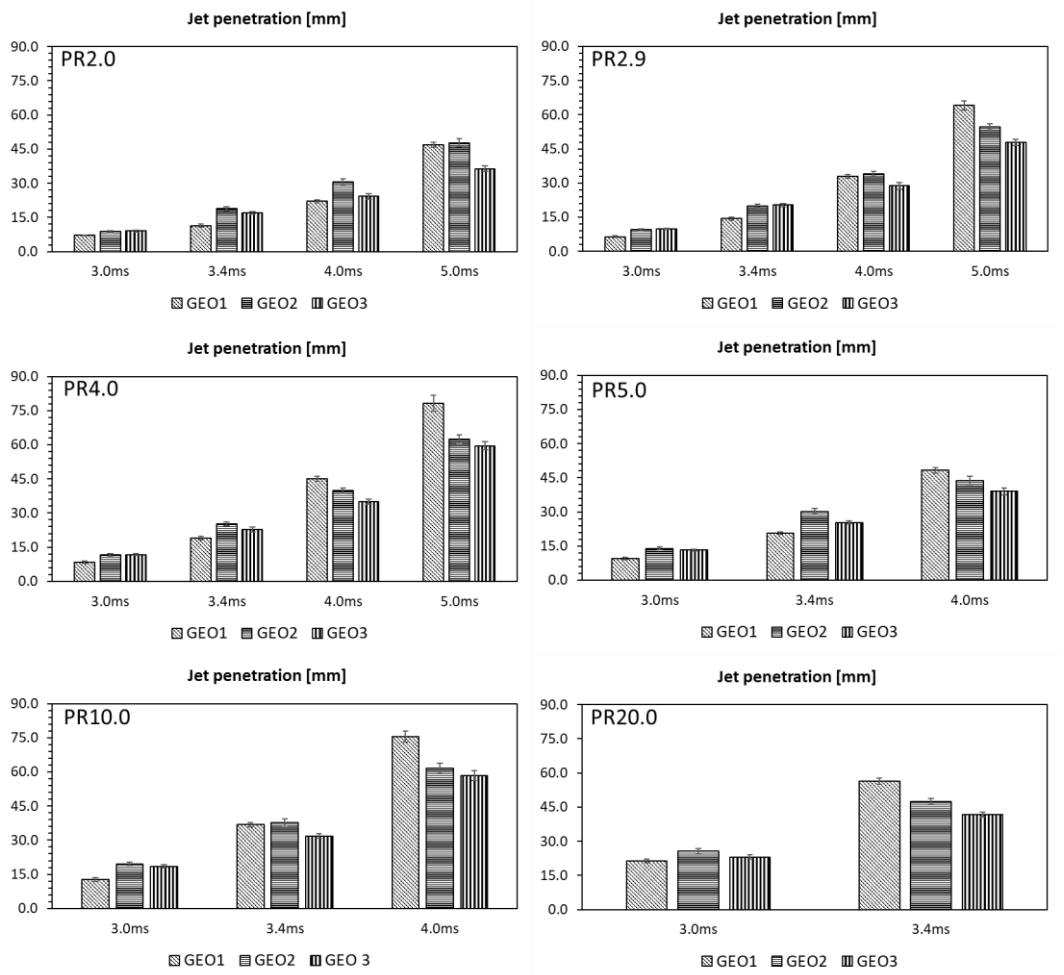


Figure 27. Helium jet penetration for different PRs.

Figure 27 shows the jet penetrations values calculated by using the procedure described previously. The graphs confirm how the first geometry is always the "slowest" in the early stages, thus in line with the previous considerations on velocity magnitude. Then, due to the low orientation of the nozzle pattern holes, the jet starts rapidly increasing, overcoming the extension of the other configurations. The growth rate of the jet penetration was observed to be linear, regardless of the PR condition and geometry. Furthermore, the variability was always at low values, ranging from 1 to 5%, thus suggesting a good repeatability of the jet extension. In terms of gap, the difference between the 1$^{st}$ geometry and other configurations reaches its peak of around 20% before the gaseous structure reaches the lower limit of the ROI. On the other hand, the jet length of the 2$^{nd}$ and 3$^{rd}$ geometries appear more comparable, with the first slightly "faster" to

propagate, thus resulting in a positive gap of about 5%. As for the plume angle, it would be more correct to refer to it as half the plume angle measured for this work. In fact, considering the three nozzle tips analysed for this study, the second geometry is the only one that does not feature a symmetrical view of the jet structure. It was therefore decided to measure only half of this parameter. The approach used for measuring this value is directly dependent on the accuracy of the detection of edges. Figure 28 shows an example of the procedure used to calculate the half plume angle. Specifically, the distance of the out-of-plane hole was known, thus it was possible to define the straight line between its y-coordinate and the outermost point along the edge. The angle between this line and the horizontal was defined as half plume angle.

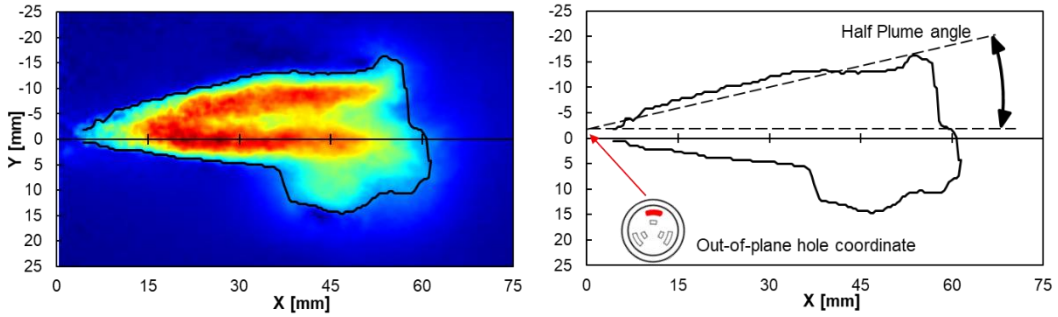


Figure 28. Example of half plume angle measurement procedure, 2nd nozzle pattern, PR5, 4ms aSOE, averaged frames.

Figure 29 illustrates these values as histograms for all the configurations investigated. Both first and second geometries resulted in an almost linear trend of narrowing radial propagation with time (except the broadening observed at very early stages of injection). On the contrary, the third geometry featured a constant value of the half plume angle until the occurrence of the "collapse event" corresponding to the breakup of the lateral structures formed by the out-of-plane jets. The data recorded within the ROI showed that the gaseous structure formed by the 1st geometry reduced to a half plume angle of around 5-9°, the second from 15 to 25° and the third up to 30°, depending on the PR condition. More in detail, contrary to the considerations on the jet penetration, the half plume angle highlights the compromise in nozzle pattern choice.

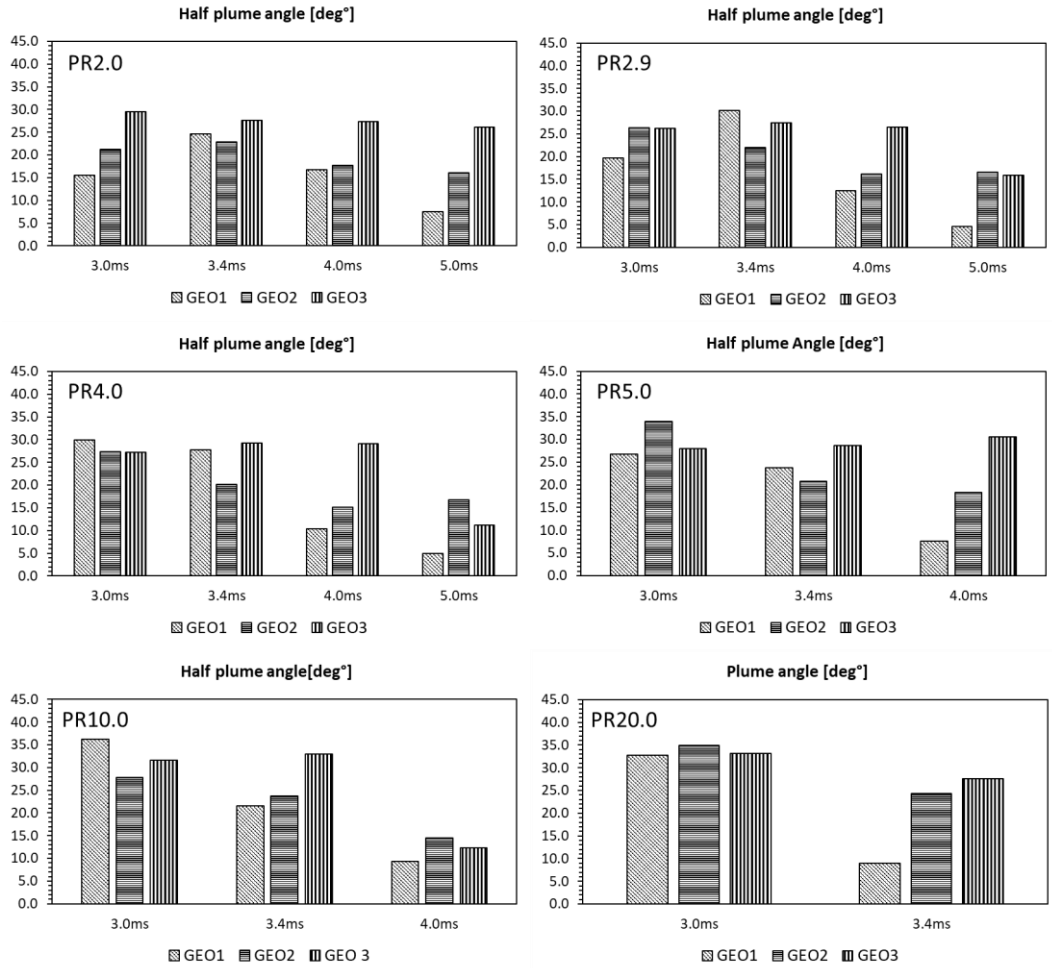


Figure 29. Helium jet plume angle for different PRs.

In this chapter the PIV technique has been to analyse the velocity and vorticity characteristics of helium jets delivered by a light-duty gas injector. Among main results, the use of nozzle patterns with low orientation hole paths, like first geometry, was observed to lead to the generation of jets capable of keeping momentum, thus fastening the resulting jet at expense of a limited radial propagation (more detail in Summary and conclusions), opposite to the behaviour of the 2$^{nd}$ and 3$^{rd}$ geometries. Moreover, the current investigation emphasized the role of major vortex structures in early and middle stages after injection in promoting mixing phenomena. The same structures were therefore observed to rapidly collapse, regardless of the nozzle pattern and PR condition, leaving room to the rise in number of small eddies. These results can represent a starting point for the design of piston bowl shapes and the development of injection strategies on the base of targeted effect such as homogeneous distribution or stratification of the fresh charge.

# Chapter 5

# Reactive analysis results

This chapter discusses the data obtained through experimental tests performed on the single cylinder engine; it is focused on an in-depth investigation of thermodynamic and morphological aspects of the flame. The cases with methane–hydrogen blends fuelling is discussed first, followed by those with pure hydrogen operation.

Considering the objective of this doctoral thesis, i.e. optically characterization of hydrogen combustion, thermodynamic parameters are briefly discussed in order to provide a quick overview of performance and cycle-to-cycle variability. The following sections are therefore organised to focus primarily on the analysis of data obtained from natural flame emissions, i.e. morphological and spectroscopic analysis. The first type of analysis was performed to gain insights on the phenomena governing the flame front development, starting from its inception, and their correlation to the cycle-to-cycle variability.

The spectroscopy was applied for measuring emissions that feature plasma and flame kernel and connect these to the air-fuel ratio. Specifically, this approach paid particular attention to the detection of hydrogen emissions, ranging from atom to molecule spectral evidence.

## 5.1 Rate of heat release analysis

Before proceeding with the discussion of the proposed results, it is noteworthy to emphasise the challenge in characterizing the heat exchange and mass losses of the in-cylinder charge in an optical engine. These difficulties are

mainly caused by the large contact surface area between the piston and cylinder walls and the heat release profile which differs from that of commercial engines due to the presence of the quartz window on the piston crown. To calculate the net heat release rate (NHRR) the approach described in [91] was adopted. The main engine performance and combustion parameters, e.g. the Indicated Mean Effective Pressure (IMEP), its Coefficient of Variation (COV) and NHRR required the development of a dedicated script by using National Instrument (NI) LabView 2020 software. IMEP and NHRR were calculated on the ensemble average of 200 consecutive engine cycles for each condition under investigation. The Mass Fraction Burned (MFB) was then calculated on the basis of the integral of the net heat release rate, obtained by means of equation (1), as follows:

$$dQ_n = \frac{\gamma}{\gamma - 1} * p * dV + \frac{1}{\gamma - 1} * V * dP$$

Eq. 3

where $dQ_n$ is the net heat rate release measured in Joule per crank angle, $p$ the in-cylinder pressure in Pa, $V$ is the instantaneous cylinder volume in $m^3$, and $\gamma$ is the ratio of specific heats of the in-cylinder charge, which was set to 1.35. MFB was therefore calculated as:

$$MFB = \frac{Q_k - Q_{ST}}{Q_{EVO} - Q_{ST}}$$

Eq. 4

where the subscript "*k*" is related to the current crank angle position, while the subscript "*ST*" refers to crank angle at spark timing and "*EVO"* to the crank angle at the exhaust valve opening. Once MFB was calculated, it was possible to identify the CA corresponding to 0–5%MFB (CA5) and 0-50%MFB (CA50), taken as representative for kernel development angle and for flame propagation, respectively. Noteworthy are the differences in the heat release rate measured by an optical motor when compared to its series counterparts. In fact, the presence of the quartz window instead of the metal material and the larger volume crevices result in an overall slowing of the heat release rate and a continuous increase in MFB even during the expansion phase.

## 5.2 Methane – Hydrogen: Thermodynamic parameters

Six operative conditions were examined for methane-hydrogen fuelling. The $H_2$-$CH_4$ blend was supplied from externals tanks (high pressure bottles containing the gas mixtures at 200 bar) and was delivered to the intake manifold of the engine through the use of a PFI gas injector. The duration of injection, as well as the spark timing, were varied as shown Table 6. Specifically, the first set of cases entailed stoichiometric conditions, spark timing at 10 CAD bTDC, and the mixture composition varying from pure methane to the 50/50 blend. For the remaining cases the air-fuel mixture was diluted and featured an $AFR_{rel}$ (lambda) of 1.3, and spark timing was varied to investigate its influence.

Table 6. Methane – Hydrogen operative conditions

| **Engine speed [rpm]** | **Start of Injection [CAD bTDC]** | **Lambda [-]** | **Blend Composition [-]** | **Spark timing [CAD bTDC]** |
|---|---|---|---|---|
| 2000 | 340 | 1.0 | 100% $CH_4$ | 10 |
| | | | 80%$CH_4$ - 20%$H_2$ | |
| | | | 50%$CH_4$ - 50%$H_2$ | |
| | | 1.3 | 50%$CH_4$ - 50%$H_2$ | 10 |
| | | | | 15 |
| | | | | 20 |

The blend compositions shown in Table 6 refer to the volumetric ratios. The upper limit for hydrogen addition was therefore fixed at 50% to avoid possible occurrence of abnormal combustion phenomena in stoichiometric conditions. In fact, during fuelling with pure $H_2$ it was found that knock-free operation could only be achieved for λ values over 2.0 (See Table 7).

Figure 30 shows in-cylinder pressure traces for the first set of data. Hydrogen addition was observed to cause a significant increase in peak pressure inside the combustion chamber, even though the same spark timing was employed. Specifically, the maximum increased from 26.7 bar for the case with 100% $CH_4$, to 30.1 and 35.8 bar for 20% and 50% $H_2$ content respectively. What is immediately evident is the difference in pressure ramp-up after ignition. 100% methane implies a maximum pressure rise rate (MPRR) of around 0.55 bar/ CAD. As the hydrogen content increases, this value rapidly jumps to 0.80 and 1.35 bar/

CAD respectively. The underlying causes of this phenomenon can be attributed to the much higher laminar flame speed for hydrogen, that resulted in "quick" combustion and therefore an abrupt pressure increase compared to methane fuelling. On one hand, this increases efficiency through lower constant volume losses, but it can become a problem in terms of stress gradients that may reach the limit of the piston-connecting rod-crankshaft ensemble. This emphasizes the need for multi-objective choice of combustion timing indicators for alternative fuels [92].

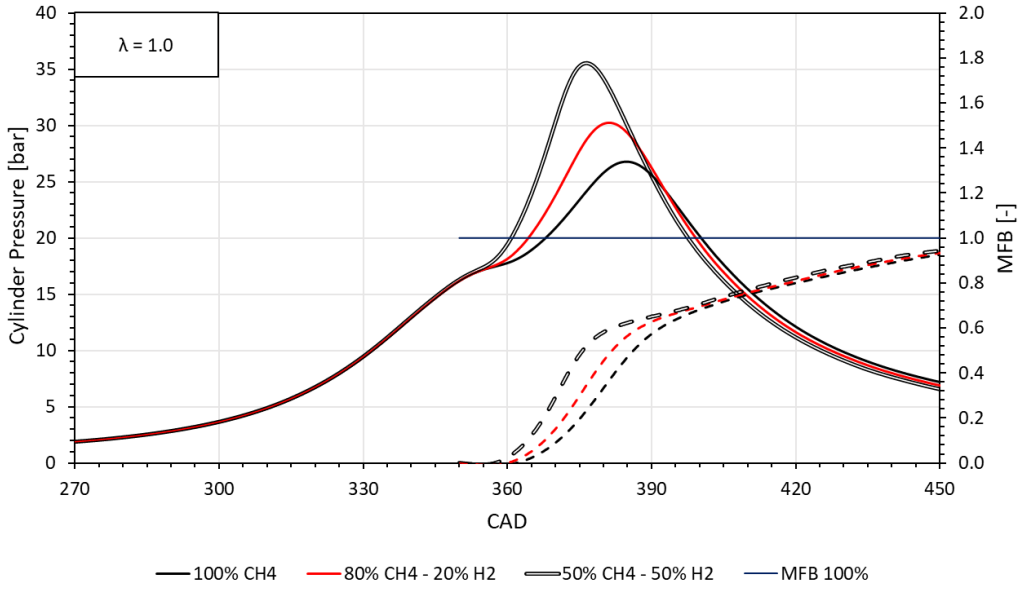


Figure 30. In-cylinder pressure traces (solid lines) and mass fraction burnt (dashed lines). λ 1.0, spark timing 10 CAD bTDC.

The differences in flame propagation speed can be identified from the mass fraction burnt (MFB) traces (Figure 30, dashed lines). In stoichiometric condition the flame development phase (0% - 10% MFB) is strongly influenced by the presence of hydrogen, which results in a reduction of this stage from 20.6 to 14.2 CAD. Similarly, as the fresh charge burns, this "boost" effect continues its influence during rapid flame burning (10% - 50% MFB) which duration reduces from 15.6 to 11.2 CAD as hydrogen content increases.

For the other selected cases, the duration of injection was set so as to increase the global value of λ to around 1.3. Hydrogen volumetric content was fixed at 50%, and spark timing ranged from 10 to 20 CAD bTDC. The measured in-cylinder pressure peaks increase in magnitude as the ignition trigger is anticipated, with a MPRR that ranged from 0.60 to 1.10 and 1.60 bar/ CAD (See Figure 31).

Furthermore, rather than the in-cylinder traces, it is interesting to observe the resulting trend from the mass fraction burnt traces. Unlike the change in blend composition, the advance of the spark timing seemed to play a minor role in influencing the early stage of combustion process. Specifically, the flame development phase duration (0% - 10% MFB) reduces from 17.4 (ST10) to 16.4 (ST15) and 16.0 CAD (ST20). In contrast, the entire duration of the flame development phase (0% - 50% MFB) was more influenced by the spark advance conditions, as its duration reduced from 14.8 to 11.2 CAD when spark timing was advanced.

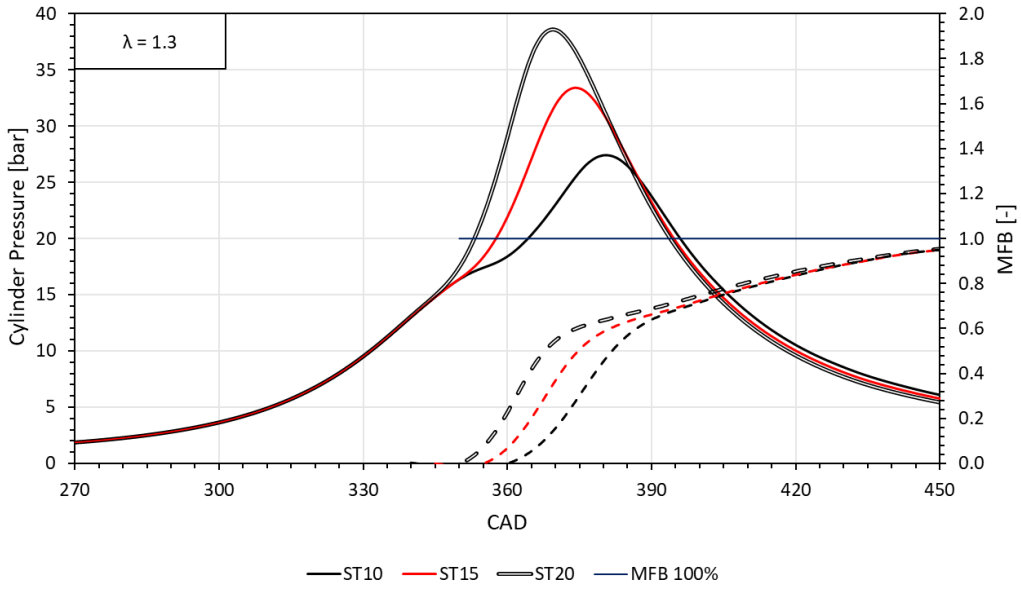


Figure 31. In-cylinder pressure traces (solid lines) and mass fraction burnt (dashed lines). λ 1.3, blend 50% $CH_4$ – 50% $H_2$.

### 5.2.1 Cycle-to-cycle performance and variability

The cycle-to-cycle performance and variability are discussed in this section. The data shown were calculated as ensemble average of 200 consecutive cycles, resulting in a number of sequences high enough for drawing reliable conclusions. The indicated mean effective pressure (IMEP) and corresponding variability (COV) was chosen for characterizing engine output. Figure 32 presents the values of IMEP and its COV as the volumetric content of hydrogen in the blend increases. It immediately stands out that the differences in terms of performances remain almost negligible, with the IMEP dropping by around 3% from 6.9 bar of the 100% methane condition to around 6.7 for 50% $CH_4$ – 50% $H_2$ case. This was

due to a combination of the fact that spark timing was kept constant (most likely resulting in combustion phasing that was too advanced for the blends, even if for the 50% blend decreased constant volume combustion losses most likely resulted in better efficiency compared to 20%) and slightly lower volumetric efficiency when adding $H_2$. Nonetheless, the interesting fact is that stability was significantly augmented (even though the process is already quite stable in stoichiometric conditions); the COV dropped from 1.6% (pure $CH_4$) to just under 0.6% (50% $CH_4$–50% $H_2$). This result is quite remarkable considering that a volumetric addition of hydrogen equal to 50% corresponds to a mass contribution around 11% on the total amount of the blend; a relatively small quantity of $H_2$ can therefore lead to a significant CCV reduction [93]-[94].

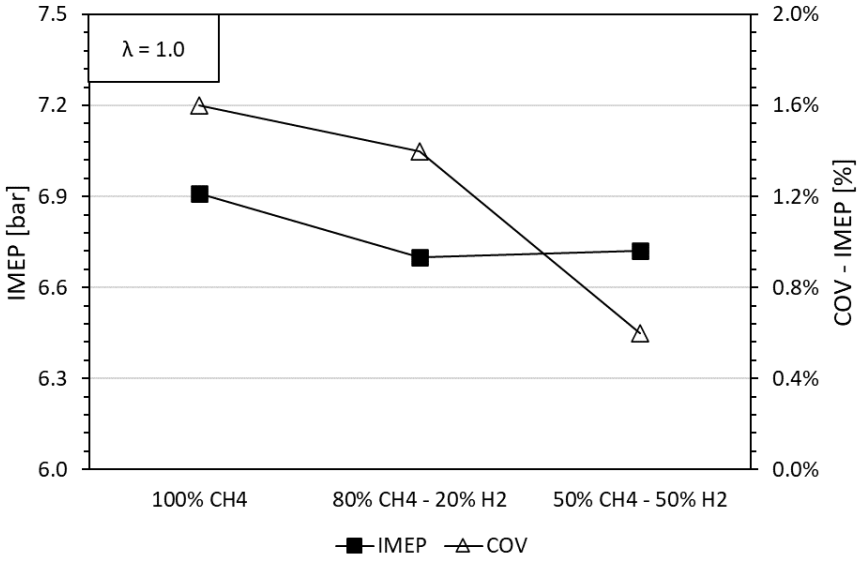


Figure 32. IMEP and COV-IMEP. λ 1.0, spark timing 10 CAD bTDC.

During lean fuelling, for which the $AFR_{rel}$ was increased to 1.3, moving the combustion process away for the TDC by advancing the spark timing from 10 to 20 CAD bTDC resulted in more prominent increase of variability. Figure 33 shows that ST has less dramatic effects on engine output, but resulted in a relatively marked increase in COV, i.e. from 1.1 to 3.3%. This effect can be attributed to more evident influence of tumble and turbulence on flame development, i.e. as ignition takes place earlier during the compression stroke, the kernel is more likely to get displaced in its early stages and the effects of localized turbulence intensity (less homogeneous compared to TDC conditions) results in more dispersed distribution of the location of peak pressure (LPP) parameter. More detailed analysis of the optical data will provide further insight into these

phenomena. It is worth noting though that the COV was below the 5% threshold that is suggested for ensuring operation with acceptable engine borne noise and vibration in automotive applications.

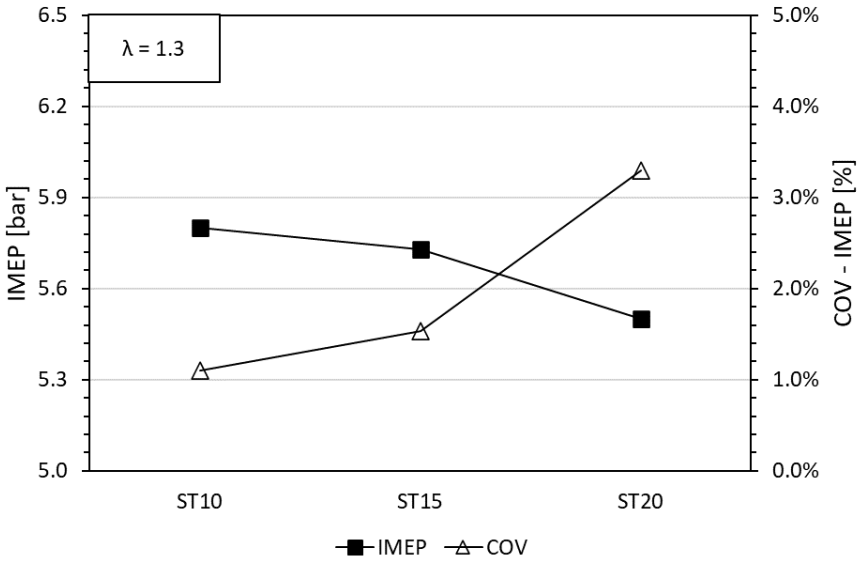


Figure 33. IMEP and COV-IMEP. λ 1.3, blend 50%$CH_4$ – 50%$H_2$.

## 5.3 Methane – Hydrogen: Flame morphology analysis

Before proceeding with the discussion of the results obtained from the morphological analysis, it is important to detail the approach used to define related parameters. The results are presented based on a time sequence logic, i.e. starting with the initial stages of combustion and then proceeding with the flame propagation process. The operative conditions examined in the following sections are listed in Table 6. Specific parameters that were used during the discussion are defined as follows:

- **Feret Diameter (FD)**; it is defined as the measure of an object's size along a specified direction. Its maximum value implies the measurement of the segment corresponding to the distance between the two most distant points of the object that is being visualized.
- **Heywood circularity factor (HCF);** considering a generic 2D object, it is defined as the ratio between the perimeter of the object under investigation and the circumference of a circle with the same area.

### 5.3.1 Early stages

The morphological analysis performed in this section is based on the results obtained by applying the custom post processing procedure; it was aimed at evaluating the effects of hydrogen addition in the conditions listed in Table 6. The analysis was performed for the entire sequence for each cycle, that covered up to 35 CAD aST. For the initial part, it was focused on the flame kernel inception phase (i.e. 0-2% MFB), covering the frames recorded at 4.8 CAD aST. It should be noted that for each operating condition 100 consecutive sequences of frames were recorded (along with the corresponding 100 cycles.

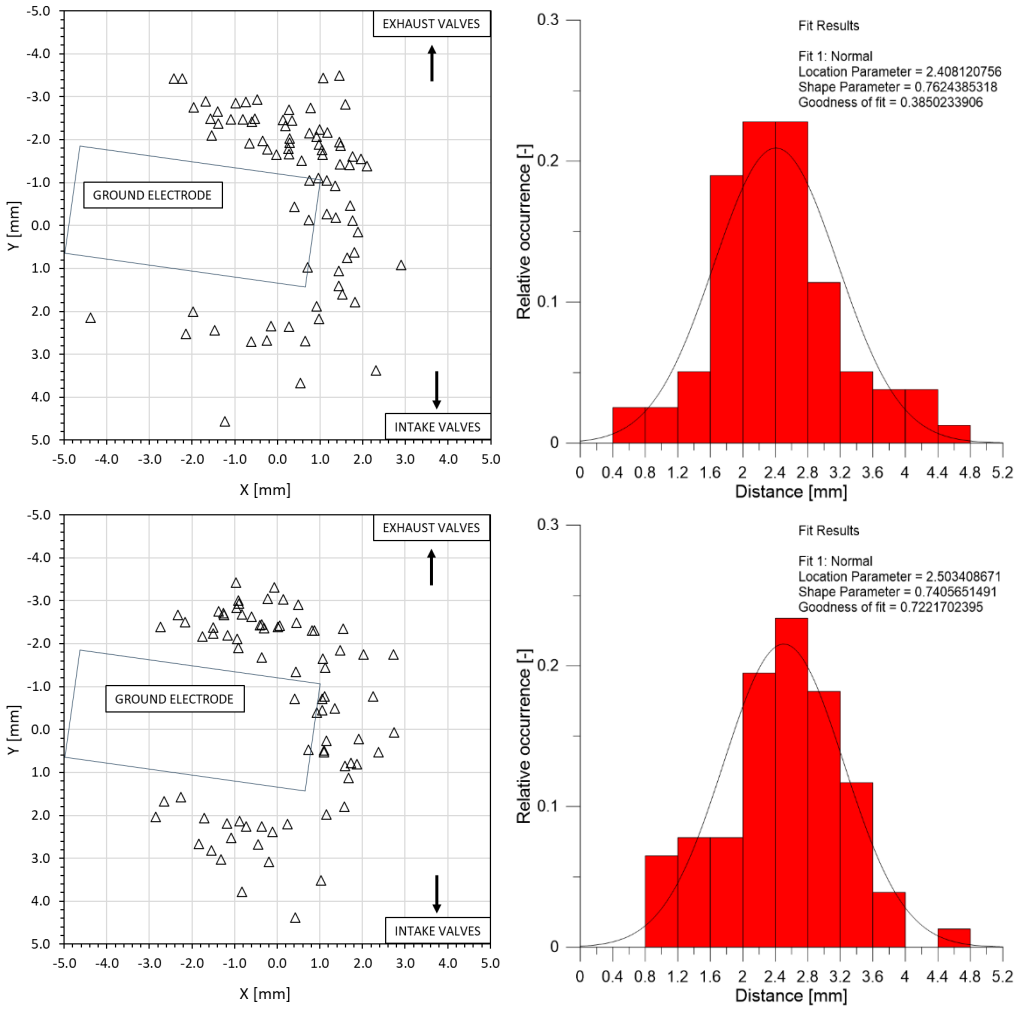

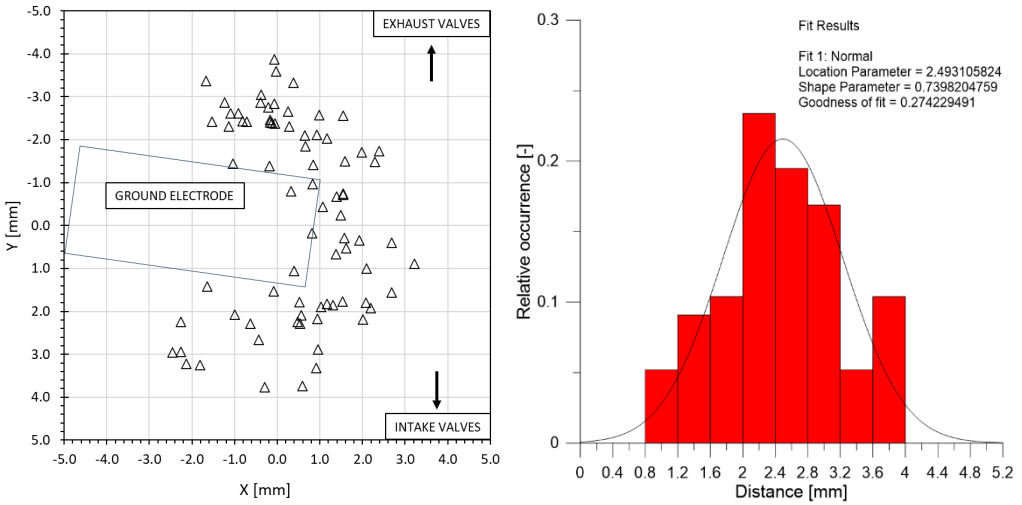


Figure 34. Flame kernel position (100%$CH_4$ top, 80 % $CH_4$ – 20 % $H_2$ at middle and 50 % $CH_4$ – 50% $H_2$ bottom), and corresponding radial distribution (right column).

Figure 34 illustrates the influence of hydrogen addition on kernel position as the blend composition was varied; the corresponding distribution of radial distances from the system's coordinate origin (See A.1 Research engine calibration and optical setup for more details) is also shown. What is interesting is that the flame kernel dislocation seems to be affected to a minor degree by hydrogen addition; the centre moves in proximity of the electrode edge, following a stochastic distribution. Moreover, when switching from the pure methane condition (Figure 34, top) to the 50/50 case (Figure 34, bottom), it is possible to observe that the shape parameter of the Gaussian curve decreases slightly. The three histograms highlight in fact that hydrogen addition results in a narrowing of the possible range of kernel distribution, reducing it from 0.4–4.8 mm (100% $CH_4$) to 0.8–4.0 mm (50% $CH_4$–50% $H_2$) respectively. This result can be correlated with the previous observation (See Figure 32) made for cyclic variability. Specifically, the narrower distribution of the maximum radial distance of the kernel centre suggests that hydrogen results in more stable combustion inception, thus reducing cycle-to-cycle variability. Instead, the average distance of kernel object from the centre was observed to slightly increase as hydrogen content augmented. More to the point, this value passes from 2.40 (100% $CH_4$) to around 2.5 mm for the other two cases.

However, it is noteworthy to underline that the figures above do not take into account the frames in which the arc was positioned between the two electrodes. This effect became relevant as hydrogen content in the blend increases, thus resulting in an increased number of frames in which the arc was hidden by the

ground electrode. To correct this lack of information, for all empty frames the dislocation of centre of the kernel was fixed equal to half the distance between the origin coordinates and the closest electrode edge. This step was of paramount importance for measuring the radial distance and the Feret Diameter. Figure 35 shows that the Feret diameter increases with hydrogen addition; from 5.8 to 7.5 mm. In addition, the number of sequences with hidden arc at 4.8 CAD aST also increases. Specifically, contrary to the considerations on the overall flame object that increases in size, $H_2$ addition influences the arc in an opposite way, thus shortening it. This phenomenon results in an increasing size of the flame kernel, while reducing the arc contained within it. To this end, it is important to note that the data discussed so far  featured the spark plug in crossflow configuration. With this orientation the arc inception zone is fully exposed to tumble and turbulent motion. It is therefore plausible to assume that hydrogen reactivity is high enough to "boost" combustion since its very early stages.

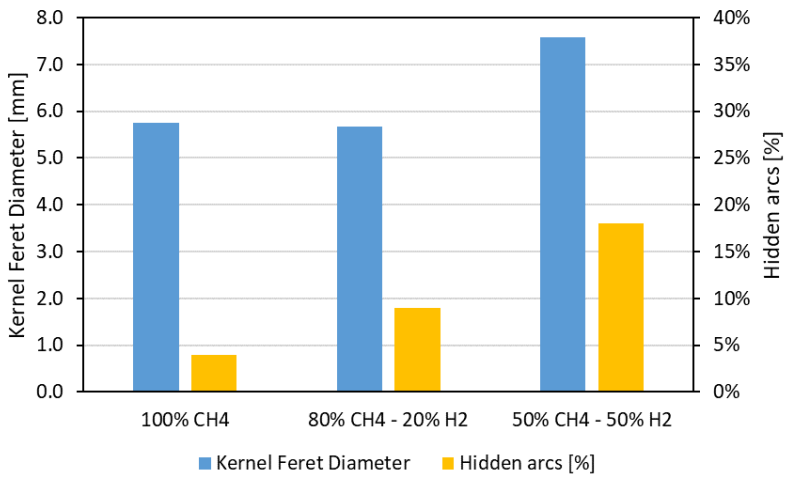


Figure 35. Kernel Feret Diameter and percentage of empty frames. λ 1.0, spark timing 10 CAD bTDC.

The remaining cases focus on the role of spark timing in defining the kernel dislocation and its morphology. Figure 36 illustrates the evolution of kernel displacement and radial distance distribution as spark timing is advanced. In these conditions even though the air-fuel mixture is leaner, the average distance between the kernel centre and the axes origin features pretty much the same distribution. The most probable value of around 2.5 mm is quite close to that recorded with different fuel types; there seems to be a slight increase in the dispersion of distances when increasing spark advance, a hint that perhaps the

effect of turbulence is more consistent when moving away from the TDC. Furthermore, the flame kernel tends to follow a more exhaust-oriented trend regardless of the selected case examined. This tendency can be attributed to the enhanced tumble motion, which acts along direction Y. More to the point, the lower laminar flame speed compared to stoichiometry results in prolonged kernel inception, thus increasing the possibility of displacement due to augmented interaction with direct tumble; therefore, more locations were recorded towards the exhaust valves.

The change in spark timing therefore seems to have less influence on the early stage of combustion. Both kernel centre distance and its distribution showed no relevant trends, or no other trends emerged. Considering the COV increase previously observed in Figure 32, it is plausible to assume that the phenomena governing the increased instability when advancing ignition is more related to the rapid burn duration rather than the kernel phase.

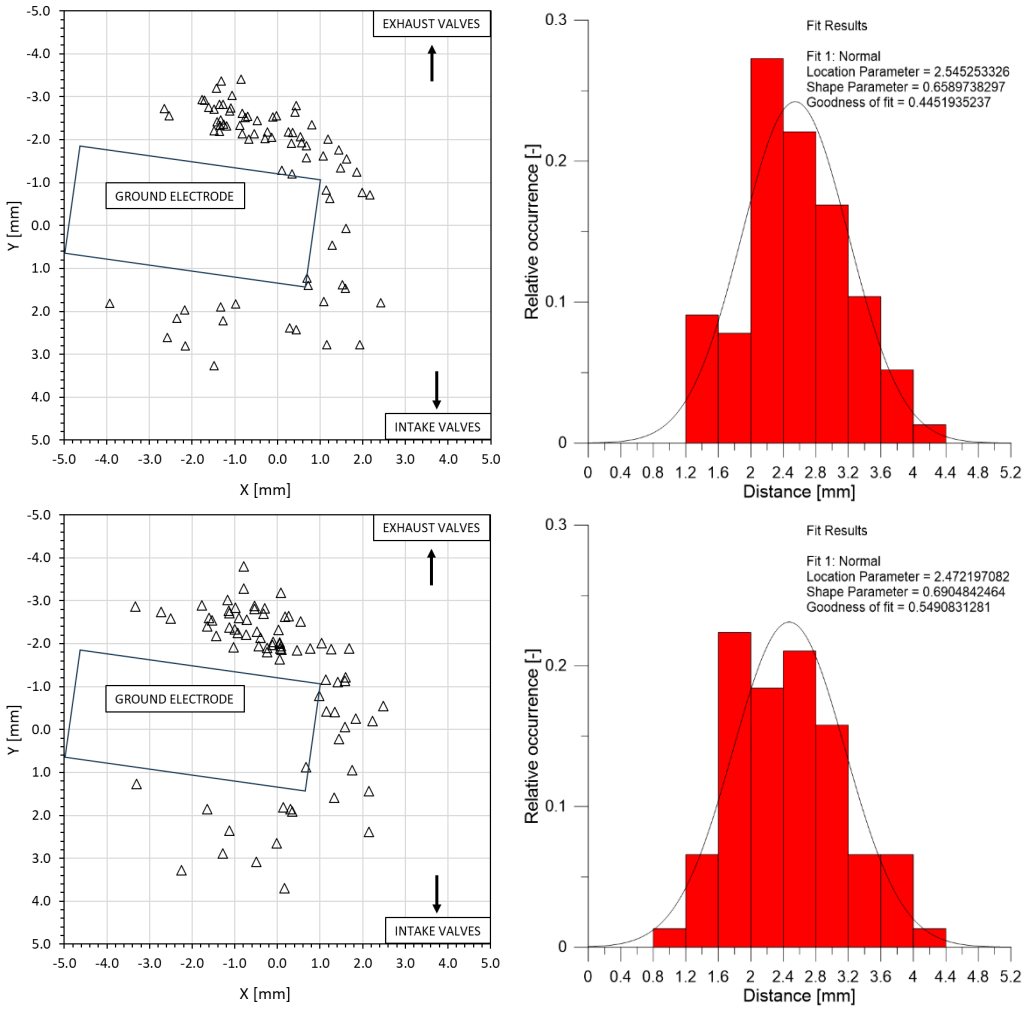

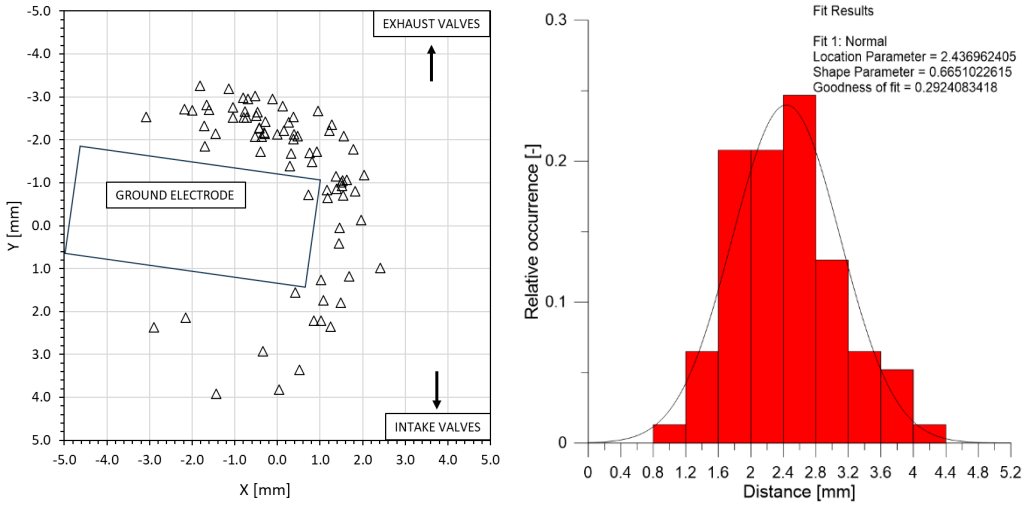


Figure 36. Flame kernel position (ST10 on top, ST15 at middle and ST20 at bottom), and corresponding distribution (right column). λ 1.3, blend 50%$CH_4$ – 50%$H_2$.

The results shown in (See Figure 37) suggest stronger interaction with the direct tumble motion (i.e. higher velocity towards the exhaust valves tends to displace the kernel in this direction), directly correlated to the higher number of visible arcs when advancing spark timing. The reduction in Feret Diameter from 5.2 to 4.8 mm (i.e. "slower" kernel evolution) hints to less favourable interactions in terms of promoting faster kernel development. No direct conclusion could be drawn on whether lower temperature or less favourable effects of turbulence were the driving phenomenon, but both mechanisms could explain the observed trends.

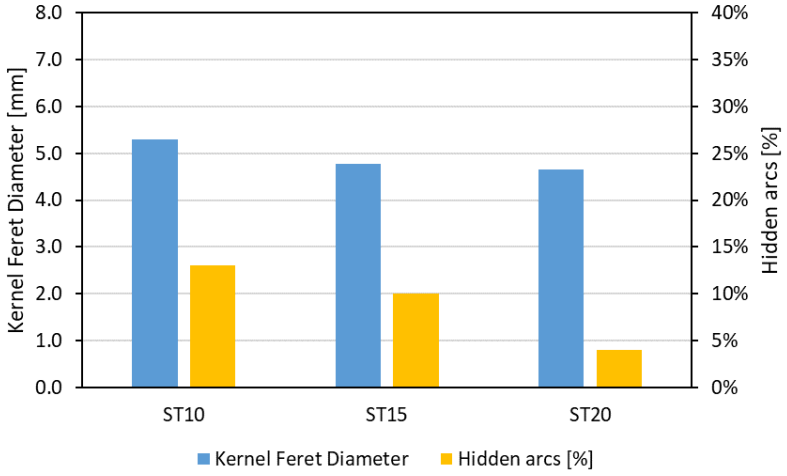


Figure 37. Kernel Feret Diameter and percentage of empty frames. λ 1.3, blend 50%$CH_4$ – 50%$H_2$.

### 5.3.2 Flame rapid burning

Subsequent to the early stages of combustion, the optical investigation was carried out on crank angle interval corresponding to the flame rapid burning phase, i.e. from 4.8 CAD aST to 36.0 CAD aST, therefore including the 50% of MFB (See Figure 30) for each case examined. the choice of considering the 50% threshold rather than the usual 90% is motivated by the optical limit boundary (that provides useful flame development analysis in the 0-50% MFB range) and the specific long duration of the final combustion stage characteristics for this engine (mainly due to the large top-land region volume). Flame was evaluated through calculations of the overall area of the visualised object (i.e. flame area), as well as morphology parameters such as the Feret Diameter and Heywood Circularity Factor. For sake of brevity, examples of single sequences are not shown, but rather ensemble images of 100 consecutive cycles (i.e. basically resulting in images that correlate pixel intensity to the probability of flame locations within the combustion chamber, or more precisely within the 2D view of the visible part). The images were post-processed in NI Vision to enhance the brightness, gamma and contrast of the images to highlight the flame in the foreground. It should be noted that the raw data features an 8-bit architecture, thus on a grey scale from 0 to 255. Data on luminosity were exported and analysed in the MATLAB environment. The colour scale visible in the graphs below refers to luminosity intensity, which was been normalized for each case that was examined.

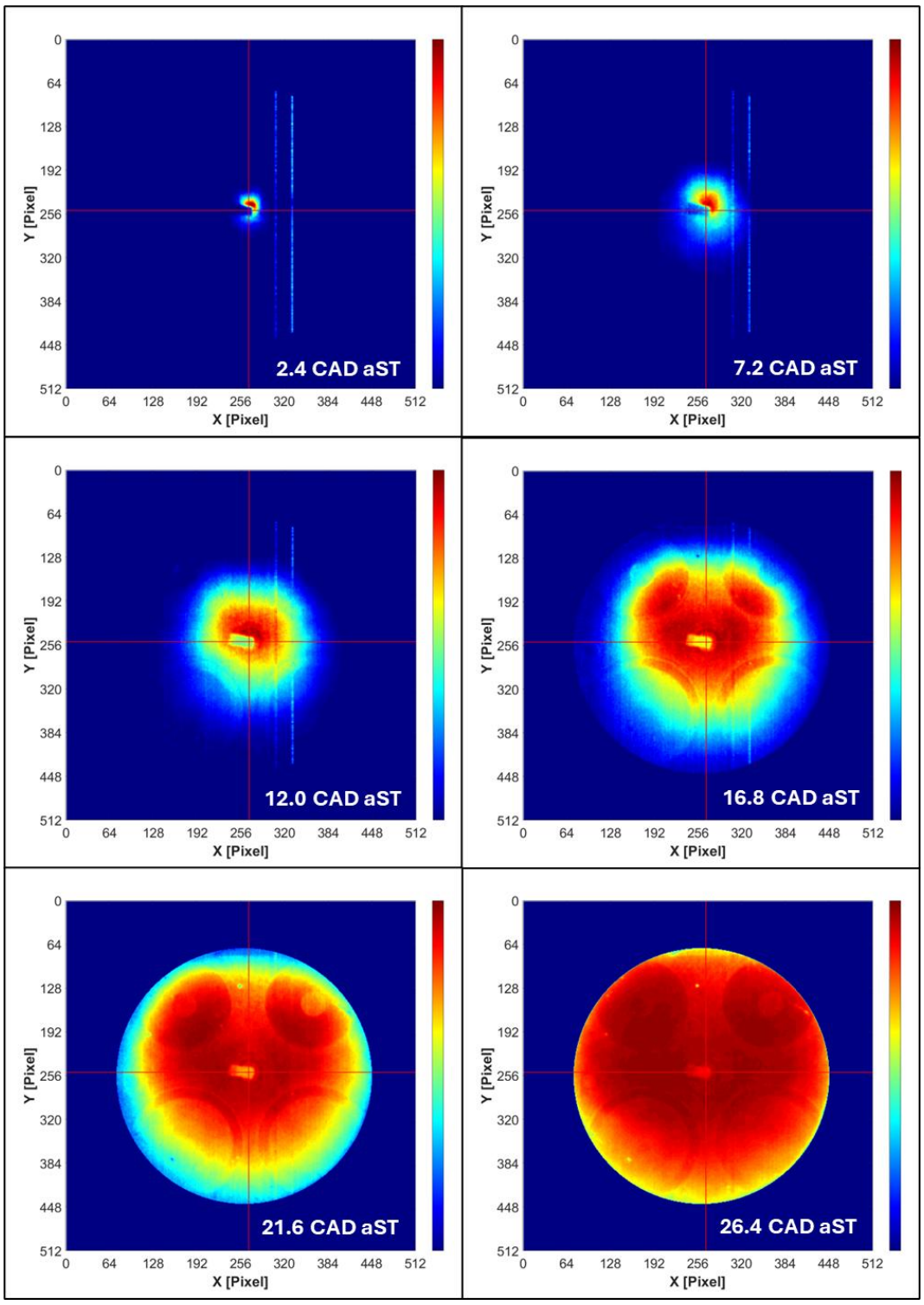

Figure 38. Coloured flame front intensity (8-bit). λ 1.0, 100% $CH_4$, averaged data.

Figure 38 shows the distribution of luminous emissions recorded during flame propagation, for methane fuelling.

Similarly, Figure 39 and Figure 40 show the $CH_4$ 80%–$H_2$ 20% and $CH_4$ 50%–$H_2$% 50 conditions respectively. In line with previous trends observed for the MFB traces (See Figure 30), a small addition of hydrogen not only implies

faster flame development, but also increased luminosity, most likely the direct result of higher in-cylinder pressure (and therefore higher gas density)

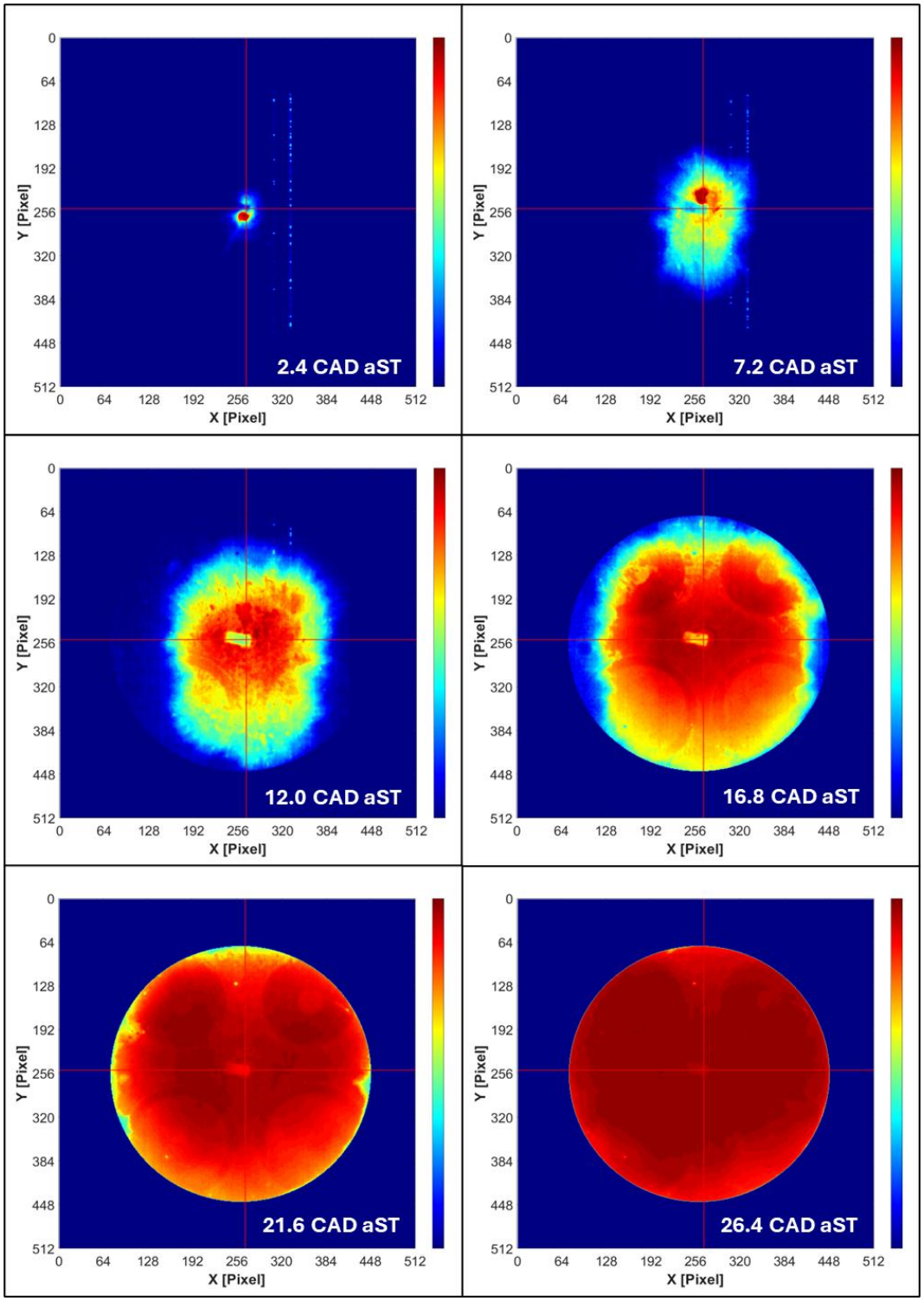


Figure 39. Coloured flame front intensity (8-bit). λ 1.0, 80% $CH_4$ – 20% $H_2$, averaged data.

Apart from the evident increase in flame propagation speed, another interesting observation is that as the content of $H_2$ is increased, the contours of the flame edges become much more defined, making it easier to distinguish between burnt

and unburnt areas, even though the data shown are the result of averaging 100 sequences. Basically, this means that the luminosity gradient in the overlaid images is steeper for the blends compared to pure methane fuelling (see Figure 44 Figure 45). This suggests more consistent propagation in the same regions of the combustion chamber, i.e. increased repeatability and stability when adding $H_2$.

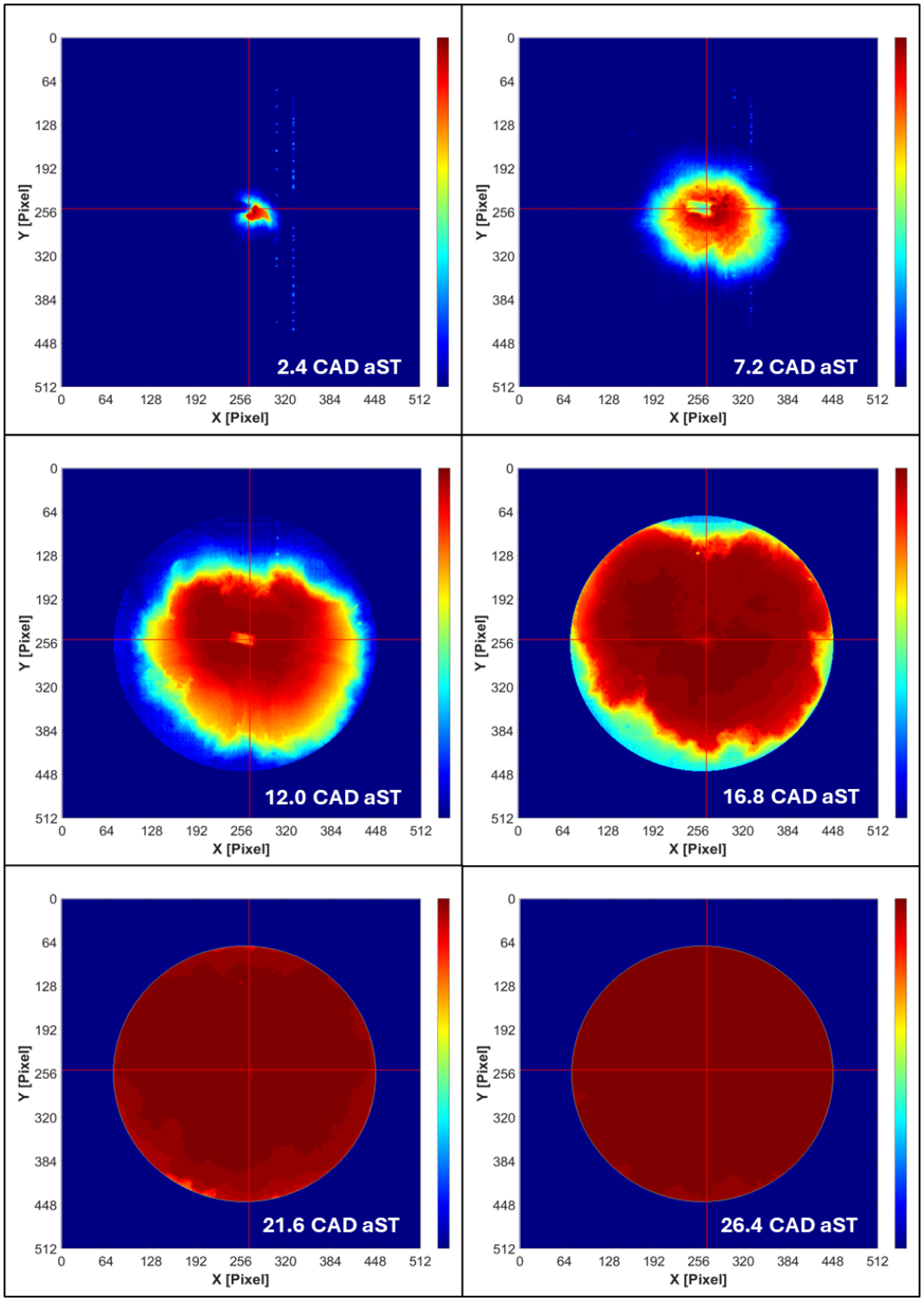


Figure 40. Coloured flame front intensity (8-bit). λ 1.0, 50% $CH_4$ – 50% $H_2$, averaged data.

In essence, the presence of hydrogen improves the repetitiveness of flame morphology and its position. Even if not directly related to the phenomenon of flame propagation per se, the images can be interpreted as flame contours that would be equivalent to the average ensemble of the 100 cycles that featured cycle-resolved recording of optical data. In these terms, adding $H_2$ contributes to clearer distinction between the burned and unburned gas regions. The luminosity gradient at the interface increases in magnitude, trend that is confirmed by the following considerations on luminosity measured along the X-Y axes (See Figure 44 - Figure 45).

Up to this point, the discussion features more qualitative analysis, capable of highlighting certain details such as cycle-to-cycle flame location or burned-unburned gas interface gradients; overall parameters give more quantitative overview and render certain levels of comparison more intuitive. Figure 41 highlights the influence of hydrogen on flame front propagation, in terms of overall flame area, its Feret diameter and the Heywood circularity factor. High laminar flame speed specific for $H_2$ allows for significant reduction in kernel inception (0 - 2%MFB) duration and also influences the rapid burning phase. The crank angle interval necessary to reach the optical limit, equal to around 60% of total bore area of the combustion chamber, drops from 30 CAD for pure methane to slightly more than 15 CAD for the 50/50 blend (it should be noted that the spark timing is fixed for these three cases). A similar effect can be inferred from the maximum Feret diameter traces (with the upper limit fixed at 61 mm, equal to the optical window diameter) that also suggests faster flame development as hydrogen addition increases. The Heywood circularity factor features comparable values for all three fuel types during the kernel phase, i.e. $\approx$ 1.3 (Figure 41, Bottom). As expected, it is during this phase that the flame shape tends to be less circular and with more extensive wrinkling. No clear trend can be identified in this phase when switching from one fuel type to another. One common feature is that the flame front tends towards a circular shape as it grows, an aspect that intuitively was to be expected, given that local turbulence effects are less evident once the flame grows beyond a certain size. More to the point, all three fuel types start at the higher end of HCF range and tend to the circular shape with steeper change as the content of $H_2$ in the blend is increased. This suggests speed profiles that tend to follow a symmetric path along X-Y directions (See Figure 42). This

equilibrium causes only small variations in HCF values until the flame reaches the optical limit.

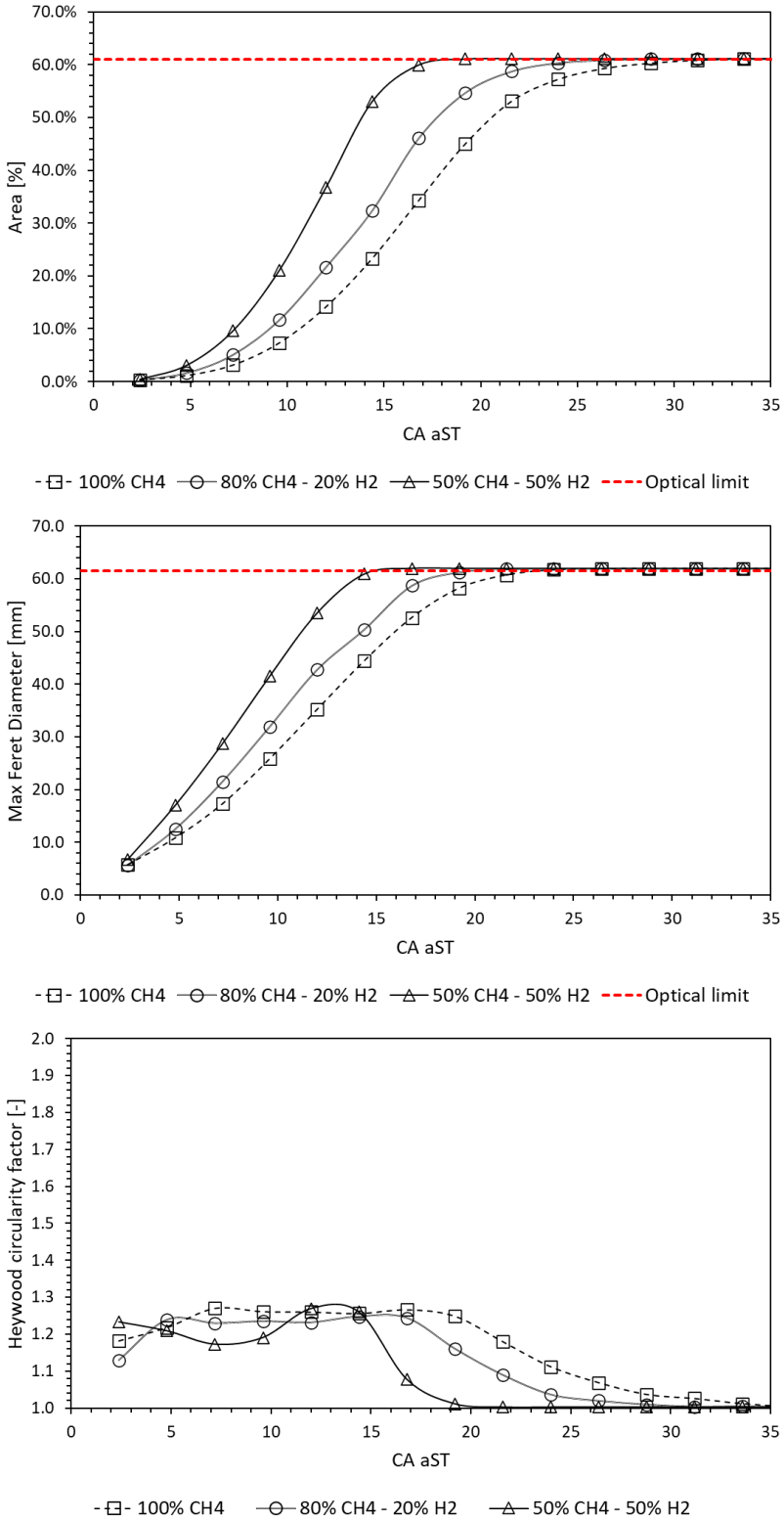


Figure 41. Flame area development (top), Max Feret Diameter (middle) and Heywood circularity factor (Bottom). 1.0, spark timing 10 CAD bTDC.

Basically, all three cases follow the same route of increased wrinkling effects due to more prominent influence of turbulence at a certain scale during the kernel ("small" flame) phase and less evident distortion of the flame by (presumably) similar turbulence scales that have less impact on the larger burned gas region during the rapid burn stage; the major difference is identified in the slope of this change, seemingly directly linked with the higher laminar flame speed specific for blends containing $H_2$.

The velocity profiles along X and Y directions are shown in Figure 42 for the three fuel compositions; evidently, once the flame reaches the optical limit, flame expansion speed tends to zero. The data reported were calculated by using a clamp tool on the vertical and horizontal axes. Calibration was performed by measuring ground electrode size to obtain the pixel/mm ratio, while time interval between two consecutive frames was known a priori, i.e. equal to 2.4 CAD at 2000 rpm, thus 0.2 ms. As it is possible to note, the graph is comprehensive of negative values. These indicate the advancement of the flame front in a "negative direction", according to the system coordinates defined by the software (See annex A.1 Research engine calibration and optical setup). To this end, the vertical component of the velocity named "Vel Up" is directed towards the exhaust valves, while "Vel Down" towards the intake valves. For each of the cases that were examined, it can be therefore observed that the speed profiles on the same direction are within a relatively narrow range on an absolute basis, with a small tendency to be unbalanced towards left side during the last phase of flame development, before the flame front reaches the optical limit. The differences in speed profiles in the early stages of combustion are directly identifiable as the main contributors to the shape irregularities seen previously (see Figure 38, Figure 39 and Figure 40). The morphological irregularities are present throughout the flame propagation process, as the speed profiles develop following similar patterns. Furthermore, the case with the highest content of hydrogen shows the most symmetric velocity values during the early stages, thus improving the circular-like shape tendency of the flame area since its inception. Although there is certain degree of scatter in the velocity data (to be expected, given that derivatives tend to feature high sensitivity to noise), there seems to be a clear trend of more consistent reduction in the difference of propagation velocity in the various directions when adding hydrogen. In terms of magnitude, the hydrogen

addition implies an increase in the maximum speed from around 23 m/s for the 100% $CH_4$ case, to 25-26 m/s for the 20% $H_2$ blend and 30-32 m/s for the 50% $H_2$% case.

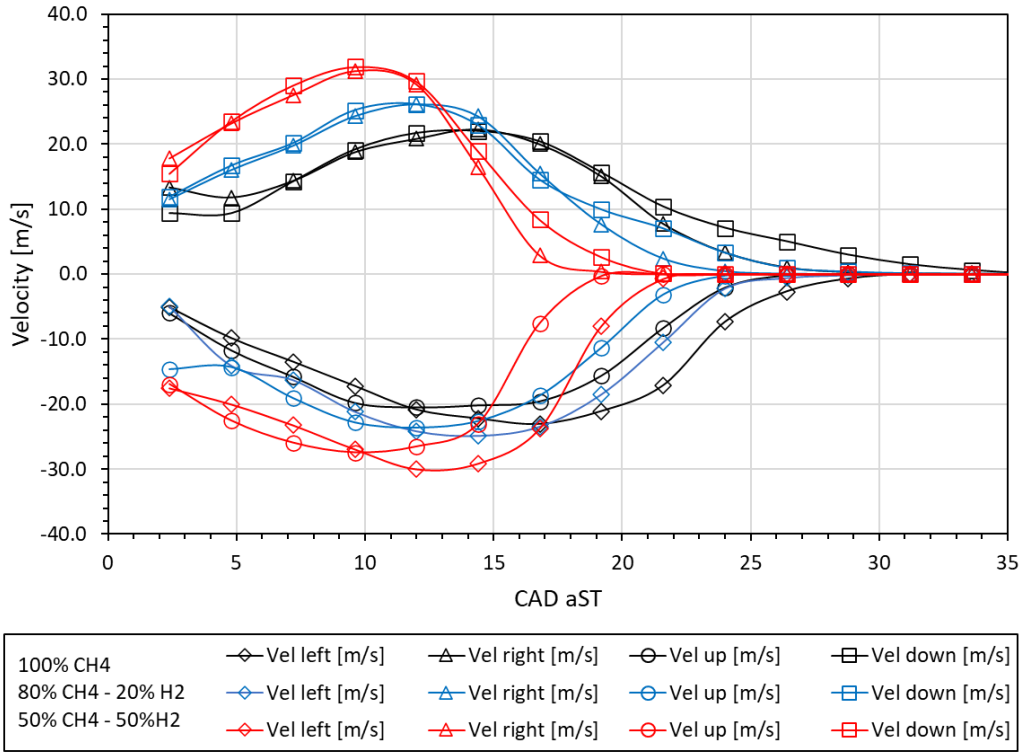


Figure 42. Flame front speed profiles along X-Y axes. λ 1.0, spark timing 10 CAD bTDC.

Intensity evaluations can also give further insight on the influence of hydrogen addition; this parameter is directly related to the concentration of active species during combustion and can therefore be seen as an indicator of local reactivity. Indeed, the luminosity gradient seems to correlate very well with the evolution of the combustion process (See Figure 43). Hydrogen addition therefore leads to a significant increase in luminosity gradients, a result that is in line with the observed improvement of spatial repetitiveness of the flame identified previously. Apart from the overall evaluation that covers the entire field of view, performing the analysis in certain part of the combustion chamber can also give a certain idea on the degree of local effects. The two red lines overlaid in the previous figures (i.e. Figure 38, Figure 39 and Figure 40) were set to intersect in the point of the central spark plug electrode. Luminous intensity was therefore measured along these lines, and the resulting signals are shown in Figure 44 and Figure 45. During the early stages of kernel formation, the increase of the luminosity signal follows similar patterns for all three cases. The grey object

overlaid on the graphs represents the ‘shadow’ of the ground electrode that is blocking the view. At 2.4 CAD aST, the signals are almost equal, except for the peaks which show small differences.

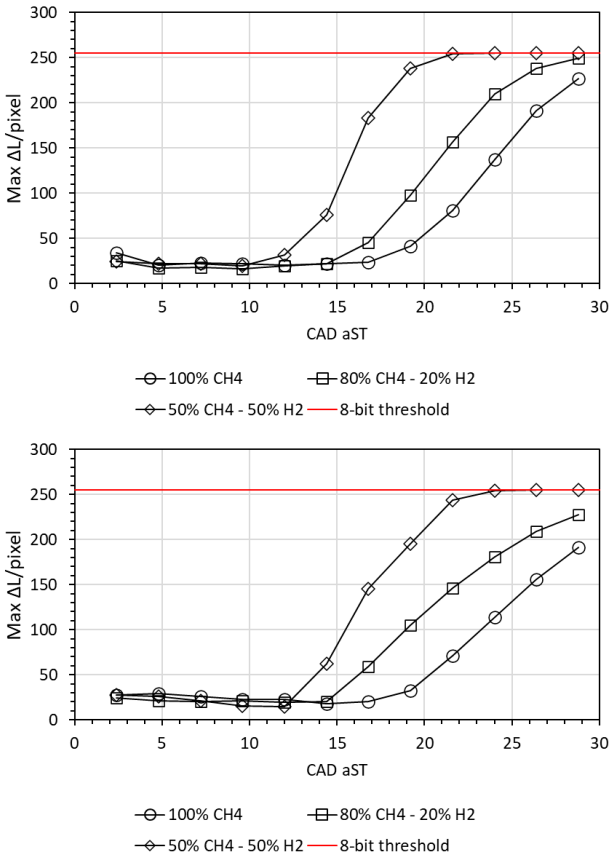


Figure 43. Maximum luminosity gradient over X (top) and Y (bottom) direction. λ 1.0, spark timing 10 CAD bTDC.

During the very early stages of ignition, indeed the differences between the three cases are quite contained. Nonetheless, the presence of hydrogen already seems to have an effect, with the 50% H2 blend consistently showing slightly higher intensity even at 2.4 CAD aST. Once the kernel is formed and the transition to the turbulent propagation regime starts, the differences between one fuel type and another begin to become more evident. As early as 12 CAD aST, the blend with the highest concentration of hydrogen resulted in saturated pixels; this is due to the compromise that was required for achieving acceptable signal-to-noise ratio during the very early stages of ignition but nonetheless emphasizes the significant contribution of H2 addition. As the flame propagation process progressed, overall intensity increased for all three cases, with evidence of a certain degree of local stratification, most likely in terms of local temperature. More to the point, the central region of the combustion chamber reaches higher

temperature and thus resulted in higher luminosity. The relative trend of difference between one fuel type and another was roughly the same throughout combustion, perhaps more easily evaluated for pure methane and the 20% H2 blend, for which saturation was much more contained.

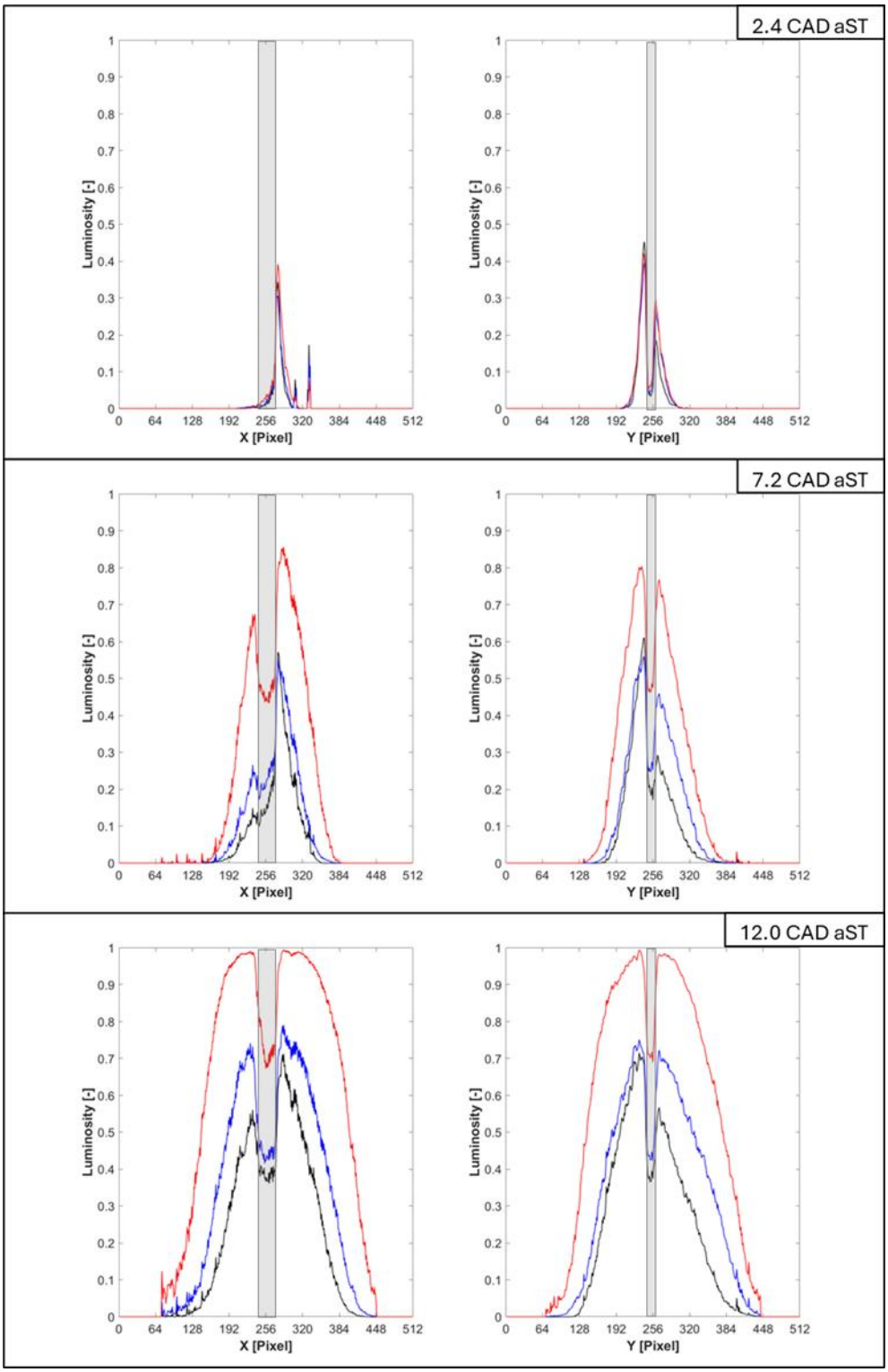


Figure 44. Luminosity signal along horizontal direction (left) and vertical (right). Time steps 2.4 – 7.2 – 12.0 CAD aST. 100% $CH_4$ (Black), 80% $CH_4$ – 20%$H_2$ (Blue) and 50%$CH_4$ – 50%$H_2$ (Red).

One other interesting observation is that the data seems to suggest slight asymmetry (along both axes) especially during the early stages of flame propagation; as to be expected, this effect was less evident during late combustion, given the tendency of homogenization (due to turbulent mixing within the burned charge) once the propagation process was completed.

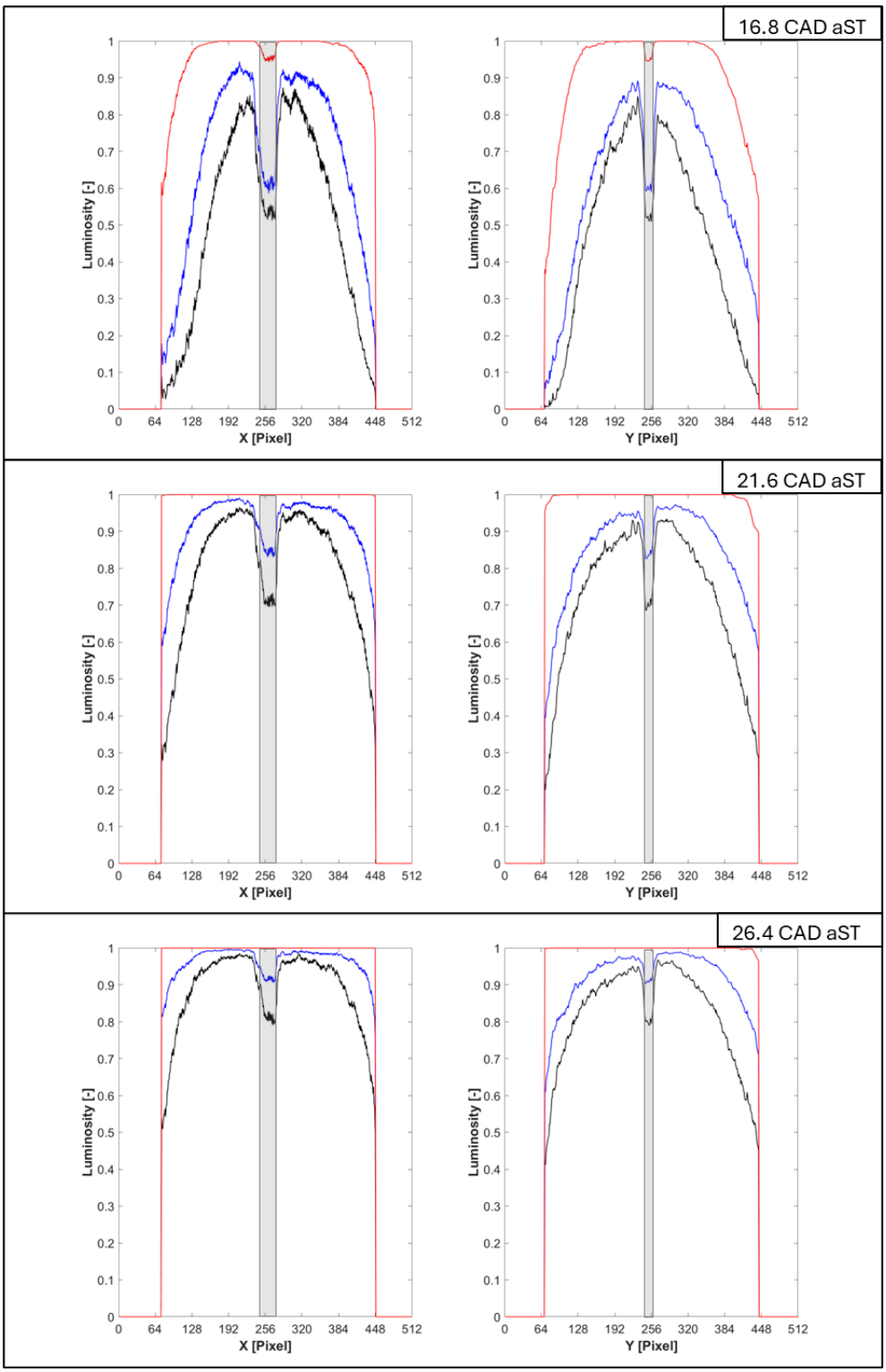


Figure 45. Luminosity signal along horizontal direction (left) and vertical (right). Time steps 16.8 – 21.6 – 26.4 CAD aST. 100% $CH_4$ (Black), 80% $CH_4$ – 20%$H_2$ (Blue) and 50%$CH_4$ – 50%$H_2$ (Red).

Once covered the entire field of view provided by the optical window, the information that could be extracted from the luminosity signal along the axes was less useful, and so an overall evaluation was implemented. Figure 46 illustrates the overall average value of luminosity and its standard deviation. The latter

parameter refers to the variability of measured signals, that can be caused by the presence of bright spots or macro-regions with very different values of luminosity intensity. Similar to previous graphs, luminosity was normalized, as well as the standard deviation. These traces reveal an initially elevated inhomogeneity in luminosity signal. As expected, maximum deviation is recorded during the flame development stage. One other explanation for the observed trend in standard deviation is the presence of the spark arc; the discharge process lasts around 7.0 - 8.0 CAD, and can significantly contribute to luminous inhomogeneity. The subsequent propagation of the flame leads to a further increase of variability, given by the expanding burned gas, with luminosity gradients recorded at the edges of the interface with the unburnt charge. This value then rapidly falls for all the cases that were examined. The prolonged duration of inhomogeneity for the cases with low content of hydrogen (or pure methane) can be partially attributed to higher frequency of bright spots, mostly found to occur during the late stages of combustion.

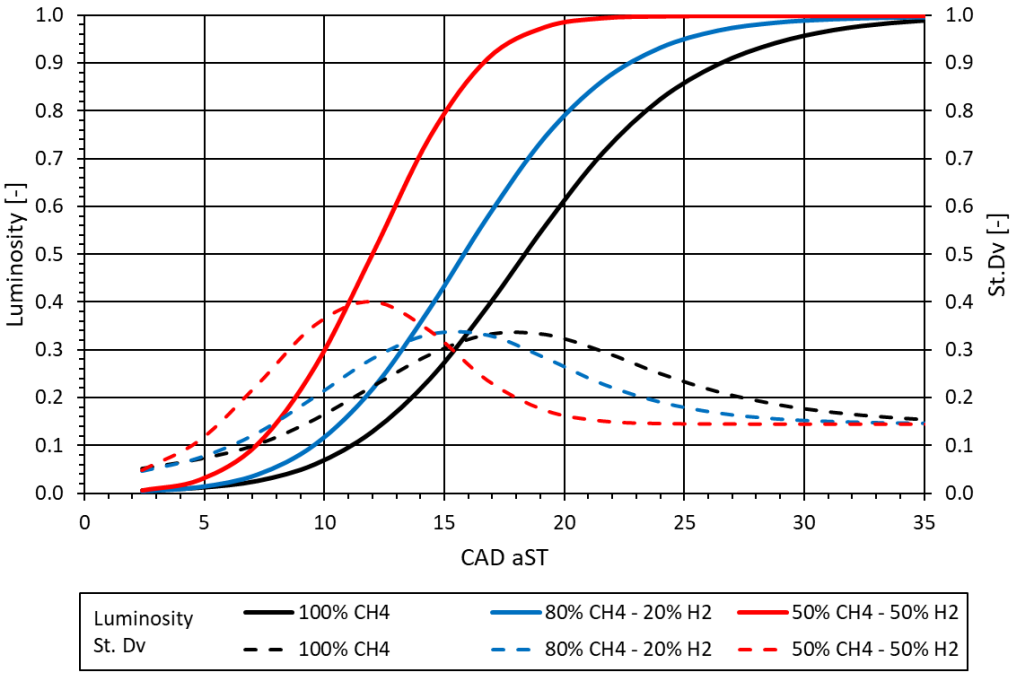


Figure 46. Overall luminosity evolution (solid lines) and corresponding standard deviation (dashed lines). λ 1.0, spark timing 10 CAD bTDC.

For diluted conditions running with λ set at 1.3, and 50% $CH_4$–50% $H_2$ blend fuelling, the analysis was focused on evaluating the influence of spark timing, thus highlighting the role of turbulent motion on flame development. Similar to previous cases, Figure 47, Figure 48 and Figure 49 illustrate the average luminous

intensity reached by each case at different time intervals after ignition. The first evidence, as to be expected when employing diluted operation (i.e. with higher $AFR_{rel}$), is that the intensity maps resemble more those that were obtained with methane during stoichiometric fuelling. More to the point, rather than a steep gradient, a smoother "passage" can be observed between the central regions and those at the edge of the combustion chamber. These results suggest wider distribution of flame locations, and the observed qualitative dispersion is completely in line with the observed cycle-to-cycle variability derived from in-cylinder pressure data (see Figure 33).

In terms of kernel inception and its location, the tumble-based geometry of the combustion chamber makes arc prone to extend towards the same direction, regardless of spark timing. In line with MFB trends (see Figure 31), flame propagation follows similar paths for each case, most likely due to the fact that laminar flame speed is quite similar for all three spark timing settings; there a certain influence to be expected, given that when changing ignition timing the initial temperature also changes, but this aspect seems to be less important. One other interesting aspect is the fact that flame propagation appears to be quite symmetric for all three cases after around 12 CAD aST. A possible explanation is that the initial displacement towards the exhaust valves caused by direct tumble is later compensated by charge stratification (even if gaseous fuels were employed, slightly richer mixture (or with less residual gas) close to intake valves is not uncommon. Another aspect is that compared to pure methane fuelling the 50% $H_2$ blend features high enough laminar flame speed to ensure more stable combustion (even for lean conditions) and reduce the overall effect of turbulence. This of course would also explain the fact that even though spark timing was swept in a relatively wide crank angle range (during which tumble motion is converted to turbulence), overall effects on flame propagation were quite contained.

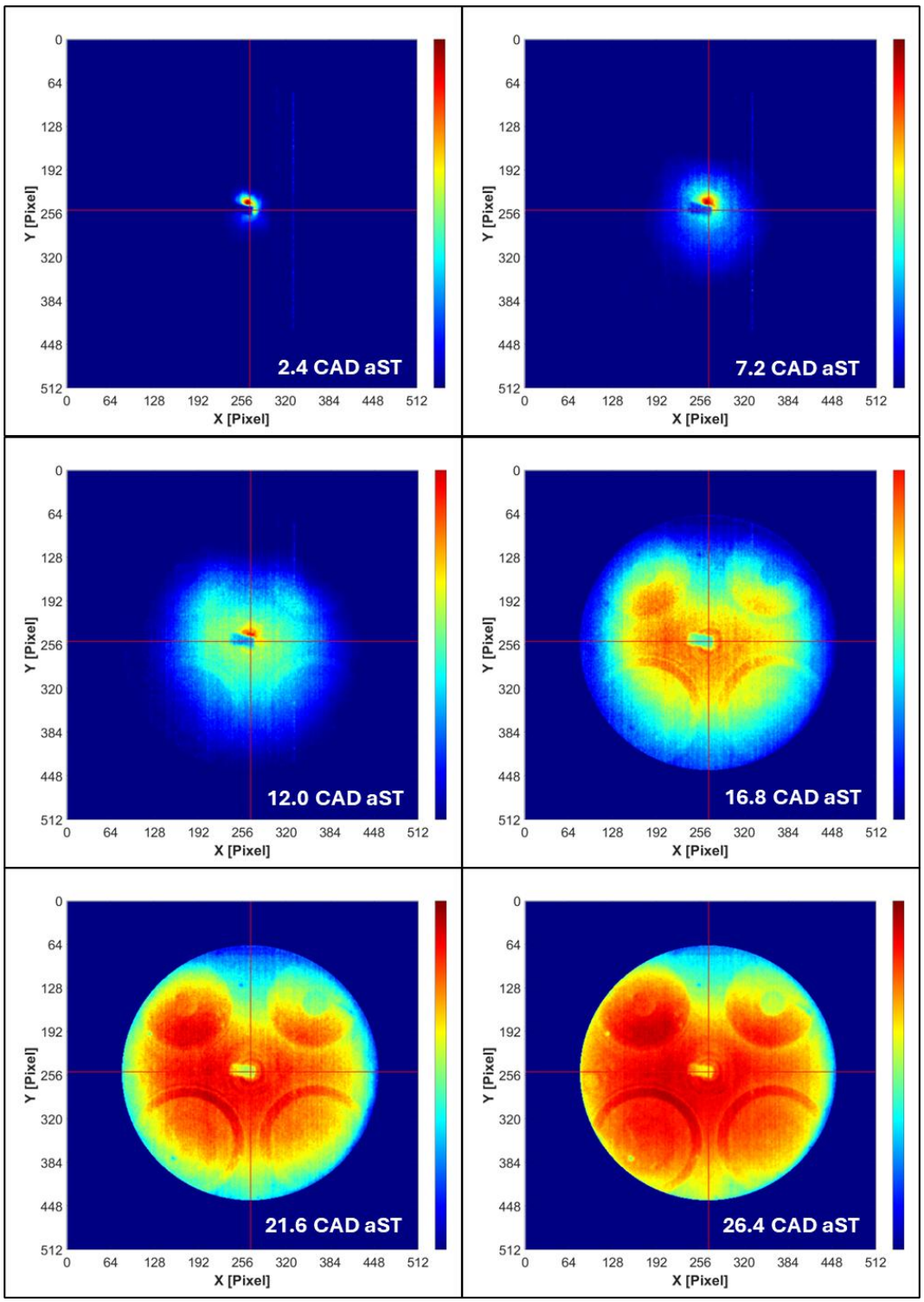

Figure 47. Coloured flame front intensity (8-bit). λ 1.3, blend 50%$CH_4$ – 50%$H_2$, ST10.

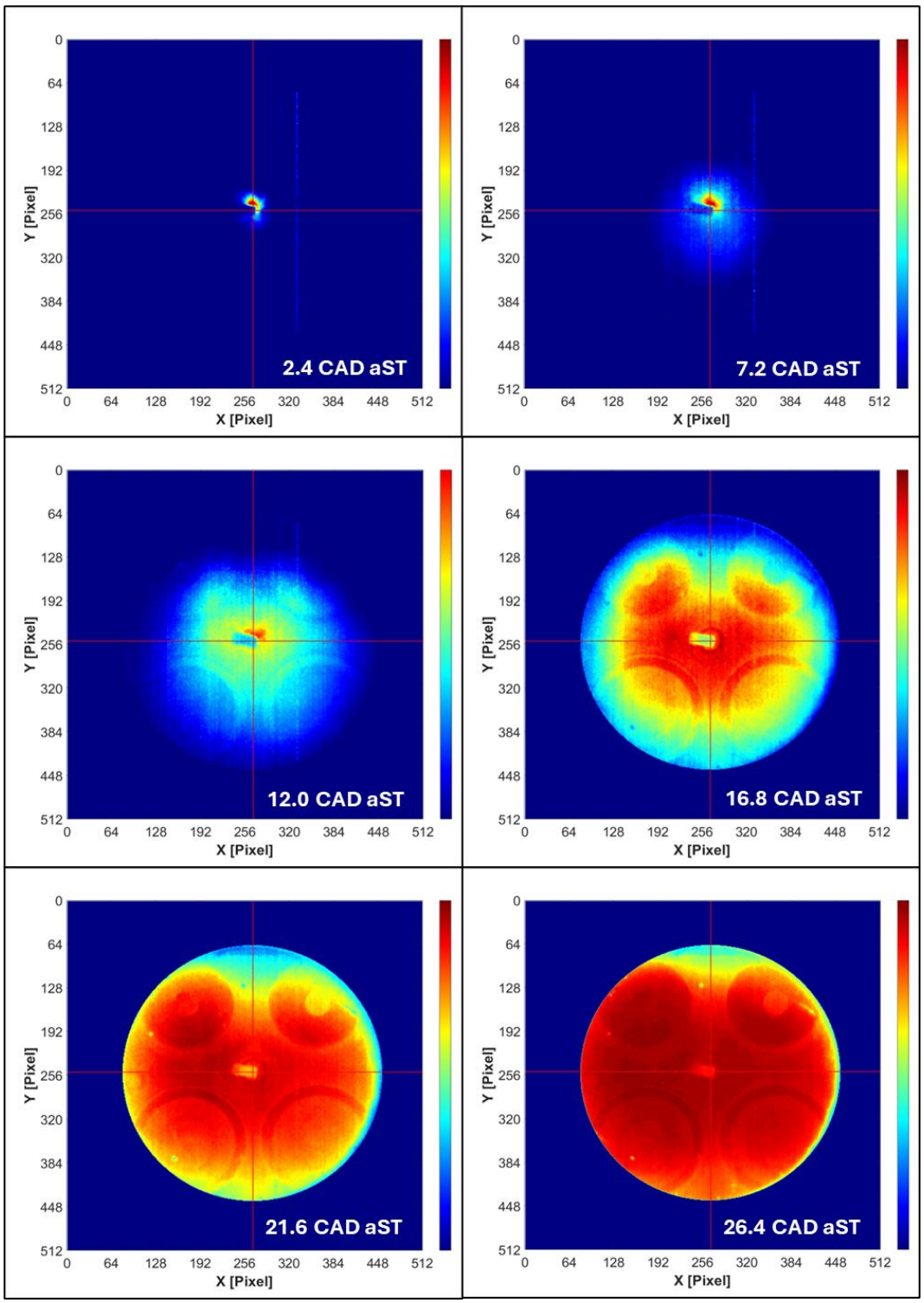

Figure 48. Coloured flame front intensity (8-bit). λ 1.3, blend 50%$CH_4$ – 50%$H_2$, ST15.

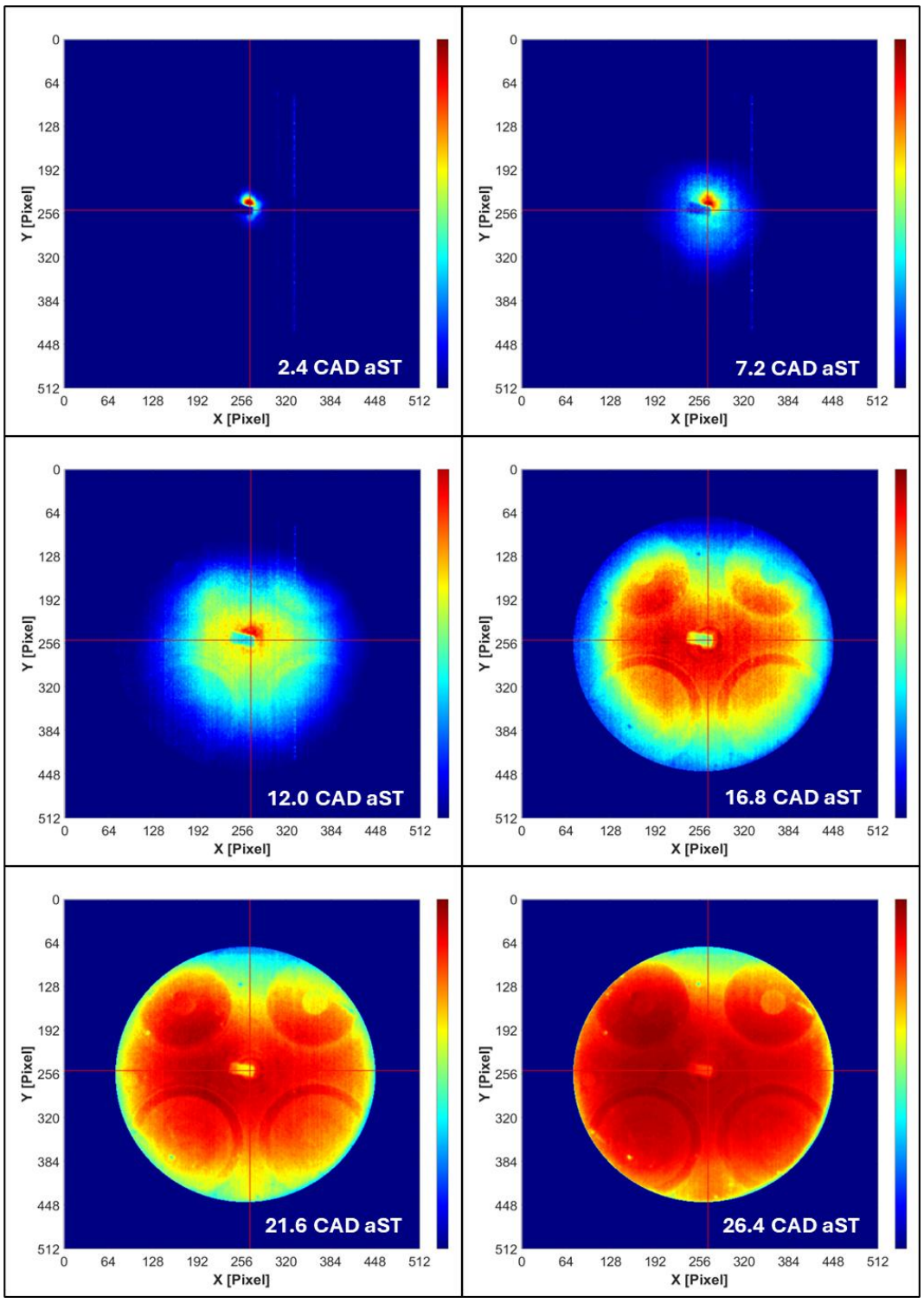

Figure 49. Coloured flame front intensity (8-bit). λ 1.3, blend 50%$CH_4$ – 50%$H_2$, ST20.

The measurement of the flame area growth rate shown in Figure 50 (top) highlights that during kernel inception there are no appreciable differences in size. As the flame develops, a small gap can be noted among the three traces, with a peak in difference of about 5% between the most delayed case (ST10) and the intermediate condition; in a certain way this was to be expected, given that turbulence intensity would be higher for the more advanced ignition settings of

the three; one possible explanation is that when advancing the spark timing from 10 to 15 CAD bTDC more intense turbulence results in slightly shorter rapid burn angle, while when further advancing ignition to 20 CAD bTDC, the process moves in a region with higher tumble but less intense turbulence, thus resulting in practically the same propagation speed. In line with the MFB traces (see Figure 31), the optical data illustrates a similar trend, with the flame completely covering the field of view in 28.0-29.0 CAD after spark timing. The maximum Feret diameter (Figure 50, middle), which is directly linked to the flame area morphology, does not reveal significant differences. The gap among traces is of the order of a few millimetres, not enough to suggest a clear trend. The HCF was evaluated under all operative conditions and the results (Figure 50, bottom) reveal that with increased fuel-to-air ratio, the flame front propagation became more chaotic, resulting in a pronounced flame distortion. Compared to previous cases (with stoichiometric fuelling), the maximum HCF was around 1.6, higher than the previous value of around 1.3. Given the definition of this parameter, its magnitude can be directly correlated to wrinkling of the flame front and the global distortion; the two phenomena can be concurrent. The analysis performed on the post processed images revealed the major contribute of the first one, thus showing an appreciable fragmentation of the flame front. In this respect, it is interesting to note that the peaks in HCF do not follow a coherent trend as the spark timing is advanced. Indeed, the condition with the ST fixed at 20 CAD bTDC showed the highest value of HCF, of about 1.60, while the intermediate condition the lowest, i.e. 1.46. Specifically, once it reached its peak, the ST10 condition is the "slowest" to decrease, suggesting prolonged and more pronounced fragmentation of the flame object edges. In any case, it should be noted that there is an overall increasing contribution of wrinkling phenomena as the mixture was diluted. This fragmentation of the flame front partially mitigates the reduced reactivity due to the charge dilution by extending the interface surface between burnt and unburnt gases. In fact, this hypothesis seems to be confirmed by the speed profiles presented in Figure 51. More to the point, the velocity peaks were found to be quite comparable to those recorded during stoichiometric operation; this of course is also explained by the fact that turbulent flame propagation is dominated by turbulence intensity rather than laminar flame speed.

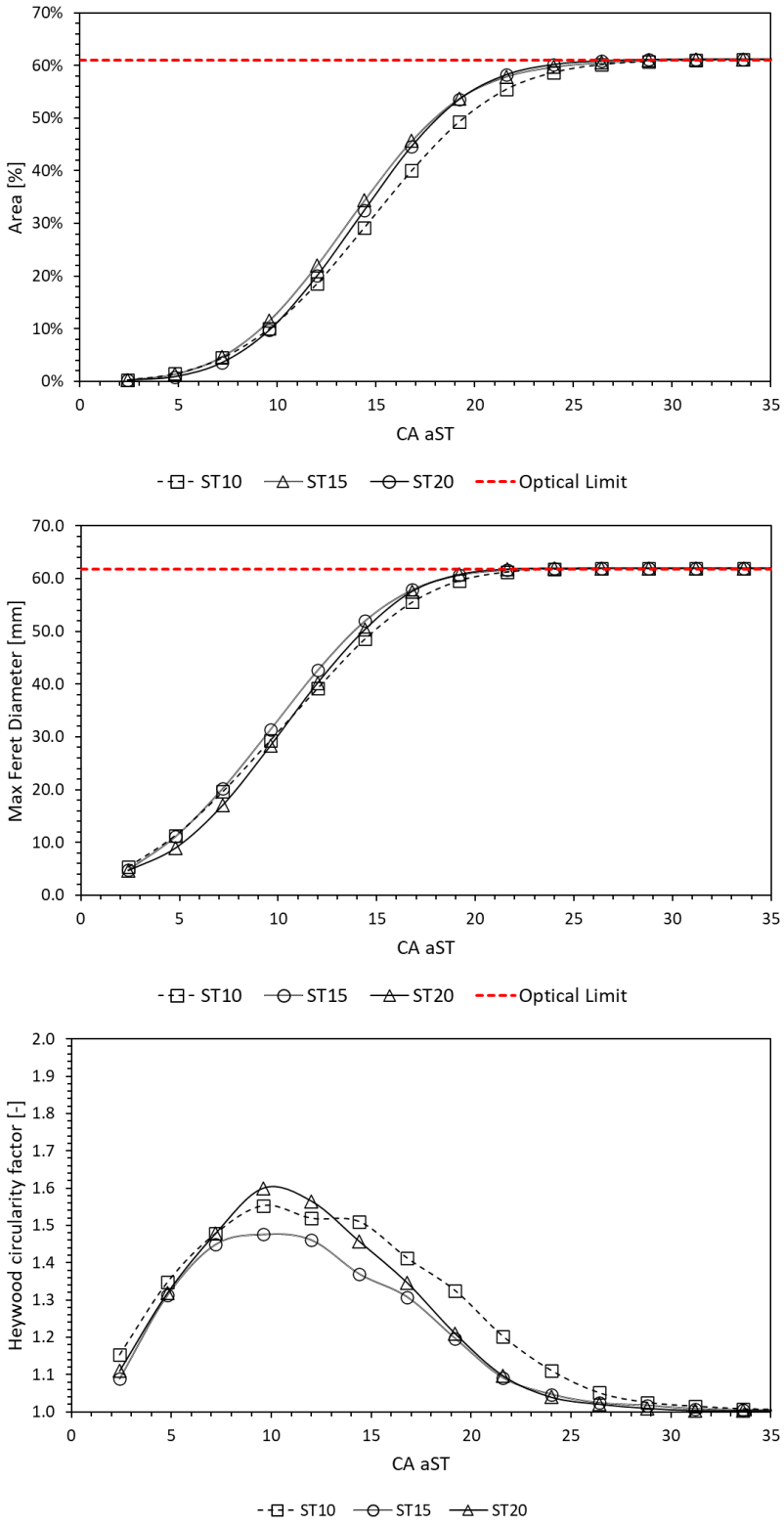


Figure 50. Flame area development (top), Max Feret Diameter (middle) and Heywood circularity factor (Bottom). λ 1.3, 50% $CH_4$ – 50% $H_2$.

The speed profiles measured along X and Y direction are presented in Figure 51. The change in spark timing implies a more contained influence on flame velocity, not comparable to the effect of laminar flame speed seen for the previous stoichiometric cases. Air-fuel mixture dilution resulted in lower overall magnitude

of speed. Specifically, when changing the spark timing from 10 to 20 CAD bTDC, the peaks varied from about 24 m/s to slightly less than 30 m/s. The differences in turbulent motion intensity seem to play a minor role in hydrogen flame development. The velocity peaks undergo a limited reduction, considering the 30% dilution of the charge. In these conditions, rather than the global deformation of the flame object, the corrugation of the flame front can be considered as a key factor in increasing the speed and contributing to symmetric propagation. These results further confirm a partial independence of fuels with hydrogen addition from turbulent motion, consideration that results even more significant when considering the dilution of the air-fuel charge of the current operative conditions.

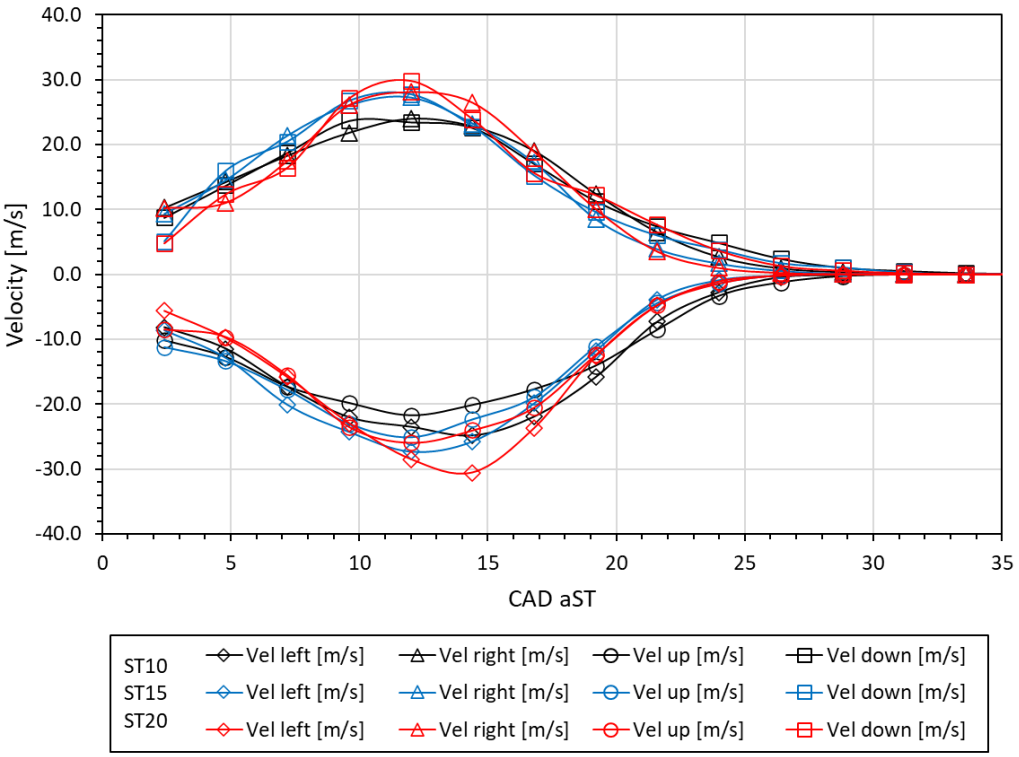


Figure 51. Flame front speed profiles along X-Y axes. λ 1.3, blend 50% $CH_4$ – 50% $H_2$.

Lean fuelling also influenced the luminous intensity of images recorded during the combustion process. As expected, the more advanced ignition case featured the highest gradient of luminosity (See Figure 52); this can be directly correlated to higher peak pressure (and therefore higher peak temperature). Quite similar values were observed along the X and Y axes, with the same consistent trend when switching from one ignition setting to another.

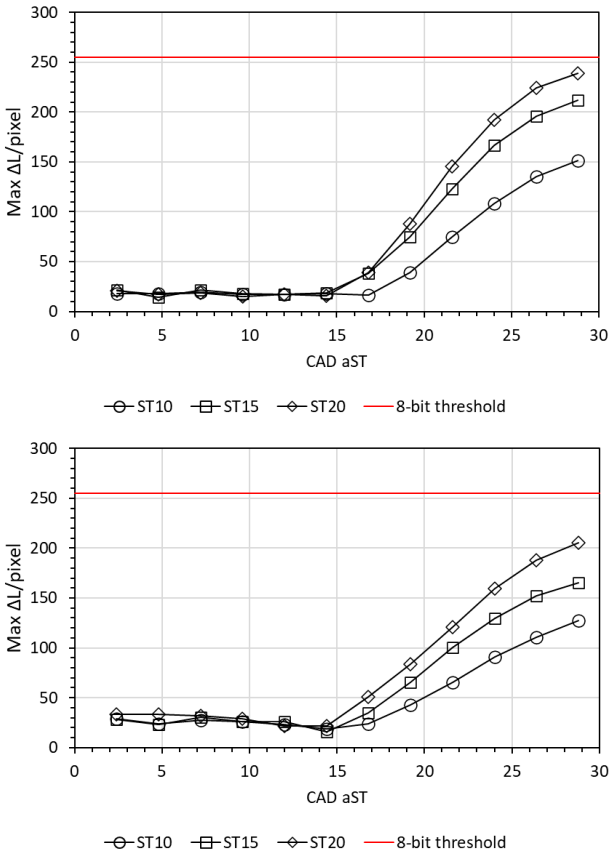


Figure 52. Maximum luminosity gradient over X (top) and Y (bottom) direction. λ 1.3, blend 50% $CH_4$ – 50% $H_2$.

The density distribution of luminosity intensity is presented in Figure 53 and Figure 54. Starting with kernel inception, the three signals are practically overlapped, suggesting completely comparable spark-fluid interaction. During the flame development phase, representative of the 0-10% MFB range, the only operative condition to slightly detach from the others is that with the spark timing fixed at 10 CAD bTDC. At 16.8 CAD aST, cases ST10 and ST20 still featured comparable values, with the intermediate case showing the highest values of emission. It is interesting to note that the luminosity profiles along the Y direction are asymmetric, with a tendency to drop towards the intake valves. This phenomenon can be correlated to the interaction with tumble motion (i.e. direct tumble during the initial stages and the complete effect during fast burning). Compared to the stoichiometric cases, this effect is most likely to be more prominent, in part because spark timing was set as retarded, but also because possible charge stratification effects, as previously iterated. As the combustion process proceeded, a small gap opened between the ST15 and ST20 cases, with the latter that emits higher values of luminosity.

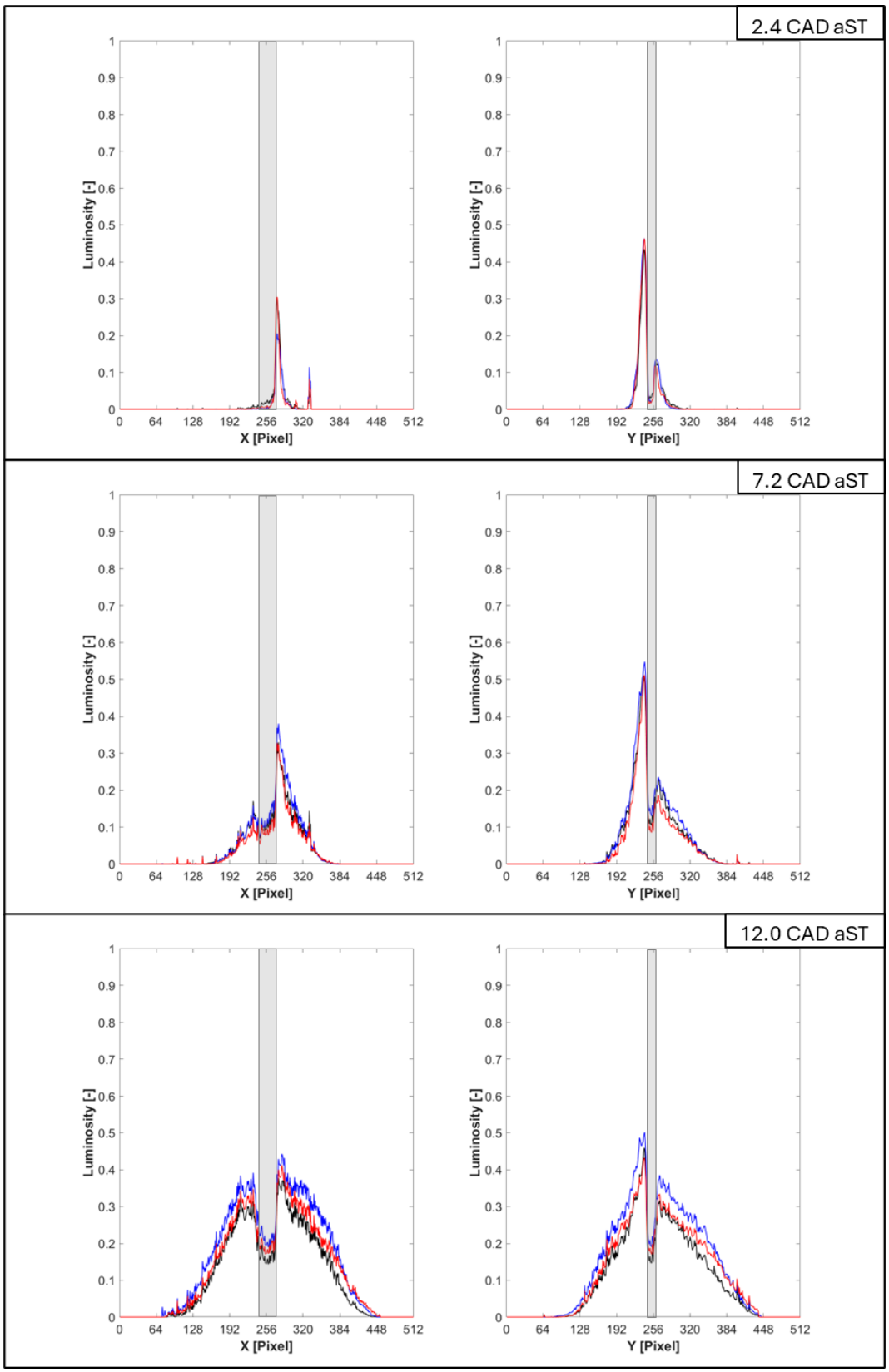


Figure 53. Luminosity signal along horizontal direction (left) and vertical (right). Time steps 2.4 – 7.2 – 12.0 CAD aST. 50% $CH_4$ – 50% $H_2$, ST10 (Black line), ST15 (Blue line) and ST20 (Red line).

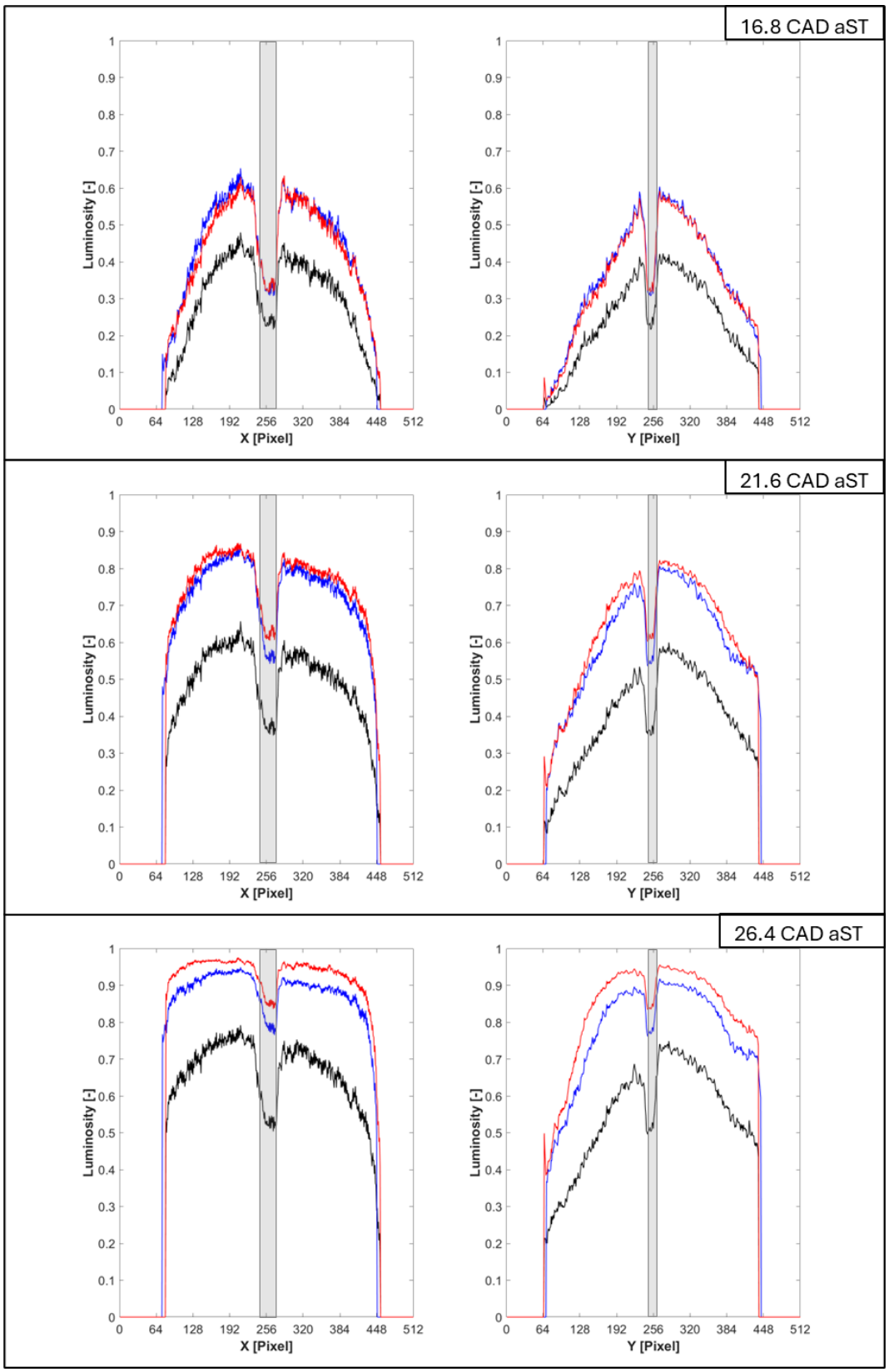


Figure 54. Luminosity signal along horizontal direction (left) and vertical (right). Time steps 16.8 – 21.6 – 26.4 CAD aST. 50% $CH_4$ – 50% $H_2$, ST10 (Black line), ST15 (Blue line) and ST20 (Red line).

Figure 55 illustrates the growth rate of the average visible emissions measured over the recorded sequence; the standard deviation of this parameter is also

shown. The two cases with ST15 and ST20 feature comparable intensity values throughout flame development phase (0 - 10%MFB). Only during the flame rapid burning stage it's possible to observe a more significant gap between the two profiles. Furthermore, the variability of luminosity was characterized by a smoother trend than that observed in stoichiometric conditions. Charge dilution strongly limited the rising of bright spots, as well as the magnitude of luminosity close to flame front. In other words, luminous St.Dv featured an almost constant trend. Once again, the intermediate case seems to ensure higher luminosity during the early stages; the standard deviation was also higher. Lastly, a drop in luminosity was observed after the peak was reached around 32 CAD aST. If related to the MFB traces (see Figure 31), the drop in luminosity occurs during rapid burning, around of 40 - 50% MFB.

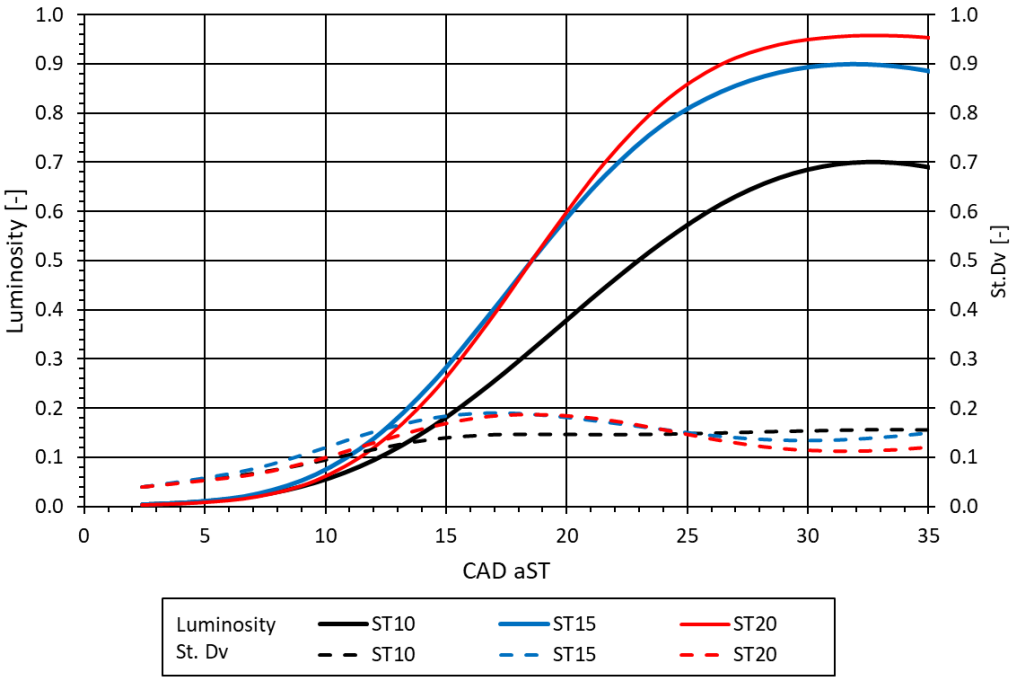


Figure 55. Overall luminosity evolution (solid lines) and corresponding standard deviation (dashed lines). λ 1.3, 50% $CH_4$ – 50% $H_2$.

## 5.4 Hydrogen: Thermodynamic parameters

The idea of the experimental campaign implemented with pure hydrogen fuelling was to cover a range of engine speed, spark timing and air-fuel ratio, that is representative for the intended applications; Table 7 lists the operating conditions. Given the specific properties of hydrogen, lean- and ultra-lean conditions were investigated, so as to illustrate situations in which the relatively

wide flammability range is exploited for gaining the maximum benefits of this carbon free fuel. Thus, lambda was swept from 1.9 to 3.6.

Table 7. Hydrogen thermodynamic operative conditions.

| Fuel | Start of Injection [CAD bTDC] | Engine speed [rpm] | Lambda [-] | Spark timing [CAD bTDC] |
|---|---|---|---|---|
| Hydrogen | 320 | 1000 | 2.6 | 10 |
| | | | | 15 |
| | | | 2.3 | 5 |
| | | | | 10 |
| | | | | 15 |
| | | | | 20 |
| | | | 2.1 | 5 |
| | | | | 10 |
| | | | | 15 |
| | | | 2.0 | 5 |
| | | | | 10 |
| | | | 1.9 | 5 |
| | | 2000 | 3.6 | 20 |
| | | | 3.0 | 10 |
| | | | | 20 |
| | | | 2.6 | 10 |
| | | | | 20 |
| | | | 2.3 | 10 |

Similar to the operation with methane-hydrogen blends, the thermodynamic analysis was centred on acquiring the in-cylinder pressure signal, along with the measurement of other parameters related to it. In this section, the selected operative cases are divided according to the two-engine crankshaft rotational velocity. More to the point, the 1000 rpm regime featured the recording of a large number of conditions of paramount importance in the goal of gaining in-depth understanding of the phenomena governing the hydrogen lean burn combustion. Figure 56 to Figure 60 show the in-cylinder pressure traces and mass fraction burnt (MFB) profiles. The diluted condition with λ 2.6, led to the recording of an almost motored-like pressure curve (See Figure 56). Engine output is quite low in these conditions, much lower than that usually obtained for this engine at wide

open throttle, with conventional fuels with stoichiometric operation [77]-[78]. Nevertheless, this point emphasizes the wide flammability range of hydrogen. As expected, when looking at the pressure profiles, the pressure peaks increase in magnitude as the air-fuel mixture was enriched; evidently, it also requires less advanced spark timing, closer to the TDC compared to methane or its blends with $H_2$. In fact, the empirical rule of keeping the pressure peak around of 16-degree aTDC for optimal combustion phasing does not seem to be valid for hydrogen. Indeed, the retarded ignition settings ensured higher IMEP.

Apart from the peak pressure parameter, the rate of pressure increase is another essential value for evaluating the stress that the crank mechanism needs to withstand. This rate was around 2-3 times higher for the lambda 2.0 case compared to stoichiometric methane fuelling and already gives an idea on the flame propagation velocity. Indeed, this particular aspect most likely also determined the relatively high limit of $AFR_{rel}$ before recording abnormal combustion phenomena during $H_2$ fuelling. This limit was found to be 1.9; even if the actual magnitude of pressure oscillations was at levels quite contained compared to "classical" knocking phenomena, it was decided not to increase the equivalence ratio further, in order to avoid possible uncontrolled runaway phenomena that can be associated with abnormal combustion, albeit with minor effects initially. Nonetheless, the investigated air-fuel ratio is more than representative for many engine applications that look at maximizing beneficial efficiency effects of ultra-lean operation.

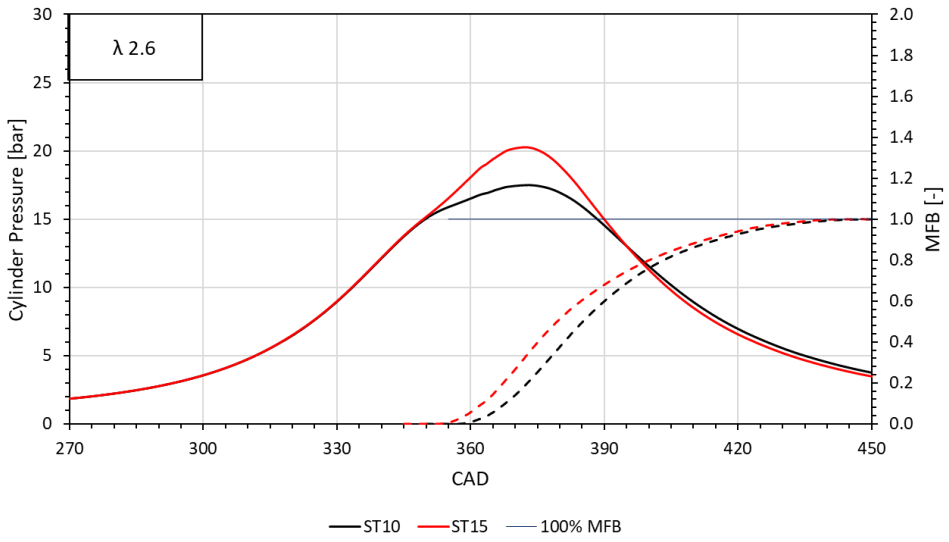


Figure 56. Cylinder pressure traces (solid lines) and mass fraction burnt (dashed lines), 1000rpm, λ 2.6.

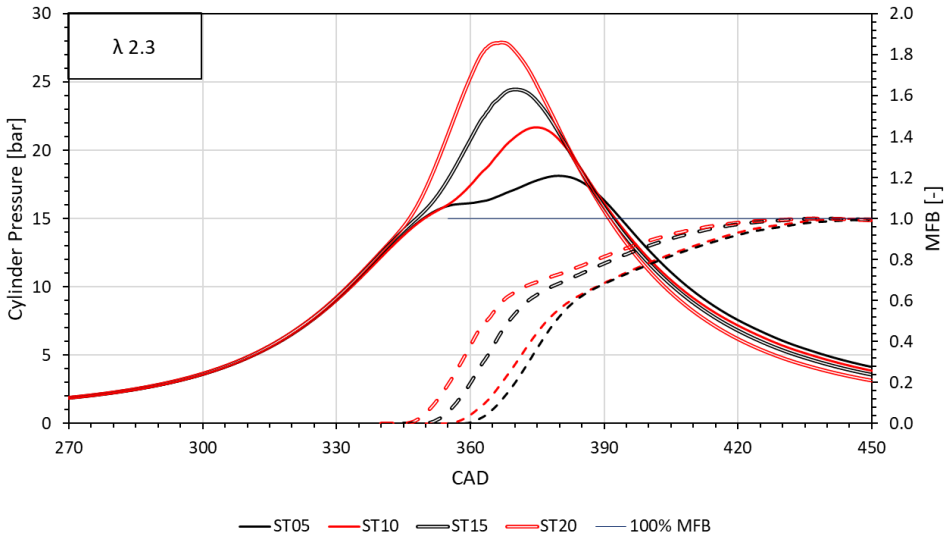


Figure 57. Cylinder pressure traces (solid lines) and mass fraction burnt (dashed lines), 1000rpm, λ 2.3.

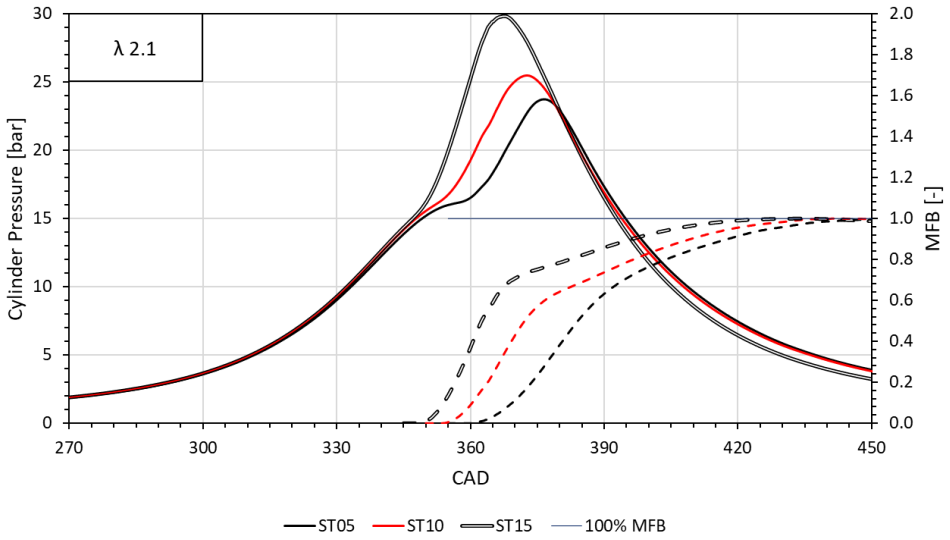


Figure 58. Cylinder pressure traces (solid lines) and mass fraction burnt (dashed lines), 1000rpm, λ 2.1.

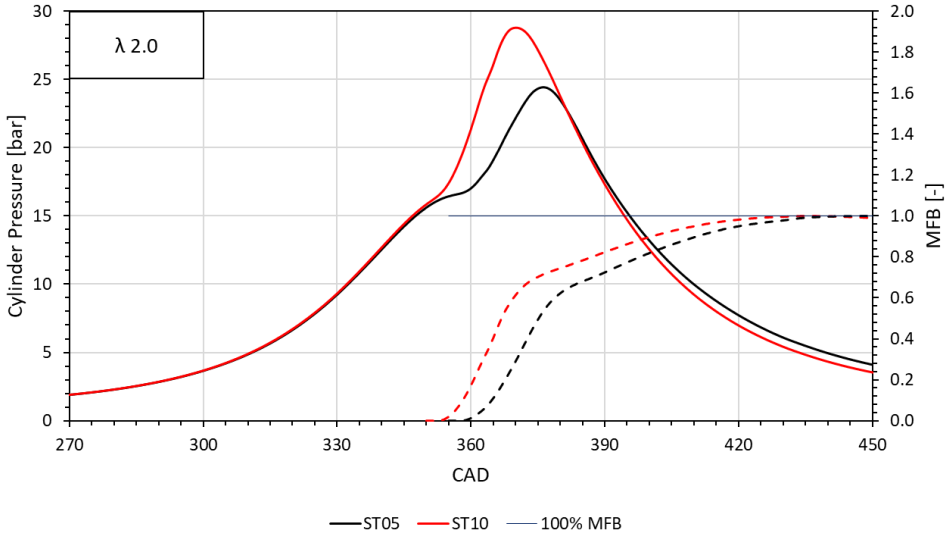


Figure 59. Cylinder pressure traces (solid lines) and mass fraction burnt (dashed lines), 1000rpm, λ 2.0.

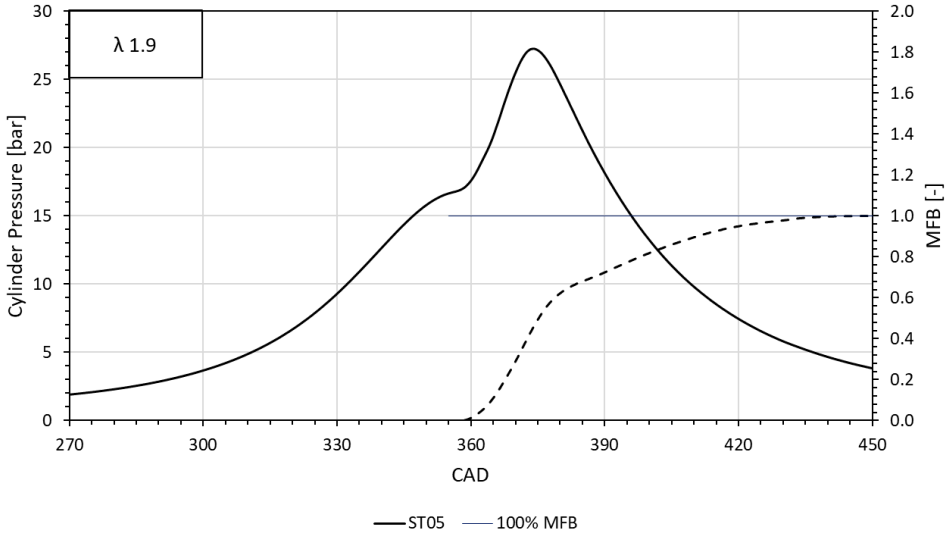


Figure 60. Cylinder pressure trace (solid line) and mass fraction burnt (dashed line), 1000rpm, λ 1.9.

Figure 61 illustrates the IMEP and COV-IMEP values as ignition timing was advanced from 5 to 20 CAD bTDC. As expected, as the combustion process is shifted away from the optimal phasing, the IMEP tends to decrease, while the COV augmented. Even if the tendency suggests more retarded optimal ignition settings, further retarding the spark timing was avoided, so as to avoid prolonged contact of the flame with the cylinder wall; nonetheless, overall, the 5 CAD spark advance setting can be identified as a good compromise for all air-fuel ratios. One interesting result is that this compromise ensures good stability (with COV values below the standard threshold of 5% used in the automotive sector) for the $AFR_{rel}$

of interest, i.e. between 2 and 2.5 (the range that maximizes efficiency benefits, with minimal $NO_x$ emissions).

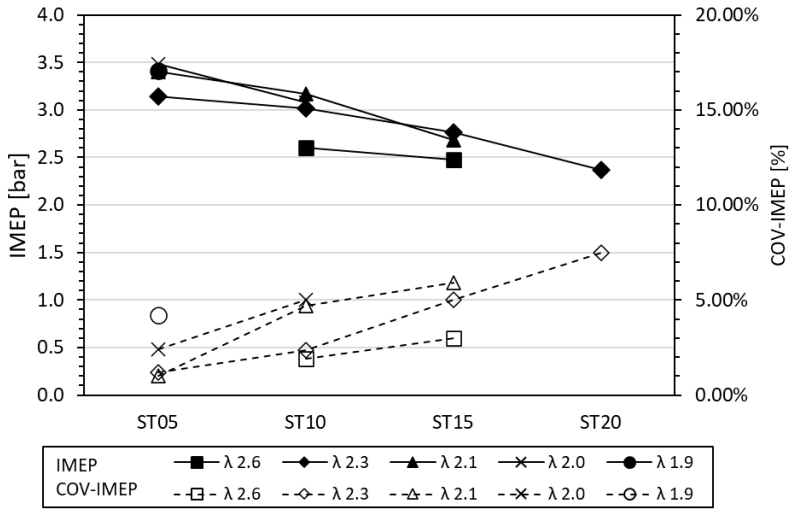


Figure 61. IMEP and COV-IMEP, 1000 rpm.

The average cylinder pressure traces obtained at 2000 rpm are shown in Figure 62 to Figure 65. Only a limited number of operating conditions were investigated at this rotational velocity settings, just to confirm the findings of the trials performed at 1000 rpm. The $AFR_{rel}$ range was extended to a maximum value of 3, as an outlier case. One of the main differences compared to the lower crankshaft speed cases is that the chemistry part of the combustion process is less evident; this is confirmed by prolonged flame development (e.g. the 0-10% MFB phase lasts more than 22 CAD for λ 3.6 ST20, and around 13 CAD for λ 2.3 at ST10). This was to be expected, given that rpm was doubled, and so turbulence effects tend to be more prominent. More contained values of pressure increase rates also confirm this hypothesis. One interesting observation is that for both rpm settings, the lower lambda threshold for avoiding abnormal combustion was around 2, suggesting chemistry effects to be dominant in terms of related load limitations. Nonetheless, the main observation is that the high laminar specific for $H_2$ allows ultra-lean operation with acceptable stability. More to the point, only the lambda 3.6 case features a COV value over the 5% threshold. Figure 66 illustrates the IMEP and COV-IMEP as spark ignition timing is advanced. As expected, the narrower set of operating conditions confirmed the findings that were formulated from the analysis of 1000 rpm data. The main conclusion is that retarded ignition is to be used for $H_2$ fuelling, even with ultra-lean operation. It

also confirmed the possibility of achieving stable combustion at low load without throttling, conditions that are of immediate interest for more in-depth evaluations.

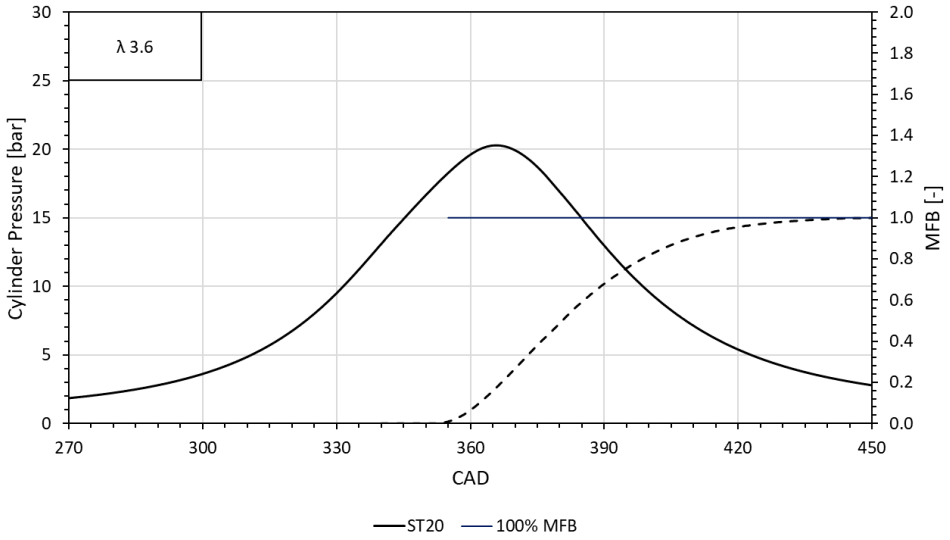


Figure 62. Cylinder pressure trace (solid line) and mass fraction burnt (dashed line), 2000rpm, λ 3.6.

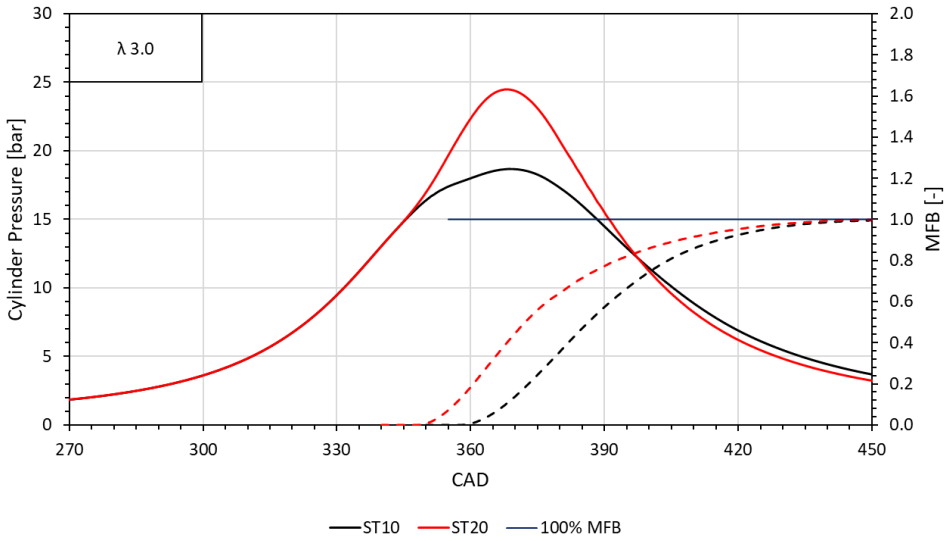


Figure 63. Cylinder pressure traces (solid lines) and mass fraction burnt (dashed lines), 2000rpm, λ 3.0.

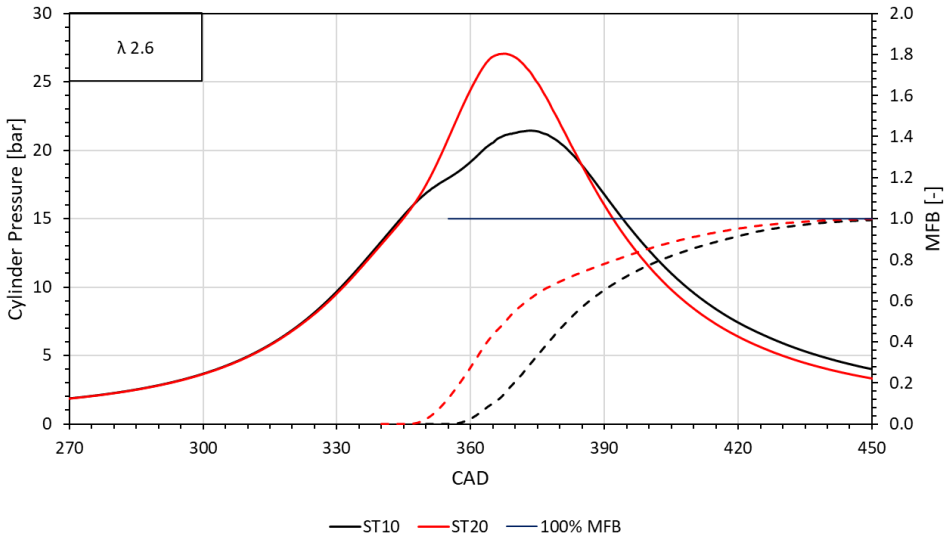


Figure 64. Cylinder pressure traces (solid lines) and mass fraction burnt (dashed lines), 2000rpm, λ 2.6.

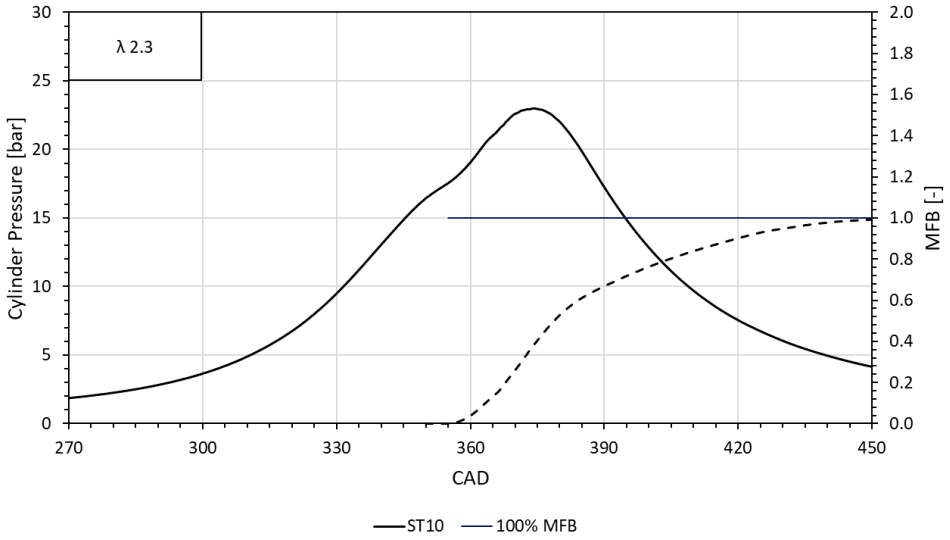


Figure 65. Cylinder pressure trace (solid line) and mass fraction burnt (dashed line), 2000rpm, λ 2.3.

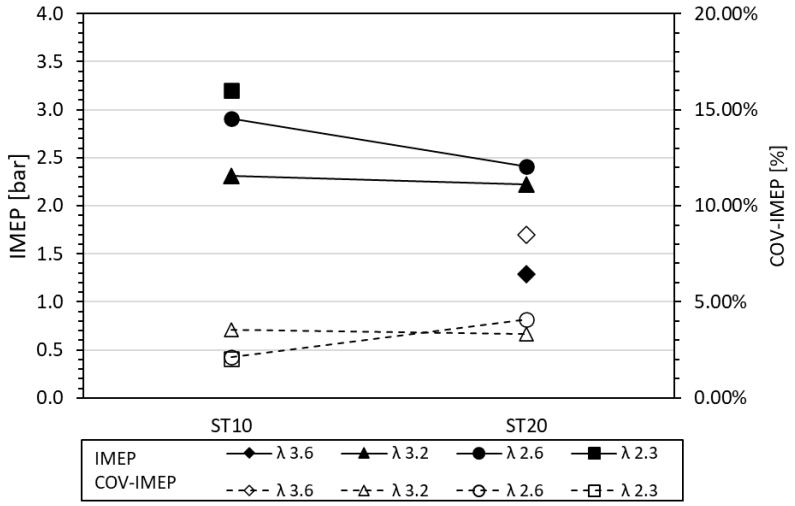


Figure 66. IMEP and COV-IMEP, 2000 rpm.

One drawback of ultra-lean operation is that the highest $AFR_{rel}$ most likely resulted in incomplete combustion (i.e. a 30% reduction of injected fuel mass, when switching from lambda 2.3 to lambda 3.6 resulted in a decrease of over 60% in IMEP); it is unclear whether this was due to flame quenching in the bulk gas or flame propagation that was simply too "slow" for completely covering the combustion chamber volume. Unfortunately, the flame imaging data did not provide enough information for clarifying this aspect (flame images featured very low intensity), but these findings do emphasize the complexity of the phenomena and the need for more detailed investigation. Indeed, the main goal of the investigation was to focus on the optical data that provides valuable insight into $H_2$ combustion specifics that cannot be identified through standard measurements based on in-cylinder pressure evaluations.

## 5.5 Hydrogen: Flame imaging

Pure hydrogen fuelling cases required a more accurate post processing procedure of the images, given that the lean burn conditions resulted in very weak luminosity of the recorded images. The $AFR_{rel}$ of the selected cases featured values in the range of λ 1.9 to 2.1 at 1000 rpm, and λ 2.3 to 2.6 at 2000 rpm (See Table 8). Similar to the methane-hydrogen blends operation, the optical investigation was approached for evaluating two categories of parameters. The first was centred on evaluating the perimeter for the flame object (and of course required a certain degree of luminosity for correctly identifying the related features). In fact, this flame characteristic can be essentially defined by measuring

the clamp distance along the X and Y direction, as well as the definition of the flame object centre. Instead, the second category of analysis implied the detection of the overall luminosity emitted during the entire combustion process. In this case the actual quality of the images is less of an issue to overcome, thus resulting in a wider range of conditions that could be examined (see Table 9). For this reason, the morphological analysis of the flame front and the light analysis are described in two separate sections, as the operative conditions are not the same.

### 5.5.1 Morphological analysis

Table 8 lists the cases examined in this section. These are representative of the 'brightest' conditions recorded during these ultra-lean fuelling trials. Only the 1000 rpm regime was considered, which was found to feature less frequent abnormal combustion phenomena (albeit with reduced intensity, as previously iterated); this was the main reason why the trials were focused on this crankshaft rotational velocity. Quite low luminosity of the recorded images (given the high $AFR_{rel}$) required lower threshold for binarization. The choice for this limit was the result of a compromise that maximized the accuracy of the study during the rapid burning phase, at the expense of the flame development stage. In fact, the presence in the early stages of the arc implied the luminous saturation of the area surrounding the spark plug, making it extremely difficult to detect the edges of the kernel without inducing extensive errors. Therefore, unlike the previous cases (see 5.3 Methane – Hydrogen: Flame morphology analysis), the current section focuses on the description of the flame development phase and correlated phenomena, rather than its inception.

Table 8. Flame morphology analysis of hydrogen fuelled cases.

| Fuel | Start of Injection [CAD bTDC] | Engine speed [rpm] | Lambda [-] | Spark timing [CAD bTDC] |
|---|---|---|---|---|
| Hydrogen | 320 | 1000 | 2.1 | 10 |
| | | | | 15 |
| | | | 2.0 | 5 |
| | | | | 10 |
| | | | 1.9 | 5 |
| | | 2000 | 2.6 | 20 |
| | | | 2.3 | 10 |

The first step of the optical analysis procedure was aimed at the evaluation of the flame object dislocation observed during the so recorded combustion cycles. Figure 67 illustrates the displacement of the averaged flame centre coordinates (at several crank angle instances) and corresponding maximum radial displacement reached during propagation (up to the point in which the flame front reached the optical limit); these values were obtained by averaging of an ensemble of 100 cycles, with the corresponding sequences of images. The edges of the double ground electrodes of the spark plug are overlaid on the background of the graph; they also indicate the orientation of the electrodes with respect to the direction of direct tumble. Compared to the setup used for characterizing methane-hydrogen combustion (similar to the situations most frequently found in the literature aimed at studying $CH_4$ use [95]-[96]-[97]), a double ground electrode geometry was chosen for this investigation; it featured uni-flow orientation with respect to direct tumble. As previously mentioned, the points of flame centre are shown for frames up to 20 CAD aST, the instance at which most cycles feature flame fronts that reach the optical limit. Showing the points evaluated for successive flame images would not add significant information, as the evaluation would be biased. An immediate observation is that the flames tended to be displaced towards the exhaust valves, regardless of spark timing or air-fuel ratio. This trend was to be expected, given the tumble prone combustion chamber design; more to the point, the incoming flow through the two intake valves generates an organized tumbling flow that is transformed into turbulence during late compression. Intuitively, tumble acts on the flame kernel as a force that displaces it towards the exhaust valves. As the propagation process continues, the flame is equally subjected to the upper part flow of the macro-tumble vortex (towards the exhaust), as well as the part below (towards the intake); therefore, most of the displacement is found during the first part of kernel development. Another aspect is the fact that the two ground electrodes represent obstacles for the flow field and also influence the flame through e.g. heat transfer effects. These two mechanisms are the main influence on flame displacement. Flame chemistry (i.e. laminar flame speed directly correlated to AFR) also plays a role: as expected, leaner cases tend to be more prone to displacement (i.e. kernel development takes longer and therefore there is more time available for the interaction with the flow field); the $\lambda$ 2.1 ST10 situation featured a maximum overall displacement of around 6 mm, while for

$AFR_{rel}$ 1.9 ST05, this parameter was only 3.0 mm (Figure 67, bottom). Even if ultra-lean operation was investigated, the interesting property of $H_2$ of high laminar flame speed acts as a limiting factor in terms of maximum flame displacement. By way of example, stoichiometric and lean operation recorded on the same engine resulted in a much wider range of flame centre dislocation values [77]-[78].

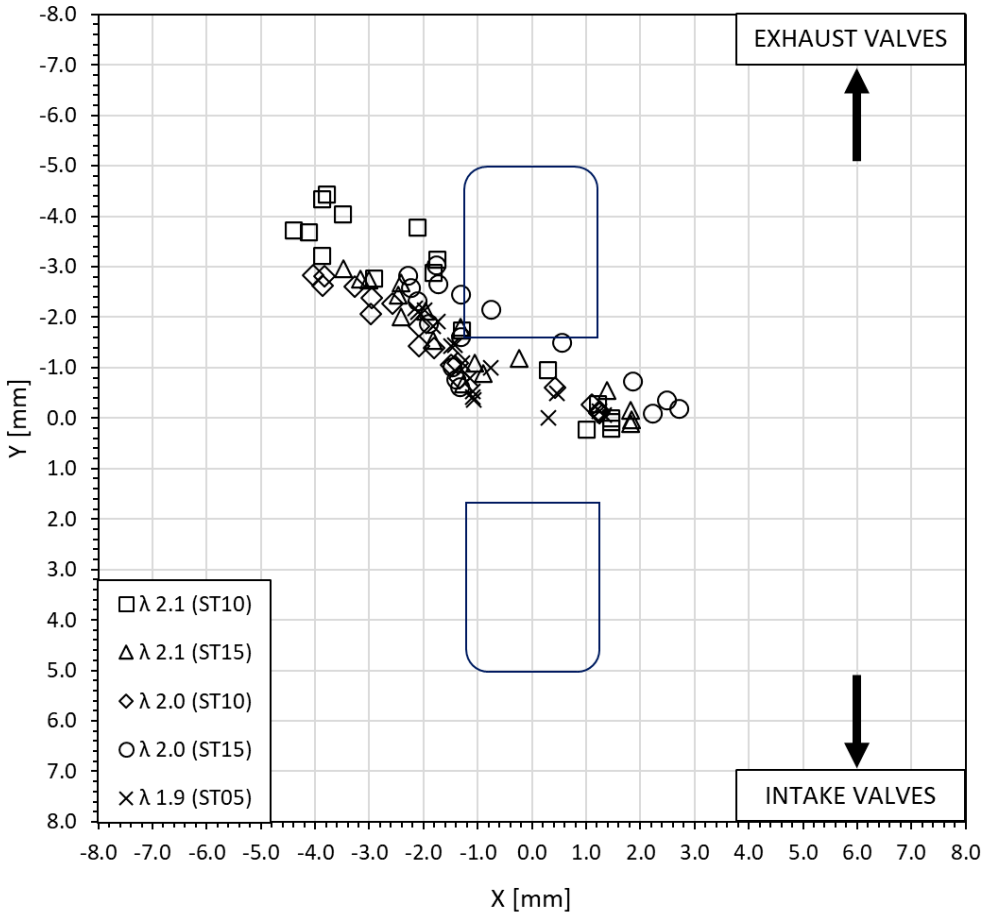

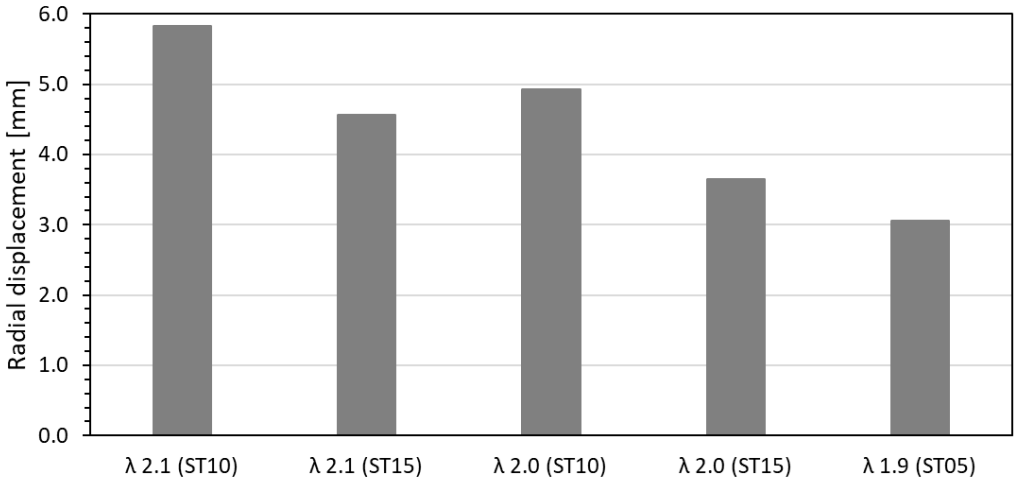

Figure 67. Flame centre coordinates (top) and maximum dislocation (bottom). Hydrogen, 1000 rpm.

The tumble interaction hypothesis seems to be further confirmed by the data recorded at 2000 rpm (See Figure 68). Indeed, the higher velocity and therefore more intense fluid motion resulted in double the displacement along the Y axis, while the values along the X axis remained roughly the same. Due to the low number of operating conditions at this crankshaft speed, no histogram graph was added. In any case, just to put thing into perspective, the average radial distance reaches value of around 9.3 mm for λ 2.6 (ST10) and 7.9 mm for λ 2.3 (ST10).

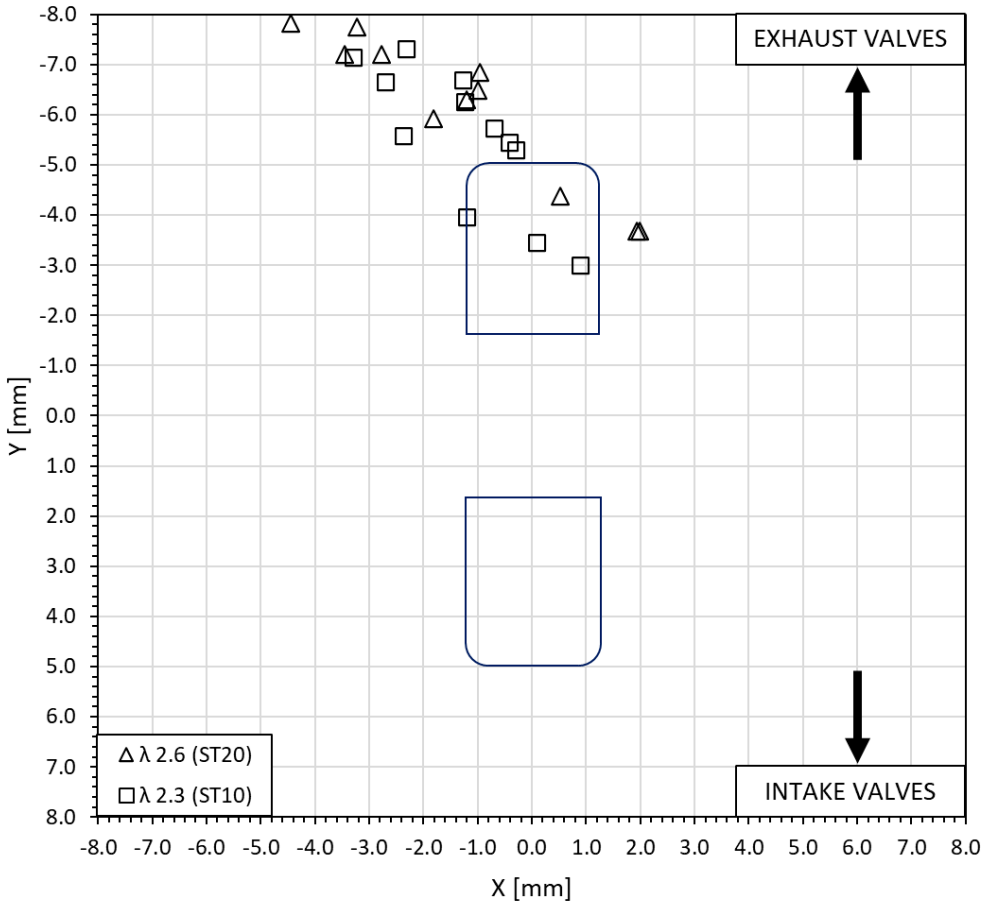


Figure 68. Flame centre coordinates (top). Hydrogen, 2000 rpm.

Figure 69 provides an overview of the flame front propagation characteristics at 1000 rpm; flame area is a direct indication of its size, while the Y/X clamp ratio gives an evaluation of flame shape. The choice of using the Y/X clamp ratio was dictated by the fact that a Fast Fourier transform (FFT) filter needed to be applied during image processing (due to their low pixel intensity). This step modifies the perimeter of the object under scrutiny, and it influences the HCF value (see 5.3 Methane – Hydrogen: Flame morphology analysis). On the other hand, perimeter filtering has a minor influence on the clamp ratio (defined as the ratio between the vertical and horizontal size of the examined object) and so information on flame stretching can be provided and correlations to fluid motion (e.g. direct tumble) can be explored with minimal error.

In Figure 69, the red rectangle overlaid on the early stages of flame propagation indicates the regions where the image analysis software was unable to provide reliable data. Starting from the flame area (Figure 69 top), except for the λ 2.1 ST10 case, all conditions follow a similar growth rate with a very limited

dispersion. Taking into account the diameter of the optical window, i.e. 61.1 mm compared to a maximum flame diameter of of 79.8 mm (i.e. bore size), the flame reached this limit in around 20 CAD. The λ 2.1 ST10 case is the only one that took longer, with the flame reaching the optical limit in 26 - 27 CAD. The maximum gap in terms of flame area growth rate is of around 6 – 7% at 13 – 15 CAD aST, between λ 1.9 (ST05) and λ 2.1 ST15 conditions.

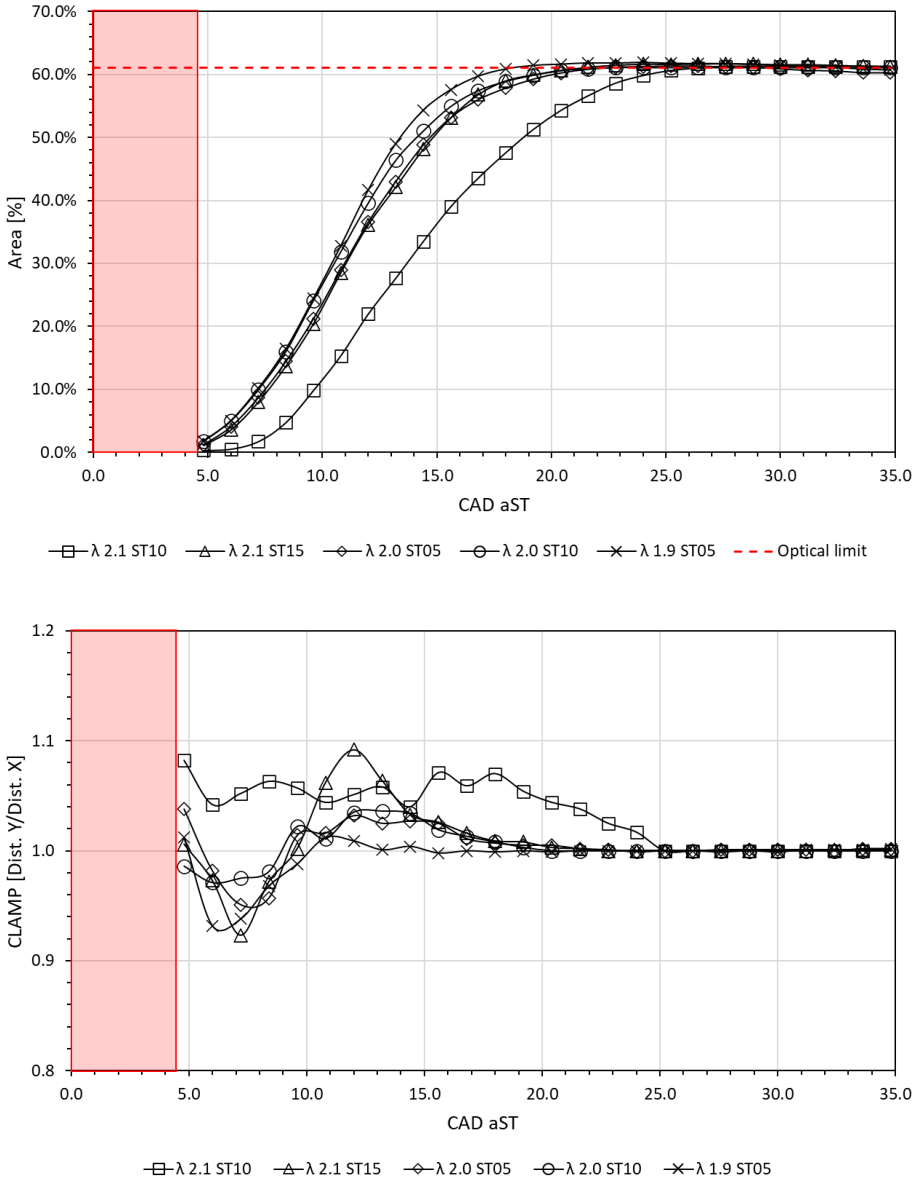


Figure 69. Flame area development (top) and Clamp Y/X (bottom). Hydrogen, 1000 rpm.

No clear trend could be identified for the clamp ratio (Figure 69, bottom). The fact that most cases exhibited a ratio below unity (i.e. flames elongated more along the X axis) in the initial stage seems to be in line with the geometry of the spark plug. The ground electrodes would indeed act as a shield with respect to

tumble flow and thus promote kernel development along the X axis; on the contrary, they act as heat sinks in terms of propagation along the Y direction. The "leanest" case is an exception in this sense. However, when considering that chemistry effects would be more contained compared to the other two $AFR_{rel}$ values, a stronger correlation with turbulence effects is plausible. This line of thought seems to be confirmed by the fact that the highest absolute stretching values were recorded for λ 2.1. In any case, the maximum absolute distortion of around 9% along one direction rather than another is in line with the expected tendency of flames to evolve towards circular shapes, even in lean burn conditions, more so when laminar flame speed is higher.

As expected, at 2000 rpm the λ 2.3 (ST10) condition showed a faster flame front propagation compared to λ 2.6 (ST20) (Figure 70, top). Even though spark timing was advanced for the leaner case (therefore shifting the main phase of flame propagation in a crank angle range with higher turbulence intensity), the lower temperature at 20 CAD bTDC most likely resulted in longer kernel development. Compared to the conditions at 1000 rpm, the effect of increased turbulence resulted in overall faster flame propagation. The optical limit was reached at around 30-34 CAD, while for the lower engine speed, this window was 20 CAD. Therefore, on a time base, the 2000 rpm conditions featured faster flame evolution compared to 1000 rpm (assuming roughly the same temperature during ignition). More elongated flames along the X axis (Figure 70, bottom) were consistent for both air-fuel ratios. The effect during kernel development was also more prominent compared to the lower engine speed conditions (i.e. the Y/X clamp ratio was as low as 0.75 at 7.2 CAD aST, while this value featured minimum of around 0.9 for 1000 rpm). As expected, the distortion reduced gradually as the flame area augmented. Compared to the cases at 1000 rpm that featured lower AFR, the evolution towards a circular shape was slower; this can also be attributed to more noticeable effect of turbulence, given the higher engine speed.

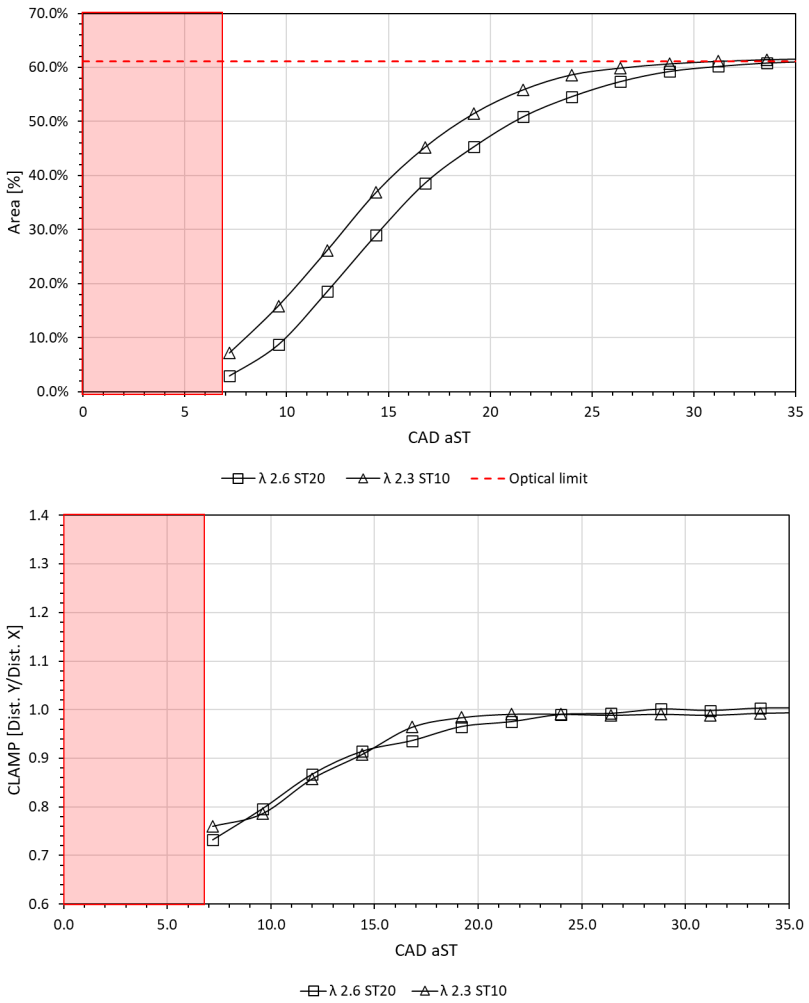


Figure 70. Flame area development (top) and Clamp Y/X (bottom). Hydrogen, 2000 rpm.

The overall evaluations made in terms of flame area are also completely in line with the traces shown in in Figure 71; the illustrated velocity profiles along the X-Y direction feature relatively narrow range at the same crank angle. One interesting observation is that for both rpm settings, the flame tends to feature higher expansion velocity towards the exhaust valves (i.e. “Vel down” traces), exactly the opposite of that towards the intake valves (i.e. “Vel up” traces). This is completely in line with the kernel displacement presented previously and is most likely the effect of flame displacement by direct tumble. In fact, this effect is strongest during the early stages (around 7-10 CAD aST) and is more prominent at 2000 rpm, thus when tumble motion is more intense. While the differences along the Y axis are somewhat intuitive, given the tumble prone combustion chamber geometry, the fact that it is present along the X axis as well is less evident. More to the point, no clear conclusion can be drawn without direct measurement of fluid motion.

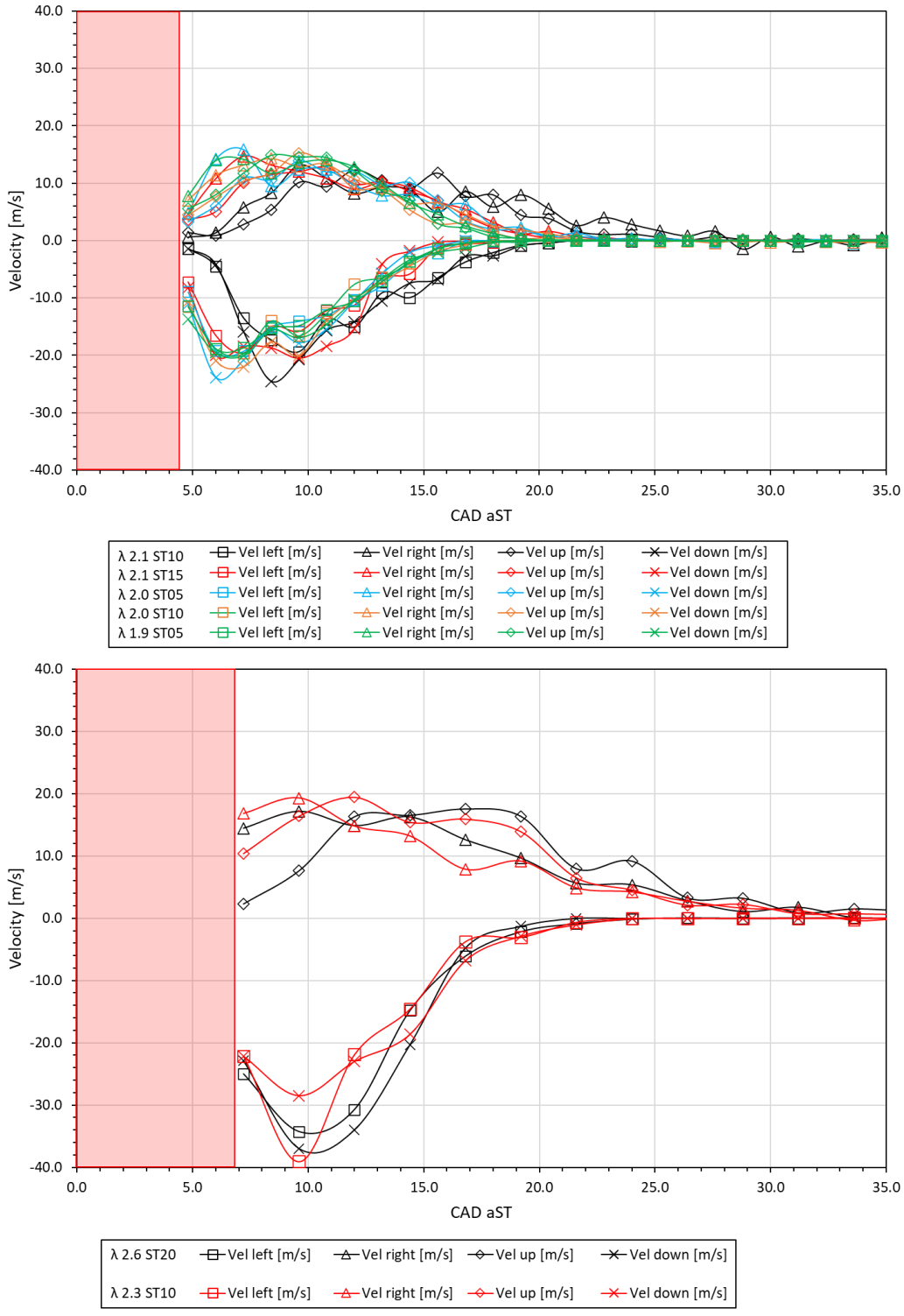


Figure 71. Flame front speed profiles along X-Y axes. Hydrogen, 1000rpm (top) and 2000 rpm (bottom).

Nonetheless, the fact that the cylinder is connected to the fourth runner of the intake manifold (the last runner if counting from the throttle valve, as shown in the figure in the experimental setup section) renders the possibility of slight swirl plausible. In this situation, slight difference in flow velocity for one of the intake valves with respect to the other may create a swirl motion that could explain the

observed flame displacement. Considering the 90 degrees bend the flow has to take before entering the 4th runner, it is possible that the 8th intake valve would feature slightly higher flow compared to the 7th. This is in line with the observed kernel displacement towards the exhaust and to the left, as direct influence of direct tumble and counterclockwise swirl. The spark plug electrode orientation (along the Y axis) would also "help" emphasize this effect. One observation that needs to be mentioned is that these effects are not as evident for the methane-hydrogen blend data. Intuitively, one would expect that the flame kernel would be displaced in the same region as that observed for the $H_2$ data; however, when considering the spark plug geometry, the interaction is not that straight forward. Nonetheless, the correlated kernel displacement points and propagation velocity traces are interesting results that would constitute good starting points for 3D CFD investigations, with simulation of the entire combustion chamber domain.

### 5.5.2 Luminosity analysis

Given that only luminosity was analysed (i.e. the flame object contour required for morphology analysis could only be treated for certain conditions in which luminosity was high enough, whereas overall pixel intensity could be calculated for the complete set of sequences), the entire set of operating conditions could be used for evaluating overall parameters. Table 9 shows the selected conditions examined at 1000 and 2000 rpm.

Table 9. Hydrogen, optical operative cases, luminosity.

| Fuel | Start of Injection [CAD bTDC] | Engine speed [rpm] | Lambda [-] | Spark timing [CAD bTDC] |
|---|---|---|---|---|
| Hydrogen | 320 | 1000 | 2.3 | 10 |
| | | | | 15 |
| | | | | 20 |
| | | | 2.1 | 5 |
| | | | | 10 |
| | | | | 15 |
| | | | 2.0 | 5 |
| | | | | 10 |
| | | | 1.9 | 5 |
| | | 2000 | 2.6 | 10 |

| | | |
|---|---|---|
| | | 20 |
| | 2.3 | 10 |

The lower engine speed setting featured more operative conditions (e.g. backfiring was more frequent at 2000 rpm and limited the spark timing sweep at certain AFRs). Figure 72 and Figure 73, illustrate the different levels of visible emissions recorded at 1000 and 2000 rpm.

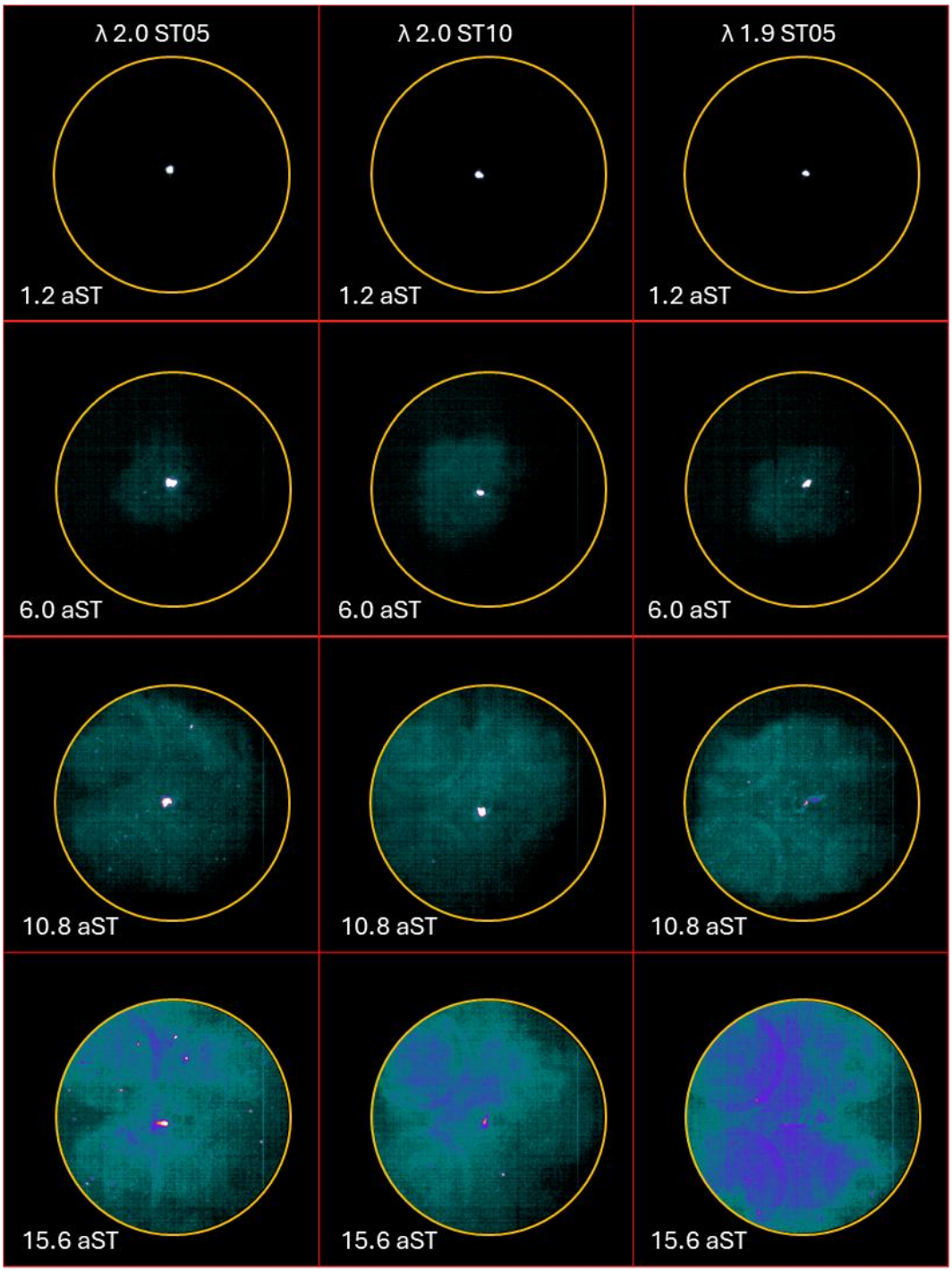


Figure 72. Luminous signal coming from flame front, 1000rpm, λ 2.0, ST05 - 10 and λ 1.9 ST05.

Unlike the methane-hydrogen fuelling cases, there was no saturation present during flame propagation (i.e. spark arcs would still result in saturated pixels during ignition). For example, the most luminous case examined in this section (λ 1.9, ST05), as an ensemble of 100 cycles, reached a peak brightness of 95 on a grey scale of 0 to 255.

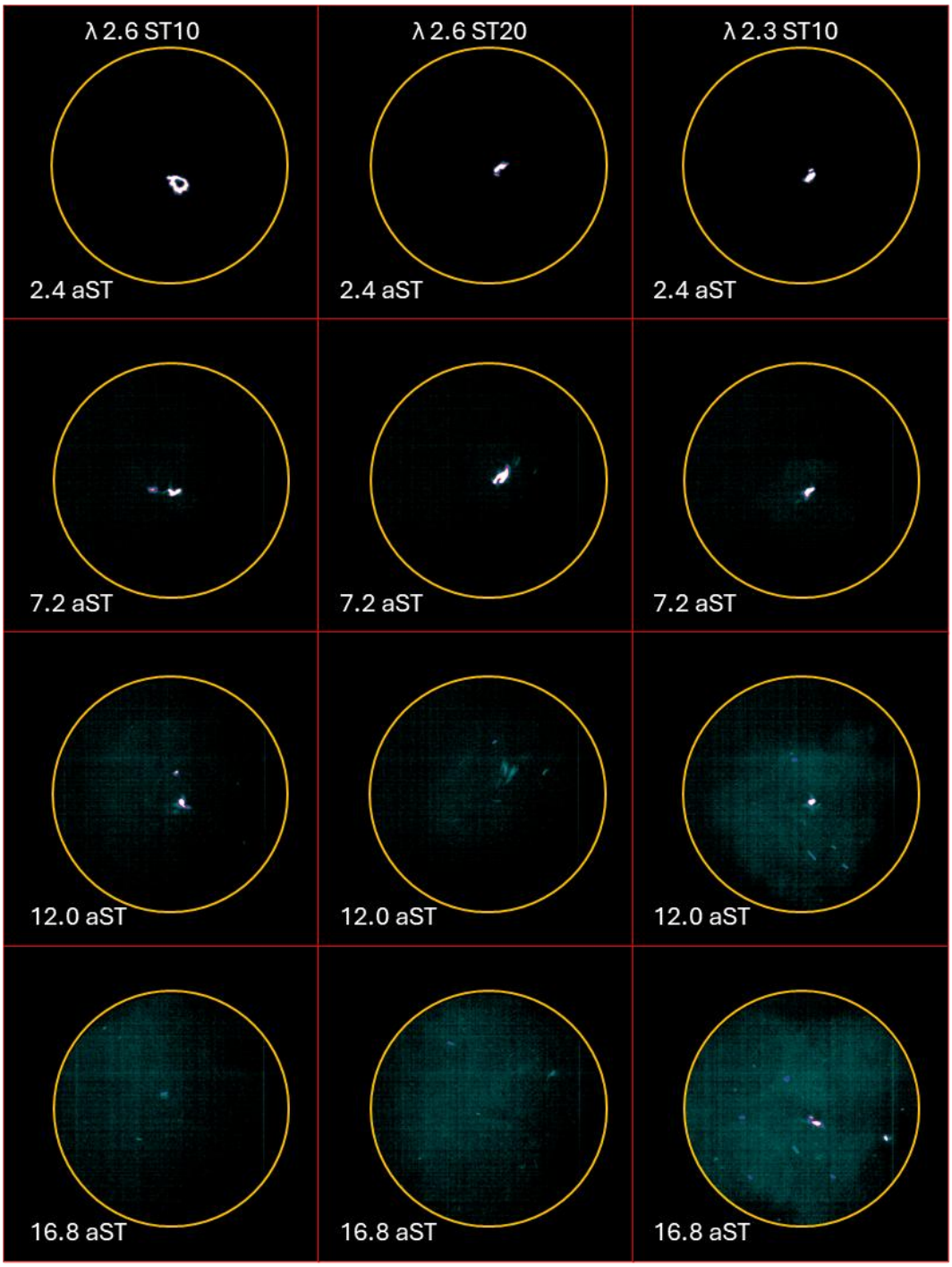


Figure 73. Luminous signal coming from flame front, 2000rpm, λ 2.6, ST10-20 and λ 2.3 ST10.

The sequences that contain images recorded up to 15.6 CAD aST for 1000 rpm and 18.0 CAD aST for 2000 rpm provide an overall idea on the level of luminosity. For both series of images, the flame kernel in the early stages is almost completely 'invisible', with the arc as the only object to be visualised. Furthermore, to emphasize the low visible emissions in these conditions, it is worthy of note to highlight that the images were post-processed for enhancing visibility. Based on these considerations, it was decided to add a second mask (in addition to the outer limit used for eliminating spurious light) that covers the spark plug. The goal was to investigate the luminosity signal coming from the flame, without the influence of spark arc luminosity, which results predominant during ignition. This step enabled more coherent analysis of the standard deviation of the luminosity related to inhomogeneities of the flame and/or the presence of bright spots. Lastly, considering the low levels of luminosity with respect to noise, it was chosen to exclude the analysis of the brightness along X-Y direction. Instead, more attention was paid to the average level of luminosity reached during the entire duration of the recorded sequences, and how this correlate to parameters such as IMEP and COV-IMEP. The size of the second mask applied in the region of the spark plug was chosen by measuring the arc elongation for all the selected cases. Then, from an ensemble of 100 cycles, the largest elongation was set as the radius of the circular mask. Figure 74 and Figure 75 presents the average signal measured for each operative condition and corresponding standard deviation. As expected, the presence of the additional mask results in an almost flat trend in the early stages, with higher increasing rates once the flame object was larger than the central mask. An interesting observation is that for the most diluted cases, the luminosity increased monotonically. As the air-fuel mixture was richer and the spark timing was advanced, the traces feature a bell-shaped curve. Specifically, the presence of a peak in the luminosity traces was noted, and its magnitude increased as the mixture was enriched. It is plausible to correlate this evolution to the local concentration of active species during combustion; evidently, mass concentration of active species was higher for lower AFR, and density was also increased given that peak pressure values augmented. In fact, the decreasing trend observed after the luminosity peak is specific for late combustion, during early expansion. Given that the leanest cases featured slower flame propagation, the effect of the peak pressure is not as evident, thus resulting

in continuous increase of luminosity as combustion was still (slowly) progressing. No direct correlation can be hypothesized in terms of actual flame propagation velocity (See Figure 71) vs. overall luminosity during combustion.

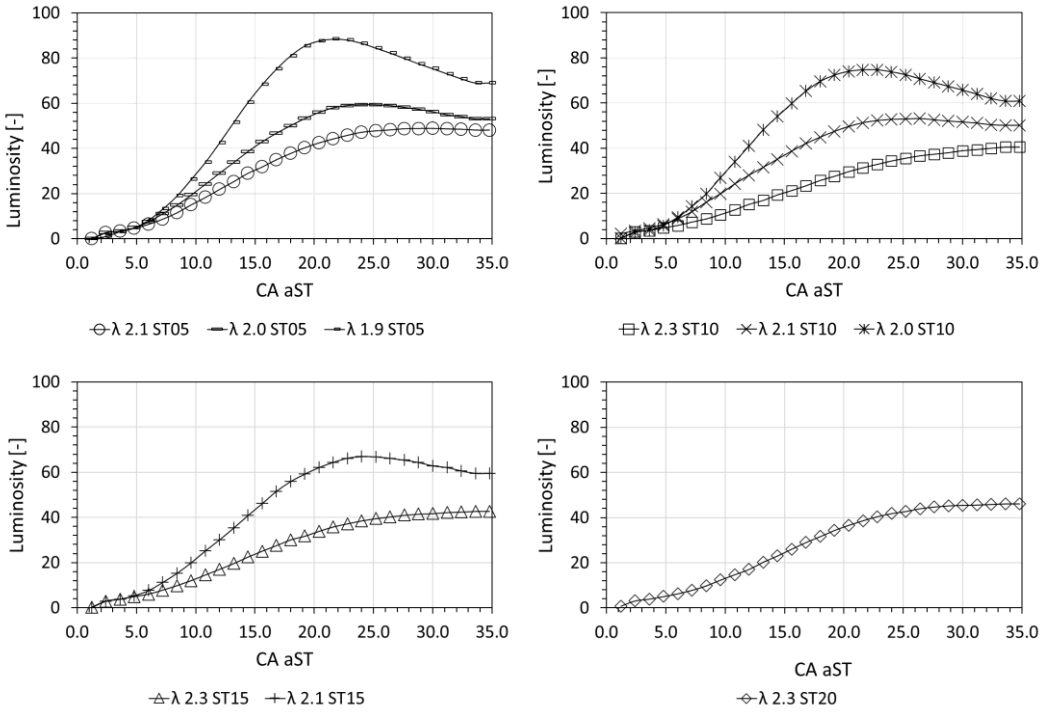


Figure 74. Luminosity traces; hydrogen, 1000rpm.

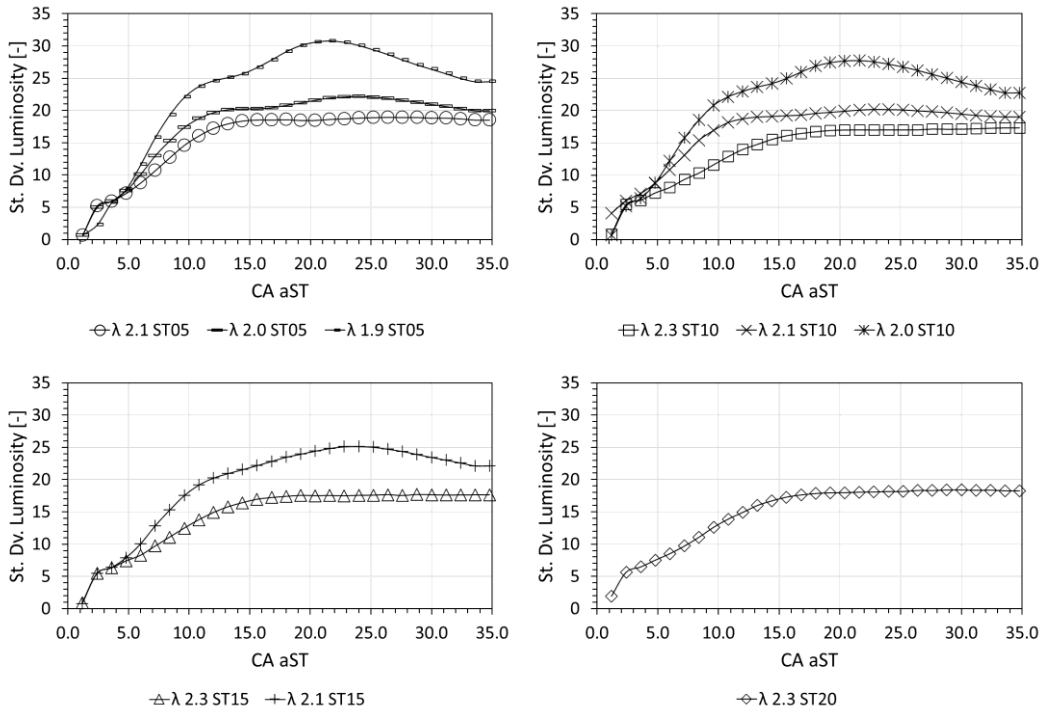


Figure 75. Luminosity standard deviation; hydrogen, 1000rpm.

Besides luminosity, standard deviation was calculated over the entire set of sequences (See Figure 75). This parameter is closely linked to the presence of inhomogeneities, either due to the influence of the interface between burnt and unburnt gases, or other non-flame related sources such as bright spots (even if a carbon-free fuel was used, and therefore such localized high intensity point should by minimal, the presence of solid material coming from the piston rings, i.e. teflon-bronze, could have caused the observed bright spots; indeed, evidence of oxidized copper was found on the surface of the quartz window; these localized small size points match the hypothesize mechanism and the fact that they were fused with the window suggests high temperature processes). An interesting observation is the varying slope of the traces, especially for the cases with lower AFR. This can be linked to the actual evolution of the flame front. More to the point, the initial stages feature relatively high slope, given that the kernel interacts with turbulent eddies of various size and intensity. After a certain propagation point, the flame reaches a size that includes interaction with the overall turbulence spectrum, thus reducing variability. A second increase in slope around the peak intensity value could be related to the end of flame propagation, characterized by quenching near the wall; a specific feature of the engine used for the trials is that it features relatively large top-land region volume, another reason for which increased variability can be expected once the peak pressure was reached. In other words, the flow returning from the crevices to the combustion chamber (and related interactions with the flame/burned gas) could be a significant source of variability.

Further insight into the correlation between flame characteristics and engine output, as well as in-cylinder thermodynamics, luminous intensity data was averaged for each operating condition (Figure 76). Once the brightness intensity was measured for each firing cycle, the average signal was calculated, and the resulting profile integrated over the entire duration of the recorded sequence. Therefore, each averaged value is representative of the total luminosity reached by a specific operative condition, from its inception up to the last frame recorded. As expected, overall luminosity increases with spark timing, given that higher peak pressure was obtained. The apparent opposite trend of IMEP and ∑Lum (Figure 76, top) is therefore more related to the fact that far as the more advanced spark timing resulted in less favourable combustion phasing rather than a true

correlation between the two parameters. On the contrary, a clear correlation is noted for the peak pressure and luminosity (Figure 76, middle), again due to the fact that higher pressure results in augmented density, as well as increased temperature, and therefore higher concentration of active species during combustion. Another interesting result is the correlation of COV-IMEP and the standard deviation of average luminosity. Increased variability of engine output was well correlated with lower repetitiveness of flame luminosity. Although not entirely clear to which part of the process this correlation is better fitted, it is an interesting finding that could be further investigated through 3D CFD simulations for highlighting specific phenomena.

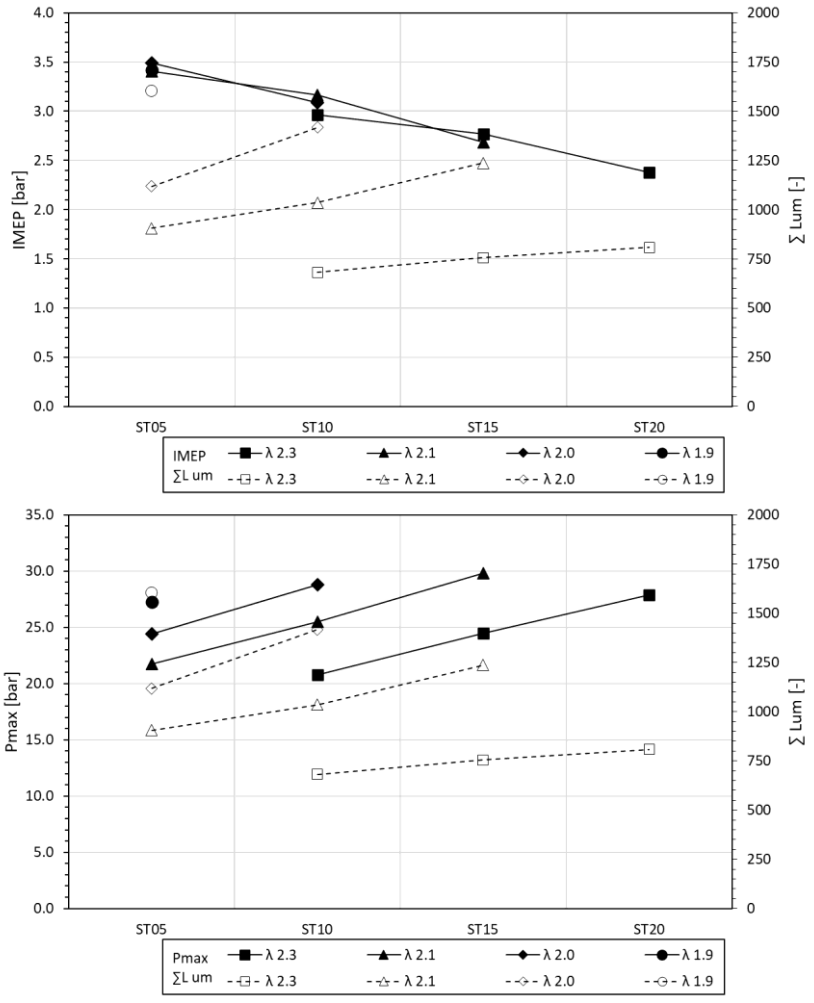

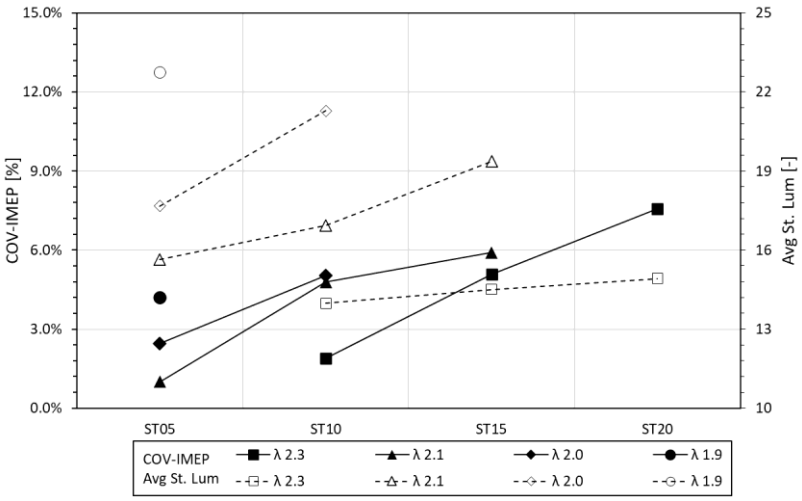


Figure 76. IMEP vs ∑Lum (top), Pmax vs ∑Lum (middle) and COV-IMEP vs St.Dv. Luminosity (bottom); hydrogen, 1000rpm.

Given the limited operative points recorded at 2000 rpm, only the traces shown in Figure 77 are discussed. The changing slope as AFR was reduced was also noted for these cases, with the same mechanism completely compatible with the shape of the three traces. The variability of the flame luminosity followed the same characteristic of higher values at lower AFR, with lower peaks compared to 1000 rpm; this can be linked with the increased stability (with COV-IMEP below 5%) that was recorded for all air-fuel mixture settings.

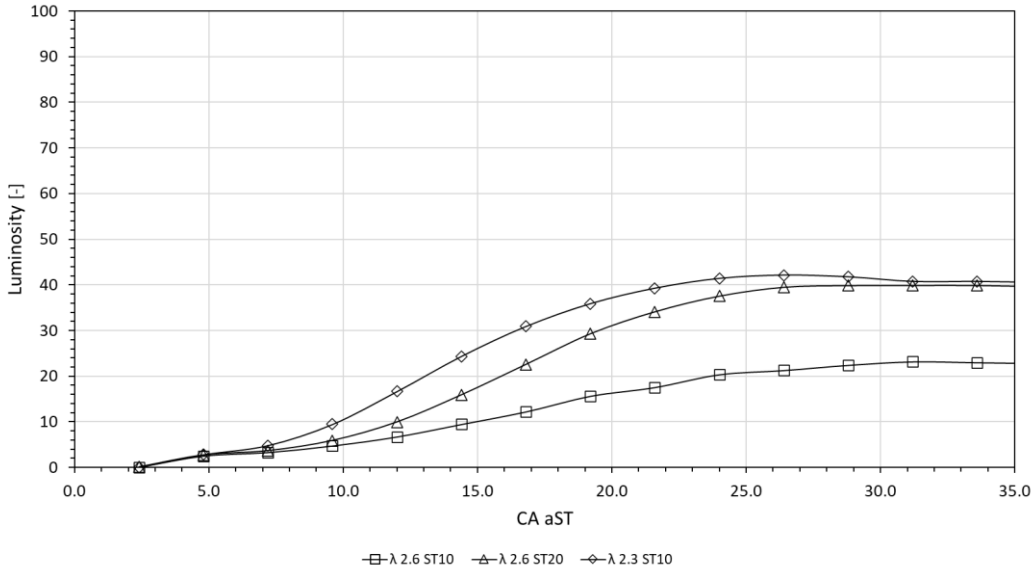

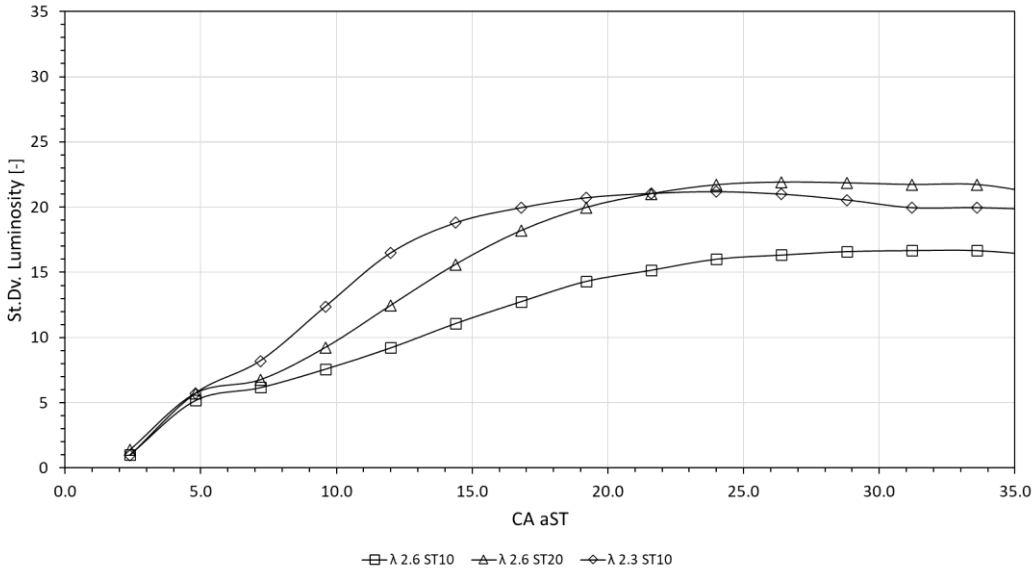


Figure 77. Luminosity traces (top) and related standard deviation (bottom). Operative conditions at 2000rpm.

## 5.6 Hydrogen: Optical Emission Spectroscopy analysis

It is consolidated that a plasma generated by an electric spark discharge can be used as a light source for spectral analysis; in this way information can be obtained in terms of air–fuel mixture concentration by analysing the light emitted by the excited species. This methodology is known as Spark Induced Breakdown Spectroscopy (SIBS) [85]. The characteristics of the discharge affect the plasma features as well as the breakdown [98] and molecular recombination in the spark plug region. As detailed in the Annex (See A.2 Optical emission spectroscopy), the spectra emitted by the plasma evolve significantly after the breakdown. Shortly after ignition was initiated (<0.1μs), the plasma emission featured an intense continuum, due to the collisions of electrons with ions and atoms (free-free emissions) and recombination of electrons with ions (free-bound emissions). Successively, in less than 1 μs, the spectral emission lines determined by the radiative decay of excited species arise and the lines characteristic for atoms and ions gradually disappear. Then, band emissions induced by the de-excitation of electronically excited molecules can be detected. In order to better understand the phenomena determined by the spark discharge in diluted hydrogen-air mixtures, SIBS was applied by changing several parameters, such as the spark plug geometry, the engine speed and the relative air-fuel ratio. Details on tested cases are reported in Table 10.

Table 10. Test cases for spectroscopic investigations.

| Spark plug | Engine speed [rpm] | Lambda [-] | ST [CAD bTDC] | Time aST [µs] |
|---|---|---|---|---|
| Double electrode | 1000 | 2.9 | 10 | 1000 |
| | | 2.7 | | |
| | | 2.6 | | |
| | | 2.3 | | |
| | | 2.1 | | |
| J – plug | 2000 | 3.6 | 20 | From 8 to 1000 |
| | | 3.2 | | |
| | | 2.6 | 10 | |
| | | 2.3 | | |

The spectra recorded in the first stages after breakdown (from 8 to 32 µs) permitted to clearly follow the evolution of the plasma emissions from atomic lines (Balmer-α at 656 nm and nitrogen lines at 501 nm) superimposed on a continuum, to the molecular Fulcher band (around 600 nm). Typical results obtained by fixing the relative air fuel ratio (lambda value) at 3.2 are shown in Figure 78. The lines of Balmer series are detectable until ≈50 µs after spark timing, when the discharge phase is still in progress; afterwards only the emission due to the Fulcher band is well resolvable in the visible wavelength range. The fast switch from the Balmer α band to the Fulcher band can be roughly associated to the decreasing energy transferred from the plasma to the gas. Specifically, the energy yielded by electrons to atoms reduces below the 16.6 eV threshold necessary for the Balmer α to be evident, but higher than 13.5 eV typical of the Fulcher evidence (See A.2 Optical emission spectroscopy).

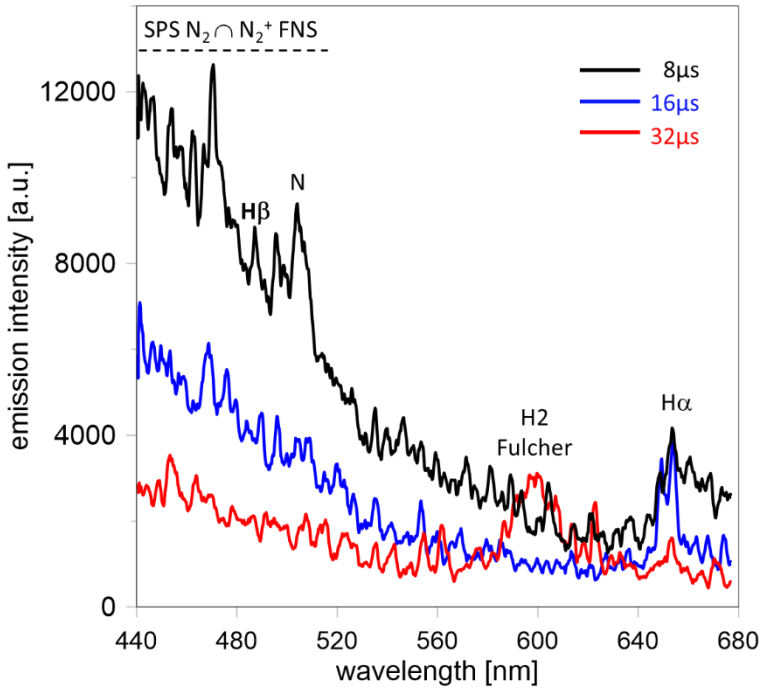


Figure 78. Single cycle spectrum acquisition; 2000 rpm, λ 3.2, spark timing 10 CAD bTDC, acquisition timing from 8 to 32 µs aST.

Following the evolution of the spark discharge, it was possible to observe a progressive change in the behaviour of detected emissions; the atomic continuum strongly decreased and additional contributions of nitrogen content species emerged, due to recombination effects. Spectral evidence of the N2 second positive systems and ammonia radicals were detected. Figure 79 shows a typical emission spectrum recorded at 400 µs after spark timing (fixed at 10 CAD bTDC), for the case with 2000 rpm engine speed and λ equal to 3.2; the three bands due to the de-excitation of $NH_3$, $NH_2$ and NH radicals resulted weak but still detectable. Simultaneously, the strong emission due to OH radicals centred at 306 nm occurred. The presence of hydroxyl radicals demonstrated flame kernel inception when the spark discharge was still in progress. It should be noted that the Fulcher α band at 600 nm was well recognizable; for this reason, in the present work the band was used as spectral feature of hydrogen specific, ignition since it resulted less sensitive than the Balmer bands to the quenching phenomena caused by high turbulence and pressure variation typical of an internal combustion engine. Thus, the evolution of the Fulcher band emission was evaluated in the several operative conditions reported in Table 10.

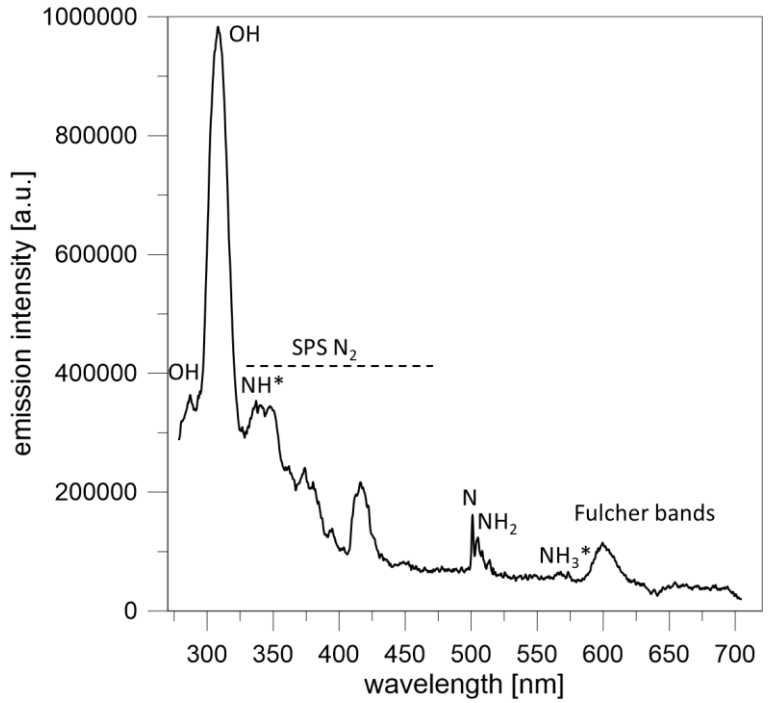

Figure 79. Average spectrum acquisition on 100 cycles. Operative condition; 2000 rpm, λ 3.2, Spark timing 10 CAD bTDC. Acquisition time 400μs aST.

For each detected spectrum, a procedure developed in LabView 2020 environment [99] was applied for calculating the band emission. Specifically, the intensity level of the species under investigation was calculated considering the difference between the emission peak $I_{max}$ in a selected range and the minimum value $I_{min}$ measured by linearly interpolating the intensities of the two lowest emissions value close to the examined range, $I_{min1}$ and $I_{min2}$. Eq. 3 illustrates the calculation procedure.

$$I = I_{max} - I_{min}$$

$$I_{max} = I(\lambda_{max})$$

$$\frac{\lambda_{max} - \lambda_{min1}}{\lambda_{min2} - \lambda_{min1}} = \frac{I_{min} - I(\lambda_{min1})}{I(\lambda_{min2}) - I(\lambda_{min1})}$$

Eq. 5

As shown in Figure 80 (top), $H_2$ Fulcher intensity evolved during the spark discharge with a behaviour that resulted in good agreement with the current intensity of the secondary circuit. Similar trends were observed for all tested $AFR_{rel}$ conditions, as reported in Figure 80 (bottom). Very good match between the secondary current and emission intensity throughout spark discharge, until the late phase of the process, confirmed the relevance of the Fulcher band as spectral marker of hydrogen plasma in engine-like conditions.

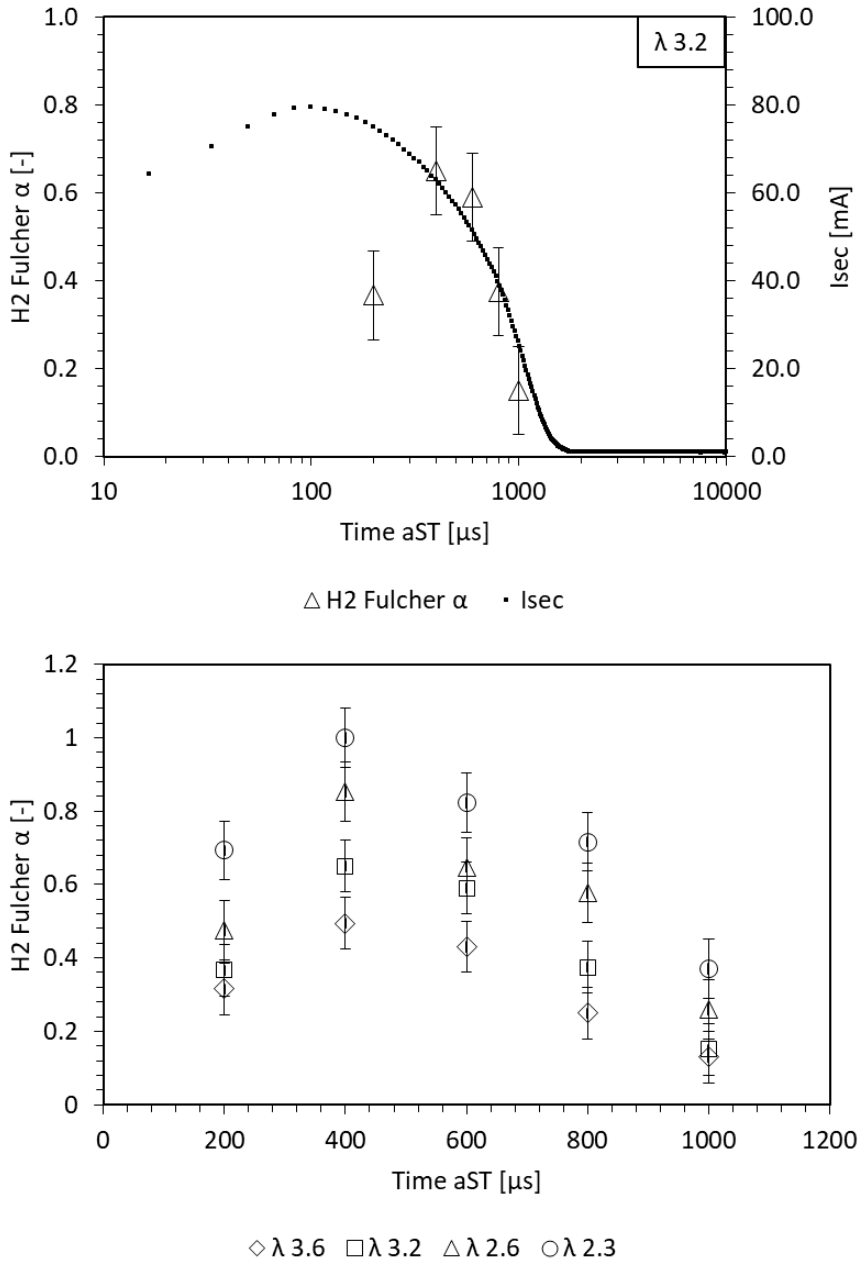


Figure 80. Evolution of $H_2$ Fulcher intensity (average on 100 cycles) after the spark timing (10 CAD bTDC) recorded at 2000 rpm.; comparison of emissions (top) at fixed λ (3.2) with the corresponding secondary current signal and (bottom) at different λ values. All intensities were normalised to the absolute maximum.

To better understand the relationship between Fulcher emissions and hydrogen concentration, the normalised band intensity was plotted as a function of λ values. Figure 81 clearly demonstrated a linear correlation of Fulcher intensity (recorded throughout the spark discharge phase) with the experimental values of lambda measured by using the UEGO sensor.

To consolidate the previous results, spectroscopic investigations in the visible wavelength range were performed by changing the spark plug geometry from

single J electrode to the double electrode configuration and considering two engine speeds (1000 and 2000 rpm). As shown in Figure 82, for both engine speed settings the intensity resulted linearly correlated to the relative air-fuel ratio; the agreement was very good even late during the phase of spark discharge (1000 µs), instances in which the energy transferred to the gas reached the limit in terms of evidence of the Fulcher band emissions.

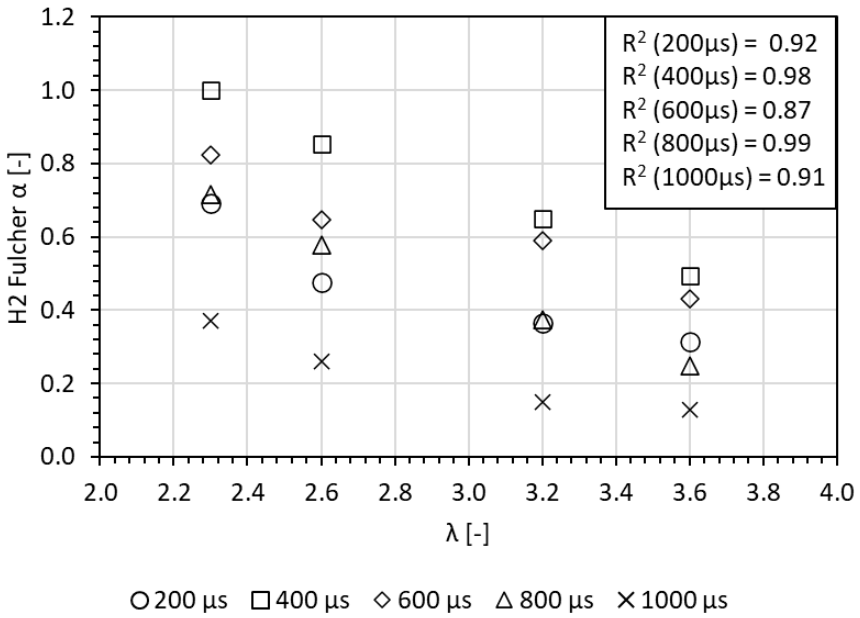


Figure 81. $H_2$ Fulcher intensity (average on 100 cycles) at different times after the spark timing (10 CAD bTDC) recorded at 2000 rpm versus the measured λ values. All intensities were normalised to the absolute maximum.

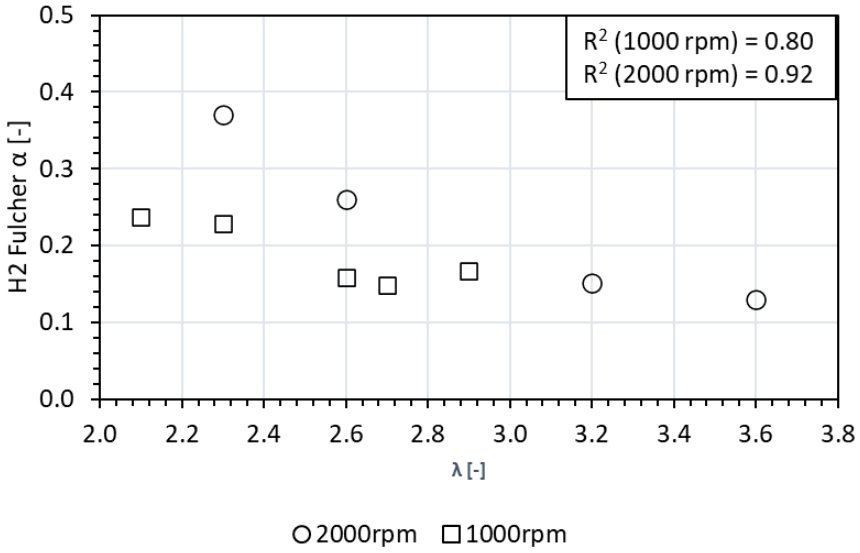


Figure 82. $H_2$ Fulcher α average intensity at 1000 and 2000 rpm. Acquisition time 1000 µs.

All the reported results confirmed the Fulcher band as a very good marker of plasma induced by spark discharge in engine like conditions. The advantage to detect the emission intensity in the visible wavelength range at 600 nm without interference of other species suggests the possibility to design a new optical sensor based on optical fibre used for monitoring the local concentration of hydrogen.

# Chapter 6

# Summary and conclusions

With a central focus on the application of optical techniques, this doctoral thesis resumes the results obtained in terms of characterizing mixing properties and combustion of hydrogen in an optically accessible SI engine. Apart from applying PIV and flame visualization, SIBS was also employed for studying ignition and kernel inception. The methodology allowed to gain insights on the hydrogen (H Balmer α and $H_2$ Fulcher bands) emissions and how these correlate to the AFR.

Parallel to this investigation, the research activity concerning the use of helium as hydrogen substitute to mimic and evaluate its mixing properties are discussed in this thesis.

## 6.1 Non – reactive study conclusions

Given its properties that are close to those of hydrogen, helium was used as a substitute for evaluating mixing properties. A dual cavity Nd:YAG laser was used as light source to perform a PIV analysis on the jet structure. Three different complex geometries of the nozzle tip (intended for low pressure direct injection applications) were examined to gain a comprehensive understanding of the influence of hole's shape/orientation on velocity distribution vorticity intensity. This contributed to provide a broad overview of the various aspects related to the use of ultra-low density gases and the conclusions can summarized as follows

- The use of nozzle patterns with low orientation hole paths, like the first geometry, leads to the generation of jets capable of keeping

momentum, thus resulting in increased jet penetration at the expense of limited radial propagation, i.e. half plume angle 5–9° at 8.0 ms aSOE. Specifically, the 1st configuration recorded the highest values of velocity peaks, ranging from 105 to 309 m/s at 8.0 ms aSOE, regardless of the PR condition examined.

- The 2nd and 3rd geometries, both with more complex multi-hole nozzle patterns and a higher degree of orientation of the hole paths, resulted in improved radial propagation of the jet, i.e. of around 25–30° at 8.0 ms aSOE. In contrast, the greater surface of the jet impacting with the air implied a reduction in its propagation along the injector axis. Specifically, the velocity was measured to be around of 10–20% less compared to the 1st geometry.
- The investigation of the velocity distribution showed that the area characterised by the highest velocity values moves away from the nozzle tip as the PR increases, regardless of the nozzle patterns. In addition, the vortex structures tend to persist longer and accompany the jet extension (first and second geometry) before breaking up.
- The PIV research activity highlighted the key role of major vortex structures in promoting mixing phenomena during the early and intermediate stages after injection. Afterwards these structures rapidly collapse, regardless of the nozzle pattern and PR condition, leaving room to the increase in the number of small eddies randomly distributed over the jet edge. Specifically, these were observed to form close to the nozzle tip (0–25 mm) at low PRs and shifted along the injector axis (15–40 mm) in high PR conditions. These observations could become of paramount importance for the design of injection strategies, i.e. injection duration and interactions with the piston or cylinder walls, to improve the mixing efficiency depending on the application.
- Once the PR condition was set, it was observed that the magnitude of the velocity increases (almost) linearly with time for all configurations examined. After 3.5 – 4.0 ms aSOE, the vorticity intensity featured an almost constant trend for each case that was considered. These results are in line with the absence of large vortex structures observed during

jet development and the increase in the number of small vortices. Specifically, these tiny rings are characterised by a very small instantaneous radius, which compensates for the greater speed reached by the jet when it is fully developed.

## 6.2 Reactive study conclusions

### 6.2.1 Thermodynamic-based outcomes

*Methane – Hydrogen blends*

- For stoichiometric conditions and fixed the spark timing, the addition of hydrogen (0%, 20% and 50% volumetric basis) to methane was found to play a primary role in defining the duration of the early stage of combustion process. The higher flame laminar speed of $H_2$ influences the flame development phase (MFB 0-10%) by reducing its crank angle duration by around 30% (i.e. from 20 to 14 CAD).
- On the contrary, once the early stage of combustion was completed, hydrogen addition appeared to exert reduced influence on the rapid burning phase (chosen as 10–50% MFB for the engine used for the trials, as representative for complete flame propagation).
- Lean operation for the 50/50% blend, with an $AFR_{rel}$ of 1.3, the variation of spark timing was observed to impact flame development (0–10 % MFB) in a negligible way. Instead, the rapid burning phase was influenced to a larger degree, most likely due to different interactions with the fluid motion such as tumble and turbulence around the TDC.
- Fast laminar flame speed specific for hydrogen resulted in significant reduction of combustion variability (i.e. COV-IMEP), even in stoichiometric conditions.

*Hydrogen*

- Occurrence of abnormal combustion phenomena limited the $AFR_{rel}$ values to a lower threshold of around 1.9. To avoid these undesired effects, lean and close to ultra-lean conditions were applied.
- Even though the dilution levels were far beyond what could be achieved with standard fuels (such as methane), combustion stability

was found to be more than acceptable for $AFR_{rel}$ values as high as 3, with COV-IMEP below the 5% threshold considered as acceptable for automotive applications.

### 6.2.2 Morphological analysis results

*Methane – Hydrogen blends*

- In line with the observed reduction of CCV, the morphological analysis performed in the early stages of flame development in stoichiometric conditions showed a narrower distribution of kernel positions. This suggests more repeatable combustion, especially during its early stages. As expected, $H_2$ addition promoted faster kernel development, confirmed by an increasing trend of the Feret diameter as the concentration of hydrogen was increased.
- The effect of spark timing in lean conditions (λ 1.3, 50% $CH_4$-50% $H_2$) showed that the interaction with the fluid motion is a determinant factor in terms of flame evolution, as well as the ignition phase.
- Flame front macro- and micro-stretching effects were limited during stoichiometric operation, with minimal influence of hydrogen addition; this was inferred from HCF values close to unity, with maximum deviations of around 0.15 to 0.30. This parameter was instead found to feature higher values during lean operation, i.e. with peaks around 1.6, especially in the flame kernel development phase.
- Overall intensity distribution confirmed that hydrogen addition contributes to more repetitive flame location from one cycle to the next. This trend was confirmed by the analysis performed on the luminosity gradient at the interface between high and low probability regions (in a certain way representative of the separation between burned and unburned gas zones), which increased when augmenting hydrogen content.

*Hydrogen*

- The analysis of flame centre coordinates identified the role of high laminar flame speed, even though lean operation was employed. Kernel displacement was completely comparable to that measured in

stoichiometric conditions with the methane-hydrogen blends. An interesting observation is that the analysis identified slight swirl to be most likely present and that spark plug geometry plays a decisive role in flame kernel location.

- The effect of tumble motion on flame displacement and deformation was more prominent at higher engine speed, confirmed by an clamp ratio values; this parameter featured peaks of around ±10% compared to unity at 1000 rpm, while at 2000 rpm close to 30% was recorded during kernel development.
- As expected, flame luminosity was lower compared to the stoichiometric cases that featured stoichiometric operation; pixel intensity peaks were around 90/255 (on an 8-bit greyscale) for the $H_2$ cases at 1000 rpm with $AFR_{rel}$ of 1.9, with saturation events correlated to bright spots (most likely due to the presence of particles coming from piston rings wear) rather than flame propagation directly.
- The analysis of overall luminosity integrated over the entire field of view revealed high variability during the early stages of flame propagation, most likely correlated to flame-turbulence interactions; a second increase in the standard deviation of luminosity during late combustion was correlated to the flow of fresh charge returning from the top-land region to the combustion chamber.

### 6.2.3 Spectroscopic-based outcomes

- Hydrogen fuelling was characterized through spectroscopic analysis, focused on the ignition process, made it possible to gain insights about the chemical kinetics of combustion process. SIBS was applied for gaining insight into the specific markers of $H_2$ ignition and flame kernel formation. Spectra recorded in the UV-visible range identified the $H_2$ Fulcher α band as directly correlated to the AFR. The results obtained with the conventional J-plug at 2000 rpm showed a significant accuracy of the proposed approach to correlate the marker intensity to the measured air-fuel ratio; coefficients of determination ranged from 0.87 to 0.99. Similar (even if slightly lower) $R^2$ values was also recorded for the double ground electrode spark plug

configuration, further confirming the validity of the approach. Apart from the potential of developing a hardware solution (i.e. sensor precursor configuration) for measuring $AFR_{rel}$ in the region of the spark plug in $H_2$ SI engines, the new procedure has the advantage of being more easily implemented, as it entails monitoring the spectrum in the visible range, which requires less costly optics.

# References


[1] IEA (2023), World Energy Outlook 2023, IEA, Paris https://www.iea.org/reports/world-energy-outlook-2023, Licence: CC BY 4.0 (report); CC BY NC SA 4.0 (Annex A).

[2] Energy Institute Statistical Review of World Energy 2024 , https://www.energyinst.org/statistical-review.

[3] Zauli-Sajani, S., Thunis, P., Pisoni, E. et al. Reducing biomass burning is key to decrease PM2.5 exposure in European cities. Sci Rep 14, 10210 (2024). https://doi.org/10.1038/s41598-024-60946-2

[4] Britannica, The Editors of Encyclopaedia. "Indian Ocean tsunami of 2004". Encyclopedia Britannica, 4 May. 2024, https://www.britannica.com/event/Indian-Ocean-tsunami-of-2004. Accessed 8 July 2024.

[5] PwC, Green hydrogen economy – predicted development of tomorrow, https://www.pwc.com/gx/en/industries/energy-utilities-resources/future-energy/green-hydrogen-cost.html. Accessed 10 July 2024.

[6] Züttel, Andreas, Louis Schlapbach, and Andreas Borgschulte. "History of hydrogen." Hydrogen as a Future Energy Carrier (2008): 7-21.

[7] Hoffmann, P. (1982). The Forever Fuel: The Story Of Hydrogen (1st ed.). Routledge. https://doi.org/10.4324/9780429311000.

[8] Levi, J. and Kittelson, D., "Further Studies with a Hydrogen Engine," SAE Technical Paper 780233, 1978, https://doi.org/10.4271/780233.

[9] Adt, Jr., R. R., et al. "Hydrogen engine performance analysis. First annual report." , Aug. 1978. https://doi.org/10.2172/6350586.

[10] J. O'M. Bockris, A Hydrogen Economy. Science176, 1323-1323 (1972) .DOI:10.1126/science.176.4041.1323.

[11] Roman J. Hennig, Laurens J. de Vries, Simon H. Tindemans, Risk vs. restriction—An investigation of capacity-limitation based congestion management in electric distribution grids, Energy Policy, Volume 186, 2024, 113976, ISSN 0301 4215, https://doi.org/10.1016/j.enpol.2023.113976.

[12] Felix Schreyer, Falko Ueckerdt, Robert Pietzcker, Renato Rodrigues, Marianna Rottoli, Silvia Madeddu, Michaja Pehl, Robin Hasse, Gunnar Luderer, Distinct roles of direct and indirect electrification in pathways to a renewables-dominated European energy system, One Earth, Volume 7, Issue 2, 2024, Pages 226-241, ISSN 2590-3322, https://doi.org/10.1016/j.oneear.2024.01.015.

[13] Durkin, K.; Khanafer, A.; Liseau, P.; Stjernström-Eriksson, A.; Svahn, A.; Tobiasson, L.; Andrade, T.S.; Ehnberg, J. Hydrogen-Powered Vehicles: Comparing the Powertrain Efficiency and Sustainability of Fuel

Cell versus Internal Combustion Engine Cars. Energies 2024, 17, 1085. https://doi.org/10.3390/en17051085.

[14] G.J. Offer, D. Howey, M. Contestabile, R. Clague, N.P. Brandon, Comparative analysis of battery electric, hydrogen fuel cell and hybrid vehicles in a future sustainable road transport system, Energy Policy, Volume 38, Issue 1, 2010, Pages 24-29, ISSN 0301-4215, https://doi.org/10.1016/j.enpol.2009.08.040.

[15] Pearson, G., Leary, M., Subic, A., Wellnitz, J. (2011). Performance Comparison of Hydrogen Fuel Cell and Hydrogen Internal Combustion Engine Racing Cars. In: Hung, S., Subic, A., Wellnitz, J. (eds) Sustainable Automotive Technologies 2011. Springer, Berlin, Heidelberg. https://doi.org/10.1007/978-3-642-19053-7_11.

[16] Christopher Depcik, Truman Cassady, Bradley Collicott, et al, Comparison of lithium ion Batteries, hydrogen fueled combustion Engines, and a hydrogen fuel cell in powering a small Unmanned Aerial Vehicle, Energy Conversion and Management, Volume 207, 2020, 112514, ISSN 0196-8904, https://doi.org/10.1016/j.enconman.2020.112514.

[17] Nisa Nur Atak, Battal Dogan, Murat Kadir Yesilyurt, Investigation of the performance parameters for a PEMFC by thermodynamic analyses: Effects of operating temperature and pressure, Energy, Volume 282, 2023, 128907, ISSN 0360-5442, https://doi.org/10.1016/j.energy.2023.128907.

[18] Hong Wei, Zhen Hu, Junjie Ma, Wenzhong Ma, Shuang Yuan, Yinuo Hu, Ke Hu, Lei Zhou, Haiqiao Wei, Experimental study of thermal efficiency and NOx emission of turbocharged direct injection hydrogen engine based on a high injection pressure, International Journal of Hydrogen Energy, Volume 48, Issue 34, 2023, Pages 12905-12916, ISSN 0360-3199, https://doi.org/10.1016/j.ijhydene.2022.12.031.

[19] Ujwal Shreenag Meda, Nidhi Bhat, Aditi Pandey, K.N. Subramanya, M.A. Lourdu Antony Raj, Challenges associated with hydrogen storage systems due to the hydrogen embrittlement of high strength steels, International Journal of Hydrogen Energy, Volume 48, Issue 47, 2023, Pages 17894-17913, ISSN 0360-3199, https://doi.org/10.1016/j.ijhydene.2023.01.292.

[20] C.L. Tang, Z.H. Huang, C.K. Law, Determination, correlation, and mechanistic interpretation of effects of hydrogen addition on laminar flame speeds of hydrocarbon–air mixtures, Proceedings of the Combustion Institute, Volume 33, Issue 1, 2011, Pages 921-928, ISSN 1540-7489, https://doi.org/10.1016/j.proci.2010.05.039.

[21] Morovatiyan, Mohammadrasool, et al. "Effect of argon concentration on laminar burning velocity and flame speed of hydrogen mixtures in a constant volume combustion chamber." Journal of Energy Resources Technology 143.3 (2021): 032301. https://doi.org/10.1115/1.4048019

[22] F. Halter, C. Chauveau, N. Djebaïli-Chaumeix, I. Gökalp, Characterization of the effects of pressure and hydrogen concentration on laminar burning velocities of methane–hydrogen–air mixtures, Proceedings of the Combustion Institute, Volume 30, Issue 1, 2005, Pages 201-208, ISSN 1540-7489, https://doi.org/10.1016/j.proci.2004.08.195.

[23] Wu Gu, Xiao Liu, Zhiqiang Wang, Hongtao Zheng, Applications of PLIF in fundamental research on turbulent combustion of hydrogen and hydrogen hybrid fuels: A brief review, International Journal of Hydrogen Energy, Volume 78, 2024, Pages 1240-1274, ISSN 0360-3199, https://doi.org/10.1016/j.ijhydene.2024.06.350.

[24] Gürbüz, Habib, and Dinçer Buran. "Experimental study on the effect of concentrated turbulence around the spark plug zone in a swirling flow on a hydrogen SI engine performance and combustion parameters." Journal of Energy Engineering 142.3 (2016): 04015031. https://doi.org/10.1061/(ASCE)EY.1943-7897.0000297.

[25] A. Hamzehloo, P.G. Aleiferis, Large eddy simulation of highly turbulent under-expanded hydrogen and methane jets for gaseous-fuelled internal combustion engines, International Journal of Hydrogen Energy, Volume 39, Issue 36, 2014, Pages 21275-21296, ISSN 0360-3199, https://doi.org/10.1016/j.ijhydene.2014.10.016.

[26] Sören Krebs, Clemens Biet, Predictive model of a premixed, lean hydrogen combustion for internal combustion engines, Transportation Engineering, Volume 5, 2021, 100086, ISSN 2666-691X, https://doi.org/10.1016/j.treng.2021.100086.

[27] Jian An, Hanyi Wang, Bing Liu, Kai Hong Luo, Fei Qin, Guo Qiang He, A deep learning framework for hydrogen-fueled turbulent combustion simulation, International Journal of Hydrogen Energy, Volume 45, Issue 35, 2020, Pages 17992-18000, ISSN 0360-3199, https://doi.org/10.1016/j.ijhydene.2020.04.286.

[28] Biernat, K.; Samson-Bręk, I.; Chłopek, Z.; Owczuk, M.; Matuszewska, A. Assessment of the Environmental Impact of Using Methane Fuels to Supply Internal Combustion Engines. Energies 2021, 14, 3356. https://doi.org/10.3390/en14113356.

[29] M.I. Khan, T. Yasmeen, A. Shakoor, Niaz Bahadur Khan, Muhammad Wakeel, Bin Chen, Exploring the potential of compressed natural gas as a viable fuel option to sustainable transport: A bibliography (2001–2015), Journal of Natural Gas Science and Engineering, Volume 31, 2016, Pages 351-381, ISSN 1875-5100, https://doi.org/10.1016/j.jngse.2016.03.025.

[30] Valentino Cruccolini, Gabriele Discepoli, Alessandro Cimarello, Michele Battistoni, Francesco Mariani, Carlo Nazareno Grimaldi, Massimo Dal Re,Lean combustion analysis using a corona discharge igniter in an optical engine fueled with methane and a hydrogen-methane blend,Fuel,Volume 259,2020,116290,ISSN 0016-2361, https://doi.org/10.1016/j.fuel.2019.116290.

[31] Christina Ingo, Jessica Tuuf, Margareta Björklund-Sänkiaho, Experimental study of the performance of a SI-engine fueled with hydrogen-natural gas mixtures, International Journal of Hydrogen Energy, Volume 63, 2024, Pages 1036-1043, ISSN 0360-3199, https://doi.org/10.1016/j.ijhydene.2024.03.252.

[32] Mansour Keshavarzzadeh, Rahim Zahedi, Reza Eskandarpanah, Sajad Qezelbigloo, Siavash Gitifar, Omid Noudeh Farahani, Amir Mohammad Mirzaei, Estimation of NOx pollutants in a spark engine fueled by mixed methane and hydrogen using neural networks and genetic algorithm, Heliyon, Volume 9, Issue 4, 2023, e15304, ISSN 2405-8440, https://doi.org/10.1016/j.heliyon.2023.e15304.

[33] V. Cruccolini, G. Discepoli, A. Cimarello, M. Battistoni, F. Mariani, C. N. Grimaldi, M. Dal Re, Lean combustion analysis using a corona discharge igniter in an optical engine fueled with methane and a hydrogen-methane blend, Fuel, Volume 259, 2020, 116290, ISSN 0016-2361, https://doi.org/10.1016/j.fuel.2019.116290.

[34] S. Di Iorio, P. Sementa, and B. M. Vaglieco, "Analysis of combustion of methane and hydrogen–methane blends in small DI SI (direct injection spark ignition) engine using advanced diagnostics," Energy, vol. 108, 2016

[35] X. Yu, Y. Du, P. Sun, L. Liu, H. Wu, and X. Zuo, "Effects of hydrogen direct injection strategy on characteristics of lean-burn hydrogen–gasoline engines," Fuel, vol. 208, 2017.

[36] Bo Zhang, Shuofeng Wang, Yifan Zhai, Estimating the charge burning velocity within a hydrogen-enriched gasoline engine, International Journal of Hydrogen Energy, Volume 48, Issue 27, 2023, Pages 10264-10271, ISSN 0360-3199, https://doi.org/10.1016/j.ijhydene.2022.12.154.

[37] Pucillo, Francesco, et al. Turbocharging System Selection for a Hydrogen-Fuelled Spark-Ignition Internal Combustion Engine for Heavy-Duty Applications. No. 2024-01-3019. SAE Technical Paper, 2024. https://doi.org/10.4271/2024-01-3019.

[38] Misul, D.A.; Scopelliti, A.; Baratta, M. High-Performance Hydrogen-Fueled Internal Combustion Engines: Feasibility Study and Optimization via 1D-CFD Modeling. Energies 2024, 17, 1593. https://doi.org/10.3390/en17071593.

[39] Onur Barış, İlker Güler, Anıl Yaşgül, The effect of different charging concepts on hydrogen fuelled internal combustion engines, Fuel, Volume 343, 2023, 127983, ISSN 0016-2361, https://doi.org/10.1016/j.fuel.2023.127983.

[40] Ricci, F.; Zembi, J.; Avana, M.; Grimaldi, C.N.; Battistoni, M.; Papi, S. Analysis of Hydrogen Combustion in a Spark Ignition Research

Engine with a Barrier Discharge Igniter. Energies 2024, 17, 1739. https://doi.org/10.3390/en17071739.

[41] Arsie, I.; Battistoni, M.; Brancaleoni, P.P.; Cipollone, R.; Corti, E.; Di Battista, D.; Millo, F.; Occhicone, A.; Peiretti Paradisi, B.; Rolando, L.; et al. A New Generation of Hydrogen-Fueled Hybrid Propulsion Systems for the Urban Mobility of the Future. Energies 2024, 17, 34. https://doi.org/10.3390/en17010034.

[42] E. Distaso, R. Amirante, G. Calò, P. De Palma, P. Tamburrano, R.D. Reitz, Predicting lubricant oil induced pre-ignition phenomena in modern gasoline engines: The reduced GasLube reaction mechanism, Fuel, Volume 281, 2020, 118709, ISSN 0016-2361, https://doi.org/10.1016/j.fuel.2020.118709.

[43] De Renzis, E., Mariani, V., Bianchi, G., Cazzoli, G. et al., "A Numerical Methodology to Test the Lubricant Oil Evaporation and Its Thermal Management-Related Properties Derating in Hydrogen-Fueled Engines," SAE Int. J. Engines 17(2):255-267, 2024, https://doi.org/10.4271/03-17-02-0015.

[44] A. Irimescu, S. Merola, B. M. Vaglieco, and V. Zollo, Conversion of a Small Size Passenger Car to Hydrogen Fueling: 0D/1D Simulation of Port- vs Direct-Injection and Boosting Requirements, SAE Technicals, New York, NY, USA, 2023

[45] Masakuni Oikawa, Yoshihisa Kojiya, Ryota Sato, Keisuke Goma, Yasuo Takagi, Yuji Mihara, Effect of supercharging on improving thermal efficiency and modifying combustion characteristics in lean-burn direct-injection near-zero-emission hydrogen engines, International Journal of Hydrogen Energy, Volume 47, Issue 2, 2022, Pages 1319-1327, ISSN 0360-3199, https://doi.org/10.1016/j.ijhydene.2021.10.061.

[46] Karsten Wittek, Vitor Cogo, Geovane Prante, Development of a pneumatic actuated low-pressure direct injection gas injector for hydrogen-fueled internal combustion engines, International Journal of Hydrogen Energy, Volume 48, Issue 27, 2023, Pages 10215-10234, ISSN 0360-3199, https://doi.org/10.1016/j.ijhydene.2022.12.023.

[47] MohammadReza Yosri, Rahul Palulli, Mohsen Talei, Joel Mortimer, Farzad Poursadegh, Yi Yang, Michael Brear, Numerical investigation of a large bore, direct injection, spark ignition, hydrogen-fuelled engine, International Journal of Hydrogen Energy, Volume 48, Issue 46, 2023, Pages 17689-17702, ISSN 0360-3199, https://doi.org/10.1016/j.ijhydene.2023.01.228.

[48] Cheng Shi, Changwei Ji, Shuofeng Wang, Jinxin Yang, Zedong Ma, Yunshan Ge, Combined influence of hydrogen direct-injection pressure and nozzle diameter on lean combustion in a spark-ignited rotary engine, Energy Conversion and Management, Volume 195, 2019, Pages

1124-1137, ISSN 0196-8904, https://doi.org/10.1016/j.enconman.2019.05.095.
[49] Zeldovich, Y., 2014. Oxidation of nitrogen in combustion and explosions. Selected Works of Yakov Borisovich ZeldovichVolume I. Princeton University Press, https://doi.org/10.1515/9781400862979.404.
[50] Malte, P., Pratt, D., 1975. Measurement of atomic oxygen and nitrogen oxides in jet-stirred combustion. Symp. (Int.) Combust 15, 1061–1070. https://doi.org/10.1016/S0082-0784(75)80371-7.
[51] C.P. Fenimore, Formation of nitric oxide in premixed hydrocarbon flames, Symposium (International) on Combustion, Volume 13, Issue 1, 1971, Pages 373-380, ISSN 0082-0784, https://doi.org/10.1016/S0082-0784(71)80040-1.
[52] Anmol L. Purohit, Armen Nalbandyan, Philip C. Malte, Igor V. Novosselov, NNH mechanism in low-NOx hydrogen combustion: Experimental and numerical analysis of formation pathways,Fuel, Volume 292, 2021, 120186, ISSN 0016-2361, https://doi.org/10.1016/j.fuel.2021.120186.
[53] Liu S, Li H, Liew C, Gatts T, Wayne S, Shade B, et al. An experimental investigation of NO2 emission characteristics of a heavy-duty H2-diesel dual fuel engine. Int J Hydrogen Energ 2011;36(18):12015–24.
[54] Ling-zhi Bao, Bai-gang Sun, Qing-he Luo, Experimental investigation of the achieving methods and the working characteristics of a near-zero NOx emission turbocharged direct-injection hydrogen engine, Fuel, Volume 319, 2022, 123746, ISSN 0016-2361, https://doi.org/10.1016/j.fuel.2022.123746.
[55] Rajasegar, R., Srna, A., Barbery, I., and Novella, R., "On the Phenomenology of Hot-Spot Induced Pre-Ignition in a Direct-Injection Hydrogen-Fuelled, Heavy-Duty, Optical-Engine," SAE Int. J. Adv. & Curr. Prac. in Mobility 6(3):1535-1547, 2024, https://doi.org/10.4271/2023-32-0169.
[56] Shuman Guo, Jiahui Liu, Chuanhao Zhao, Lijun Wang, Zhenzhong Yang, Research on pre-ignition in hydrogen internal combustion engines based on characteristic parameters of hot spot, International Journal of Hydrogen Energy, Volume 65, 2024, Pages 548-554, ISSN 0360-3199, https://doi.org/10.1016/j.ijhydene.2024.03.375.
[57] Akshey Marwaha, K.A. Subramanian, Experimental investigation on backfire occurrence, duration and termination in a hydrogen-fueled automotive spark ignition engine, Process Safety and Environmental Protection, Volume 189, 2024, Pages 322-342, ISSN 0957-5820, https://doi.org/10.1016/j.psep.2024.06.091.
[58] Ahmad Hilmi Khalid, Mohd Farid Muhamad Said, Ibham Veza, Mohd Azman Abas, Muhammad Faizullizam Roslan, Shitu Abubakar, M.R. Jalal, Hydrogen port fuel injection: Review of fuel injection control

strategies to mitigate backfire in internal combustion engine fuelled with hydrogen, International Journal of Hydrogen Energy, Volume 66, 2024, Pages 571-581, ISSN 0360-3199, https://doi.org/10.1016/j.ijhydene.2024.04.087.

[59] Eicheldinger S, Karmann S, Prager M, Wachtmeister G. Optical screening investigations of backfire in a large bore medium speed hydrogen engine. International Journal of Engine Research. 2022;23(5): 893-906. https://doi.org/10.1177/14680874211053171.

[60] Jiaqing He, Erdem Kokgil, Liangzhu (Leon) Wang, Hoi Dick Ng, Assessment of similarity relations using helium for prediction of hydrogen dispersion and safety in an enclosure, International Journal of Hydrogen Energy, Volume 41, Issue 34, 2016, Pages 15388-15398, ISSN 0360-3199, https://doi.org/10.1016/j.ijhydene.2016.07.033.

[61] Stella G. Giannissi, Ilias C. Tolias, Daniele Melideo, Daniele Baraldi, Volodymyr Shentsov, Dmitriy Makarov, Vladimir Molkov, Alexandros G. Venetsanos, On the CFD modelling of hydrogen dispersion at low-Reynolds number release in closed facility, International Journal of Hydrogen Energy, Volume 46, Issue 57, 2021, Pages 29745-29761, ISSN 0360-3199, https://doi.org/10.1016/j.ijhydene.2020.09.078.

[62] Aryadutt Oamjee, Rajesh Sadanandan, Suitability of helium gas as surrogate fuel for hydrogen in H2-Air non-reactive supersonic mixing studies, International Journal of Hydrogen Energy, Volume 47, Issue 15, 2022, Pages 9408-9421, ISSN 0360-3199, https://doi.org/10.1016/j.ijhydene.2022.01.022.

[63] Erdem, E.; Kontis, K.; Saravanan, S. Penetration Characteristics of Air, Carbon Dioxide and Helium Transverse Sonic Jets in Mach 5 Cross Flow. Sensors 2014, 14, 23462-23489. https://doi.org/10.3390/s141223462.

[64] Nikolay A. Vinnichenko, Aleksei V. Pushtaev, Yulia Yu. Plaksina, Alexander V. Uvarov, Performance of Background Oriented Schlieren with different background patterns and image processing techniques, Experimental Thermal and Fluid Science, Volume 147, 2023, 110934, ISSN 0894-1777, https://doi.org/10.1016/j.expthermflusci.2023.110934.

[65] Scarano, Fulvio. "Tomographic PIV: principles and practice." Measurement Science and Technology 24.1 (2012): 012001, https://doi.org/10.1088/0957-0233/24/1/012001.

[66] Gary S. Settles, Alex Liberzon, Schlieren and BOS velocimetry of a round turbulent helium jet in air, Optics and Lasers in Engineering, Volume 156, 2022, 107104, ISSN 0143-8166, https://doi.org/10.1016/j.optlaseng.2022.107104.

[67] Wanstall, C.T., Bittle, J.A. & Agrawal, A.K. Quantitative concentration measurements in a turbulent helium jet using rainbow

schlieren deflectometry. Exp Fluids 62, 53 (2021). https://doi.org/10.1007/s00348-021-03154-2.

[68] Joschka M. Schulz, Henning Junne, Lutz Böhm, Matthias Kraume, Measuring local heat transfer by application of Rainbow Schlieren Deflectometry in case of different symmetric conditions, Experimental Thermal and Fluid Science, Volume 110, 2020, 109887, ISSN 0894-1777, https://doi.org/10.1016/j.expthermflusci.2019.109887.

[69] M. Angioletti, E. Nino, G. Ruocco, CFD turbulent modelling of jet impingement and its validation by particle image velocimetry and mass transfer measurements, International Journal of Thermal Sciences, Volume 44, Issue 4, 2005, Pages 349-356, ISSN 1290-0729, https://doi.org/10.1016/j.ijthermalsci.2004.11.010.

[70] Lukas Metzger, Matthias Kind, On the transient flow characteristics in Confined Impinging Jet Mixers - CFD simulation and experimental validation, Chemical Engineering Science, Volume 133, 2015, Pages 91-105, ISSN 0009-2509, https://doi.org/10.1016/j.ces.2014.12.056.

[71] Bruchhausen, M., Guillard, F. & Lemoine, F. Instantaneous measurement of two-dimensional temperature distributions by means of two-color planar laser induced fluorescence (PLIF). Exp Fluids 38, 123–131 (2005). https://doi.org/10.1007/s00348-004-0911-2.

[72] Turner JS. The 'starting plume' in neutral surroundings. Journal of Fluid Mechanics. 1962;13(3):356-368. https://doi:10.1017/S0022112062000762.

[73] Zhao, Jianhui, Weilong Liu, and You Liu. "Experimental investigation on the microscopic characteristics of underexpanded transient hydrogen jets." International Journal of Hydrogen Energy 45.33 (2020): 16865-16873. https://doi.org/10.1016/j.ijhydene.2020.04.140.

[74] Wang, Xi, et al. "Visualization research on hydrogen jet characteristics of an outward-opening injector for direct injection hydrogen engines." Fuel 280 (2020): 118710. https://doi.org/10.1016/j.fuel.2020.118710.

[75] Paul C. Miles, 2014, THE HISTORY AND EVOLUTION OF OPTICALLY ACCESSIBLE RESEARCH ENGINES, Sandia National Laboratories.

[76] Bowditch, F.W., "Cylinder and Piston Assembly," in US Patent App. 2,919,688, 2,919,688.

[77] Cecere, G.; Irimescu, A.; Merola, S.S.; Rolando, L.; Millo, F. Lean Burn Flame Kernel Characterization for Different Spark Plug Designs and Orientations in an Optical GDI Engine. *Energies* **2022**, *15*, 3393. https://doi.org/10.3390/en15093393.

[78] Cecere, G., et al. "Effect of coil charge duration on combustion variability and flame morphology in a GDI engine working in lean burn

conditions." Journal of Physics: Conference Series. Vol. 2385. No. 1. IOP Publishing, 2022. https://doi.10.1088/1742-6596/2385/1/012082.

[79] Dongchan Kim, Quancen Wan, Qing Nian Chan, Yoshimitsu Kobashi, Nobuyuki Kawahara, Sanghoon Kook, Hydrogen concentration measurements using spark induced breakdown spectroscopy in a real engine, Proceedings of the Combustion Institute, Volume 40, Issues 1–4, 2024, 105209, ISSN 1540-7489, https://doi.org/10.1016/j.proci.2024.105209.

[80] Kawahara, N.; Tomita, E.; Takemoto, S.; Ikeda, Y. Fuel concentration measurement of premixed mixture using spark-induced breakdown spectroscopy. Spectrochim. Acta Part B At. Spectrosc. 2009, 64, 1085–1092. https://doi.org/10.1016/j.sab.2009.07.016

[81] Rahman, K.M.; Kawahara, N.; Matsunaga, D.; Tomita, E.; Takagi, Y.; Mihara, Y. Local fuel concentration measurement through spark-induced breakdown spectroscopy in a direct-injection hydrogen spark-ignition engine. Int. J. Hydrog. Energy 2016, 41, 14283–14292. https://doi.org/10.1016/j.ijhydene.2016.05.280

[82] M. Balmelli, L. Merotto, Y. Wright, D. Bleiner, J. Biela, P. Soltic, Optical and thermodynamic investigation of jet-guided spark ignited hydrogen combustion, International Journal of Hydrogen Energy, Volume 78, 2024, Pages 1316-1331, ISSN 0360-3199, https://doi.org/10.1016/j.ijhydene.2024.06.221.

[83] Irimescu, A., Merola, S., and Martinez, S., “Influence of Engine Speed and Injection Phasing on Lean Combustion for Different Dilution Rates in an Optically Accessible Wall-Guided Spark Ignition Engine,” SAE Int. J. Engines 11(6):1343–1369, 2018, doi:10.4271/2018-01-1421.

[84] Simona Silvia Merola, Silvana Di Iorio, Adrian Irimescu, Paolo Sementa, Bianca Maria Vaglieco, Spectroscopic characterization of energy transfer and thermal conditions of the flame kernel in a spark ignition engine fueled with methane and hydrogen, International Journal of Hydrogen Energy, Volume 42, Issue 18, 2017, Pages 13276-13288, ISSN 0360-3199, https://doi.org/10.1016/j.ijhydene.2017.03.219.

[85] T. Kammermann, W. Kreutner, M. Trottmann, L. Merotto, P. Soltic, D. Bleiner, Spark-induced breakdown spectroscopy of methane/air and hydrogen-enriched methane/air mixtures at engine relevant conditions, Spectrochimica Acta Part B: Atomic Spectroscopy, Volume 148, 2018, Pages 152-164, ISSN 0584-8547, https://doi.org/10.1016/j.sab.2018.06.013.

[86] S. Breda, F. D'Orrico, F. Berni, A. d'Adamo, S. Fontanesi, A. Irimescu, S.S. Merola, Experimental and numerical study on the adoption of split injection strategies to improve air-butanol mixture formation in a DISI optical engine, Fuel, Volume 243, 2019, Pages 104-124, ISSN 0016-2361, https://doi.org/10.1016/j.fuel.2019.01.111.

[87] Merola, Simona Silvia, et al. "Effect of the fuel-injection strategy on flame-front evolution in an optical wall-guided DISI engine with

gasoline and butanol fueling." Journal of Energy Engineering 142.2 (2016): E4015004. https://doi.org/10.1061/(ASCE)EY.1943-7897.00003.

[88] Tambasco, C., Hall, M., and Matthews, R., "Spark Discharge Characteristics for Varying Spark Plug Geometries and Gas Compositions," SAE Technical Paper 2022-01-0437, 2022, https://doi.org/10.4271/2022-01-0437.

[89] Ahmed A. Abdel-Rehim, Impact of spark plug number of ground electrodes on engine stability, Ain Shams Engineering Journal, Volume 4, Issue 2, 2013, Pages 307-316, ISSN 2090-4479, https://doi.org/10.1016/j.asej.2012.09.006.

[90] Lee, Y. G., and J. T. Boehler. “Flame Kernel Development and Its Effects on Engine Performance with Various Spark Plug Electrode Configurations.” SAE Transactions, vol. 114, 2005, pp. 1001–14. JSTOR, http://www.jstor.org/stable/44722059. Accessed 30 Aug. 2024.

[91] Heywood, J.B. Internal Combustion Engine Fundamentals. McGraw Hill. New York, USA, 1988.

[92] Irimescu, A., Cecere, G., and Sementa, P., “Combustion Phasing Indicators for Optimized Spark Timing Settings for Methane Hydrogen Powered Small Size Engines,” SAE Technical Paper 2022-01-0603, 2022, doi:10.4271/2022-01-0603.

[93] G.M. Kosmadakis, D.C. Rakopoulos, C.D. Rakopoulos, Assessing the cyclic-variability of spark-ignition engine running on methane-hydrogen blends with high hydrogen contents of up to 50%, International Journal of Hydrogen Energy, Volume 46, Issue 34, 2021, Pages 17955-17968, ISSN 0360-3199, https://doi.org/10.1016/j.ijhydene.2021.02.158.

[94] Fanhua Ma, Yu Wang, Haiquan Liu, Yong Li, Junjun Wang, Shangfen Ding, Effects of hydrogen addition on cycle-by-cycle variations in a lean burn natural gas spark-ignition engine, International Journal of Hydrogen Energy, Volume 33, Issue 2, 2008, Pages 823-831, ISSN 0360-3199, https://doi.org/10.1016/j.ijhydene.2007.10.043.

[95] Ravi, K., et al. "Effects of spark plug configuration on combustion and emission characteristics of a LPG fuelled lean burn SI engine." IOP Conference Series: Materials Science and Engineering. Vol. 263. No. 6. IOP Publishing, 2017, DOI: 10.1088/1757-899X/263/6/062070.

[96] Oğuz Baş, Mustafa Atakan Akar, Hasan Serin, Mustafa Özcanlı, Erdi Tosun, Variation of spark plug type and spark gap with hydrogen and methanol added gasoline fuel: Performance characteristics, International Journal of Hydrogen Energy, Volume 45, Issue 50, 2020, Pages 26513-26521, ISSN 0360-3199, https://doi.org/10.1016/j.ijhydene.2020.03.110.

[97] Tawfik Badawy, XiuChao Bao, Hongming Xu, Impact of spark plug gap on flame kernel propagation and engine performance, Applied Energy, Volume 191, 2017, Pages 311-327, ISSN 0306-2619, https://doi.org/10.1016/j.apenergy.2017.01.059.

[98] Oliveira, C., Reis, J. L., Souza-Corrêa, J. A., Dal Pino, A., & Amorim, J. (2012). Optical and electrical diagnostics of a spark-plug discharge in air. Journal of Physics D: Applied Physics, 45(25), 255201.

[99] Martinez, S.; Irimescu, A.; Merola, S.S.; Lacava, P.; Curto-Riso, P. Flame Front Propagation in an Optical GDI Engine under Stoichiometric and Lean Burn Conditions. Energies 2017, 10, 1337. https://doi.org/10.3390/en10091337.

[100] Ley, Hood-Hong. "Analytical methods in plasma diagnostic by optical emission spectroscopy: A tutorial review." Journal of Science and Technology 6.1 (2014).

[101] Shicong Wang, Amy E. Wendt, John B. Boffard, Chun C. Lin, Svetlana Radovanov, Harold Persing; Noninvasive, real-time measurements of plasma parameters via optical emission spectroscopy. J. Vac. Sci. Technol. A 1 March 2013; 31 (2): 021303. https://doi.org/10.1116/1.4792671.

[102] Greenfield, S., et al. "High-pressure plasma as spectroscopic emission sources." Analyst 114.11 (1989): 1357-1357. DOI https://doi.org/10.1039/AN9891401357.

[103] Hunter, A. J. R., Morency, J. R., Senior, C. L., Davis, S. J., & Fraser, M. E. (2000). Continuous Emissions Monitoring Using Spark-Induced Breakdown Spectroscopy. Journal of the Air & Waste Management Association, 50(1), 111–117. https://doi.org/10.1080/10473289.2000.10463982.

[104] John P. Walters ,Spark Discharge: Application Multielement Spectrochemical Analysis.Science198,787-797(1977). DOI:10.1126/science.198.4319.787.

[105] Sharath Nagaraja, Vigor Yang, Zhiyao Yin, Igor Adamovich, Ignition of hydrogen–air mixtures using pulsed nanosecond dielectric barrier plasma discharges in plane-to-plane geometry, Combustion and Flame, Volume 161, Issue 4, 2014, Pages 1026-1037, ISSN 0010-2180, https://doi.org/10.1016/j.combustflame.2013.10.007.

[106] Park, J.H., Pfender, E. & Chang, C.H. Reduction of Chemical Reactions in Nitrogen and Nitrogen–Hydrogen Plasma Jets Flowing into Atmospheric Air. Plasma Chemistry and Plasma Processing 20, 165–181 (2000). https://doi.org/10.1023/A:1007087105887.

[107] Wiese, W. L., Kelleher, D. E., & Paquette, D. R. (1972). Detailed study of the Stark broadening of Balmer lines in a high-density plasma. Physical Review A, 6(3), 1132. https://doi.org/10.1103/PhysRevA.6.1132.

[108] Svanberg, Sune, and S. Svanberg. Atomic and molecular spectroscopy. Heidelberg: Springer-Verlag, 2001. https://doi.org/10.1007/978-3-031-04776-3.

[109] Minesi, Nicolas, et al. "Ionization mechanism in a thermal spark discharge." AIAA Scitech 2021 Forum. 2021. https://doi.org/10.2514/6.2021-1698.

[110] Billoux, Tommy, et al. "Calculation of the net emission coefficient of an air thermal plasma at very high pressure." Journal of Physics: Conference Series. Vol. 406. No. 1. IOP Publishing, 2012. DOI 10.1088/1742-6596/406/1/012010.

[111] Basics of plasma spectroscopy Plasma Sources Sci. Technol. 15 (2006) S137–S147 doi:10.1088/0963-0252/15/4/S01.

[112] Herzberg, G. (1989). Molecular spectra and molecular structure. 1. Spectra of diatomic molecules reprint of the 2nd edition.

[113] Bernath, Peter F. Spectra of atoms and molecules. Oxford university press, 2020.

[114] Jeong-Jeung Dang, Kyoung-Jae Chung, Y. S. Hwang; A simple spectroscopic method to determine the degree of dissociation in hydrogen plasmas with wide-range spectrometer. Rev. Sci. Instrum. 1 May 2016; 87 (5): 053503. https://doi.org/10.1063/1.4948919.

[115] Qin, Z., Zhao, J. M., & Liu, L. H. (2017). Radiative transition probabilities for the main diatomic electronic systems of N2, N2+, NO, O2, CO, CO+, CN, C2 and H2 produced in plasma of atmospheric entry. Journal of Quantitative Spectroscopy and Radiative Transfer, 202, 286-301. https://doi.org/10.1016/S0022-4073(01)00141-8.

[116] Watson, J. K. G., Majewski, W. A., & Glownia, J. H. (1986). Assignment of the Schuster band of ammonia. Journal of Molecular Spectroscopy, 115(1), 82-87. https://doi.org/10.1016/0022-2852(86)90277-8.

[117] de Izarra, G., & Cormier, J. M. (2013). New methods to determine temperatures from UV OH spectrum. Journal of Physics D: Applied Physics, 46(10), 105503. doi:10.1088/0022-3727/46/10/105503.

[118] Reza, A.M. Realization of the Contrast Limited Adaptive Histogram Equalization (CLAHE) for Real-Time Image Enhancement. The Journal of VLSI Signal Processing-Systems for Signal, Image, and Video Technology 38, 35–44 (2004). https://doi.org/10.1023/B:VLSI.0000028532.53893.82.

# Chapter 7

# Appendix A

## A.1 Research engine calibration and optical setup

Optical accessibility to the combustion chamber was ensured through a Bowditch extended piston (See 2.6 Optical technique for characterizing $H_2$ combustion). This entailed specific solutions that cannot include standard lubrication systems (e.g. with oil, as this would smear the quartz window); through a combination of larger liner-piston gap and the use of Teflon-bronze piston rings, oil-free operation can be achieved, with acceptable sealing and wear timeline. Increased blow-by is a drawback of this solution, but the advantage of high spatial resolution is far too important; commercial power units feature around 1-3% loss of in-cylinder charge during the working cycle, while for the engine used for the trials this parameter can be as high as 10%. One other particular detail is that piston rings are intrinsically protected by being fitted at a large distance from the combustion chamber. This also increases the top-land region, resulting in higher percentage of unburned charge. Such characteristics renders their 0D/1D and 3D CFD models quite challenging to implement, but again, the advantages offered by optical accessibility are of unparalleled importance, especially when considering the chemical species and their evolution during complex processes such as combustion. Figure A.1 shows two assemblies' representative of the current setup that was employed for the trials, compared to a commercial piston.

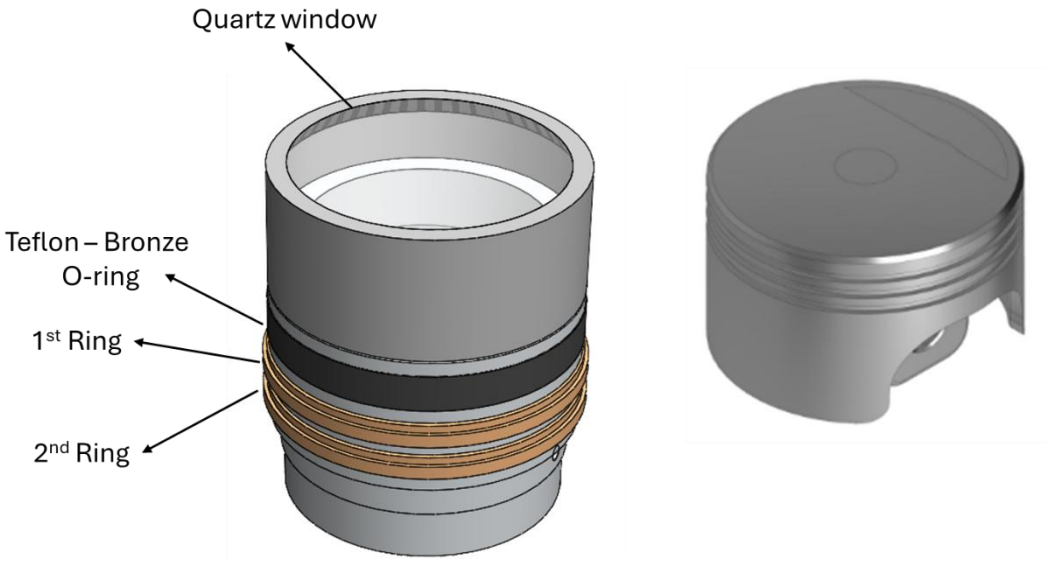


Figure A.1 Bowditch design piston (left) and conventional counterpart (right).

Another aspect that needs to be put into context when using hydrogen is that the aforementioned high tolerance tends to promote flame propagation into the top-land region. Even though the rings are fitted relatively far from the combustion chamber, $H_2$ flames can penetrate into the bottom part of the top-land region and interact with the piston rings. This phenomenon can increase piston rings wear, and the resulting particles can even be the source for abnormal combustion phenomena such as pre-ignition.

Figure A.2 shows the Teflon-bronze deposits on the quartz window observed after disassembling the engine for substituting the piston rings.


Figure A.2. Teflon – bronze deposits on the piston quartz window.

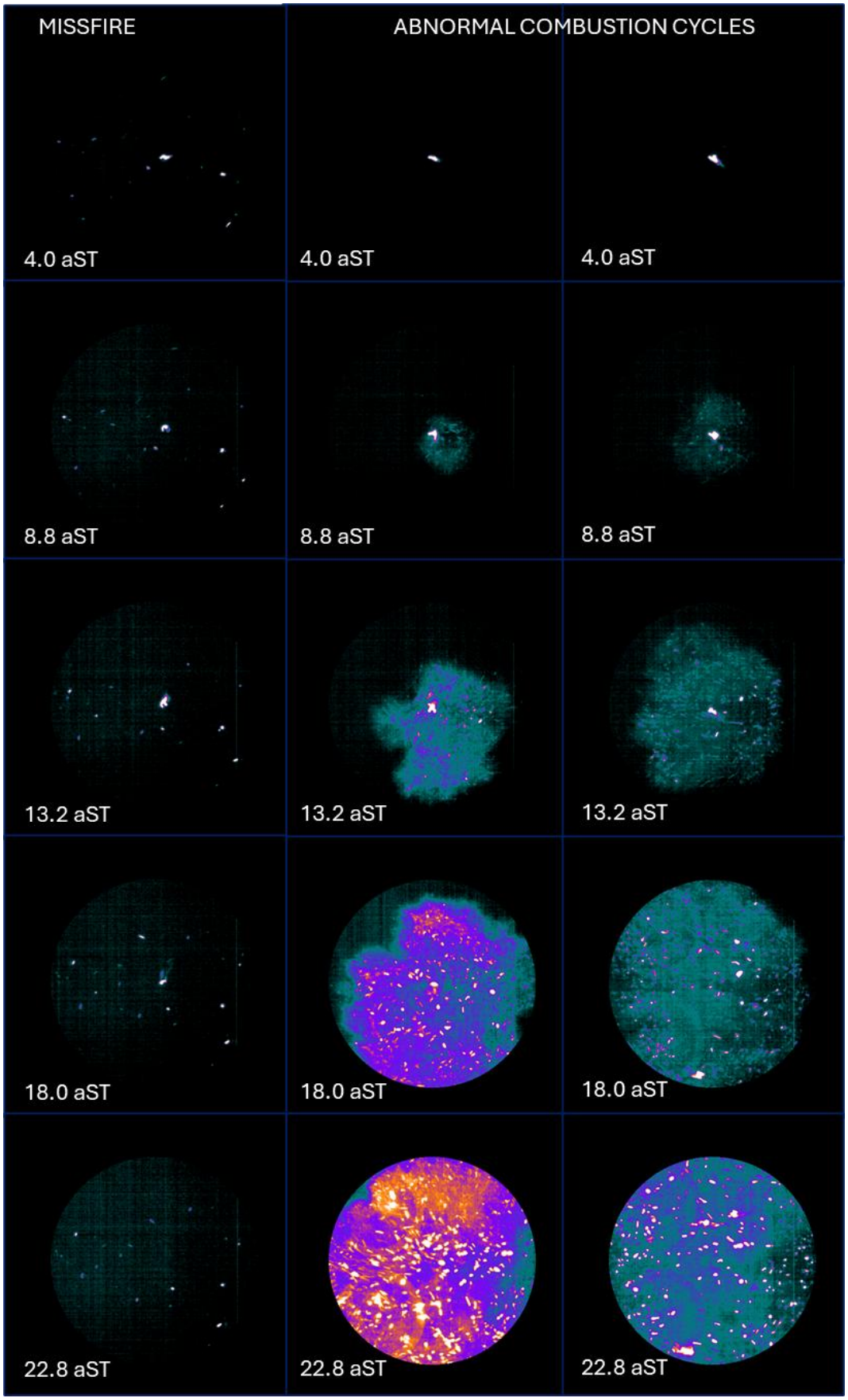

Figure A.3. Backfire – Misfire phenomena (left column) and subsequent knocking occurrence (middle – right columns).

Backfiring also has specific implications for the optical engine used for the experimental campaigns. Given the sudden pressure increase in the intake, deposits on the inner surface of the manifold most likely were detached and ingested by the cylinder. Evidence of these particles was observed directly in the recorded images, but also indirectly by lower AFR measured by the UEGO. Figure A.3 illustrates the recording of multiple cycles that start with backfiring, then several cycles with increased luminosity due to the presence of bright spots. These particles can easily result in other abnormal combustion phenomena such as pre-ignition.

A specific post-processing procedure was developed in the NI Vision environment for evaluating flame morphology when using $H_2$. This was required because the images recorded with the CMOS camera featured fairly low intensity (apart from abnormal combustion phenomena), even with the maximum opening of 2.8 f-stop of the objective. The steps are resumed in Figure A.4, which shows the improvement of the final image.

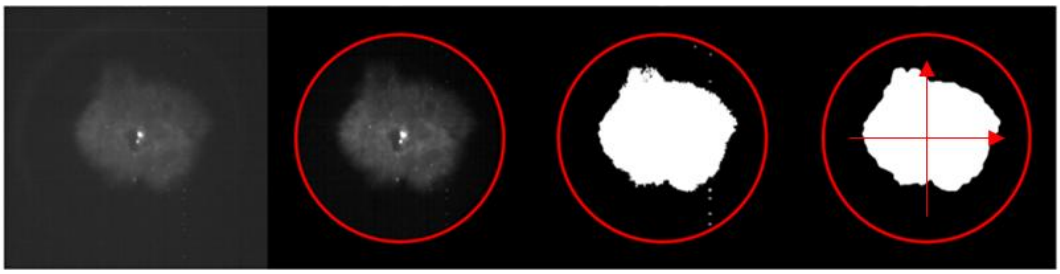

Figure A.4. Sequence of steps applied for image processing: original raw data, circular mask and gamma/brightness improvement, image binarization, FFT correction.

The first step of the procedure involved the application of a circular mask to the images, to limit the investigated area to the quartz window fitted on the piston top and to cut light from reflections at the boundaries of the optical access. The level of contrast, gamma and brightness were varied to improve the quality of the images and reach a suitable level of luminosity of the “foreground” for successive binarization. Then, the recognition of the flame object was obtained by applying a threshold level to separate the background from the investigated subject. In this phase, this parameter was chosen and fixed depending on the AFR. Then, each binary image was treated with a Fast Fourier Transform (FFT) filter to correct drifts and remove small objects out of the foreground. A morphological function enabled the evaluation of main area parameters, such as edge coordinates X-Y and flame object centroid with respect to the origin of the reference system fixed on

the spark plug axis. Finally, the centroid coordinates displacements along the Y-direction and X-direction were calculated.

## A.2 Optical emission spectroscopy

Optical emission spectroscopy (OES) is a consolidated methodology for detecting chemical species, including atoms and ions, that are generated in plasma ,independently if thermal or non-thermal [100] - [101]. There are several challenges to be faced when implementing OES, mainly due to the complexity of identifying the emitters due to overlapping of several spectral features corresponding to different excited states. When employed through the generation of a spark discharge, OES is commonly defined as Spark Induced Breakdown Spectroscopy (SIBS); it is applied for detecting radiative emissions specific for concomitant phenomena. This is particularly relevant when the plasma is induced in gaseous mixtures under high-pressure conditions [102]-[103]-[104].

In case of hydrogen plasma, chemical markers are largely investigated through experiments in thoroughly controlled environments [105]-[106]. Additionally, most of the results are obtained in low-density conditions in order to minimise the collisional quenching and self-absorption phenomena. These studies identified the spectral markers of hydrogen plasma in the Balmer lines [107]. A spectral line corresponds to a transition between the upper electronic level i and the lower level j and its intensity is given by $I_{ij}= \varepsilon\eta_{ij}A_{ij}h\nu_jN_i$ where $\eta_{ij}$ is function of the plasma volume and solid angle of observation, $\varepsilon$ is the spectral response of the optical system, $A_{ij}$ is the transition probability between the levels i and j, h is the Planck constant, $\nu_{ij}$ is the transition frequency, and $N_i$ is the population number density of the level i. Several vibrational and rotational levels can be associated to each electronic level, constituting the fine and hyperfine structure of the spectral line [108].

In the case of the Balmer lines, these are determined by the dissociative excitation of hydrogen molecules as a consequence of the collisions with high-energy electrons produced by the discharge:

$$e(\mathcal{E}_1) + H_2(X^1\textstyle\sum_g^+) \rightarrow H^*(n \geqslant 3) + H + e(\mathcal{E}_2)$$
$$H^*(n \geqslant 3) \rightarrow H^*(n = 2) + h\nu$$

The electron loses part of its energy for dissociating the hydrogen molecule into a ground state (H) and an excited state (n>2) atom (H*). Without further external supply of additional energy, a radiative transition to lower excited level (n=2) occurs. Specifically, the first lines of the Balmer series correspond to transition 3→ 2 (Hα at 656 nm), 4→ 2 (Hβ at 486 nm), 5→ 2 (Hγ at 434 nm). The line intensity ratio depends on the electron temperature and density. The transition probability of the Balmer line reduces from α→ β→ γ and so on. There are several other transitions that can occur between atomic levels of hydrogen, but they are characterized by wavelengths outside the spectral range of this work (See Figure A. 5).

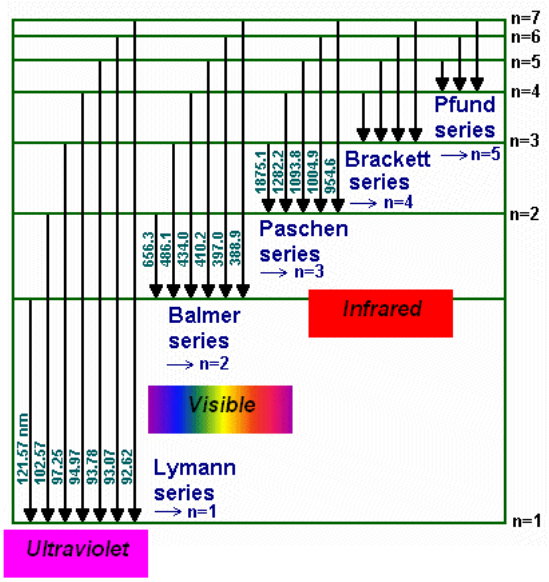


Figure A. 5 Energy levels of Hydrogen atom with the wavelength associated to each emission line of the different series.

When a plasma is induced in air-hydrogen mixture at high-pressure (>1 bar), the spectra are characterized by additional contributions due to nitrogen and oxygen content species. More in details, the emissions are determined by the sum of all the radiative phenomena occurring in the mixture: atomic continuum, molecular continuum, atomic lines and molecular bands. The atomic continuum results from the combination of the free-free radiation (also called Bremsstrahlung) and the free-bound radiation (also called recombination continuum) [109] - [110]. The bremsstrahlung is caused by the collision between a free electron and an ion. The resulting emission is called free–free radiation because the electron is not captured by the ion and is free both before and after the

interaction. The Bremsstrahlung spectrum has typical exponential behaviour, like a Planck's curve. Instead, the free-bound radiation occurs when an electron collides with an ion and is captured by forming an ion or an atom. The molecular continuum is very weaker than the atomic continuum and does not effectively affect the plasma spectral behaviour in the UV-Visible range. Regarding the atomic lines, their occurrence and shape are function of the plasma temperature and environment pressure; likewise, more complex is the mixture and more relevant is the overlapping between the lines in a system that can also appear as a sort of thin band.

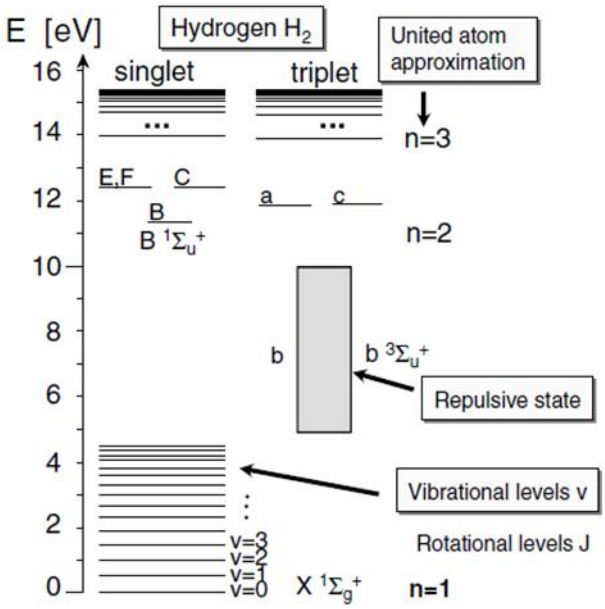


Figure A. 6. Example of an energy level diagram of Hydrogen molecule [111].

With reference to molecular bands, these are due to radiative transitions among several energy levels that are properly identified; the electronic levels are usually abbreviated by upper- and lower-case letters, where X is generally ground state [112]. Due to the additional degrees of freedom with respect to atoms, each electronic state contains vibrational levels (labelled with v) and each vibrational level contains rotational levels (labelled with J) which appear with decreasing energy distances. Figure A. 7 shows the energy level diagram for Hydrogen molecule where $X^1\Sigma_g^1$ is the ground state. The state $b^3\Sigma_u^+$ is repulsive and can be achieved with relatively low energy; when molecules reach this state then dissociate. Details on the rules for distinguishing between permitted and prohibited transitions are reported in [113].

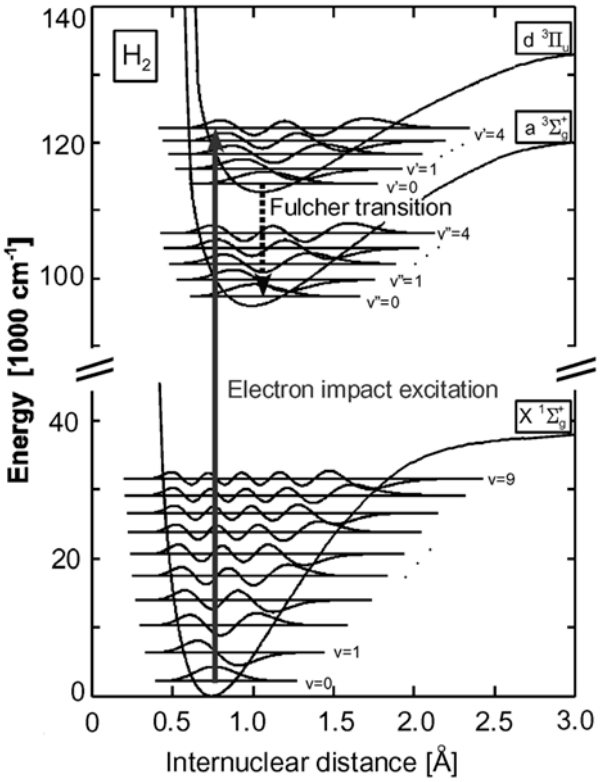


Figure A. 7. Molecular excitation and radiation for the ground state and two excited states of molecular hydrogen [111].

In case of diatomic molecule, such as $H_2$, $N_2$ and $O_2$, the internuclear distance of the two nuclei is another parameter to consider for defining the energy levels and, as a consequence, the associated potential curves. Figure A. 7 shows energy levels of ground state and two electronically excited states of hydrogen together with the vibrational levels. Under the hypothesis that the electron impact excitation process and the decay by spontaneous emission do not modify the internuclear distance, the processes of excitation and de-excitation can be considered as vertical lines in the diagram of Figure A. 7. Thus, the de-excitation of electronically excited molecules can follow other radiative mechanisms that can result in $H_2$ Fulcher band emissions. The $H_2$ Fulcher band is generally not considered for plasma diagnostics because it is difficult to diagnose, given its limited brightness, as shown in Figure A. 8. However, in this work, the wide range of spectral acquisition was used for simultaneously detecting multi-species features, even if this approach affects the possibility of resolving the several fine lines that constitute the Fulcher band (See Figure A. 9).

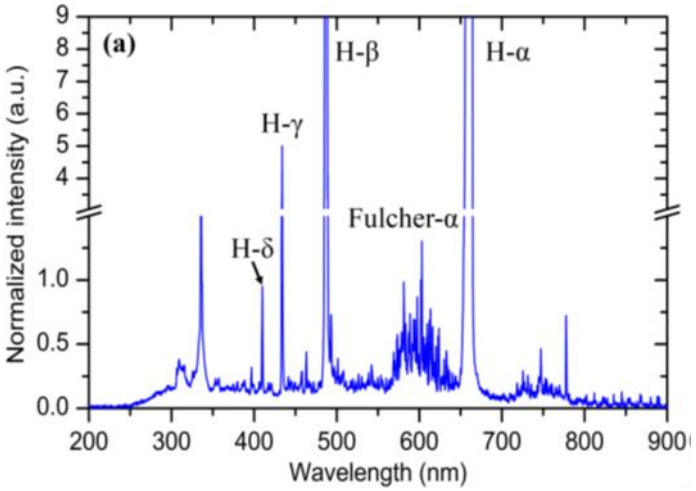


Figure A. 8. $H_2$ plasma spectrum detected at 2Pa gas pressure. From [114].

It should be noted, that when a plasma is induced in air-hydrogen mixtures, the detected spectra are characterized by additional contributions of nitrogen and oxygen species. The molecular systems (such as $N_2$ first- and second-positive, $N_2$+ Meinel first- and second-negative, O2 Schumann–Runge and NO γ->ε) cover the spectral range from vacuum UV to Infrared [115]. Moreover, three bands centred around 565 nm, 510 nm and 336 nm can be detected due to the deexcitation of electronically NH3 (Schuster band [116]), $NH_2$ radicals and NH radicals, respectively (See Figure A. 9).

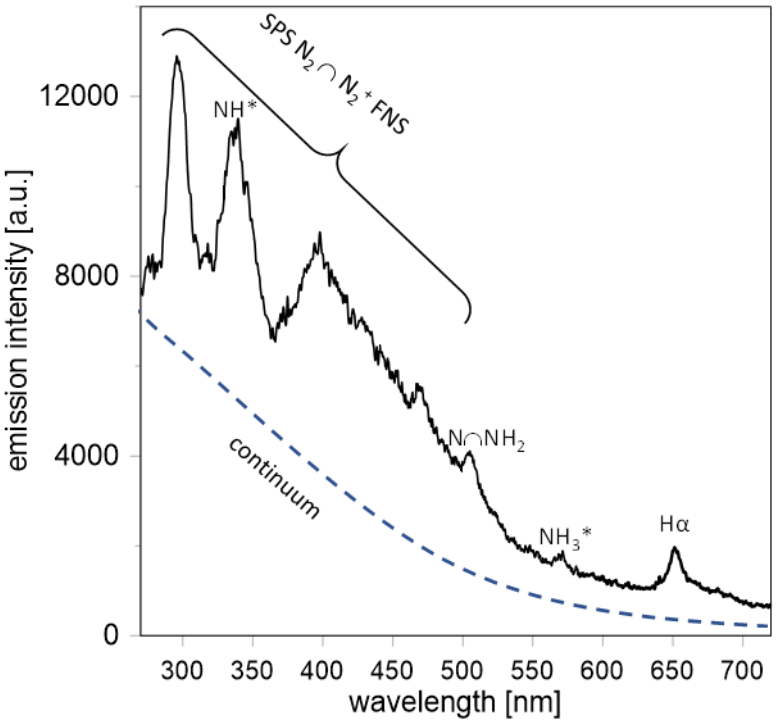


Figure A. 9. Typical UV-Visible emission spectrum detected in region near the plug in the first 16μs after the spark timing fixed at 10 CAD BTDC (engine speed 2000 rpm and λ≅3.2).

The energy threshold required for reaching the condition for inducing $H_2$ Balmer α radiative transitions was estimated around 16.6 eV; this parameter ranged between 13.8 and 14.5 eV for the Fulcher α band. Thus, the occurrence of the different spectral markers can be coarsely associated to the energy transferred from the discharge to the surrounding gas.

When plasma is induced in specific conditions, such as those typical of the combustion chamber of a spark ignition engine, the discharge can initiate a combustion process that starts with the flame kernel inception. Hydroxyl radicals represent the well-known markers of this phenomenon; the photon emission from the excited OH* ranges from 280 nm to 330 nm but the most intense (0,0) band is identified by a red-degraded band head located at 306.4 nm. Generally, this prominent band emission is used as an indicator of flame condition thanks to its strong stable signal intensity and negligible spectral overlap with other spectral evidence [117].

# Appendix B

## B.1 PIV optical technique: applied methodology

The cross-correlation algorithm was applied to evaluate the displacement of tracer particles; the software used for this purpose was the Matlab tool PIVlab v2.61. The working principle of this algorithm is based on the size of single particles and the user defined interrogation area (IA). To render the images suitable for this methodology, it is necessary to post process the scattered frames through various steps aimed at improving the image properties and defining the centre of the reference system as shown in Figure B.1. The jet was put in the foreground by using the contrast limited adaptive histogram equalization (CLAHE) and auto-contrast (AC) algorithms. The first algorithm is an image pre-processing technique that improves the contrast in images. This elaborates several histograms, each corresponding to a distinct region of the raw image and uses these to redistribute the luminous values of the image [118]. The AC algorithm linearly stretches and offsets the image intensities. For example, for an 8-bit

image the algorithm set the stretch (contrast) and offset (intensity) correction parameters in order that in the post processed image the 5th percentile will be equal to 0, and the 95th percentile to 255. The next step regarded the definition of the region of interest (ROI). This is the area within which the software performs the cross-correlation analysis. For the specific analysis of He jets, the ROI was set at a size of 50x75 mm and the centre of the reference system was fixed on the nozzle tip, as shown in Figure B.1. The diameter of the nozzle tip was used for calibrating the spatial resolution of the PIV images, by defining the pixel/millimetres ratio. Next, it was necessary to choose the dimensions of the interrogation area (IA), as it defines the size of the sub-cells that compose the images. To improve the quality of the results, it was decided to use a square-shaped IA with a multi-step approach. With this methodology the software starts performing the cross-correlation analysis by imposing an initial oversized interrogation area (defined by the user). This preliminary operation delivers a "rough" vectors distribution; then the software repeats the cross-correlation step with a reduced size of the IA (normally it gets halved with respect to the initial value) thus resulting in a more detailed vector distribution. This working principle makes it possible to define a multi-step approach; its major advantage consists in the gradual increase in accuracy of the results achieved by evaluating the agreement of each vector plot generated during computational operations. In view of this, a 3-steps cross-correlation approach was used. The starting size of the IA was fixed at 64x64 pixels, then decreased to 32x32 and finally to 16x16 pixels. A 25% overlap between neighbouring cells was applied for the correlation of the two consecutive frames. It is important to emphasize that the theory suggests that the IA should be chosen to contain at least 10-20 particles. Given the pixel/mm ratio of around 20, the 16x16 pixel IA (≈ square of 0.8 mm per side) was calculated to contain from 9 to 25 particles, depending on the uncertainty of the particle seeder (size of particles detailed in 3.2.1 Constant volume chamber).

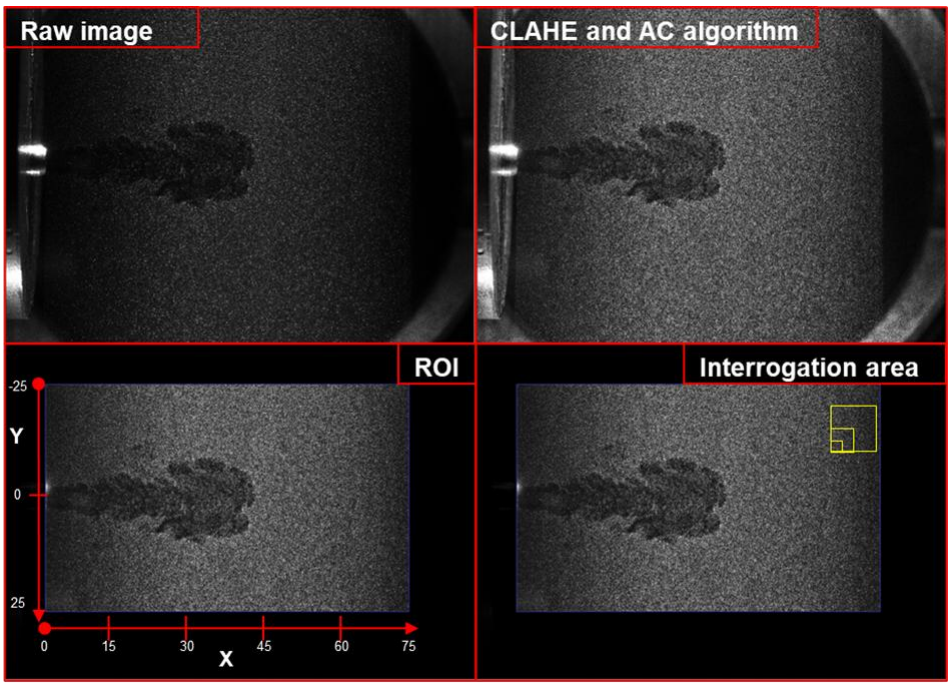


Figure B.1. Steps of the PIV image post processing procedure.

Figure B.2 shows the influence of the interrogation area on the PIV results. When choosing an IA that is too large, the velocity magnitude itself does not change significantly, with peaks that are within the same range. On the other hand, there would be a loss of information about the distribution of vortex structures over several areas. As the size of the IA is reduced, the improved spatial resolution of the vector mesh allows for a detailed understanding of the local phenomena, but it also requires a precise regulation of the particle seeder flowrate to avoid an excessive release of tracers inside the chamber. At this stage, the vector plots drawn from cross-correlation analysis reflect the displacement carried out by the vegetable oil particles following the jet induced motion. It is worth noting the description of the phenomenon observed near the nozzle tip. During the preliminary tests, when the injector was triggered, most part of the tracer particles was pushed away. In this condition the software was unable to carry out a reliable cross-correlation analysis, resulting in the presence of several spur vectors. This phenomenon was observed to occur for each conditions examined, regardless of the PR. Based on the latter parameter, the extension of this region was defined in a range from 5 to 15 mm.

Concerning the edge detection required for measuring the gas jet penetration and plume angle, it was not possible to directly obtain this information from the raw data. In fact, the high density of the pixels and the local inhomogeneity that

characterize this type of analysis, caused the raw images to be taken as point-like from the optical software, thus making it impossible to define a coherent border between the gaseous jet and surrounding air. For this reason, edge detection was performed using a dedicated code written in the Matlab environment. Starting from the coordinates corresponding to the centre of the reference system, proceeding along the axis of the injector with a step equal to that defined by the spatial resolution, the code detected the first and last point to overcome a specific velocity threshold defined by the user. This value was set to be equal to 20% of the maximum velocity, calculated by averaging the 20 pair of frames. Figure B. 3 illustrates how the resulting edges correctly define the jet, prioritising the measurement accuracy of penetration at the expense of a limited loss of accuracy alongside the borders.

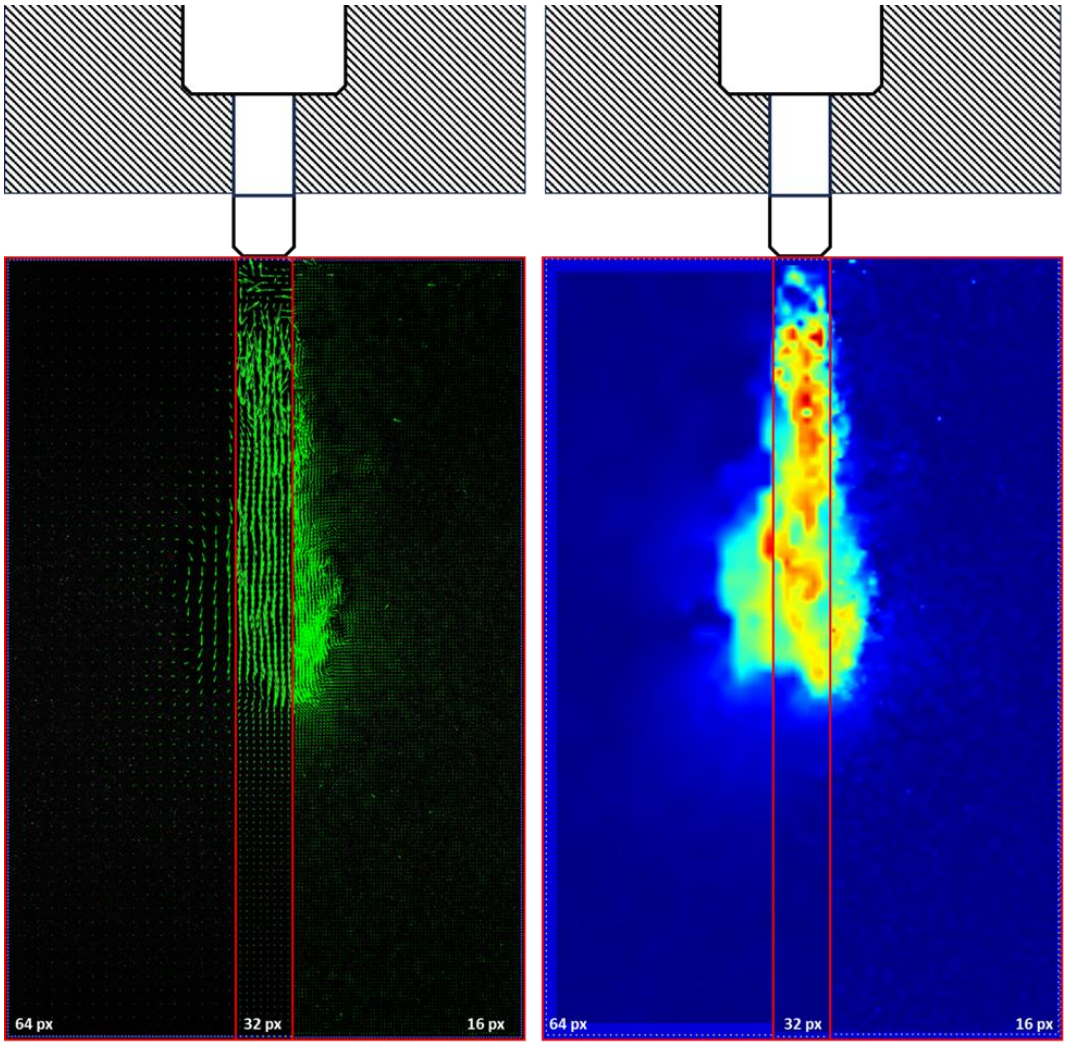


Figure B.2. Influence of the interrogation area dimension on vector distribution (left) and velocity magnitude (right).

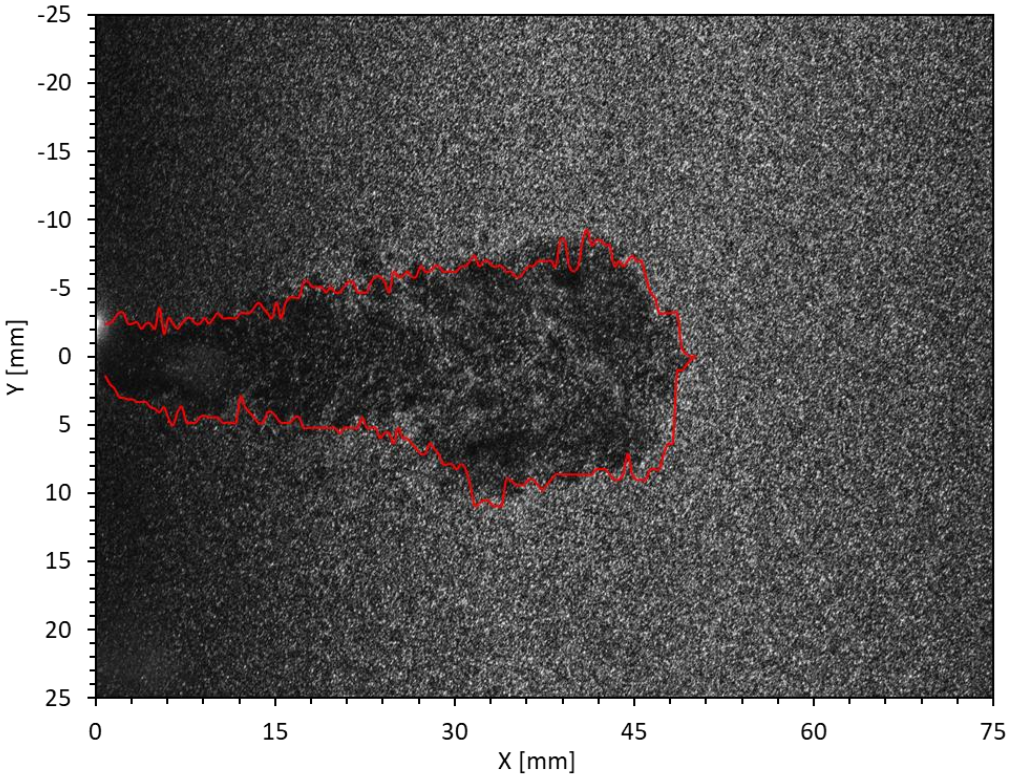


Figure B. 3 Edge detection for first geometry. Operative condition:4.0 ms aSOE, PR5, Single pair of frames.